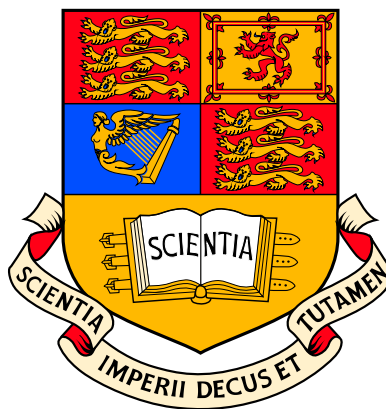


Ion Acceleration from High Intensity Laser Plasma Interactions: Measurements and Applications

Louise Willingale



August 2007

Submitted in partial fulfilment of the requirements for the degree of Doctor of
Philosophy of the University of London and for the Diploma of Membership of the
Imperial College London

Department of Physics
Imperial College London
Prince Consort Road
London SW7 2BZ

The copyright of this thesis rests with the author and no quotation from it or
information derived from it may be published without prior consent of the author.

Abstract

This thesis presents measurements of high energy ion beams accelerated from high intensity laser interactions, with underdense through to near critical density plasmas, and also presents an application of laser generated ion beams.

The first experimental measurements of longitudinally accelerated ion beams from high intensity ($\sim 10^{20} \text{ Wcm}^{-2}$) laser interactions with an underdense ($0.04n_c$) helium plasma are presented. The ion beam was found to have a maximum energy for He^{2+} of (40_{-8}^{+3}) MeV, with the highest energy ions being collimated to a cone of less than 10° . Two dimensional particle-in-cell simulations show that additional effects, due to the time varying magnetic field associated with the fast electron current, enhance the accelerating electric field and provides a focusing mechanism on the ions.

Very low density foam targets were used to investigate proton acceleration from near to critical density plasmas. Experimental results show a decrease in acceleration efficiency just above the critical density. Simulations of the interactions show the proton acceleration is very sensitive to the ability of the laser to propagate through the plasma. The lowest density foams allow the best laser propagation, thus enabling proton beams to be accelerated to energy and numbers comparable to those from a solid target.

The suitability of a laser generated proton beam for the measurement of self-generated magnetic fields in laser generated plasma has been investigated. The technique was then used to study a novel magnetic reconnection geometry using two laser beams. Proton probing provides evidence for the formation of the reconnection layer and the corresponding instabilities.

The role of the author

This section describes the contribution of the author to this thesis. The Vulcan laser system requires a large team of people to perform the experiments, with the experimental data being collected with the help of the co-experimenters, and the technical assistance being provided by the Central Laser Facility staff. The author was involved in the planning, setting up and running of the experimental diagnostics. All of the ion diagnostics were fielded by the author and the analysis of the presented data was performed by the author, unless stated otherwise. In particular, diagnostics other than the proton probing contained in chapter 6 were fielded and analysed largely by P. M. Nilson. The author also helped to set up and run many of the other diagnostics run on the experiments and in addition, the author was responsible for running many of the experiments, either as the operator or deputy operator of the target area. The OSIRIS code was developed by the OSIRIS consortium (UCLA/USC/IST). The OSIRIS simulations presented in this thesis were all run and analysed by the author.

Declaration

I hereby certify that the material of this thesis, which I now submit for the award of Doctor of Philosophy, is entirely my own work unless otherwise cited or acknowledged within the body of the text.

Signed,

Louise Willingale

21st August 2007

Publications

The following publications present work discussed in this thesis:

1. **L. Willingale**, S. P. D. Mangles, P. M. Nilson, R. J. Clarke, A. E. Dangor, M. C. Kaluza, S. Karsch, K. L. Lancaster, W. B. Mori, Z. Najmudin, J. Schreiber, A. G. R. Thomas, M. S. Wei and K. Krushelnick, *Collimated Multi-MeV Ion Beams from High-Intensity Laser Interactions With Underdense Plasma*, Physical Review Letters, **96**, 245002 (2006)
2. **L. Willingale**, S. P. D. Mangles, P. M. Nilson, R. J. Clarke, A. E. Dangor, M. C. Kaluza, S. Karsch, K. L. Lancaster, W. B. Mori, Z. Najmudin, J. Schreiber, A. G. R. Thomas, M. S. Wei and K. Krushelnick, *Comment on “Collimated Multi-MeV Ion Beams from High-Intensity Laser Interactions With Underdense Plasma”*, Physical Review Letters, **98**, 049504 (2007)
3. P. M. Nilson, **L. Willingale**, M. Kaluza, C. Kamperides, S. Minardi, M. S. Wei, M. Notley, S. Bandyopadhyay, M. Sherlock, R. J. Kingham, M. Tatarakis, Z. Najmudin, W. Rosmus, R. G. Evans, M. G. Haines, A. E. Dangor and K. Krushelnick, *Magnetic Reconnection and Plasma Dynamics In Two Beam Laser-solid Interactions*, Physical Review Letters **97**, 255001 (2006)

The following publications present work that the Author participated in but is not presented in this thesis:

4. P. M. Nilson, S. P. D. Mangles, **L. Willingale**, M. C. Kaluza, A. G. R. Thomas, Z. Najmudin, R. G. Evans, A. E. Dangor, K. Krushelnick, M. Tatarakis, R. J. Clarke, K. L. Lancaster, C. Hernandez-Gomez, S. Karsch, J. Schreiber,

Optical probing of high-intensity laser interactions with underdense plasmas using the VULCAN petawatt laser facility, Journal De Physique IV, **133**, 543 (2006)

5. M. S. Wei, J. R. Davies, E. L. Clark, F. N. Beg, A. Gopal, M. Tatarakis, **L. Willingale**, P. M. Nilson, A. E. Dangor, P. A. Norreys, M. Zepf and K. Krushelnick, *Reduction in proton acceleration in high intensity laser interaction with double-layer solid targets*, Physics of Plasmas **13**, 123101 (2006)
6. J. Pasley, P. M. Nilson, **L. Willingale**, M. G. Haines, M. Notley, M. Tolley, D. Neely, W. Nazarov, O. Willi, *Streaked extreme ultraviolet imaging of the motion of low-Z foam buffered indirectly driven intermediate and high-Z payloads*, Physics of Plasmas, **13**, 032702 (2006)
7. P. M. Nilson, **L. Willingale**, M. Kaluza, C. Kamperides, S. Minardi, M. S. Wei, P. Fernandes, M. Notley, S. Bandyopadhyay, M. Sherlock, R. J. Kingham, M. Tatarakis, Z. Najmudin, W. Rosmus, R. G. Evans, M. G. Haines, A. E. Dangor and K. Krushelnick, *Plasma dynamics and jet formation in two-beam laser-solid interactions*, submitted to Physics of Plasmas (2007)
8. B. Dromey, S. Kar, C. Bellei, D. C. Carroll, R. J. Clarke, J. S. Green, S. Kneip, K. Markey, S. R. Nagel, P. T. Simpson, **L. Willingale**, P. McKenna, D. Neely, Z. Najmudin, K. Krushelnick, P. A. Norreys and M. Zepf, *Bright multi-keV harmonic generation from relativistically oscillating plasma surfaces*, Physical Review Letters, **99**, 085001 (2007)

Acknowledgments

I would like to thank my supervisors Prof. Karl Krushelnick and Dr. Zulfikar Najmudin. They, along with Bucker Dangor, have offered me sound advise throughout my PhD and I am extremely grateful for their guidance and support.

Thanks to John Pasley and Phil Nilson for introducing me to the Vulcan laser system on my first experiment there. On the many subsequent experiments, I am grateful to Stuart Mangles, Kate Lancaster, Stefan Karsch, Jörg Schreiber, Alec Thomas, Ming-Sheng Wei, Malte Kaluza, Christos Kamperidis, Michael Tatarakis, Paulo Fernandes, Sabrina Nagel, Claudio Bellei, Ken Marsh, Nelson Lopes and Stefan Kneip for all of the support and assistance you've given me. It has been a pleasure to work with you all and it's a bonus that I've made some great friends too. I'd particularly like to single out Stuart, Phil and Alec to who I am especially grateful, for being so patient with me, not only during the (long) experiments, but during the analysis as well.

I gratefully acknowledge the OSIRIS consortium (IST Portugal, UCLA and USC) for the use of the OSIRIS code. I am also grateful to Roger Evans and Wojciech Rozmus for the helpful plasma physics discussions. Most of the members of the Imperial College Plasma Physics group, past and present, have at some stage of my PhD provided assistance in some way, discussions, advise and encouragement, so many thanks to you all.

Of course the experiments would have never worked without the expertise of the Central Laser Facility staff. The target area staff, Rob Clarke, Rob Heathcote, Margaret Notley, Dave Neely and Sujit Bandyopadhyay provided invaluable assistance for making the experiments successful. Thanks to the Vulcan laser staff who have

spent hours bashing the OPCPA into shape, the engineering staff were incredibly patient with my last minute requests and the target preparation staff who make the tiny things. Thanks to the Coseners house staff for giving me a pleasant second home. I am very grateful for the foam targets produced by Wigen Nazarov.

I am obliged to Nerena Moodley, who has patiently proof read this thesis to find my grammar and spelling errors. Hopefully not too many remain.

I am grateful to the EPSRC for funding my PhD and to AWE for my CASE student award.

Finally, Alec gets another thank you for being so supportive during my whole PhD. You are my rock.

Contents

1	Introduction	22
1.1	Particle acceleration	23
1.1.1	Electron acceleration	23
1.1.2	Ion acceleration	24
1.2	Inertial confinement fusion	26
1.3	Laboratory astrophysics	30
1.4	Thesis outline	32
2	Theoretical background	34
2.1	Laser plasma basics	34
2.1.1	Description of the laser field	34
2.1.2	Ionisation processes	35
2.1.3	Interaction of a single electron with a laser field	36
2.1.4	Laser propagation in a plasma	38
2.1.5	Ponderomotive force	39
2.1.6	Collective plasma effects	40
2.2	Intense laser interactions with underdense plasmas	40
2.2.1	Self-focusing and optical guiding	40
2.2.2	Parametric instabilities	43
2.2.3	Filamentation	44
2.2.4	Electron acceleration	45
2.2.5	Ion acceleration in the Coulomb explosion	46
2.2.6	Ion shock acceleration	48

2.2.7	Ion acceleration in an induced electric field	50
2.3	Intense laser interactions with overdense plasmas	51
2.3.1	Absorption mechanisms	51
2.3.2	Electron transport	55
2.3.3	Ion acceleration from solid targets	58
2.3.4	The $\nabla n_e \times \nabla T_e$ magnetic field generation mechanism	62
2.4	Magnetic field reconnection	63
3	Experimental methods	67
3.1	The Vulcan laser	67
3.1.1	Chirped pulse amplification	68
3.1.2	Optical parametric chirped pulse amplification	68
3.1.3	The Vulcan Petawatt laser	69
3.1.4	The Vulcan Target Area West (TAW) facility	74
3.2	Ion detectors	75
3.2.1	CR39	75
3.2.2	Radiochromic film	77
3.2.3	Image plate detector	78
3.3	Ion diagnostics	79
3.3.1	Thomson ion spectrometer	79
3.3.2	Charged particle spectrometer	84
3.3.3	Imaging detector stacks	85
3.3.4	Activation detector stacks	86
4	Longitudinal ion acceleration	92
4.1	Previous work	92
4.2	The experiment	95
4.2.1	Laser parameters	95
4.2.2	Supersonic gas jet targets	96
4.2.3	Diagnostics	98
4.3	Experimental results	99
4.4	PIC simulations	103

4.4.1	Simulation setup	103
4.4.2	Simulation results	105
4.5	Discussion	118
4.5.1	Comparison to sheath acceleration models	118
4.5.2	Effect of laser intensity and pulse length	119
4.5.3	Plasma density effects	122
4.5.4	Plasma ramp length effects	122
5	Near-critical density ion acceleration	124
5.1	Previous work	125
5.2	The experiments	127
5.2.1	Laser parameters	128
5.2.2	Low density foam targets	128
5.2.3	Diagnostics	130
5.3	Experimental results	133
5.3.1	2005 experimental results	133
5.3.2	2006 experimental results	134
5.4	PIC simulations	140
5.4.1	Simulation setup	140
5.4.2	Simulation results	141
5.5	Discussion	147
5.5.1	Effect of the foam structure	148
5.5.2	Laser propagation at near critical density	150
5.5.3	Transition through the critical density	152
5.5.4	Proton beam structure	153
6	Proton radiography	155
6.1	Previous work on magnetic field measurements from laser plasma in- teractions	156
6.2	Experimental method	157
6.2.1	Experimental layout	157
6.2.2	Proton deflectometry diagnostics	159

6.2.3	Other experimental diagnostics	163
6.3	Proton probing results	167
6.3.1	A single beam interaction on aluminium targets	169
6.3.2	Time dependance of the two beam interaction on aluminium targets	171
6.3.3	Spot separation effects on the two beam interaction from aluminium targets	172
6.3.4	Proton probing of gold targets	173
6.4	Other experimental results	174
6.4.1	Optical probe data	174
6.4.2	Thomson scattering data	177
6.4.3	X-ray pinhole camera data	179
6.5	Discussion	179
6.5.1	Magnetic field measurements	180
6.5.2	Evidence for magnetic reconnection	184
7	Summary	192
7.1	Longitudinal ion acceleration from underdense plasma	192
7.2	Longitudinal ion acceleration from near-critical density plasma	194
7.3	Proton radiography of a two-beam laser interaction	195
	Appendices	198
	A Single electron in a laser field	198
	B Inverse bremsstrahlung absorption	201
	C Target normal sheath acceleration	203
	Bibliography	206

List of Figures

1.1	A schematic of the fast ignition approach to inertial confinement fusion: (a) shows the DT fuel being compressed by radiation to high density, (b) shows the heating beam being guided by the cone to the dense plasma core and (c) shows the ignition of the dense fuel and the burn wave consuming the fuel, releasing fusion energy.	30
2.1	The three main Optical Field Ionisation (OFI) processes: (a) multiphoton ionisation, (b) tunneling ionisation and (c) barrier suppression ionisation.	36
2.2	Plots for the case of a plane, linearly polarised electromagnetic wave showing (a) the trajectory of an electron and (b) the “figure-8” trajectory in the drift frame.	38
2.3	The effect of (a) diffraction and (b) self-focusing on a Gaussian laser beam in plasma (figure adapted from P. Gibbon’s book [1]).	42
2.4	The transmitted spectra through a plasma with a density of $3.2 \times 10^{19} \text{ cm}^{-3}$. The fundamental laser frequency is labeled ω_0 and ω_1 and ω_2 are the first and second satellites respectively (data is courtesy of B. Walton).	44
2.5	A single electron trajectory, tracked from a particle in cell simulation to illustrate the betatron resonance mechanism (figure courtesy of S. P. D. Mangles).	46
2.6	A schematic showing resonance absorption of p-polarised light obliquely incident to the plasma gradient at an angle of θ	53

2.7	A schematic showing the main mechanisms for forward ion acceleration for a high-intensity laser interaction with solid target.	58
2.8	The $\nabla n_e \times \nabla T_e$ magnetic field generation mechanism.	62
2.9	A schematic of the Sweet-Parker model for magnetic reconnection. . .	65
2.10	A schematic of the Petschek model for magnetic reconnection.	66
3.1	A schematic of the chirped pulse amplification (CPA) technique. . . .	68
3.2	A schematic of the Vulcan petawatt laser system.	70
3.3	(a) Proton stopping power in CR39 and (b) the energy deposition of protons of different energies as they pass through mylar.	76
3.4	A schematic showing the structure of (a) the MD-55-2 type and (b) the HD-810 type GafChromic dosimetry film.	77
3.5	The photo-stimulated luminescence process	78
3.6	The Thomson ion spectrometer. The magnets are shown in green and the electric plates are shown in blue.	80
3.7	An example of the ion tracks from a Thomson ion spectrometer: (a) shows a scan of a CR39 from a shot onto a foam target (the important features are labeled) and (b) shows the same piece of CR39 with the analytic solutions for different ion species overlaid.	81
3.8	Helium ion pits from a laser gas-jet experiment, as seen under an optical microscope.	83
3.9	Schematic of the basic design of the electron spectrometers (courtesy of S. P. D. Mangles, based on a technical drawing courtesy of B. Fell, CCLRC Rutherford Appleton Laboratory).	84
3.10	Cross section data for the reactions caused by incident protons and γ s likely to generate measurable contributions to the activation. The fits to the reaction with ^{63}Zn products are shown.	88
4.1	Schematic of the Vulcan Petawatt target vacuum chamber (based on a technical drawing by B. Fell, CCLRC Rutherford Appleton Laboratory). . .	95
4.2	A cross section of a conical gas jet nozzle.	96

4.3	Gas jet interferometry: (a) is an interferogram of a 2 mm nozzle with a backing pressure of 100 bar, (b) is the phase map obtained from the interferogram and (c) show the neutral gas density at different heights above the nozzle recovered using an inverse Abel transform (images are courtesy of M. C. Kaluza).	97
4.4	Schematic of the experimental setup showing the on-axis charged-particle spectrometer (based on a figure by S. P. D. Mangles).	98
4.5	The electron spectra for the shot into a helium plasma of density $4 \times 10^{19} \text{ cm}^{-3}$. The temperature of the electron spectra at 0° is 7.4 MeV and at 10° is 9.8 MeV.	100
4.6	An optical microscope image of the pits etched into the CR39 to show the identification of the He^{2+} and the He^{1+} ion pits.	101
4.7	He^{2+} ion spectra at angles of 0° , 10° , 45° and 90° to the laser axis.	101
4.8	He^{1+} ion spectra at angles of 0° , 10° , 45° and 90° to the laser axis.	102
4.9	A polar plot showing the number of He^{2+} ions at different diagnostic angles for 2 MeV and 5 MeV ions.	102
4.10	Results from a simulation of a $0.05n_c$ plasma showing (from left to right) the azimuthal magnetic field, the longitudinal electric fields, the radial electric fields, the electron number density and the ion number density. These are all shown for each time step in the simulation, 0.5 ps, 1.0 ps, 1.5 ps, 2.0 ps and 2.5 ps. The simulation box size is $251 \mu\text{m} \times 251 \mu\text{m}$	107
4.11	The longitudinal electric field components at 1 ps: (a) the total longitudinal electric field seen in the simulation, E_{sim} , (b) the charge separation contribution, E_ρ and (c) the time varying magnetic field contribution, $E_{\dot{B}}$. The simulation box size is $251 \mu\text{m} \times 251 \mu\text{m}$	108
4.12	(a) The simulation longitudinal electric field and the relative contributions to the longitudinal electric field from (b) the charge separation and (c) the time-varying magnetic field. These are shown as a function of time, averaged in the radial direction over a $34 \mu\text{m}$ wide selection in the centre of the simulation box.	109

- 4.13 He²⁺ ion p_x against p_y momentum at times of 0.5 ps, 1.0 ps, 1.5 ps, 2.5 ps, and 3.5 ps. 110
- 4.14 He²⁺ ion p_x against x -direction at times of 1.5 ps, 2.5 ps, and 3.5 ps. The initial boundaries of the rear density ramp are shown by the green dashed lines. 111
- 4.15 Simulated He²⁺ ion spectra at 3.5 ps for plasma densities of (a) $0.1n_c$, (b) $0.05n_c$ and (c) $0.01n_c$ 112
- 4.16 The simulated proton spectra for the different ramp lengths at a time when the ion front has expanded $100 \mu\text{m}$ 114
- 4.17 The half-width divergence angles as a function of energy for the different ramp lengths at a time when the ion front has expanded $100 \mu\text{m}$. 114
- 4.18 Time histories of the longitudinal electric field, azimuthal magnetic field and radial electric field for each of the ramp lengths. The longitudinal electric field is averaged over the central $50 \mu\text{m}$ of the width of the box and the azimuthal magnetic field and radial electric field are averaged over a $200 \mu\text{m}$ length centred on each of the ramps. . . . 115
- 4.19 The maximum longitudinal electric fields for each of the ramp lengths; for the $0 \mu\text{m}$ ramp this is at 1.7 ps, for the $100 \mu\text{m}$ ramp this is at 2.2 ps and for the $200 \mu\text{m}$ ramp this is at 2.5 ps. The initial rear density ramp positions are shown for each simulation. The simulation box size is $598 \times 168 \mu\text{m}$ 116
- 4.20 The azimuthal magnetic fields, 2.3 ps after the start of the simulation for density ramp lengths of $0 \mu\text{m}$, $100 \mu\text{m}$ and $200 \mu\text{m}$. The initial rear density ramp positions are shown for each simulation. The simulation box size is $598 \times 168 \mu\text{m}$ 117
- 4.21 The focusing radial electric fields for density ramp lengths of $0 \mu\text{m}$, $100 \mu\text{m}$ and $200 \mu\text{m}$ at 2 ps into the simulations. The initial rear density ramp positions are shown for each simulation. The simulation box size is $598 \times 168 \mu\text{m}$ 117
- 4.22 On-axis electron spectra from three shots with different laser energies into a $2 \times 10^{19} \text{ cm}^{-3}$ helium gas jet (data courtesy of S. R. Nagel). . . 119

4.23	A self-emission image of a helium plasma interaction with a $n_e = 4 \times 10^{19} \text{ cm}^{-3}$ using a 450 TW, 650 fs duration laser pulse (data courtesy of P. M. Nilson). This shows the laser initially guiding over a distance longer than the Rayleigh range ($\approx 30 \mu\text{m}$) before breaking up into a pair of filaments.	120
4.24	Electron beam profiles from an interaction with helium plasma of $n_e = 1.5 \times 10^{19} \text{ cm}^{-3}$. The circular contours mark 3° , 5° , 10° and 15° and are centred on the principle electron beam at that energy. The images show the signal above the given energy cutoff and are normalised to the peak signal (data courtesy of S. P. D. Mangles). . .	121
5.1	(a) The foams were mounted in washers of $250 \mu\text{m}$ thickness, and (b) and (c) are high magnification SEM images showing the structures in the low density foams (gold coated). The $5 \mu\text{m}$ scale is similar to the focal spot diameter (images taken by C. Spindloe).	128
5.2	The stack composition for the 2005 campaign and the range at which different energy protons are stopped.	130
5.3	The 2006 experimental set up for (a) the foam targets and (b) the mylar targets.	131
5.4	The number of ^{63}Zn atoms per incident proton as a function of proton energy for each layer in the activation stack.	132
5.5	The electron spectra taken on the laser axis during the 2005 campaign. (On-axis means in the target normal direction for the foam shots, at 45° to the back surface for the mylar.)	133
5.6	The initial number of ^{63}Zn atoms per μm obtained from the activation stacks for the different targets.	135
5.7	Proton spectra obtained from the activation stacks calculated by finding best fit to the measured initial number of ^{63}Zn	136
5.8	The maximum proton energy at 10^9 per MeV and the conversion efficiency of laser energy into protons with $> 4 \text{ MeV}$ against foam density and maximum plasma density for the stack shots.	137

- 5.9 Proton beam profile from the RCF interleaved in the activation stacks. The labels at the top show the target type and laser energy on target. The labels down the side show the proton energies detected by the layer. The angles at the bottom indicate the FWHM of the proton beams for the > 22 MeV protons. 138
- 5.10 The proton beam profiles recorded on the second copper layer in the stacks from the 20 mg/cm^3 , 45 mg/cm^3 and 100 mg/cm^3 foam targets. (Beam intensity not on the same scale) 138
- 5.11 The top row of images show scattered ω light from the burn paper during the shots (scale is normalised for the filtering and laser energy). The lower row of images are background corrected burn paper images (on the same scale). 139
- 5.12 The z -direction electric field at a time of 1.08 ps into the moving box simulations for initial plasma densities of $0.5n_c$, $0.9n_c$ and $1.5n_c$. (NB: the full length of the box is not shown.) 142
- 5.13 For a time of 1.08 ps into the $0.5n_c$ density simulation showing (a) the z -direction electric field (the laser pulse), and (b) the longitudinal electron momentum, p_x , across the y -direction to show the effect on the laser beam filamentation on the electron acceleration. 142
- 5.14 The longitudinal electric fields seen in the simulations of different density plasmas, (a) $0.9n_c$, (b) $1.5n_c$, (c) $4.5n_c$ and (d) $15n_c$. These are shown as a function of time, averaged in the y -direction over a $17 \mu\text{m}$ wide selection in the centre of the simulation box. The dashed red line shows the position of the leading edge of the laser pulse travelling at c . The pulse peak is approximately 650 fs behind this. 143
- 5.15 The maximum longitudinal electric fields seen in the central region of the simulations and the experimentally measured maximum proton energy at 10^9 per MeV plotted as a function of plasma density. 144

5.16	(a) The ion density at a time of 2.0 ps into the simulation from the $0.9n_c$ plasma density simulation and (b) the longitudinal momentum, p_x , against the y -direction at a time of 1.7 ps into the simulation, showing structure in the accelerated beam.	145
5.17	The ion density at a time of 2.0 ps into the simulation from the $1.5n_c$ plasma density simulation.	146
5.18	From the $4.5n_c$ plasma density simulation showing (a) the longitudinal momentum, p_x , against the x -direction showing the shock accelerated ions from the front surface at a time of 1.5 ps into the simulation, and (b) the ion density at a time of 2.0 ps into the simulation.	147
5.19	The ion density at a time of 1.5 ps into the simulation from the $15n_c$ plasma density simulation.	148
6.1	A schematic of the heater beams and their magnetic field geometry in the reconnection geometry; (a) is a face-on view and (b) is a side-on view.	157
6.2	The multiple beam geometry into the chamber (modified from a CLF engineering drawing).	158
6.3	A schematic showing the rear projection geometry of the proton probing diagnostic.	160
6.4	Proton stopping ranges in the proton detector stacks. Layers A to F are HD-810 type (the active layer is on the front surface) and layers G to N are MD-55 type (the active layer is sandwiched in the middle).	161
6.5	Assuming a thickness, $L = 100 \mu\text{m}$ and $b = 20 \text{ mm}$, then (a) shows magnetic field strength against proton energy for different detector plane deflections and (b) shows detector plane deflections against proton energy for different magnetic field strengths.	163
6.6	A schematic of the Thomson scattering geometry showing the positions of the scattering volumes with respect to the target surface. Shown on the right are the wave vectors for the incident light, \mathbf{k}_i , the scattered light \mathbf{k}_s , and the electron plasma wave, \mathbf{k}	165

- 6.7 The transmission curve for a 10 μm magnesium filter up to a photon energy of 2 keV. 166
- 6.8 RCF pieces from a stack with proton data from a shot with the main interaction on an aluminium target at a time of $t_0 + 500\text{ps}$. The layer labels and proton energy stopped by the RCF are given. 168
- 6.9 The analysis process for the layer J from figure 6.8 showing (a) the raw image, (b) a bandpass filtered image, showing the enhanced mesh structure, (c) a trace of the warped mesh pattern (yellow) over the enhanced image and the laser focal spot (red), (d) the warped mesh matched with a regular grid, (e) the magnetic field map in units of $\mu\text{m MG}$ with the overlaid grid on top and (f) the magnetic field map with the green areas indicating where no measurement could be made. 169
- 6.10 Proton radiographs of single spot interactions using the proton energy indicated on the images to look at times after t_0 of 50 ps, 100 ps, 500 ps and 800 ps. The top row shows the raw images and the bottom row shows the magnetic field maps. The green areas are regions where no measurement could be made. 170
- 6.11 The product of the magnetic field and the spatial extent ($\mathbf{B}\cdot\mathbf{L}$) against distance from the focal spot for times after t_0 of 50 ps, 100 ps, 500 ps and 800 ps. 171
- 6.12 Proton radiographs of two beam interactions using 9.8 MeV protons to show interactions with focal spot separations of between 350 μm and 450 μm , for times of $t_0 + 100$ ps, $t_0 + 500$ ps, $t_0 + 800$ ps and $t_0 + 1200$ ps as labelled. The top row of images shows the raw image of the RCF and the bottom row shows the images after the bandpass filtering to enhance the mesh structure. 172
- 6.13 Proton radiographs of two beam interactions using 12.2 MeV protons at $t_0 + 100$ ps for various spot separations of 750 μm , 600 μm , 450 μm and 250 μm as shown by the labels at the top. The top row of images are of the raw image of the RCF and the bottom row of images are after the bandpass filtering process to enhance the mesh structure. . . 173

6.14	Proton radiographs of gold target interactions using 9.8 MeV protons at times after t_0 of 0.1 ns and 0.8 ns.	174
6.15	Transverse shadowgrams for spot separations of $\sim 150 \mu\text{m}$, on (a) an aluminium target at $t_0 + 1.5$ ns and (a) a gold target at $t_0 + 2.0$ ns (data is courtesy of P. M. Nilson).	175
6.16	Transverse images for spot separations of $\sim 400 \mu\text{m}$ onto aluminium targets, where (a) shows a shadowgram at a time of $t_0 + 0.4$ ns, (b) shows a deconvolved electron number density map of the midplane plasma region at a time of $t_0 + 0.4$ ns and (c) shows a shadowgram at a time of $t_0 + 1.5$ ns (data courtesy of P. M. Nilson).	176
6.17	For spot separations of $\sim 400 \mu\text{m}$ onto gold targets, where (a) shows a transverse shadowgram at a time of $t_0 + 2.5$ ns and (b) shows an interferogram with an oblique viewing angle so that the spots are aligned at a time of $t_0 + 0.7$ ns (data courtesy of P. M. Nilson).	176
6.18	Experimental data for scattering volume 1, where (a) shows the time resolved raw data. (b) and (c) show lineouts at $t_0 + 1.5$ ns and $t_0 + 2.25$ ns respectively with the experimental data in red and the theoretical fits in black (experimental data is courtesy of M. C. Kaluza and the fit data is courtesy of W. Rozmus).	178
6.19	Experimental data for scattering volume 2, where (a) shows the time resolved raw data and (b) shows the experimental lineout at $t_0 + 1.2$ ns in red and the non-equilibrium theoretical fit in black (experimental data is courtesy of M. C. Kaluza and the theoretical fit is courtesy of W. Rozmus).	179
6.20	Time integrated x-ray pinhole camera images of ~ 1 keV emission from a gold target: (a) is the emission seen side-on and (b) is the emission seen face-on (data courtesy of C. Kamperidis).	180
6.21	The electron density maps of plasma plumes from aluminium targets at times of $t_0 + 100$ ps and $t_0 + 400$ ps (data is courtesy of P. M. Nilson).	181
6.22	A schematic to show the 3 dimensional nature of the jet formation.	189

List of Tables

3.1	A summary of the laser parameters for each of the experiments. . . .	73
3.2	The possible products from reactions with cross sections ≥ 0.1 barns which decay by β^+ emission from proton and γ interactions with ^{63}Cu and ^{65}Cu . The cross section for the interaction and the product decay information is given. The threshold is the lowest energy of p or γ at which a particular reaction can occur.	87
4.1	The normalised units used by OSIRIS.	104
5.1	Table of the foam densities and the corresponding maximum electron number densities assuming a fully ionised plasma.	129
5.2	Table of the activation stack composition used to measure the proton spectra in the 2006 experimental campaign.	132
5.3	Summary of the maximum proton energies seen in the imaging stacks from the 2005 campaign.	134
6.1	Table of the plasma parameters for a typical aluminium plasma created by a single heater beam. The critical surface and coronal parameters are shown for comparison. The estimate that $Z = 13$ and that $T_i = T_e$ were made to complete this table.	185

Chapter 1

Introduction

Modern laser technology can now produce conditions with incredibly high energy densities, which is providing many new regimes to research. Chirped pulse amplification, conceived in the 1980s by Strickland and Mourou at the University of Rochester [2], allows incredibly short laser pulses to be amplified to Petawatt powers. This method stretches the laser pulse in time so amplification to high energy does not damage the gain medium. Finally the pulse is compressed, which increases the power. Terawatt facilities are now common in universities and many Petawatt class lasers are now becoming available for research. Focusing down these high energy, short pulse laser pulses enables intensities exceeding 10^{21} Wcm^{-2} to be achieved [3, 4]. At such high laser intensities, matter is subjected to extreme conditions so that electrons are driven to speeds approaching the speed of light, thus making the interactions highly relativistic.

Many fields of research have resulted from studying these high intensity laser pulses interacting with matter. The electromagnetic fields found in plasmas can be extremely high and are promising for use as a next generation of particle accelerators [5]. Tunable, short duration radiation sources based on free electron lasers or harmonic generation would provide useful diagnostics for many areas of scientific research. The intensities of the next generation of lasers [6] would reach into a regime where the energy densities are so high that production of exotic matter could test quantum electrodynamic (QED) theory [7].

Aside from these interests, the main focus of the experiments presented in this thesis, namely particle acceleration, inertial confinement fusion and laboratory astrophysics, are discussed in more detail in the following sections.

1.1 Particle acceleration

1.1.1 Electron acceleration

Fundamental physics experiments which strive to answer questions about the origins of our universe require large scale facilities (kilometers in length) that cost billions of pounds, such as SLAC in the USA [8] and CERN in Europe [9]. The limitations on these conventional accelerators is the breakdown voltage ($\sim 100 \text{ MVm}^{-1}$) for the accelerating fields, implying that for the next generation of particle accelerators it will be necessary to build even longer and therefore, even more costly facilities. Plasmas may offer an interesting alternative as an acceleration medium because the accelerating fields can be arbitrarily high due to the plasma already being ‘broken down’. First proposed by Tajima and Dawson in 1979 [10], relativistic plasma waves, formed in the wake of a laser, are capable of accelerating electrons to high energies. This is known as the laser wakefield accelerator scheme. Recently, laser technology and experiments have developed sufficiently so that laser plasma wakefield acceleration can produce high energy, low energy spread (i.e. monoenergetic) electron bunches [11–13]. Already, electrons have been accelerated to energies as high as $\sim 1 \text{ GeV}$ in monoenergetic bunches over a short distance of 3.3 cm [14] using this laser plasma scheme. Laser plasma accelerators have very promising consequences, such as reducing the size of particle accelerators from kilometres, to a few metres.

An application of the high energy monoenergetic electron beams generated by laser acceleration is x-ray radiation production by synchrotron radiation. Synchrotron emission has a vast number of applications in science and engineering, ranging from cell biology, disease mechanisms, toxicology, atmospheric research, plant imaging, minerals exploration, high resolution imaging of defects in structures and forensics through to exploring advanced materials such as nanostructures. The

Diamond light source [15] has just opened at the Rutherford Appleton Laboratory in the UK at a cost of £300-million for applications such as these. Table top laser electron accelerators could bring down the cost of such facilities. Free electron lasers, such as DESY in Germany [16], convert high energy electrons into radiation by making the electrons oscillate in a periodic magnetic field. Free electron lasers could also benefit from cheap, tuneable electron beams, making facilities available on a university scale.

1.1.2 Ion acceleration

Acceleration of protons and ions can be achieved, of up to energies of 10's of MeV per nucleon, from laser plasma interactions. At current laser intensities, the ions are too heavy to be accelerated from the laser fields directly, but are accelerated by the longer time scale secondary fields generated as the plasma electrons move under the influence of the laser fields. Perhaps the most investigated ion acceleration mechanism is target normal sheath acceleration (TNSA) [17, 18], which is when laser accelerated fast electrons attempt to leave the plasma, creating a space charge electric field. Collimated proton beams with maximum energy of 58 MeV have been measured from the interaction of a picosecond petawatt laser (peak intensity of $3 \times 10^{20} \text{ Wcm}^{-2}$) with thin foil targets [17]. With shorter pulses from a high-rep rate system, (40 fs, peak intensity of $6 \times 10^{19} \text{ Wcm}^{-2}$), maximum proton energies of up to 10 MeV have been achieved [19]. The efficiency of conversion of the laser energy into the proton beam can be as much as 12% [17, 20]. The transverse and longitudinal emittance for protons with energy $> 10 \text{ MeV}$ has been measured to be $< 0.004 \text{ mm mrad}$ and $< 10^{-4} \text{ eVs}$ respectively, which is at least 100 times better than conventional accelerators [21]. Other ion acceleration mechanisms using laser interactions, such as shock acceleration [22, 23], induced electric fields [24–28] and ponderomotive force mechanisms [29–32], are also under research.

More advanced schemes are being pursued to attempt to generate monoenergetic ion beams through different methods of energy selection. Experimental demonstrations so far have relied on target normal sheath acceleration using reduced mass tar-

gets. Schwoerer et al. [33] used microdot targets to produce a quasi-monoenergetic proton beam and Hegelich et al. [34] carefully prepared the target to achieve a thin carbon layer on a palladium substrate to get a quasi-monoenergetic C^{+5} beam. Other experiments have used energy selection to achieve a quasi-monoenergetic proton beam [35]. Theoretical schemes include using ultra thin targets in the laser-piston regime [36], shaped targets and weighting the mass-to-charge ratio of ions in the target [37].

A wide range of applications for these ion and proton beams are being contemplated, some of which are examined here. Protons and ions are a promising treatment for cancer because they deposit a large amount of energy at a well known localised distance into material. This allows cancerous cells to be targeted, without damaging healthy surrounding tissue. More conventional x-ray radiotherapy radiates healthy tissue in its path and chemotherapy affects the entire body. Proton and ion beams can be carefully controlled to target and destroy only cancerous cells, even internally, without the need for surgery [38–42]. A table-top, high repetition rate laser system capable of producing 200 MeV protons (for the deepest internal cancer treatment) could significantly reduce the size and costs of the treatment facilities making the therapy more widely available. The largest challenge for this to be a successful application of laser generated ion beams lies in generating a large enough flux at the required energy at a high enough rate.

Another medical application is the production of isotopes for positron emission tomography (PET), in which short lived radioactive isotopes decay to produce the positrons used for this powerful imaging technique, enabling areas in the body such as tumors to be mapped. The radionuclides required for PET have very short half lives so they have to be produced close to the PET scanner. At present cyclotrons, which are expensive, create the radionuclides and this limits the availability of PET. It is hoped that using high-repetition rate tabletop laser systems to produce the radionuclides would make treatments more widely available [43–45].

A potentially useful application for laser plasma interactions is proton radiography. Protons are able to diagnose electromagnetic fields as they are deflected by the fields. Laser generated sources are ideal for this proton radiography technique

due to a combination of favourable characteristics. The effective source size of the proton beams is very small, $\sim 3 \mu\text{m}$, meaning that the spatial resolution is very high [46]. The proton beams have a high luminosity and are well collimated with a half divergence angle of between 10° and 15° [47]. The protons are generated on a very short temporal scale, comparable to the laser pulse length ($\lesssim 1 \text{ ps}$), which leads to high temporal resolution [48]. A useful feature of the detection process is that different proton energies can be captured as different images. Since different energy protons travel with different velocities, faster protons capture earlier information than the slower moving low energy protons, which provides the temporal evolution of the probed interaction. Proton probing has been successfully used to investigate various laser plasma interactions including the sheath electric fields responsible for accelerating protons [49], plasma channel evolution in the wake of a high-intensity laser through an underdense plasma [50] and self-generated magnetic fields around laser focal spots [51, 52].

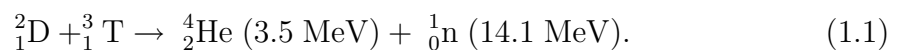
A final application to mention here is the potential development of short pulse neutron sources. Neutron spallation sources, such as ISIS in the UK [53], fire high energy protons into materials with high cross sections for neutron production. The neutrons are then used for research in physics, chemistry, materials science, geology, engineering and biology. Neutron radiography is also useful for imaging dense objects, such as would occur in inertial confinement fusion experiments (see section 1.2). High yields of neutrons have been obtained in laser experiments by generating a proton beam and colliding it with a secondary target [54] and can also be produced directly from laser interactions with deuterated targets such as deuterium gas or droplets [55] or deuterated plastic [56, 57]. The high yield in a short duration is an attractive feature of these laser interaction produced neutron sources.

1.2 Inertial confinement fusion

As technology has developed and the population of mankind has escalated, energy requirements have increased dramatically. It is expected that many of the traditional fuels, i.e. oil, coal and gas, will run out in the near future. Alternative energy sources

need to be found to replace these. Since the 1950s, fission power has been harnessed to generate electricity. The primary fuel, uranium, is fairly abundant in availability to be mined. Touted as an environmentally friendly alternative to fossil fuels by some due to the lack of greenhouse gas emissions, the potential radioactive pollution of the fuel is disliked by many. The disposal of the spent fuel is hazardous as the products of the reactions are also radioactive and require storage for a significant time. Meltdown of the reactors can have disastrous environmental consequences such as the Chernobyl accident in 1986.

It is hoped that a different type of nuclear reactor may one day be able to supply energy on a large scale. This would make use of the energy released during fusion, where small atoms combine to make large atoms and release energy in the process in the same way that the Sun and stars are powered. The product nuclei contain slightly less mass, δm , than the fuel nuclei, which means that according to Einstein's mass-energy relationship, $\delta E = \delta m c^2$, energy is released through fusion. The most promising fuel under investigation are the isotopes of hydrogen, deuterium and tritium because the DT reaction has the largest cross section at relatively modest temperatures (10 keV) which can be reached in the laboratory, making this fuel the most viable. For each DT fusion reaction, 17.6 MeV of energy is released and distributed between the products, as shown in the following equation:



The energy released from 1 gram of DT fuel is 340×10^9 Joules, which is the equivalent of burning 8 tons of oil.

Deuterium is found abundantly in sea water, making the fuel supply relatively easy to access. Tritium can also be obtained with relative ease. The main obstacle to fusion is the enormous repulsive force between two nuclei. For the Coulomb barrier to be overcome, the fuel must be heated to a very high temperature, ~ 10 keV, so that the nuclei are travelling very fast. At these temperatures atoms are ionised and exist as a plasma. Therefore, a large amount of energy needs to be put into heating the fuel first before the reaction can occur and the energy extracted. Once the fuel has been heated to such high temperatures, it has to be contained for long enough

for a significant number of fusion reactions to occur.

There are two confinement routes being considered to harness fusion energy. The first is magnetic confinement fusion (MCF), which confines the plasma with magnetic fields, such as in a tokamak. A relatively low density plasma ($n_e \sim 10^{15} \text{ cm}^{-3}$) has to be confined for a relatively long time ($\tau \sim 1 \text{ s}$) for energy breakeven. Tokamak research is at a fairly advanced stage and ITER [58] is an international collaboration that aims to demonstrate the scientific and technological feasibility of prolonged fusion power production for peaceful purposes.

The second route is inertial confinement fusion (ICF). Here the fuel is compressed to high density ($n_e \sim 10^{26} \text{ cm}^{-3}$) for a relatively short time ($\tau \sim \text{few nanoseconds}$). This research is largely driven and funded for defense interests. Since 1996, nuclear testing has been internationally outlawed, so research related to the operation and safety of nuclear weapons has to be performed in other ways. Large scale facilities such as the National Ignition Facility (NIF) in the USA [59], the Laser Mégajoule (LMJ) in France [60] and AWE Orion laser in the UK [61] are all defense-funded.

However, this is not the only motivation for ICF. For instance, the Japanese, who have taken an anti-nuclear weapon stance, have the Institute of Laser Engineering [62] devoted to ICF research, where here the main emphasis is on the generation of energy in a controlled, useful way. There are also proposals for a European facility for a high power laser energy research facility, or HiPER facility [63], dedicated to demonstrating the feasibility of laser driven fusion as a future energy source. Aside from the energy source research, these facilities should produce neutron sources two or three orders of magnitude more powerful than those currently available [64].

Inertial confinement fusion requires the implosion of a hollow, spherical DT pellet to reach high densities at peak compression. Investigation is underway to drive the compression using pulsed power machines, particle beams or the route to be discussed here, via lasers. The compression can either be driven directly by the laser beams or driven indirectly [65], using soft x-rays generated by laser plasma interactions in a holraum. The ablation pressure at the critical surface of the fuel pellet drives the implosion and high densities can only be achieved if there is a very high degree of symmetry in the driving radiation and the pellet. Otherwise,

hydrodynamic instabilities ruin the implosion symmetry and the achievable densities are dramatically reduced. To achieve ignition using this basic inertial confinement method, it is estimated that greater-than a megajoule of laser energy is required. The compression needs to be high enough, combined with a high enough temperature for ignition to be attained in the central hotspot. A burnwave then propagates out through the plasma consuming the fuel.

The fast ignition concept, proposed by Tabak et al. in 1994 [66], is a variation on the basic ICF scheme. It separates the compression and heating stages. In the basic ICF scheme, compression becomes increasingly difficult as the temperature of the fuel increases. Therefore, if the plasma can be compressed whilst keeping the temperature low, higher maximum compression densities can be achieved. The fuel is then ignited by a particle beam, which deposits a large amount of energy into the fuel at the time of maximum compression. This lessens the driver laser energy requirements compared with the conventional approach.

Currently the most popular method for the delivery of the ignition energy is in the form of hot electrons. To get the electrons to the hot plasma core there is either a plasma boring method, where a high intensity laser hole bores a path into the fuel [66], or a guiding cone fitted into the side of the fuel shell [67]. A schematic of the cone guided fast ignitor concept is shown in figure 1.1. A cone fitted into the side of the fuel shell keeps a path clear of high density plasma, so that a multi-Petawatt class laser is able to reach the dense cool fuel and interact to generate hot electrons. Guiding cone experiments have been shown to not impede the symmetry of the implosion [67], while the laser interaction and fast electron production and transport via the cone is being researched [68]. The subject of fast electron transport and energy deposition of the fast electrons through high density plasma is under substantial investigation. Filamentation of the hot electrons due to instabilities and large divergence angles from the electron source are potential problems.

Alternatively, the ignition energy could be delivered by ions. Advantages of ions over electrons include a well determined position for stopping to provide localised heating of the dense plasma. Focusing target designs have been investigated to

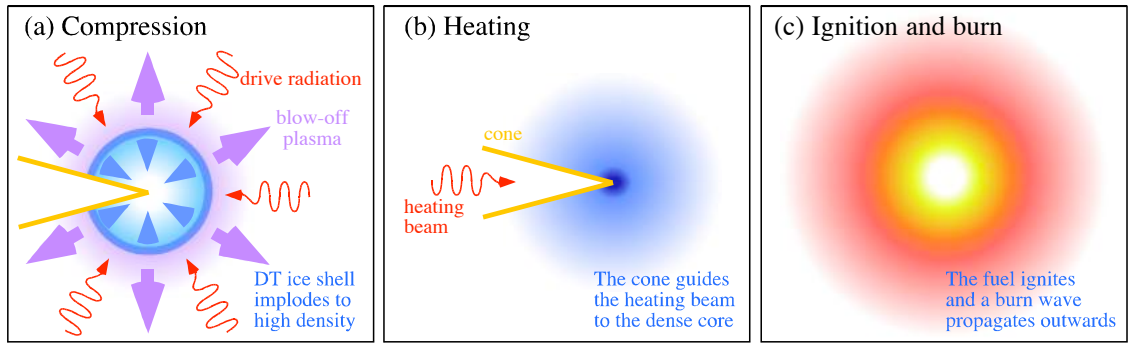


Figure 1.1: A schematic of the fast ignition approach to inertial confinement fusion: (a) shows the DT fuel being compressed by radiation to high density, (b) shows the heating beam being guided by the cone to the dense plasma core and (c) shows the ignition of the dense fuel and the burn wave consuming the fuel, releasing fusion energy.

overcome beam divergence [69]. Of course, there are also problems with using ions as the ignition energy source. It is difficult to efficiently produce an ion beam from laser plasma interactions with the required number of ions with sufficient energy for the fast ignition scheme. Efficient production of monoenergetic ion beams would be ideal for this application.

1.3 Laboratory astrophysics

Experiments to investigate astrophysics can be performed on a laboratory scale using dimensionless scaling laws [70]. Of the visible universe, as much as 99% may exist as plasma, but our diagnostics of astrophysical events are limited since we are confined to the Earth and its local environment. Some of the extreme high energy density conditions found in these astrophysical plasmas can be recreated, albeit on a small scale, in the laboratory using high intensity lasers. This makes laser plasma interactions a very attractive means of understanding fundamental physical processes occurring in our universe. Experiments can be designed to investigate strong shocks, high Mach-number jets, radiation flow, compressible hydrodynamic instabilities and fundamental properties such as opacities and equations of state, which can occur in energetic astrophysical systems.

The sun provides the energy for life on Earth in the form of light and is our closest star, being fairly typical of the $\sim 10^{21}$ stars in our universe. Particles also escape the sun and travel out across the solar system, dragged along by the magnetic field lines emanating from the sun. This solar wind interacts with the Earth's atmosphere and magnetic field. The strength of the solar wind and the direction of the incident magnetic field can have significant effects on earth's atmosphere and climate. It is even possible to observe the solar wind as it is guided along magnetic field lines into the poles of the Earth as the aurora, where the solar wind plasma collides with atoms in the upper atmosphere. The magnetic field structures, their evolution and reconnection events, leading to solar flares and the associated coronal mass ejections, are not yet fully understood. The energy emerging from the sun's surface, or photosphere, has travelled long distances through extremely dense plasma in the sun's core. To understand the plasma opacities including those in the sun, laboratory experiments can be performed to benchmark codes used to estimate the opacity in the sun [71].

Phenomenon such as shocks and blast waves are common in astrophysical plasmas and are thought to play an important role in transporting energy through the interstellar medium. This lends an interest to experiments where lasers are used to drive blast waves in plasmas [72, 73]. Shocks can accelerate particles to extremely high energies. Cosmic rays are typically relativistic protons with energies of 10^{15} eV [74]. In the laboratory, more modest accelerations have been observed of ions accelerated from laser driven shocks [23, 28].

The formation of well-collimated jets are observed from astrophysical objects such as active galactic nuclei and young stellar objects. The reasons for the jets being so narrow and highly collimated are not well understood, which makes them interesting to study under laboratory conditions. Experiments to create jets in the laboratory have been performed using both lasers [75] and z-pinches [76, 77].

1.4 Thesis outline

In this thesis, longitudinal ion acceleration from underdense and near critical density targets is studied. Experiments and numerical modelling were used to investigate the acceleration mechanisms involved. The relative importance of the charge separation compared with induced fields for generating the accelerating sheath field is investigated.

The work in this thesis covers several areas particularly of relevance to ICF. The first is ion and proton generation, which has possible applications as an energy source for ignition in the fast ignitor concept. The second is the interaction of Petawatt class lasers with underdense to near critical density plasma also being important for the fast ignitor concept, because the ignition laser is likely to be required to travel through some length of underdense plasma before reaching its target. This is relevant to the hole boring of a high intensity laser into the compressed fuel for the fast ignition concept. Filamentation of the laser pulse as it propagates through a plasma is studied in this thesis. Finally, the investigation into the interaction of two laser focal spots in close proximity is important for both indirect drive ICF, where many beams are focused inside a holraum to generate the soft x-ray drive and direct drive ICF, where many laser focal spots are arranged over the fuel capsule surface. Multiple laser beams (the American National Ignition Facility has 192 beams) are focused into the holraum to generate the x-ray drive. The plasma conditions created within the holraum are of vital importance to produce a uniform x-ray source to drive a symmetric implosion.

The investigation into the interaction of two neighbouring laser focal spots and their self-generated magnetic fields provides an interesting opportunity to study magnetic reconnection. There are a number of unanswered questions in magnetic reconnection theory, so benchmarking experiments are helpful to deduce reconnection rates. It was found as a consequence of magnetic reconnection events that well-collimated jets were formed originating in the reconnection regions, giving insight into jet formation.

This thesis is presented as follows:

Chapter 2 provides a brief description of the relevant theory of laser plasma interactions.

Chapter 3 introduces the Vulcan laser system used to perform the experiments and describes the basic experimental methods used to collect the data.

Chapter 4 presents the first measurements of ion acceleration in the longitudinal direction from underdense plasma interactions with a high intensity laser. The results are compared with particle-in-cell code simulations to investigate the acceleration mechanism.

Chapter 5 presents an extension of the results in chapter 4 and investigates the ion acceleration from plasmas with near critical densities using low density foam targets.

Chapter 6 presents the results of an investigation into the interaction of the self generated magnetic fields around two laser generated plasma spots in close proximity. The focus of the results is on the proton radiography data which, combined with other experimental diagnostics, provides evidence for magnetic reconnection.

Chapter 7 provides the summary and conclusions of the work described in the thesis. Possible extensions into future research are suggested.

Chapter 2

Theoretical background

2.1 Laser plasma basics

2.1.1 Description of the laser field

Consider the vector potential of an electromagnetic wave,

$$\mathbf{A} = \mathbf{A}_0 \sin(\mathbf{k}_L \cdot \mathbf{r} - \omega_L t), \quad (2.1)$$

where $k_L = 2\pi\eta/\lambda_L$ is the wavenumber of the laser, $\omega_L = 2\pi c/\lambda_L$ is the angular frequency of the electromagnetic wave, λ_L is the wavelength of the laser and η is the refractive index. Assuming that the electric field is in the x -direction and the magnetic field is in the y -direction, the electric and magnetic fields are:

$$\mathbf{E} = -\frac{\partial \mathbf{A}}{\partial t} = \mathbf{E}_0 \cos(k_L z - \omega_L t), \quad \text{where } \mathbf{E}_0 = \omega_L A_0 \hat{\mathbf{x}}, \quad (2.2)$$

$$\mathbf{B} = \nabla \times \mathbf{A} = \mathbf{B}_0 \cos(k_L z - \omega_L t), \quad \text{where } \mathbf{B}_0 = k_L A_0 \hat{\mathbf{y}}. \quad (2.3)$$

When describing how intense a focused laser is, it is often useful to use the normalised vector potential. The normalised vector potential for an electromagnetic wave is given by,

$$a = \frac{eA}{m_e c} = \frac{eE}{m_e c \omega_L}, \quad (2.4)$$

where e is the charge on an electron, E is the electric field in Vm^{-1} . It is usual for the peak normalised vector potential, a_0 , to be used and it is proportional to the

peak electric field, E_0 :

$$a_0 = \frac{eE_0}{m_e c \omega_L}. \quad (2.5)$$

The time averaged normalised vector potentials will be $\langle a \rangle = \frac{1}{2}a$ for linearly polarised light and $\langle a \rangle = a$ for circularly polarised light. When the normalised vector potential approaches unity, electrons will be oscillating in the field at a speed approaching the speed of light, c , and relativistic effects become important.

The intensity of the laser, I , is given by the magnitude of the Poynting vector, \mathbf{N} , averaged over a laser period:

$$I = \langle |\mathbf{N}| \rangle = \frac{1}{\mu_0} \langle |\mathbf{E} \times \mathbf{B}| \rangle = \frac{\epsilon_0 c}{2} E_0^2, \quad (2.6)$$

where ϵ_0 is the permittivity constant. Combining this with equation 2.5 allows the laser intensity to be related to the normalised vector potential:

$$I \lambda_\mu^2 = a_0^2 \cdot 1.387 \times 10^{18} \text{ Wcm}^{-2} \mu\text{m}^2. \quad (2.7)$$

The intensity of an electromagnetic wave, I , is often normalised in this way by multiplying it with the square of the wavelength of the light in units of microns, λ_μ^2 , to give $I \lambda_\mu^2$, which is in units of $\text{Wcm}^{-2} \mu\text{m}^2$.

2.1.2 Ionisation processes

The ionisation process, which takes place when an electromagnetic wave is incident upon atoms to create a plasma, is dependent upon the intensity of the laser. The Keldysh parameter, γ_K , compares the ionisation energy to the electron oscillation energy in the laser's electric field (the ponderomotive energy, discussed further in section 2.1.5). It can be used to identify the regime of ionisation that will be dominant at a particular intensity and can be written as follows:

$$\gamma_K = \sqrt{\frac{\epsilon_i}{2U_p}}, \quad (2.8)$$

where ϵ_i is the ionisation energy and U_p is the ponderomotive potential (see equation 2.20).

Figure 2.1 shows the three main optical field ionisation (OFI) processes. For

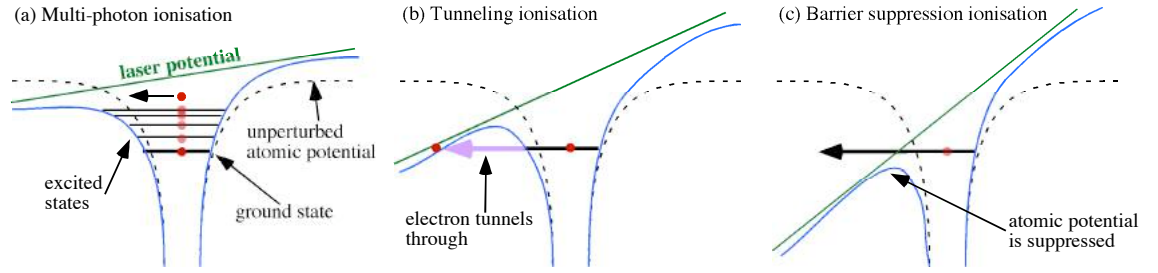


Figure 2.1: The three main Optical Field Ionisation (OFI) processes: (a) multi-photon ionisation, (b) tunneling ionisation and (c) barrier suppression ionisation.

$\gamma_K \gg 1$ a large number of photons must be absorbed by a single electron to release it from its potential well, so this is known as multi-photon ionisation (figure 2.1 (a)). The electron can escape from the atom's Coulomb potential when it has gained enough energy from absorbing a number of photons, each with energy $E_\gamma = \hbar\omega_L$, to raise it into a state from which it can escape. For shorter wavelengths fewer photons need to be absorbed before the electron gains enough energy to escape the potential well. If $\gamma_K \ll 1$ the electric field of the laser can suppress the Coulomb potential of the atom so that electrons can tunnel through and the tunneling ionisation rates become significant (figure 2.1 (b)). Tunneling ionisation becomes the dominant mechanism when $I\lambda_\mu^2 \sim 10^{14} \text{Wcm}^{-2} \mu\text{m}^2$. Barrier suppression ionisation can occur when the electric field of the laser distorts the Coulomb barrier of an atom so much that the electron can escape (figure 2.1 (c)). Beyond $I\lambda_\mu^2 \sim 10^{18} \text{Wcm}^{-2} \mu\text{m}^2$ the work done on an electron during a laser wavelength is comparable to the electron rest mass and relativistic effects become important.

2.1.3 Interaction of a single electron with a laser field

A simple equation of motion can be written for a single electron in an electromagnetic wave, $E(\mathbf{r}, t), B(\mathbf{r}, t) \propto \exp[i(\mathbf{k}\cdot\mathbf{r} - \omega_L t)]$ using the Lorentz force:

$$\frac{d\mathbf{p}}{dt} = -e(\mathbf{E} + \mathbf{v} \times \mathbf{B}), \quad (2.9)$$

where \mathbf{v} and $\mathbf{p} = \gamma m_e \mathbf{v}$ are the electron quiver velocity and quiver momentum respectively and $\gamma = (1 - v^2/c^2)^{-\frac{1}{2}} = (1 + p^2/m_e c^2)^{-\frac{1}{2}}$ is the relativistic Lorentz

factor. The $\mathbf{v} \times \mathbf{B}$ force due to the laser field only becomes significant when the momentum of the electron, \mathbf{p} , becomes comparable to the rest mass of an electron because $|\mathbf{E}| = c|\mathbf{B}|$. Therefore for an $a_0 < 1$, the electron motion will be primarily due to the electric field and will oscillate linearly along the electric field direction with the laser frequency.

For high intensity, $a_0 \gtrsim 1$, the equation of motion (equation A.1) can be solved analytically to find the electron trajectories in a linearly polarised, plane, electromagnetic wave [78]. The derivation of the momentum relations (equations A.8 and A.15) are presented in appendix A:

$$\frac{p_x}{m_e c} = a, \quad (2.10)$$

$$\frac{p_z}{m_e c} = \frac{a^2}{2}, \quad (2.11)$$

where a is the normalised vector potential. From these momentum relations the x and z components of the electron trajectory can be found by integration as shown in appendix A:

$$x(\tau) = \frac{ca_0}{\omega_L} \sin(\omega_L \tau), \quad (2.12)$$

$$z(\tau) = \frac{ca_0^2}{4} \left(\tau + \frac{1}{2\omega_L} \sin(2\omega_L \tau) \right). \quad (2.13)$$

The x component is the same as for the non-relativistic case. However, for $a_0 \geq 1$ there is a large movement of the electron in the direction of laser propagation, the z -direction. This drift velocity, \mathbf{v}_D , as seen in the laboratory frame is found by time averaging the z component.

$$\mathbf{v}_D = \left\langle \frac{dz}{dt} \right\rangle = \frac{a_0^2}{4 + a_0^2} c \hat{\mathbf{z}}. \quad (2.14)$$

The second part of the z component in equation A.23 is a rapid oscillation at twice the laser frequency and is the effect of the B-field. If the electron is observed in the drift frame then the electron has a “figure-8” trajectory. Figure 2.2 (a) shows plots of the trajectory of the electron in the lab frame and figure 2.2 (b) is the “figure-8” trajectory in the drift frame of the electron.

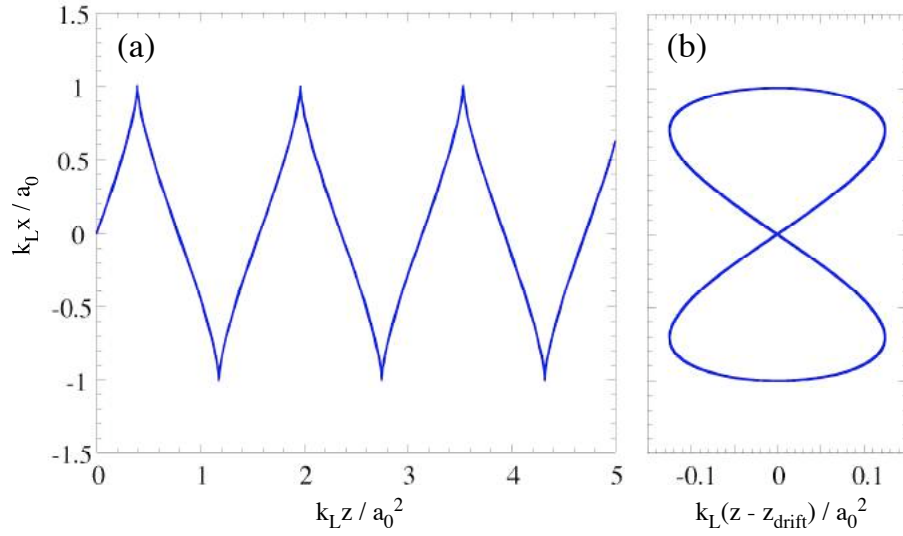


Figure 2.2: Plots for the case of a plane, linearly polarised electromagnetic wave showing (a) the trajectory of an electron and (b) the “figure-8” trajectory in the drift frame.

2.1.4 Laser propagation in a plasma

Using Maxwell’s equations and the equation of motion for a single electron in an electromagnetic field of $a_0 \ll 1$ (i.e. the $\mathbf{v} \times \mathbf{B}$ term is insignificant), (equation 2.9), the plasma dispersion relation can be found, which describes the propagation of an electromagnetic wave through an underdense plasma:

$$\omega_L^2 = k^2 c^2 + \omega_{pe}^2, \quad (2.15)$$

where the non-relativistic electron plasma frequency, ω_{pe} , is defined as

$$\omega_{pe} = \sqrt{\frac{n_e e^2}{\epsilon_0 m_e}}. \quad (2.16)$$

When $a_0 \geq 1$, the m_e can be replaced by $\langle \gamma \rangle m_e$ to get the relativistic electron plasma frequency. If the laser frequency, ω_L , is larger than the electron plasma frequency, the electromagnetic wave is unable to propagate. The critical density, n_c , above which the laser is unable to propagate is

$$n_c = \frac{m_e \epsilon_0 \langle \gamma \rangle \omega_L^2}{e^2} = 1.12 \times 10^{21} \frac{\langle \gamma \rangle}{\lambda_\mu^2} \quad [\text{cm}^{-3}]. \quad (2.17)$$

Densities above this critical density are referred to as overdense plasma and below the critical density as underdense plasma.

2.1.5 Ponderomotive force

In a laser-plasma interaction, the light beam is usually focused down to a small spot size, which leads to intensity gradients in the pulse in time and space. The oscillatory motion of an electron will move it into regions with different intensities. For example, an electron may move from a higher intensity region to a lower intensity region, during the first half of the quiver motion (the first half of the laser period). In the lower intensity region the return force will be smaller and therefore the electron does not move back to its original position during the second half of the laser period. Over a number of these oscillations the electrons will see a net force and gain energy, which removes them from the regions of highest intensity. By these mechanisms, a channel depleted of electrons may form as a laser pulse travels through a plasma. The process is known as ponderomotive channeling and continues until the space charge due to the electron motion equals the ponderomotive force.

To calculate how strong this ponderomotive force is, again consider the equation of motion A.5 for the interaction of a single electron in a laser field. If this equation is time averaged and the slowly varying components are considered, it gives,

$$\mathbf{F}_p = -\frac{e^2}{2m_e \langle \gamma \rangle} \nabla \langle \mathbf{A}^2 \rangle = -\frac{m_e c^2}{2 \langle \gamma \rangle} \nabla \langle a^2 \rangle, \quad (2.18)$$

where $\langle \rangle$ denotes time-averaging. For linearly polarised light, $\langle \mathbf{A}^2 \rangle = \frac{1}{2} A_0^2$ and $\langle a^2 \rangle = \frac{1}{2} a_0^2$, and for circularly polarised light, $\langle \mathbf{A}^2 \rangle = A_0^2$ and $\langle a^2 \rangle = a_0^2$. The Lorentz factor can be conveniently written as $\langle \gamma \rangle = (1 + \langle a^2 \rangle)^{\frac{1}{2}}$ so that 2.18 can be written as

$$\mathbf{F}_p = \frac{m_e c^2}{2 \langle \gamma \rangle} \nabla (\langle \gamma \rangle^2 - 1). \quad (2.19)$$

From this a ponderomotive potential can be found:

$$U_p = m_e c^2 (\langle \gamma \rangle - 1). \quad (2.20)$$

This is the energy an electron gains as it quivers in the field of the laser. The electrostatic potential, $\nabla \phi$, in the equation of motion A.5, will act to try and counteract the ponderomotive potential as the electrons are moved and separated from the ions.

2.1.6 Collective plasma effects

In laser plasmas, the quasi-neutrality of the plasma is often upset, leading to the generation of large space-charge electric fields. It is usually the electrons which move to compensate for charge imbalances due to them being significantly lighter and therefore quicker to respond. Providing the ion temperature is much less than the electron temperature, the Debye length is the distance over which the electric field is screened. The Debye length is given by

$$\lambda_D = \sqrt{\frac{\epsilon_0 k_B T_e}{n_e e^2}}. \quad (2.21)$$

2.2 Intense laser interactions with underdense plasmas

2.2.1 Self-focusing and optical guiding

In the case of the propagation of electromagnetic waves in plasma, an important parameter that needs to be considered is the refractive index, η , which is given by

$$\eta = \sqrt{1 - \left(\frac{\omega_{pe}}{\langle\gamma\rangle \omega_L}\right)^2} = \sqrt{1 - \left(\frac{n_e}{\langle\gamma\rangle n_c}\right)}, \quad (2.22)$$

where $\omega_{pe} = \sqrt{n_e e^2 / \epsilon_0 m_e}$ is the electron plasma frequency, ω_L is the electromagnetic wave frequency and n_c is the non-relativistic critical density. The group and phase velocities of the laser through the plasma are therefore given by the following:

$$v_g = \frac{\partial \omega_L}{\partial k_L} = \eta c, \quad (2.23)$$

$$v_\phi = \frac{\omega_L}{k_L} = \frac{c}{\eta}. \quad (2.24)$$

The laser is only able to propagate in an underdense plasma $n_e < n_c$, therefore the refractive index, η , is always less than 1. This means that the group velocity is $v_g < c$ and the phase velocity is $v_\phi > c$.

At intensities above $\sim 10^{18} \text{ Wcm}^{-2}$, the electrons oscillate with a speed approaching the speed of light, c and relativistic effects become significant. The regions of highest intensity, usually in the centre of the focused laser beam, will have

the highest relativistic mass correction, $\langle \gamma \rangle m_e$, and the refractive index in these high intensity regions will be larger than in the wings of the pulse, which leads to a focusing of the beam. This is known as relativistic self-focusing.

The expulsion of the electrons by the ponderomotive force from the highest intensity regions lowers n_e in the central region and creates density gradients in the plasma. The effect of this is also to focus the laser into the lowest density regions and is referred to as ponderomotive self-focusing.

The effect of both the relativistic and ponderomotive self-focusing gives a high refractive index on the axis of the laser pulse and a lower refractive index away from the axis. The phase velocity, $v_\phi = c/\eta$, near the edge of the beam will therefore be faster than that on axis. This results in the tilting of the phase front towards the axis. Since the Poynting vector, $\mathbf{N} = \mathbf{E} \times \mathbf{B}/\mu_0$, is perpendicular to the phase front, the energy will flow towards the axis, which is equivalent to focusing the laser.

In the radial direction, the self-focusing of the beam competes against diffraction — the natural tendency for the beam to defocus. Considering geometric optics, the relative effects of the self-focusing to diffraction can be estimated [1]. Figure 2.3 presents the geometric view of (a) diffraction and (b) self-focusing of a Gaussian laser beam, with a radial profile of $a(r) = a_0 \exp(-r^2/\sigma^2)$. The divergence angle that the beam will diffract in the absence on non-linear effects is:

$$\theta_d = \frac{dR}{dz} = \frac{\sigma_0}{Z_R} = \frac{1}{k_L \sigma_0}, \quad (2.25)$$

where $Z_R = 2\pi\sigma_0^2/\lambda$ is the Rayleigh length and σ_0 is the e^{-1} radius (the e^{-2} radius in intensity).

In the radial direction, $\gamma(r) = \sqrt{1 + a(r)^2/2}$, which means that the refractive index is

$$\eta(r) = \sqrt{1 - \frac{\omega_{pe}^2}{\omega_L^2 \sqrt{(1 + a(r)^2/2)}}}. \quad (2.26)$$

There is an on axis peak in the refractive index, which is equivalent to a focusing lens. From equation 2.24 the phase velocity can be approximated:

$$\frac{v_\phi}{c} = \frac{1}{\eta} \simeq 1 + \frac{\omega_{pe}^2}{2\omega_L^2} \left(1 - \frac{a(r)^2}{4}\right). \quad (2.27)$$

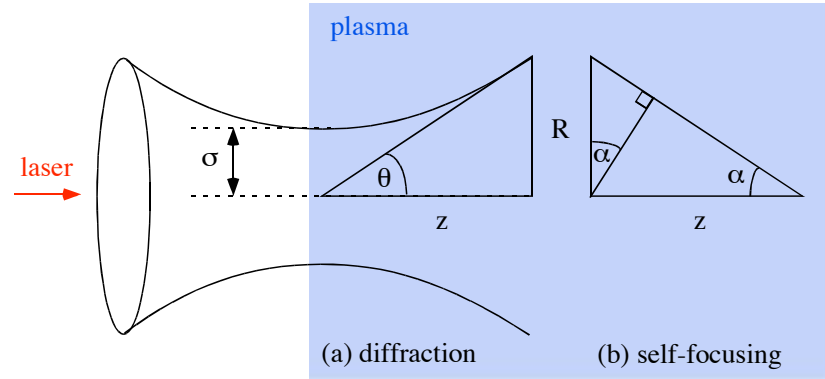


Figure 2.3: The effect of (a) diffraction and (b) self-focusing on a Gaussian laser beam in plasma (figure adapted from P. Gibbon's book [1]).

This can be used to find the maximum path difference:

$$\Delta L = |v_\phi|_{max} t = \frac{|v_\phi|_{max} z}{c} = \alpha R, \quad (2.28)$$

so the maximum focusing angle of the beam is found:

$$\alpha^2 = \frac{\omega_{pe}^2 a_0^2}{8\omega_L^2}. \quad (2.29)$$

The diffraction balances with the self-focusing when $\theta = \alpha$:

$$\left(\frac{1}{k_L \sigma} \right)^2 = \frac{\omega_{pe}^2 a_0^2}{8\omega_L^2}. \quad (2.30)$$

The power is given by, $P = \pi \sigma^2 I$ and substituting for intensity using equations 2.6 and 2.5 yields

$$P = \frac{\pi \epsilon_0 c^5 m_e^2 a_0^2}{e^2} (k_L \sigma)^2. \quad (2.31)$$

Therefore, by substituting equation 2.30 into equation 2.31, the critical laser power at which relativistic self-focusing can overcome diffraction is found [79]:

$$P_c = \frac{8\pi \epsilon_0 m_e^2 c^5 \omega_L^2}{e^2 \omega_{pe}^2} = 17.5 \frac{n_c}{n_e} \text{ [GW]}. \quad (2.32)$$

In the longitudinal direction, there is a density gradient, whereby the density increases near the front of the pulse, which means that the phase velocity at the front of the pulse is reduced [80]. The pulse length, τ_L , is shortened and there is generally a blue shifting due to ionisation [81]. Plasma wave generation, especially for short pulses, can also lead to frequency shifts [82, 83].

2.2.2 Parametric instabilities

When a laser beam propagates through a plasma, a number of parametric instabilities can be driven. Parametric instabilities are those in which one mode of a system is driven unstably by a second distinct mode. In this case the driving mode is usually the laser light. The two most important parametric instabilities are the stimulated Raman instability (SRS) and the stimulated Brillouin instability (SBS) [84]. In both of these instabilities a photon decays into a scattered photon and either an electron plasma wave, for the Raman instability, or an ion acoustic wave, for the Brillouin instability. In the case of the stimulated Raman instability, energy and momentum conservation gives the relationships:

$$\omega_0 = \omega_s + \omega_p, \quad (2.33)$$

$$\mathbf{k}_0 = \mathbf{k}_s + \mathbf{k}_p, \quad (2.34)$$

where ω_0 , ω_s and ω_p are the incident light, scattered light and plasma frequencies and \mathbf{k}_0 , \mathbf{k}_s and \mathbf{k}_p are the incident light, scattered light and plasma wavenumbers. The condition $\omega_0 \geq 2\omega_p$, which corresponds to the density condition, $n \leq \frac{n_c}{4}$, has to be met in order that the scattered photons can propagate. Raman scattering transfers energy from the incident laser light into the electron plasma waves. The instability in this process occurs when fluctuations in the plasma density couple with the light in the Raman scattering process and thus the scattered light beats with the incident light. This gives spatial variations in the incident light which in turn modulates the ponderomotive force of the laser creating further density disruptions.

The Raman instability provides a useful way to determine the electron density in underdense plasma experiments. The spectrum of the laser light after propagating through the plasma will be modulated by the Raman instability. The fundamental frequency of the laser will have additional satellites, since a photon may scatter more than once as it passes through the plasma. The satellites will have frequencies given by the following:

$$\omega_s = \omega_0 \pm n\omega_p, \quad (2.35)$$

where n is an integer. The position of these satellite peaks gives the plasma frequency [85], which in turn gives the plasma density, $n_e = \epsilon_0 m_e \omega_p^2 / e^2$.

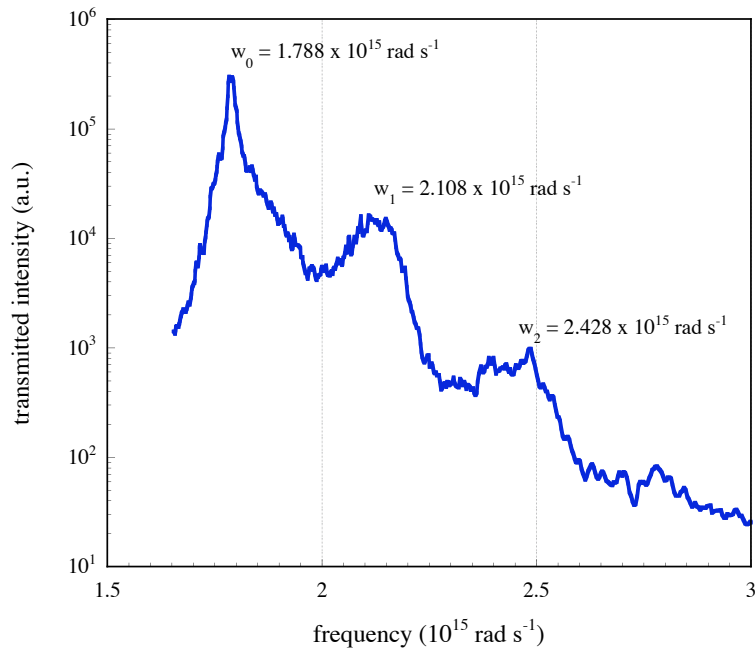


Figure 2.4: The transmitted spectra through a plasma with a density of $3.2 \times 10^{19} \text{ cm}^{-3}$. The fundamental laser frequency is labeled ω_0 and ω_1 and ω_2 are the first and second satellites respectively (data is courtesy of B. Walton).

To illustrate this calculation, see the spectra shown in figure 2.4. The laser fundamental frequency is $1.788 \times 10^{15} \text{ rads}^{-1}$. The first satellite can be seen at $2.108 \times 10^{15} \text{ rads}^{-1}$ and the second satellite is at $2.428 \times 10^{15} \text{ rads}^{-1}$. Both satellites confirm that the density of this shot was $3.2 \times 10^{19} \text{ cm}^{-3}$.

2.2.3 Filamentation

The propagation of the laser through the plasma can also be affected by processes such as filamentation [86], during which the beam breaks up. Also, multiple focusing can occur, where the beam repeatedly self-focuses. This can lead to a hosing instability, which is a transverse motion of the beam [87, 88].

The filamentation instability causes the laser beam to break up into a number of individual filaments. Feedback between transverse modulations in the laser intensity and transverse modulations in the refractive index triggers this instability. This is based on self-focusing and can therefore be triggered by ponderomotive or relativistic

effects. For example, plasma waves may modulate the radial laser profile, seeding filamentation of the beam. Laser filamentation can have a detrimental effect on electron acceleration due to reduced intensity as well as a detrimental effect on the beam divergence pattern due to electron acceleration in individual filaments. These effects have been observed experimentally [88–92] and in simulations [93, 94].

2.2.4 Electron acceleration

In the high intensity laser regimes described in this thesis, the main electron acceleration mechanism is direct laser acceleration (DLA). The term direct laser acceleration (DLA) covers several different ways in which electrons can gain energy directly from the laser. At first it may seem that, for an electromagnetic wave with only transverse field components, it is difficult for particles to be able to directly gain energy from the laser. However, at ultra-high intensities, the combination of the electric and magnetic laser fields and the disrupted plasma can lead to particle acceleration through DLA. The mechanisms described here are stochastic acceleration [95, 96], betatron resonance [97] and the B-loop [98]. Experimentally, the acceleration of electrons via a DLA mechanism has been observed by Mangles et al. [99] and Gahn et al. [100].

A stochastic mechanism is modelled by Meyer-ter-Vehn and Sheng [95] and it demonstrates how small perturbations from the ideal case can cause significant net energy transfer to the electrons. If small perturbations are given to the electrons whilst oscillating in the laser field, they may become dephased from the laser fields and there is a net energy gain. The source of these small perturbations could, in a real experiment, be caused by fluctuating electromagnetic fields in the turbulent plasma state.

Pukhov, Sheng and Meyer-ter-Vehn discuss the betatron resonance mechanism for accelerating electrons [97]. When the transverse betatron oscillations of an electron in the self-generated static electric and magnetic fields match the laser frequency, a resonance occurs. The propagating laser forms a channel as it expels electrons via the ponderomotive force, which has a self-generated transverse electric

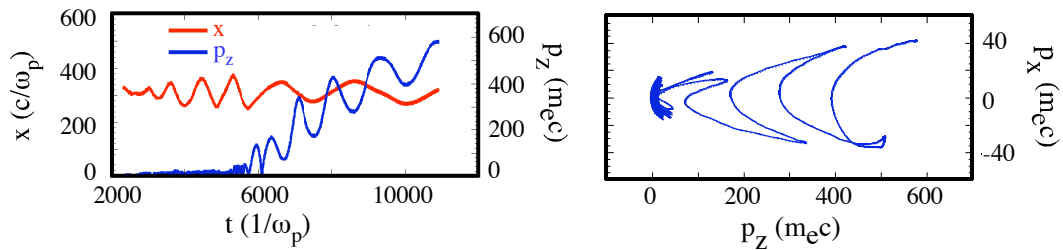


Figure 2.5: A single electron trajectory, tracked from a particle in cell simulation to illustrate the betatron resonance mechanism (figure courtesy of S. P. D. Mangles).

field associated with it. The fast electron current creates a self-generated azimuthal magnetic field. This allows an efficient exchange of energy between the laser and electrons for regimes where the laser power is significantly greater than the critical power for self-focusing. An illustration of this betatron resonance mechanism is shown in figure 2.5, which presents a single electron trajectory, tracked from a particle-in-cell simulation. As the electron oscillates across the channel in the x -direction in the electric field of the laser, the frequency of this oscillation can be seen to decrease corresponding to the increase in γ and therefore to the increase in the effective mass of the electron. As the frequency of the electron oscillation in the x -direction changes, the betatron resonance is reached and the acceleration in the laser direction, z , becomes more regular.

The B-loop mechanism is a similar, but non-resonant, mechanism shown by Pukhov and Meyer-ter-Vehn [98] to occur when an electron receives directly a $\mathbf{v} \times \mathbf{B}$ push by the laser in the presence of an azimuthal dc magnetic field. This allows electrons to gain energies exceeding the ponderomotive potential and is dominant in near-critical density plasmas or when plasma waves disappear due to wavebreaking.

2.2.5 Ion acceleration in the Coulomb explosion

Laser intensities available at present ($I \sim 10^{21} \text{ Wcm}^{-2}$) are not high enough to make ions quiver relativistically in the laser field to provide direct ion acceleration. For a proton with a mass, $m_p = 1836m_e$, the threshold for relativistic interaction is $a_0 = 1836$ or $I\lambda^2 = 4.6 \times 10^{24} \text{ Wcm}^{-2} \mu\text{m}^2$. Therefore ion acceleration, at lower

intensity regimes, relies on collective effects in the plasma due to the movement of electrons in the laser field to generate accelerating fields.

If electrons are displaced from a region of plasma and remain displaced, the electrostatic repulsion between the ions leads to their acceleration in a Coulomb explosion. The acceleration of ions through a Coulomb explosion can occur as a consequence of the ponderomotive force [29–32]. The ponderomotive force in a high intensity laser interaction forms a channel in the plasma deficient in electrons (discussed in section 2.1.5). The ions are comparatively heavy and therefore are not affected by the ponderomotive force on the same time scale as the electrons. This means the ions remain in the channel on the timescale of the expulsion of the electrons. For the ions to be significantly affected by the laser pulse, the ratio between the pulse length to pulse radius has to be suitable for the intensity [32]. A large repulsive force is felt by the ions in the channel from one another and also the attractive force from the expelled electrons in the surrounding plasma. An electrostatic field will form caused by this space-charge separation. In one dimension, Gauss’s law gives

$$\nabla \cdot \mathbf{E} = \frac{\rho_f}{\epsilon_0} = \frac{-e(n_e(x) - n_i(x))}{\epsilon_0}, \quad (2.36)$$

where ρ_f is the free charge density and n_e and n_i are the electron and ion densities. The electrons are expelled by the ponderomotive force until it balances with the space-charge field that is created, such that $F_p = -eE$. The equation of motion for an ion can be written as follows:

$$m_i \frac{dv}{dt} = -Zm_e c^2 \nabla(\gamma - 1), \quad (2.37)$$

where Z is the charge on the ion and m_e and m_i are the electron and ion masses. The ions are accelerated radially outwards from the channel by the electrostatic potential to high energies. If a large enough impulse is received by the ions then they continue to travel outwards even when the electrons return to the channel after the laser pulse has left the plasma.

Theoretically, the maximum energy of the radial ions from the Coulomb explosion is expected to be the ponderomotive potential multiplied by the charge of the ion,

Z :

$$E_{max} = Zm_e c^2 (\gamma - 1). \quad (2.38)$$

This provides a method of estimating the peak intensity of the focused laser [101].

The radial force causing the Coulomb explosion means that the ion emission from underdense plasma is expected to be at 90° to the laser propagation direction. Measurements by Krushelnick et al. [101] confirm that the majority of the emission is in the 90° direction but the emission lobe extends in the backward direction. They saw no measurable ion emission in the forward direction even though very energetic electrons of up to 100 MeV were observed coaxial to the laser propagation.

2.2.6 Ion shock acceleration

Formation of electrostatic shocks in both overdense [22, 28] and underdense plasmas [23, 102, 103] can give rise to ion acceleration. Simulations by Silva et al. [22] identified two acceleration mechanisms for protons in laser interactions (at $a_0 = 16$) with thin, solid (overdense) targets. The first is proton acceleration due to the ambipolar fields created by the expanding heated electrons at the front and rear of the target (see section 2.3.3). The second was identified as proton acceleration in a collisionless electrostatic shock formed at the front of the target by the ponderomotive force of the laser. As the shock propagates it picks up ions and reflects them to high energies with the maximum possible velocity being $v_{max} \approx 2v_{shock}$. Using momentum conservation yields:

$$\frac{(1 + R)I}{c} = m_i n_i v_i^2, \quad (2.39)$$

where I is the intensity of the laser and R is the reflection efficiency of the laser and assuming the momentum transfer into the electrons is negligible. Solving this for the ion front gives the velocity of the flow of ions:

$$\frac{v_{shock}}{c} = \sqrt{\frac{(1 + R)I}{m_i n_i c^3}}, \quad (2.40)$$

where v_{shock} is the shock velocity. After the formation of the shock the front maintains a uniform velocity. It was found that two conditions have to be met for a

collisionless shock to form. The laser intensity has to be high enough to drive (using the ponderomotive force on the electrons) the ions at the front side of the target into forming the shock. There also has to be strong electron heating in the shock formation region so that the local sound speed, $c_s = \sqrt{Zk_B T_e/m_i}$, is high and approximately equal to the velocity of the driving force so that the shock formation time is short. Electrostatic shocks were formed with a high Mach number (2-3) where the Mach number is defined as

$$M = \frac{v_{shock}}{c_s}. \quad (2.41)$$

The shock acceleration was seen to be dominant over the sheath acceleration when the velocity ions gain in the shock is larger than the velocity the ions can gain from the sheath [22]. A signature for this shock acceleration is provided by a plateau in the ion spectrum, due to the acceleration of the highest energy ions being determined only by the velocity of the shock front. The plateau signature was observed experimentally by Zepf et al. [28] in thin foil target experiments.

Shock formation in underdense plasma had previously been observed in simulation results [102, 103] and was recently observed experimentally by Wei et al. [23], showing ion acceleration in underdense plasma through a collisionless shock. The shock in the underdense case is caused largely by the radial component of the ponderomotive force.

The main spectral characteristics for higher, but still underdense ($\sim 10^{20} \text{cm}^{-3}$) plasma densities were that the maximum ion energy and number of high energy ions were greater than at lower density and a plateau to high energy was observed. A strong correlation between plasma density and maximum ion energy ($E_{max} \propto n_e^{0.70 \pm 0.05}$) was found compared with lower laser intensity interactions ($E_{max} \propto n_e^{0.125}$) [30]. The 2D3V OSIRIS [104–106] simulations performed by Wei et al. [23] found that in the low density case the maximum ion energy is approximately the ponderomotive energy. At higher densities, the plateau structure is reproduced and becomes more pronounced as the laser energy is increased. Their simulations show the interaction of multiple collisionless shocks as they are driven out radially, which enhances the ion acceleration from the Coulomb explosion.

Also noteworthy is the angular distribution of the ions from these shock interactions. For low density, the ion emission seen by Wei et al. [23] is predominately at 90° , and for ions with energies greater than 2 MeV, the angular spread is less than 4° (FWHM). At higher density, the angular spread of the ions increases greatly and even for ions with energies greater than 3.5 MeV, the angular spread is 27° . In contradiction to previous measurements which showed preferential emission in the backward direction [101], the ions were preferentially emitted in the forward direction. This too can be explained by the shock acceleration mechanism because in the interaction of two shocks the second shock often has a propagation angle just forward of 90° .

2.2.7 Ion acceleration in an induced electric field

A further ion acceleration mechanism, which has been observed to occur in 2D PIC simulations of underdense ($n_e \sim 0.2n_c$) plasmas, is an induced electric field due to the time changing magnetic field associated with the fast electron cloud expanding into the vacuum [107–109]. In the underdense plasma it is possible for a high power laser pulse to channel through to the back of the target. Electrons can be accelerated to high energies in this channel through the DLA mechanism (see section 2.2.4). With this large electron current is associated a large azimuthal magnetic field, \mathbf{B} . As the electrons leave the end of the channel and expand into the vacuum, magnetic flux needs to be conserved:

$$\Phi_B = \pi L^2 B = \text{constant}, \quad (2.42)$$

where L is the time dependent electron cloud radius. Therefore, as the electrons expand into the vacuum, L increases and the magnetic field strength decreases to conserve magnetic flux.

Faraday's law of induction says that with a time changing magnetic field an electric field will be generated:

$$\frac{\partial \mathbf{B}}{\partial t} = -\nabla \times \mathbf{E}. \quad (2.43)$$

The magnetic field in this case is azimuthal, so the generated electric field is in the longitudinal direction, along the laser axis. This acts to accelerate ions and slow

down electrons. The ion energy gained in this inducted electric field was found to be an energy gain of the same order as the Coulomb explosion [109]. Sentoku et al. observed a collimation of the ion beam in the PIC simulations [109]. This is explained by considering the pinching of the electrons in the magnetic field, which generates an electric field in the radial direction acting to focus the ions.

2.3 Intense laser interactions with overdense plasmas

2.3.1 Absorption mechanisms

For moderate intensities, $10^{12} \text{ Wcm}^{-2}\mu\text{m}^2 < I\lambda_\mu^2 < 10^{17} \text{ Wcm}^{-2}\mu\text{m}^2$, where λ_μ is the laser wavelength in microns, the classical absorption mechanisms of inverse bremsstrahlung and resonance absorption are dominant. As the intensity increases to $I\lambda_\mu^2 > 10^{18} \text{ Wcm}^{-2}\mu\text{m}^2$ and relativistic motion becomes important, vacuum heating and $\mathbf{j} \times \mathbf{B}$ heating become dominant. A review of the main absorption mechanisms is given by Wilks and Kruer [110].

Inverse bremsstrahlung absorption

The dominant absorption mechanism at moderate laser intensities is inverse bremsstrahlung or collisional heating (for $I\lambda_\mu^2 \lesssim 10^{15} \text{ Wcm}^{-2}\mu\text{m}^2$). The electric field of the laser makes the free electrons in the plasma oscillate. Energy is transferred from the laser to the plasma when an oscillating electron collides with an ion. This damps the oscillation of the electron and energy is lost from the laser.

In appendix B, the dispersion relation for inverse bremsstrahlung absorption is derived:

$$\left(\frac{kc}{\omega_L}\right)^2 = 1 - \frac{\omega_p^2}{\omega_L^2} + i\nu_{ei}\frac{\omega_p^2}{\omega_L^3}. \quad (2.44)$$

The definition for the refractive index of a plasma (equation 2.22) is $\eta = (1 - \omega_p^2/\omega^2)^{\frac{1}{2}} = kc/\omega_L$, so by using the imaginary part of the plasma refractive index,

the collisional absorption coefficient, κ_{IB} , can be found:

$$\kappa_{IB} = \frac{\nu_{ei}}{2c} \left(\frac{n_e}{n_c} \right) \left(1 - \frac{n_e}{n_c} \right)^{-\frac{1}{2}}, \quad (2.45)$$

$$\kappa_{IB} \propto \frac{Z_i n_e^2}{T_e^{\frac{3}{2}}} \left(1 - \frac{n_e}{n_c} \right)^{-\frac{1}{2}}. \quad (2.46)$$

Therefore, the absorption due to inverse bremsstrahlung is high if the electron temperature, T_e , is low, the plasma Z_i is high and the electron number density, n_e , is high. The highest plasma density in which the laser is able to propagate is the critical density, n_c (see section 2.1.4). Most of the inverse bremsstrahlung absorption is done at around the critical surface. So the shorter the laser wavelength, the higher the density and the lower the electron temperature at the critical surface, the better the absorption through inverse bremsstrahlung.

As the intensity of the laser increases the electron quiver velocity gets larger which leads to a drop in ν_{ei} (see equation B.2) [111]. Therefore κ_{IB} will drop off as the intensity increases and inverse bremsstrahlung absorption will become less important.

Resonance absorption

For irradiances of $I\lambda_\mu^2 \lesssim 10^{15} \text{ Wcm}^{-2}\mu\text{m}^2$ the observed absorption into the plasma is too high to be accounted for by the collisional inverse bremsstrahlung absorption because of high plasma temperatures. Resonance absorption is a collisionless mechanism in which laser energy is transferred to plasma waves. If a p-polarised electromagnetic wave propagates obliquely through an increasing plasma gradient, which goes to above the critical density, the light will then be specularly reflected as shown in figure 2.6. The density at which the electromagnetic wave is reflected will be lower than the critical density, n_c and is given by $n_{reflect} = n_c \cos^2 \theta$, where θ is the angle between the density gradient normal and the incident electromagnetic wave. The electric field component parallel to the density gradient can tunnel through to the critical density and excite resonant plasma waves in this region. These plasma waves are damped by particle trapping and wave breaking to heat the plasma electrons.

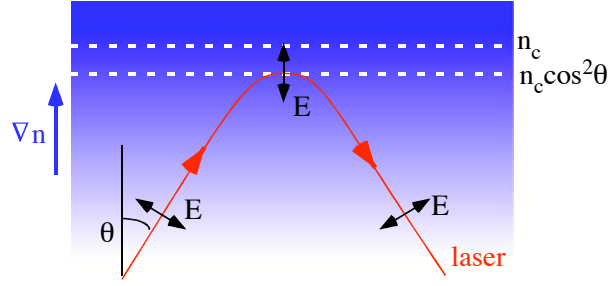


Figure 2.6: A schematic showing resonance absorption of p-polarised light obliquely incident to the plasma gradient at an angle of θ .

The fraction for resonance absorption, f_{ra} , is given below, where L_0 is the density scale length:

$$f_{ra} \approx \frac{\phi^2(\tau)}{2}, \quad (2.47)$$

where

$$\phi(\tau) \approx 2.3\tau \exp\left(-\frac{2\tau^3}{3}\right) \quad (2.48)$$

and

$$\tau = \left(\frac{\omega_0 L_0}{c}\right)^{\frac{1}{3}} \sin \theta, \quad (2.49)$$

where ω_0 is the frequency of the electron plasma wave. For maximum absorption, $\tau \approx 0.8$ and thus the incidence angle can be optimised. The hot electrons produced by the resonance absorption have a hot Maxwellian tail superimposed on the initial background temperature. Scalings for the hot electron temperature component, T_{hot} have been found via numerical modeling [110, 112, 113] to be,

$$T_{hot} \approx 14[T_{keV} I_{16} \lambda_\mu^2]^{\frac{1}{3}} \quad [\text{keV}] \quad (2.50)$$

where T_{keV} is the background electron temperature in keV, I_{16} is the laser intensity in units of 10^{16} Wcm^{-2} and λ_μ is the laser wavelength in microns.

Vacuum heating

For an intense linearly polarised electromagnetic wave, incident obliquely onto an overdense plasma with a sharp boundary, there is a non resonant absorption heating mechanism known as Brunel or vacuum heating [114, 115]. In the oscillating laser pulse, electrons can be dragged out into the vacuum and then sent back into

the plasma as the fields change direction. The number of electrons making this oscillation is given by the surface number density:

$$\Sigma = \frac{2\epsilon_0 E \sin \theta}{e}, \quad (2.51)$$

where θ is the incident angle of the laser light to the target normal. The returning velocity of these electrons is given approximately by the quiver velocity, $v_{osc} \approx eE/m_e\omega_L$ and enter the overdense plasma, where they can no longer be influenced by the laser, having gained kinetic energy directly from the laser.

This vacuum heating is more efficient than the classical resonance absorption provided that $v_{osc}/\omega_L > L_n$, where L_n is the density gradient length. For a plasma at critical density, the minimum length required to shield an electric field is v_{osc}/ω_L , which is why this mechanism is ineffective if a long plasma density length is present. The ratio, f_{vh} , of the absorbed power to incident power for a p-polarised electromagnetic wave incident at an angle of θ to the interface normal and assuming no corona (i.e. no resonance absorption) is:

$$f_{vh} = \left(\frac{\eta}{2\pi}\right) \left(\frac{v_{osc}^3}{v_L^2 c \cos \theta}\right), \quad (2.52)$$

where η is the efficiency factor and $v_L = eE_L/m_e\omega_L$. The ratio f_{vh} is modified when $v_L \gtrsim c$ and relativistic effects become important:

$$f_{vh} = \left(\frac{\eta}{\pi}\right) \left(\frac{cv_{osc}}{v_L^2 \cos \theta}\right) \left[\left(1 + \frac{v_{osc}^2}{c^2}\right)^{\frac{1}{2}} - 1\right]. \quad (2.53)$$

The efficiency of this vacuum heating mechanism can be as high as 70% [116].

$\mathbf{j} \times \mathbf{B}$ heating

The $\mathbf{j} \times \mathbf{B}$ absorption mechanism is caused by the electrostatic field driven by the oscillating component of the ponderomotive force of the laser, as discussed by Kruer and Estabrook [117]. As the intensity of the laser light becomes high enough to make the electrons move relativistically in the fields, i.e. the electrons have a $v_{osc} \sim c$, the \mathbf{B} component of the Lorentz force then becomes comparable to the \mathbf{E} component. At the vacuum plasma boundary, the electrons oscillating in the electric field will gain energy from the magnetic field twice during a single laser oscillation. This

leads to bunching of the electrons at 2ω from $\mathbf{j} \times \mathbf{B}$ heating. If the electron gains enough energy from the magnetic field, it will carry on into the overdense plasma. Unlike resonance or vacuum heating, the $\mathbf{j} \times \mathbf{B}$ heating occurs most efficiently at normal incidence to the plasma. The hot electron temperature, T_h , expected from the $\mathbf{j} \times \mathbf{B}$ heating scales as the ponderomotive potential and has been confirmed using simulations [118] and experiments [119]. For a particular $I\lambda_\mu^2$ ($\text{Wcm}^{-2}\mu\text{m}^2$), the hot electron temperature is given by

$$T_h \approx 511 \left(\sqrt{1 + \frac{I\lambda_\mu^2}{2.8 \times 10^{18}}} - 1 \right) \quad [\text{keV}]. \quad (2.54)$$

It has been shown that the $\mathbf{j} \times \mathbf{B}$ absorption efficiency reduces with increasing density [110]. This is because, as the density increases, there is a shorter absorption depth of the electromagnetic wave (the collisionless skin depth, $\sim c/\omega_{pe}$).

2.3.2 Electron transport

The transport of electrons in laser produced plasma can be broadly divided into two categories. The first is for a thermal population of electrons, which is governed by classical heat flow. The second is for a suprathermal, hot electron population whose transport is governed by non-local effects.

Heat flow

The Spitzer-Harm method [120] can be used to describe the heat flow, \mathbf{q} , for a plasma with a weak electrical field, \mathbf{E} , and an electron temperature gradient where the temperature scalelength, $T_e/\nabla T_e$, is greater than the mean free path of an electron, λ_e . Kinetic theory gives this Spitzer-Harm expression for heat flow for a local electron temperature with a maxwellian distribution function, T_e , in a plasma with no magnetic fields [84]:

$$\mathbf{q} = -\kappa_{SH}\nabla T_e. \quad (2.55)$$

The Spitzer-Harm thermal conductivity for this equation is

$$\kappa_{SH} = \frac{aT_e^{\frac{5}{2}}}{Ze^4m^{\frac{1}{2}}\ln\Lambda}, \quad (2.56)$$

where Λ is the Coulomb logarithm.

This idealised description of heat flow, based on Coulomb collisions in the plasma, may break down for a number of reasons. This description of heat flow neglects density gradients and therefore fails when large density gradients are present. It is inadequate to describe a large velocity distribution of electrons, λ_e , since the mean free path of an electron is energy dependent. The description also fails for large temperature gradients and this breakdown represents the transition from diffusive to free-streaming collisionless behaviour.

Additional magnetic fields, as could be generated by the $\nabla T_e \times \nabla n_e$ mechanism (see section 2.3.4), can affect the heat transport from the critical surface to the ablation front.

Fast electron transport

High intensity laser plasma interactions produce high energy electrons through the absorption mechanisms described in section 2.3.1. The maximum current that can propagate in a single filament is given by the Alfvén current limit, I_A [121]:

$$I_A = \frac{m_e c^3}{e} \beta \gamma = 17 \beta \gamma \quad [\text{kA}], \quad (2.57)$$

where $\beta = v_e/c$. As the fast electron beam propagates, the current, \mathbf{j}_{fast} , will generate an azimuthal magnetic field around the beam. As the magnetic field around the beam increases, the Larmor orbits of the electrons, $r_L = \gamma m_e v_{\perp} / qB$, get smaller. When these Larmor orbits become smaller than the beam radius, the electrons are no longer able to propagate, limiting the maximum current.

As the fast electron beam propagates through the plasma, an opposing return current, $\mathbf{j}_{\text{return}}$, comprising of colder background electrons, is produced to restore charge neutrality. Therefore the electric field generated by the fast electrons will be

$$\mathbf{E} = \eta \mathbf{j}_{\text{return}}, \quad (2.58)$$

where η is the resistivity. This return current also acts to reduce the magnetic field generated by the fast electron beam, which allows fast electron currents greater than the Alfvén current to propagate. The total current is therefore given by,

$\mathbf{j}_{\text{total}} = \mathbf{j}_{\text{fast}} + \mathbf{j}_{\text{return}}$. From Ampère's law, neglecting the displacement current term ($\epsilon_0\mu_0(\partial\mathbf{E}/\partial t)$), since the response of the return current is so rapid, gives

$$\nabla \times \mathbf{B} = \mu_0(\mathbf{j}_{\text{fast}} + \mathbf{j}_{\text{return}}). \quad (2.59)$$

The electric field induced by the fast electrons is therefore found by substituting equation 2.58 into equation 2.59:

$$\mathbf{E} = \frac{\eta}{\mu_0} \nabla \times \mathbf{B} - \eta \mathbf{j}_{\text{fast}}. \quad (2.60)$$

The magnetic field growth is therefore described according to

$$\frac{\partial \mathbf{B}}{\partial t} = -\nabla \times \mathbf{E} = \nabla \times \eta \mathbf{j}_{\text{fast}} - \nabla \times \left(\frac{\eta}{\mu_0} \nabla \times \mathbf{B} \right). \quad (2.61)$$

The source term is the first term on the right hand side, $\nabla \times \eta \mathbf{j}_{\text{fast}}$, and the resistive diffusion of the magnetic field term is the second term on the right hand side, $-(\eta/\mu_0)\nabla \times (\nabla \times \mathbf{B})$.

Bell and Kingham derive the condition for this magnetic field to collimate the fast electron beam [122]. They find that collimation occurs if the ratio of the beam radius, R , to the fast electron Larmor radius, r_L , is greater than the square of the half angle of the divergence of the electron beam, i.e. $R/r_L > \theta_{\frac{1}{2}}^2$. In this case the magnetic field generated is sufficient to bend the fast electrons through an angle of $\theta_{\frac{1}{2}}$. The condition for collimation can be given as $\Gamma > 1$ where, for substantial collisional heating (i.e. $T_{\text{cold}} \gg T_{\text{initial}}$),

$$\Gamma = \frac{0.13 n_{23}^{\frac{3}{5}} (Z R_{\mu\text{m}} t_{\text{psec}} \ln \Lambda)^{\frac{2}{5}}}{P_{\text{TW}}^{\frac{1}{5}} T_{511}^{\frac{3}{10}} (2 + T_{511})^{\frac{1}{2}} \theta_{\text{rad}}^2}, \quad (2.62)$$

where n_{23} is the electron density in units of 10^{23} cm^{-3} , $R_{\mu\text{m}}$ is the beam radius in units of μm , t_{psec} is the time in ps, P_{TW} is the power in the fast electron beam ($P = I\pi R^2$) in TW and T_{511} is the fast electron temperature in units of 511 keV.

There are instabilities which can occur due to either a laser filamentation instability or a Weibel electromagnetic instability. These cause the fast electron beam to break up and filament. The interaction of the fields generated by the counter-propagating fast electron current and the return current give rise to the Weibel instability [123]. This can cause the electron beam to decay into filaments with

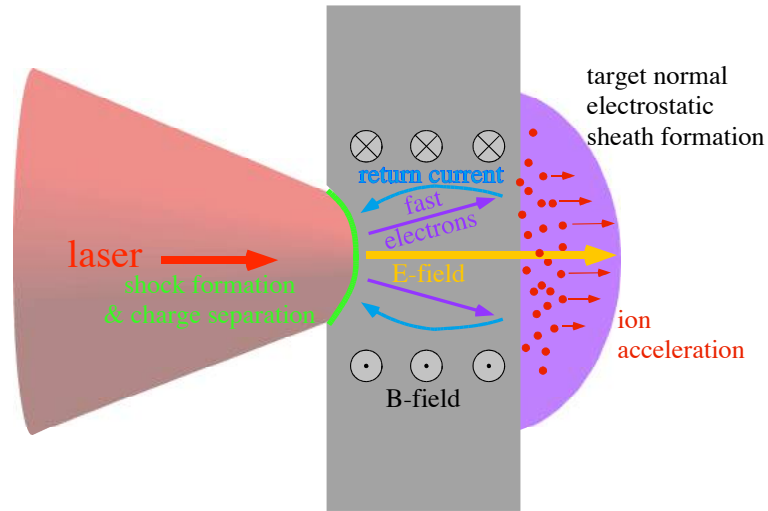


Figure 2.7: A schematic showing the main mechanisms for forward ion acceleration for a high-intensity laser interaction with solid target.

transverse dimensions of the order of the collisionless skin depth, c/ω_{pe} . Since each filament can sustain an Alfvén limited current, the total current can exceed the Alfvén limit.

2.3.3 Ion acceleration from solid targets

As discussed previously in section 2.2.5, presently available laser intensities are not high enough to produce relativistic ion quiver velocities, so ion acceleration relies on collective plasma effects due to electron movement. The accelerating fields can be of the same order of magnitude in strength as the laser fields, but have much longer time scales compared with the fast oscillations of the laser. Multi-MeV ions and protons have been observed from high-intensity laser interactions with solid targets [17, 21, 27, 28, 124–127]. The majority of the protons and ions accelerated, originate from a thin (\sim nm) hydrocarbon contamination layer found on the surface of solid targets. Protons are usually accelerated preferentially to other ions due to their high charge to mass ratio. A schematic of the main mechanisms for forward ion acceleration occurring in this type of high-intensity laser interaction with solid targets are shown in figure 2.7.

Shock acceleration

At the critical surface, the ponderomotive force of the laser can drive high Mach number ($M \sim 2-3$) electrostatic shocks. Shock acceleration has already been introduced in section 2.2.6 in relation to underdense plasmas, however many of the details are the same. The laser acts like a piston to launch a shock front which is able to propagate through the target. This produces an electric field accelerating ions into the target in the forward direction. The generated electrostatic potential is approximately equal to the ponderomotive potential, which gives an approximate limit to the ion energies that can be achieved from this acceleration mechanism, $E_i \approx Zm_i c^2 (\langle \gamma \rangle - 1)$. For high intensity ($\sim 10^{20} \text{ Wcm}^{-2}$) laser interactions with thin ($\sim 10 \mu\text{m}$) targets, shock acceleration can be the dominant ion acceleration mechanism [22, 128]. The maximum shock velocity, v_{shock} , which can be launched is determined by momentum conservation [118]:

$$\frac{v_{shock}}{c} = \left(\frac{(1+R)I}{m_i n_i c^3} \right)^{\frac{1}{2}}, \quad (2.63)$$

where R is the reflection efficiency of the laser. The maximum velocity an ion can gain from the shock is twice the shock velocity, $v_{max} = 2v_{shock}$.

Internal electromagnetic fields

Ions accelerated in the forward direction from the front surface have to travel through the target before escaping into the vacuum. The currents of electrons passing through the target generate large magnetic fields [24–26] which act to focus the forward propagating fast electron beam. For ions however, this magnetic field is deflecting. This deflection of ions in the internal fields of the target has been used to explain ring-like structures in the observed proton beams [27, 28].

Target normal sheath acceleration

The target normal sheath acceleration (TNSA) mechanism for ions occurs when a large number of electrons move out of the plasma into the vacuum. It assumes that the fields generated are strong enough to ionise the atoms on the rear surface to a plasma. The charge separation between the electrons and the plasma ions

generates a space charge electric field in the target normal direction. This acts to restore plasma quasi-neutrality either by returning the electrons into the plasma or by pulling ions out. In laser plasma interactions, large numbers of hot electrons can be generated and may attempt to leave the target from either the rear or front of the target. The TNSA mechanism can occur on both the front and rear surfaces. The ions from the front surface TNSA generally have lower maximum energy than the rear side TNSA ions because of the lower electron temperature leaving the target in that direction and a longer pre-plasma scalelength. Experimental evidence that the ions are accelerated normal to the target surface was provided by an experiment with a wedge target [17]. The ions were observed to be emitted in the direction normal to both surfaces of the wedge shaped target. The properties of the proton beams accelerated by the TNSA mechanism from the rear surface are a small source size [48], high luminosity and well defined beam characteristics such as divergence and uniformity.

An analytic estimate of the initial electric field at the beginning of the acceleration process is presented by Wilks [129] and is based on earlier papers describing hot electrons driving plasma expansion into a vacuum [130–134]. A 1D model describing the evolution of the electric field as the electrons expand into the vacuum is presented by Mora [18] and the model is followed in appendix C. Assuming that the acceleration time, t , is the same as the fast electron time or the laser pulse length, this leads to an estimate for the maximum ion energies (equation C.15):

$$\mathcal{E}_{max} = \frac{1}{2}m_i v_{front}^2 \simeq 2Zk_B T_e [\ln(\tau + \sqrt{\tau^2 + 1})]^2, \quad (2.64)$$

where v_{front} is the ion front velocity, $\tau = \omega_{pi}t/\sqrt{2e_E}$ and e_E denotes the numerical constant $2.71828\dots$. This has been shown to be able to accurately predict rear side acceleration. A further prediction of the Mora self-similar model is the form of the ion energy spectra, which gives the number of ions per unit surface (equation C.16):

$$\frac{dN}{d\mathcal{E}_i} = \frac{n_{i0}t}{\sqrt{2\mathcal{E}_i}} \exp\left(-\sqrt{\frac{2\mathcal{E}_i}{Zk_B T_e}}\right), \quad (2.65)$$

where \mathcal{E}_i is the ion energy. There is still a well defined cutoff to the spectrum as defined by \mathcal{E}_{max} due to the ion front formed in the acceleration process.

In a real experiment, there will not only be the hot electrons with $T_e = T_{hot}$, accelerated by the laser at the front of the target, but also cold electrons from the bulk of the target with a temperature, T_{cold} . Passoni considers the case for when there is also a cold electron population present and investigates the modification to the initial electric field strength, E_0 [135]. The ratio of the quasi-pressures, p_{cold}/p_{hot} , where $p_{cold} = n_{cold}k_B T_{cold}$ and $p_{hot} = n_{hot}k_B T_{hot}$ of the electron populations are considered. It is found that the hot electron component is dominant on the initial electric field strength, E_0 , for $p_{cold}/p_{hot} \leq 1$. The maximum electric field is approximately given by

$$E_{max} = \sqrt{2} \left(\frac{k_B T_{hot}}{e \lambda_{Dhot}} \right), \quad (2.66)$$

where $\lambda_{Dhot} = \sqrt{\epsilon_0 k_B T_{hot} / n_{0hot} e^2}$ is the unperturbed hot electron Debye length. The one temperature result for the maximum electric field strength can be recovered for $p_{cold}/p_{hot} \ll 1$. For the opposite case, $p_{cold}/p_{hot} \gg 1$, the peak electric field becomes further enhanced:

$$E_{max} \approx \sqrt{\frac{2}{e_E} \cdot \frac{p_{cold}}{p_{hot}}} \left(\frac{k_B T_{hot}}{e \lambda_{Dhot}} \right). \quad (2.67)$$

Clearly, increasing p_{cold} leads to more efficient ion acceleration, as the accelerating field will increase.

There are a number of factors that can be detrimental to the TNSA mechanism. For example, if the plasma vacuum interface has a scalelength of greater than the Debye length, λ_D , the plasma ions are effectively screened by the background electrons from the accelerating field. Therefore, the peak electric field is reduced and the analytic solutions do not hold. A large laser pre-pulse, a thin target or a combination of the two, may mean that a collisional shock can be sent through the target to form a pre-plasma on the rear side of a target before the fast electrons reach the rear surface. If the pre-plasma expands enough before the fast electrons arrive, the ions can be partly shielded. This has been investigated experimentally by Kaluza et al. [136].

It is sometimes desirable that an ion beam uncontaminated by protons to be produced. Methods for proton removal have been attempted and include target heating to high temperatures [137] and ion gun etching. Target heating has been

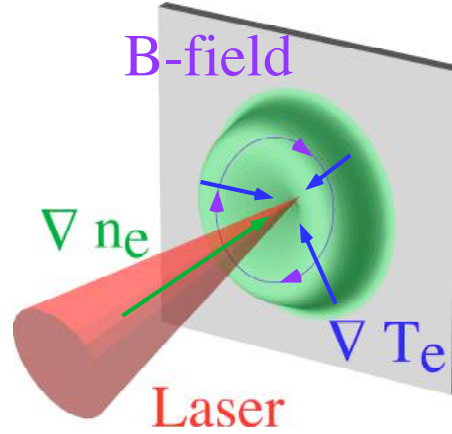


Figure 2.8: The $\nabla n_e \times \nabla T_e$ magnetic field generation mechanism.

successful in reducing proton acceleration by boiling off contaminants from the target surface, leaving a clean target surface. Ion guns remove protons by firing argon ions at the target to etch away the outermost surface containing the contaminants. These have to be running during the shot as the contamination layers will quickly reform when the etching is stopped.

2.3.4 The $\nabla n_e \times \nabla T_e$ magnetic field generation mechanism

It is possible for an interaction of a laser with a plasma to produce self generated magnetic fields [138]. To understand this mechanism, consider the electron pressure for an ideal gas, $P_e = n_e k_B T_e$ and its relationship with the electric field, \mathbf{E} :

$$\nabla P_e = -en_e \mathbf{E}. \quad (2.68)$$

Substituting this \mathbf{E} into Faraday's law and then substituting for P_e gives

$$\frac{\partial \mathbf{B}}{\partial t} = -\nabla \times \mathbf{E} = \frac{1}{e} \nabla \times \left(\frac{\nabla P_e}{n_e} \right) = -\frac{k_B}{en_e} \nabla n_e \times \nabla T_e. \quad (2.69)$$

Therefore, if there are components of the density gradient, ∇n_e , and temperature gradient, ∇T_e , that are not parallel, a magnetic field is generated. This is the case in a laser interaction with a solid target because the electron density gradient is directed towards and normal to the target surface. The temperature gradient is large outside the focal spot of the laser and is directed radially outwards. This is illustrated in figure 2.8.

The self generated magnetic field is produced azimuthally around the focal spot and can be as large as several Megagauss [139–141]. The strength of the generated magnetic field will decrease with time as the field is diffused and convected out of the generation region. The rate of generation reduces as hydrodynamic expansion reduces the density and temperature gradients.

2.4 Magnetic field reconnection

A plasma can have its composite charged particle trajectories significantly altered in the presence of a strong magnetic field, which introduces anisotropy in the plasma transport properties along or perpendicular to the field. To quantify the effect of a magnetic field on a plasma, the Hall parameter is used, which is the ratio of the gyrofrequency, $\omega_{ce} = eB/m_e c$, to the collision frequency, ν_{ei} . The transport in the plasma is affected when the Hall parameter exceeds unity.

Magnetic reconnection occurs when magnetic field lines change their topology by severing, followed by the connecting of previously isolated field lines. Energy stored in the magnetic field is lost to the plasma through heating and fast particle production as the field lines rearrange to a lower energy state. The time scales for this energy release can be very short.

There are two main models that attempt to explain the phenomenon of magnetic reconnection, the Sweet-Parker model and the Petschek model. Both of these models approach the problem using 2-D incompressible MHD (magnetohydrodynamics). The Sweet-Parker model requires a current sheet to form and the Petschek model requires a pair of slow-mode magnetohydrodynamic shocks. Magnetohydrodynamics can be used to describe the dynamics of electrically conducting fluids, assuming that the fields and fluid fluctuations have similar scalelengths and timescales.

The induction equation, or the equation of motion for the magnetic field lines in the plasma, can be derived by combining Ampère’s law (neglecting the displacement current) with Faraday’s law and Ohm’s law [142]:

$$\frac{\partial \mathbf{B}}{\partial t} = \frac{\eta}{\mu_0} \nabla^2 \mathbf{B} + \nabla \times (\mathbf{u} \times \mathbf{B}), \quad (2.70)$$

where η is the resistivity.

The magnetic Reynolds number defines the relative importance of the convective effects compared to diffusive effects. Taking the relative magnitudes of the convective term, $\nabla \times (\mathbf{u} \times \mathbf{B})$ and the diffusive term, $(\eta/\mu_0)\nabla^2\mathbf{B}$, from equation 2.70 gives the magnetic Reynolds number:

$$R_M = \frac{\mu_0 u L}{\eta}, \quad (2.71)$$

where L is a measure of the large scale of the system. For the case where $R_M \gg 1$, diffusion dominates. However, when $R_M \ll 1$, convection dominates and the magnetic field lines move with the plasma flow, which is described as “frozen in”. For ideal MHD to hold, the fluid has to be a perfect conductor and therefore needs to have very little resistivity, thus enabling the magnetic field lines to move with the plasma.

Magnetic reconnection theory requires the formation of a neutral current sheet so that $\mathbf{u} = 0$. Therefore, the electric field is given by $\mathbf{E} = \eta\mathbf{j}$. In this current sheet region, the resistivity can become very high, which means that the diffusion term becomes large. The introduction of even a small resistivity enables the magnetic field lines to decouple from the plasma flow. This allows the magnetic field lines to reorganise themselves, releasing energy from the system.

Figure 2.9 shows a schematic of the model proposed by Sweet and Parker, which considers two oppositely directed magnetic fields carried together by plasma flows. The magnetic fields are frozen in to the colliding plasma flows because the resistivity in the plasma is low. Where the plasmas collide, the magnetic field lines become stressed. As the magnetic field lines change their orientation, a current sheet forms and plasma is forced out along the merging magnetic field lines. Magnetic field lines can reconnect when the resistivity increases and the magnetic field lines are able to slip with respect to the plasma. The region where the reconnection occurs is characterised by a length, L , determined by the incoming plasma flows and the thickness of the region, δ is determined by the resistivity. The magnetic field lines in the reconnection region are compressed and store a large amount of energy, which is released during the reconnection process.

The main problem with the Sweet-Parker model is that even a simple order of

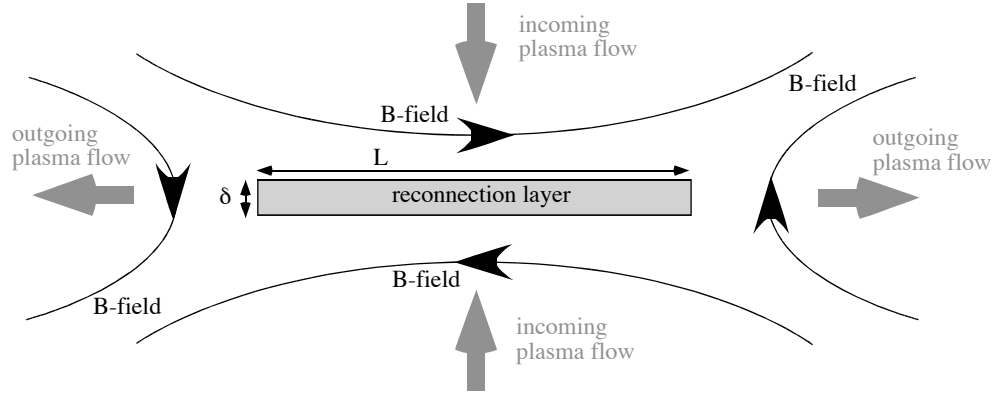


Figure 2.9: A schematic of the Sweet-Parker model for magnetic reconnection.

magnitude calculation [143] of the reconnection rates suggests that the process is very slow. Take the density, temperature, pressure and velocity of the incoming plasma to be ρ_{in} , T_{in} , P_{in} and v_{in} and the outgoing plasma to be ρ_{out} , T_{out} , P_{out} and v_{out} respectively. Firstly, the plasma flow velocity in must balance the plasma diffusion out, to define the thickness of the reconnection layer, δ :

$$v_{in} = \frac{\eta}{\mu_0 \delta}. \quad (2.72)$$

The assumption that the plasma is incompressible is used to simplify the calculation, so that $\rho_{in} = \rho_{out}$. Then mass continuity dictates that the amount of plasma going into the region through the length, L , must be equal to the amount flowing out through width, δ :

$$v_{in} L = v_{out} \delta. \quad (2.73)$$

If the magnetic energy into the diffusion region is then defined by the Poynting flux, $\mathbf{N} = \mathbf{E} \times \mathbf{B} / \mu_0$, where the electric field will be $\mathbf{E} = -\mathbf{v} \times \mathbf{B}$ so that

$$|\mathbf{N}| = \frac{v_{in} B_{in}^2}{\mu_0}. \quad (2.74)$$

If it is assumed that all of the magnetic field energy is converted into kinetic energy, then

$$\frac{v_{in} B_{in}^2}{\mu_0} = \frac{(\rho_{in} v_{in}) v_{out}^2}{2}. \quad (2.75)$$

Using equations 2.72 and 2.73, the velocity of the magnetic field into the reconnection area is therefore

$$v_{in} = \sqrt{\frac{v_{out} \eta}{\mu_0 L}} = \frac{v_{out}}{\sqrt{R_M}}. \quad (2.76)$$

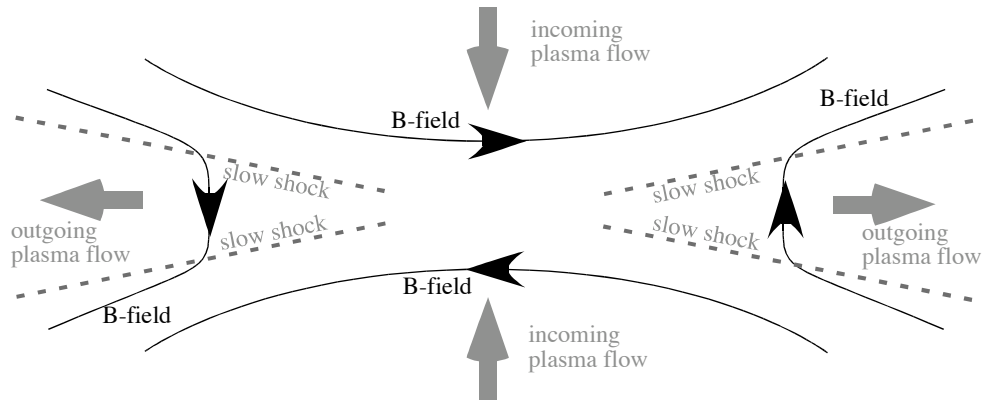


Figure 2.10: A schematic of the Petschek model for magnetic reconnection.

Because R_M is expected to be large in the reconnection region, this suggests that the reconnection rate would be very slow. Observations made of reconnection events in the solar corona suggest that the Sweet-Parker model predicts rates that are too slow by many orders of magnitude [144].

In 1964, Petschek realised that the central diffusion region does not necessarily have to be the same as the external length scale. Instead, the diffusion region is assumed to be small (far smaller than for the Sweet-Parker model) and slow mode shock waves emerge from the region. This is shown as a schematic in figure 2.10. Therefore, the magnetic energy is released in the shock wave, rather than in the diffusion region. The shock waves accelerate the incoming plasma to near the Alfvén velocity, $v_A = \sqrt{B^2/\mu_0\rho}$, along the reconnection region. The reconnection rate is comparable to the Alfvén velocity, which is much more comparable to observations.

The main problems with both of these models, however, is that neither describe the diffusion layer accurately. It is not possible to determine the length of the current sheet using the Sweet-Parker model, while the Petschek model is very sensitive to the boundary conditions and numerical solutions have never been obtained.

Chapter 3

Experimental methods

In this chapter, the experimental methods used for the experiments in this thesis are described. First, a brief overview of the Vulcan laser system is presented. This is followed by detailed descriptions of the ion detectors and diagnostics, which were used to measure the primary data presented. The data analysis processes are described.

3.1 The Vulcan laser

The Vulcan Laser is housed in the Central Laser Facility (CLF) at the Rutherford Appleton Laboratory (RAL), Oxfordshire, UK. It is a Nd:glass laser system, which runs at a wavelength of $1.05 \mu\text{m}$ and has three distinctly different target areas. The most recent upgrade to Vulcan is the Target Area Petawatt (TAP). A single beam-line capable of petawatt power ($10^{15} \text{ W} \simeq 500 \text{ J}/500 \text{ fs}$) can be focused down to intensities of $\sim 10^{21} \text{ Wcm}^{-2}$, making it among the highest intensity laser systems in the world at present. Target Area West (TAW) has a 100 TW, sub-picosecond beam along with a 10 ps probe and up to 6 other beams each of 200 J in a nanosecond. Although not used for experiments described in this thesis, Target Area East (TAE) also has 6 nanosecond beams and two shorter pulse beams. For the short pulse beam lines, the chirped pulse amplification and optical parametric amplification techniques have to be implemented and these are described below.

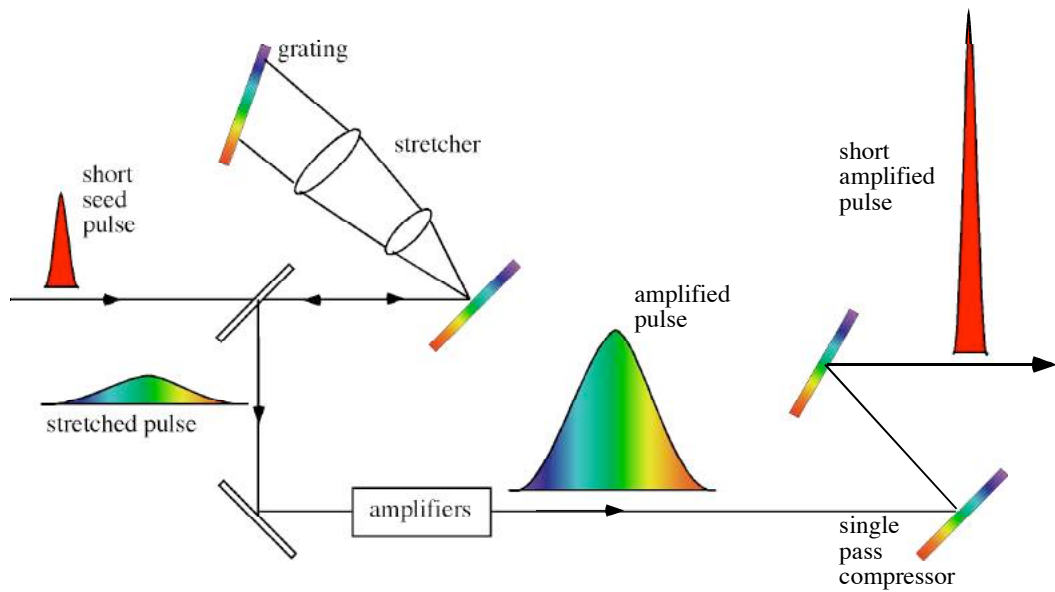


Figure 3.1: A schematic of the chirped pulse amplification (CPA) technique.

3.1.1 Chirped pulse amplification

Before the invention of the chirped pulse amplification (CPA) technique [2], the peak power of laser pulses was limited by the damage threshold of the amplifying media to GW/cm^2 fluences. The CPA technique allows an ultra-short laser pulse to be stretched out in time so that the intensity is reduced as it passes through the amplifying medium. A schematic is shown in figure 3.1. The frequency chirp that extends the pulse in time is created with a pair of anti-parallel gratings, so that after the gratings the low frequency components have traveled a shorter length and are in front of the high frequencies temporally. The elongated pulse is reduced in intensity and can thus pass safely through the amplifier without causing any damage. The stretched pulse is re-compressed after amplification by another pair of gratings to regain the ultra-short pulse length.

3.1.2 Optical parametric chirped pulse amplification

The use of CPA allowed significant improvement in the maximum intensities which could be achieved. For further increases in intensity, an increase in the energy could be made, which would require the beam size before focusing to be increased. But

increasing the beam size is more expensive because of the larger gratings, transport optics and focusing optics required. Alternatively, the pulse length could be shortened, which means the spectral bandwidth needs to be increased. CPA pulses are typically limited in pulse duration by the bandwidth of the amplifying medium. The optical parametric amplification (OPA) technique [145] provides a way to amplify a larger bandwidth.

The seed pulse for the amplification process is chirped as described in section 3.1.1. Non-linear crystals, such as beta barium borate (BBO), are pumped with a long pulse (nanoseconds) laser with an energy of a few Joules. The pulse length of the pump should match the pulse length of the broad-bandwidth chirped seed pulse for maximum efficiency. To minimise gain narrowing effects the pump needs a temporal top hat profile so that the pump energy is constant throughout the amplification of the chirped pulse and the bandwidth will remain broad. In the non-linear crystal the pump energy, ω_p , is parametrically converted into the seed frequency, ω_s . For the energy conservation condition to be met an idler pulse, ω_i , is also produced so that $\omega_p \rightarrow \omega_s + \omega_i$. The wave-vectors of the pump, seed and idler must also satisfy the phase matching condition, $\mathbf{k}_p \rightarrow \mathbf{k}_s + \mathbf{k}_i$. This can be achieved in birefringent crystals by having the polarisation of the pump pulse orthogonal to the polarisation of the seed pulse. After amplification, the pulse can be re-compressed as described in section 3.1.1.

3.1.3 The Vulcan Petawatt laser

The Vulcan Petawatt upgrade was commissioned in 2003 and held the record for being the highest-intensity focused laser in the world in 2004 [146, 147]. The specification for the laser is a pulse containing 500 J in 500 fs. To produce such a pulse, the facility needed a customised stretcher and compressor, a novel front-end amplification based on OPCPA, a mixed glass amplifier chain and adaptive optics. A schematic of this system is presented in figure 3.2 and is described in more detail below.

The front end of the Vulcan Petawatt is a commercial Ti:Sapphire Kerr lens

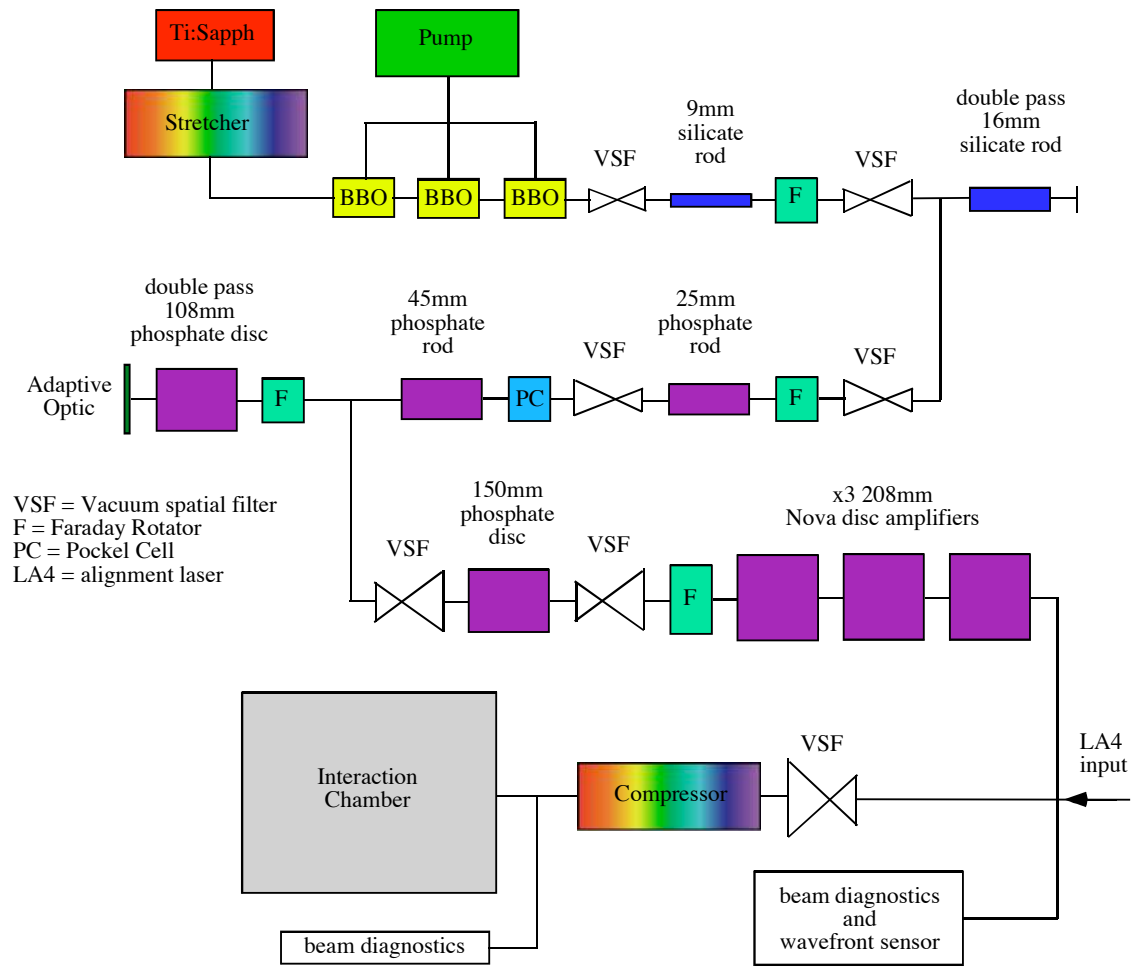


Figure 3.2: A schematic of the Vulcan petawatt laser system.

mode-locked system, which generates pulses with a duration of 120 fs and a full width half maximum bandwidth of 15 nm. The oscillator operates at a central wavelength of 1053 μm , producing 5 nJ pulses at a rate of 80 MHz. The oscillator pulse is then stretched to a pulse length of 2.4 ns with a bandwidth of 18 nm before amplification. The stretcher needs to be perfectly conjugate with the compressor to achieve the final pulse length of 500 fs.

The pre-amplification stage uses OPCPA as described in section 3.1.2. The amplification is done in three stages, using BBO crystals for the optical parametric amplification. It is seeded by the chirped oscillator pulse and pumped by a Q-switched Nd:YAG laser operating in a single longitudinal mode, producing single 1 J, 15 ns Gaussian profile pulses at a wavelength of 532 nm. The central 3 ns of this pulse is selected by a fast pockel cell to produce a near top hat profile for pumping the crystals. After amplification there is no loss of bandwidth and the gain is better than 10^8 . A requirement of the pre-amplification is for the output energy to be very stable, so the third stage of the amplification is operated in saturation to achieve this. Before the next stage of amplification the pulse is stretched again to 4.8 ns.

Phosphate glass amplifiers are the standard amplifiers used in the Vulcan system and are pumped by flash lamps. However, using the phosphate chain alone means that too much bandwidth is lost. Additional silicate glass amplifiers are used to give the effect of broadening the bandwidth, so that the full bandwidth can be amplified. The beam is increased in diameter after each amplification stage to keep the fluence below the damage threshold as the pulse energy increases. Additional energy is obtained with a final disc amplifier stage that consists of three 208 mm aperture disc amplifiers from Nova (a retired LLNL laser). This final amplification stage has gain isolation, by means of a 208 mm aperture Faraday rotator and a single polariser at the stage input. The bandwidth of the final pulse is 5 nm.

From the final amplification stage, a 19 m long vacuum spatial filter expands the beam from 208 mm to 600 mm, as well as improving the beam quality. The gold-coated, 1480 lines/mm holographic gratings, which were supplied by LLNL, are set in a single pass geometry separated by 13 m. The operational input angle for

this single pass geometry is 48° . The whole of the compressor is housed in a vacuum chamber and is isolated from the target vacuum chamber by a gate valve.

After the second grating there are two mirrors, the first for turning the beam into the target chamber and the second for turning the beam onto the $f/3$ focusing parabolic mirror. Through the back of the first of these turning mirrors, the compressed pulse is sampled by collecting and transporting the low energy leakage through a window in the vacuum chamber. The beam diagnostics include near field beam profile measurements and the spectral width and auto-correlator measurements for the pulse duration.

The 120 mm adaptive optic (AO) module [148] is important for achieving the highest possible intensity. Wavefront errors arise from static aberrations of the beam-line optics and distortions due to thermal gradients caused by firing previous shots. By improving the wavefront quality with the adaptive optic, the optimal focal spot improves by a factor of > 2 , from 3 times the diffraction limit without the AO, to being close to diffraction limited. Wavefront error correction also helps achieve the best re-compression. The focal spot decrease of a factor of > 2 means that the intensity on the target goes up by a factor of > 4 .

As with any high intensity laser system, pre-pulses can be present due to amplified spontaneous emission (ASE) and phase errors. For the Vulcan Petawatt laser, the stretched pulse is nanoseconds long and this governs the temporal width of any isolating gates, as well as the pump duration of the OPCPA. Hence, the pre-pulse is of the order of a nanosecond ahead of the main pulse. The largest contribution to the ASE is generated by the optical parametric generation in the OPCPA pre-amplification stage as this achieves the largest gain and cannot be removed by isolating gates. For full disc shots the best contrast ratio for Vulcan Petawatt is expected to be around 4×10^{-8} on a nanosecond timescale [149].

For the experiments described in this thesis there were some slight variations in the laser parameters. A summary of the laser parameters for each of the experiments is presented in table 3.1.

The pulse lengths are measured using leaked light through a mirror, after pulse compression into a single shot auto-correlator [150]. The laser energy is measured

Parameter	2004	2005	2006
Pulse length (fs)	1000	570 ± 175	550 ± 150
Pre-compression maximum energy (J)	593	694	530
Percentage onto target	60%	55%	47%
Focal spot diameter (μm)	7	5	5
Maximum average power (TW)	360	670	470
Peak intensity (Wcm ⁻²)	1.5 × 10 ²⁰	5.5 × 10 ²⁰	4 × 10 ²⁰
Peak a_0	11	21	18
Contrast ratio	10 ⁻⁵	10 ⁻⁷	10 ⁻⁷

Table 3.1: A summary of the laser parameters for each of the experiments.

on every shot before compression. A calibration of the relative amount of energy reaching the target chamber centre is made with a calorimeter in the target chamber during a test shot. For 2005 and 2006, the energy transmission through the compressor was measured with calorimetry and for the 2004 experiment, 60% was measured on other experiments at the time. The values for the energy transmission through the compressor are given in table 3.1. The energy throughput has reduced over time, largely due to the degradation of the focusing parabola. The focal spot size is determined by imaging the focal spot of a CW laser, co-linear to Vulcan, with a microscope objective. Confirmation that this is an accurate measurement of the focal spot size on a full power shot has been made by imaging 3ω emission from a solid target experiment [151], which gave a measurement of the focal spot that agreed to $\pm 0.5 \mu\text{m}$. The peak intensities given are the cycle averaged peak vacuum intensities for a Gaussian pulse in space and time:

$$I_0 = \frac{2E_{laser}}{\tau d^2} \left(\frac{\ln 2}{\pi} \right)^{\frac{3}{2}}, \quad (3.1)$$

where E_{laser} is the laser energy, τ is the full width half maximum pulse length and d is the full width half maximum focal spot diameter. Self-focusing in the interaction may enhance the intensity significantly.

3.1.4 The Vulcan Target Area West (TAW) facility

The Vulcan Target Area West (TAW) is a very flexible facility which can accommodate many experimental configurations. One of the major attractions of the area is the 100 TW beam line, which can produce pulses of 100 J in 1 ps using the CPA technique described in section 3.1.1. In addition to this, there is a second CPA line and up to 6 long pulse beams that can be fired into the area.

The front end of the 100 TW CPA line begins with a Kerr lens mode locked Tsunami oscillator. This Ti:Sapphire lasing medium is pumped by an Argon ion laser producing 5 nJ in 120 fs at 80 MHz. These pulses are then chirped in a standard telescopic, double pass mode stretcher, which uses gratings with 1740 lines per mm. The maximum bandwidth at 1053 nm is 16 nm. Amplification of the 600 ps length chirped pulse begins with the 3-stage double passed Nd:glass pre-amplifiers and then the pulse single passes flashlamp pumped rod amplifiers. Next, the pulse is double passed through 108 mm rod amplifiers and the final amplification is done with a single pass 150 mm aperture disc amplifier. As for the Vulcan Petawatt beam, the diameter of the pulse is increased as it is amplified to avoid damaging the system. Recompression of the full energy beam is done by a pair of single pass, gold coated, holographic gratings with 1740 lines per mm, separated by 3.5 m. A final pulse length of 1 ps can be achieved and the pulse is then turned into the chamber with a mirror. A reflective parabolic mirror in the target chamber focuses the beam to maximum intensities of $\sim 5 \times 10^{19} \text{ Wcm}^{-2}$ and is used to investigate high-intensity short-pulse laser-plasma interactions. The short pulse beam can produce high energy particles to be studied in their own right or used as a probe for other laser-plasma interactions. Diagnostics for the pulse length, near and far field profiles and the spectrum use light leaked through the back of the final turning mirror to diagnose the pulse parameters on each shot.

The second CPA beam, recompressed in air to 10 ps with 30 J, is often used as a probe beam. Often it is converted to 2ω and 4ω because the critical surface of an interaction will be at a higher density for shorter wavelengths and therefore allows probing to higher densities.

There are up to 6 other long-pulse beams, each of 200 J in a nanosecond. The oscillator for these beams is a single longitudinal mode (SLM) oscillator. Synchronisation between all of the beams into the area is possible by triggering the long pulse seed selection from the RF signal produced by the CPA oscillator. By setting the correct beam paths in the target area, the relative timings of the arrival of the beams can be adjusted. These long-pulse beams are often frequency doubled from ω to 2ω (527 nm) or quadrupled to 4ω (263 nm). The beam geometry into the target chamber is flexible, apart from the 100 TW beam because its entry into the chamber is under vacuum.

3.2 Ion detectors

3.2.1 CR39

Californian Resin-39, or CR39 was discovered in 1978 by physicists at the University of California, Berkeley, as a medium that could be used to detect energetic ions and neutrons. It is particularly useful because it is insensitive to x-rays and electrons (except for very large fluxes). This nuclear track detector is made from the polymer allyl diglycolcarbonate which has the chemical formula $C_{10}H_{18}O_7$ and a density of about 1.30 g/cm^{-3} . It is easily manufactured into transparent, rigid slides and the CR39 used for the experiments described in this thesis was supplied by Track Analysis Systems Ltd, Bristol, UK.

The rate at which an ion loses energy, E , at a distance into the material, x , is characterised by the stopping power of the material it is in. There are two contributions to this stopping power, the electronic stopping power and the nuclear stopping power. The stopping power of protons in CR39 is shown in figure 3.3 (a), which have been calculated using the code SRIM [152]. The material used to model the CR39 in SRIM was mylar (polyethylene terephthalate), because its density is the closest to CR39 at 1.4 gcm^{-3} . It is clear from this figure that the electronic stopping power dominates and the nuclear stopping power only becomes significant at low energy. The electronic stopping power is from interactions of the ions with

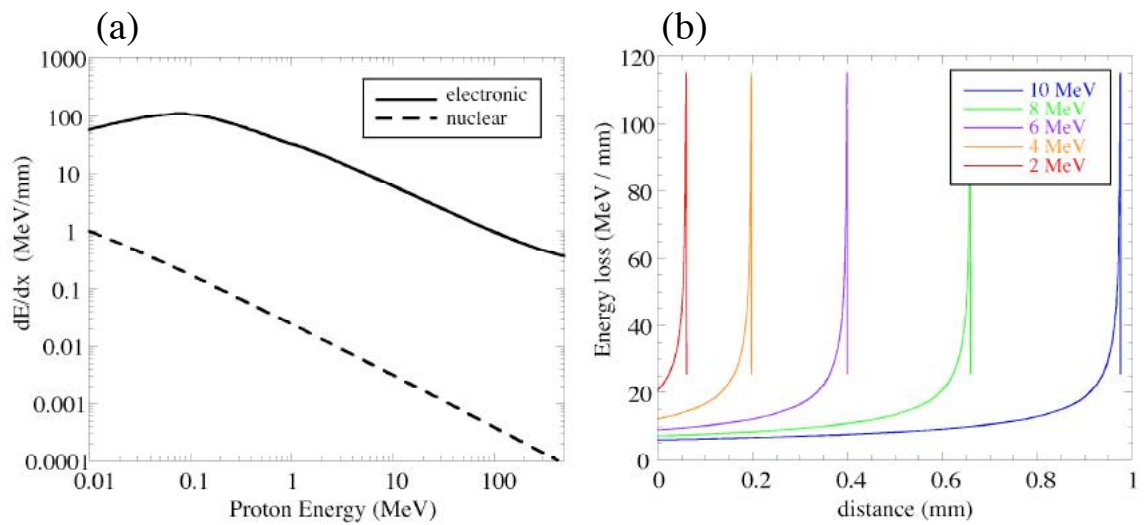


Figure 3.3: (a) Proton stopping power in CR39 and (b) the energy deposition of protons of different energies as they pass through mylar.

the electrons in the material via the Coulomb force. The electronic stopping power curve, shown in figure 3.3 (a), increases at lower energy and displays a peak at which the stopping power is greatest. This is known as the Bragg peak and is very well defined for protons and ions. When the proton or ion reaches the Bragg peak it is stopped suddenly and deposits a large amount of energy in a very localised volume. This can be seen in figure 3.3 (b). The energy deposited by the ion in the CR39 at the Bragg peak alters the chemical bonds of the polymer. However, the initial kinetic energy of the ion entering the CR39 must exceed a threshold energy to cause damage. Therefore, ions with energy below ~ 100 keV per nucleon will not be detected. Electrons, on the other hand, lose their energy more smoothly, which is why the CR39 does not detect them.

The CR39 must be etched in a warm ($\sim 85^\circ\text{C}$) bath of 20% concentrated sodium hydroxide (NaOH) solution to make the ion tracks visible. In the regions where ions lose most of their energy, the chemical bonds are damaged and are dissolved faster than the undamaged CR39. This means that a pit is etched away where an ion is stopped. The final size of the pit depends upon a number of factors including the depth at which the ion is stopped (i.e. its initial energy), how long the CR39 is etched for and the temperature of the etching solution. The deeper into the detector the

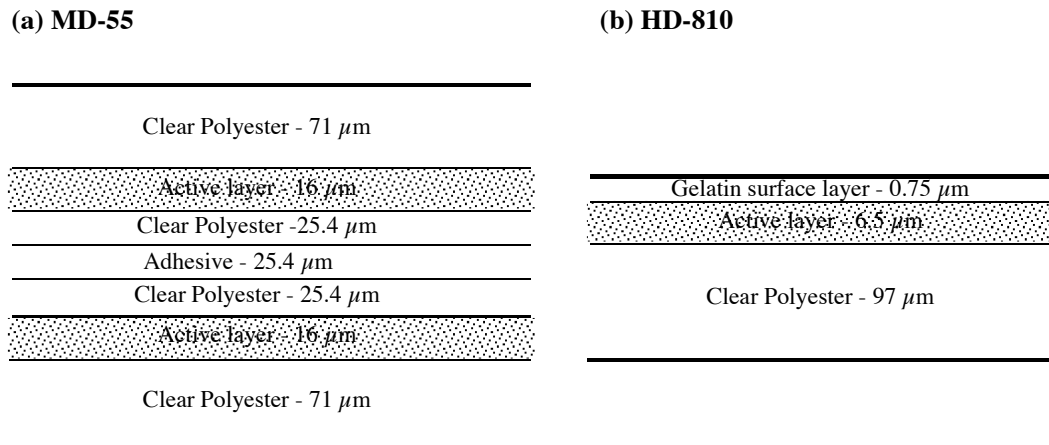


Figure 3.4: A schematic showing the structure of (a) the MD-55-2 type and (b) the HD-810 type GafChromic dosimetry film.

ion loses its energy, the smaller the visible hole on the CR39 surface. The pit sizes are of the order of several μm in diameter and can be inspected using a microscope.

3.2.2 Radiochromic film

Radiochromic film (RCF) is a thin plastic film, which can be used to detect all types of ionising radiation including electrons, ions and γ -rays. Insensitive to optical light, the RCF is very easy to handle and has a very high spatial resolution. When exposed to ionising radiation, the dye in the film, triphenyl methane dye cyanide, undergoes a photo-chemical reaction and changes from transparent to blue. The optical density of the exposed film is proportional to the radiation dose incident upon it, so the larger the radiation dose, the darker blue the film.

The types of RCF used in the experiments for this thesis are the MD-55 type GafChromic and HD-810 type GafChromic, which are commercially available and are manufactured by ISP Technologies Inc. The structure of these two types of film are shown in figure 3.4. The MD-55 type has two active layers sandwiched between a polyester substrate and has a total thickness of about $250 \mu\text{m}$. The HD-810 type has a single active layer protected by a gelatin film and has a total thickness of about $100 \mu\text{m}$. The HD-810 type has a thinner total active layer and is therefore about one order of magnitude less sensitive than the MD-55 type.

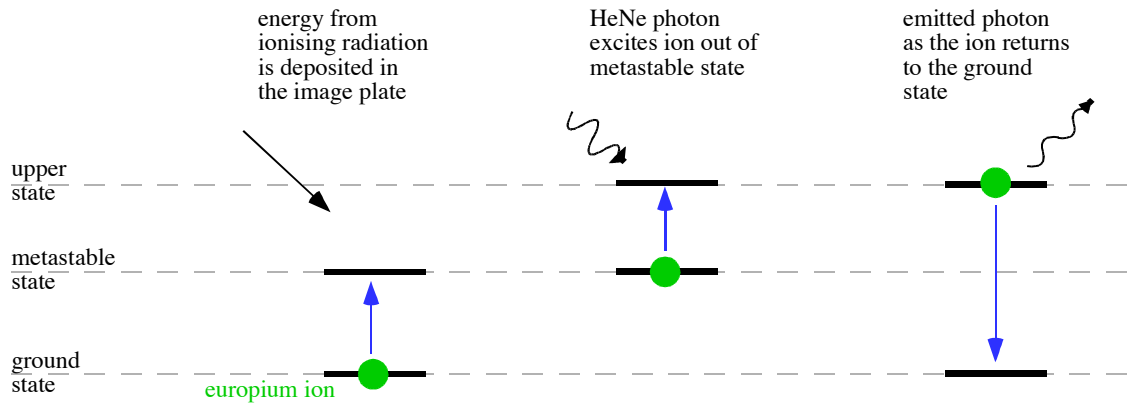


Figure 3.5: The photo-stimulated luminescence process

3.2.3 Image plate detector

The image plate detectors were used primarily to measure electrons in the experiments but, like the RCF, it will detect all ionising radiation. These detectors and the scanners are commercially available: the type of image plate used was Fuji BAS MS2325 and the scanner was a Fuji BAS 1800II. The plate contains a $100\ \mu\text{m}$ layer of $\text{BaFBr} : \text{Eu}^{+2}$, which is a luminescent material. Energy deposited in this layer excites the europium ions into a metastable state and therefore cannot decay through fast optical transitions. The stored information can be read using the scanner, which uses a helium neon laser to excite the europium ions into a higher state. This state is not metastable and the europium ion emits a photon as it returns to the ground state. This photo-stimulated luminescence process (PSL) is shown in figure 3.5.

This PSL is detected by a photomultiplier and the number of photons detected is directly proportional to the amount of energy deposited in the active layer. One major advantage of the image plate detectors is that they are reusable and after they have been read, a light box erases the remaining signal so they are ready for use again.

The response of the image plates has been calibrated by AWE plc [153]. By using a ^{60}Co source to give varying x-ray doses to an image plate, the PSL intensity for a particular x-ray dose was found. It was found that the image plate produced a very linear response to the x-rays from doses of $10^{-8}\ \text{Gy}$ to $10^{-1}\ \text{Gy}$. By considering the amount of energy lost in the active layer and therefore the radiation dose from

particles, it is possible to find a conversion from PSL to number of particles.

3.3 Ion diagnostics

3.3.1 Thomson ion spectrometer

To measure the spectra of ions with different mass to charge ratios, a Thomson ion spectrometer [154] can be used. A schematic of a Thomson ion spectrometer is shown in figure 3.6. It consists of two parallel permanent magnets, which provide an almost constant magnetic field between them. On the inside faces of each magnet there is a copper plate, electrically insulated from the magnets. By applying a voltage across the two plates, an electric field is set up in the gap, which is parallel to the magnetic field. The deflection of a charged particle in the magnetic field is proportional to $\mathbf{v} \times \mathbf{B}$, that is in a direction perpendicular to the magnetic field and the direction it is moving in. However, the size of the deflection is inversely proportional to the velocity (or energy) of the particle, because the faster particles pass through the magnetic field quicker. The deflection of the particles in the electric field is in a direction parallel to the electric field. The size of the deflection is determined by the particles charge to mass ratio (Z/A). A piece of CR39 is used to detect the ions behind the magnet. A pinhole is placed in front of the spectrometer to restrict the number of ions entering by selecting a small solid angle. A neutral point forms where high energy neutral particles, which are usually recombined accelerated particles, damage the CR39. These neutral particles are unaffected by the electric and magnetic fields in the spectrometer so they are detected in a position that is known as the ‘straight through’ or ‘neutral point’. It is from this neutral point that the deflection distances are measured.

For the parallel electric field plates, an analytical solution for the shapes of the tracks for different mass to charge ratios can be found. The force on a charged particle with a particular mass to charge ratio, A/Z , is given by the Lorentz force shown in equation 3.2:

$$\mathbf{F} = Ze(\mathbf{E} + \mathbf{v} \times \mathbf{B}). \quad (3.2)$$

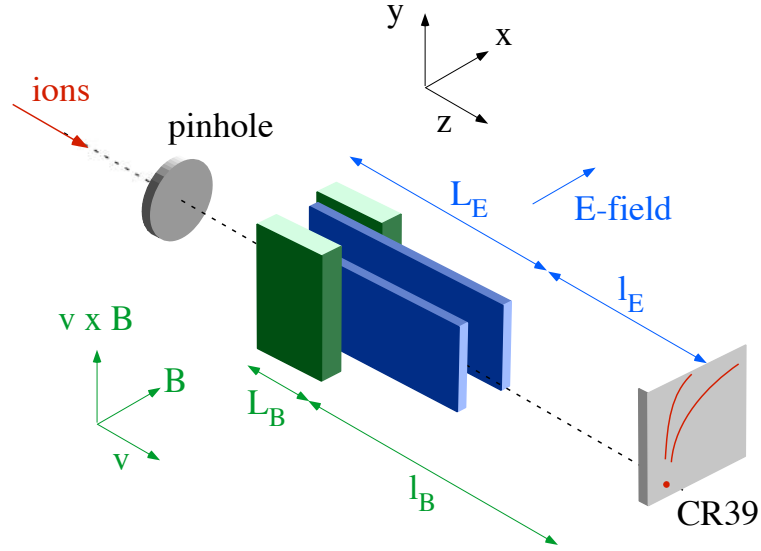


Figure 3.6: The Thomson ion spectrometer. The magnets are shown in green and the electric plates are shown in blue.

Assuming that \mathbf{E} and \mathbf{B} are in the x-direction only and that the initial velocity of the charged particle is in the z-direction, then the $\mathbf{v} \times \mathbf{B}$ force will be in the y-direction. The deflection in the x-direction is calculated from the electric field component of the force and the deflection in the y-direction is derived from the $\mathbf{v} \times \mathbf{B}$ force. If the distances are defined as in figure 3.6, where L_E and L_B are the length of the electric and magnetic fields respectively in metres and l_E and l_B are drift distances after the fields to the detector plane in metres, the equations giving the deflections in the detector plane are:

$$x = \frac{ZeEL_E}{Av^2m_u} \left[\frac{L_E}{2} + l_E \right], \quad (3.3)$$

$$y = \frac{ZeBL_B}{Avm_u} \left[\frac{L_B}{2} + l_B \right], \quad (3.4)$$

where m_u is $\frac{1}{12}$ the mass of ^{12}C . Using the equations 3.3 and 3.4, the velocity, v , can be eliminated to give an expression for the unique parabola for a given mass-to-charge ratio:

$$y^2 = \frac{ZeB^2l_B^2}{Am_uEl_E} \left[\frac{l_B}{2} + L_B \right]^2 \left[\frac{l_E}{2} + L_E \right]^{-1} x. \quad (3.5)$$

If the electric and magnetic fields have the same lengths and positions, i.e. $L_E =$

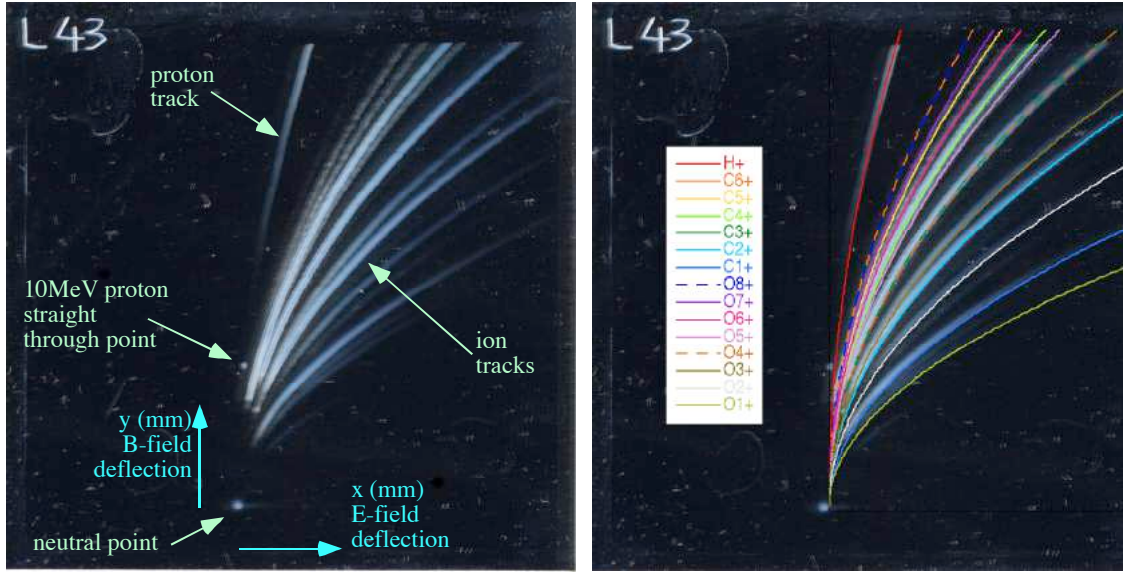


Figure 3.7: An example of the ion tracks from a Thomson ion spectrometer: (a) shows a scan of a CR39 from a shot onto a foam target (the important features are labeled) and (b) shows the same piece of CR39 with the analytic solutions for different ion species overlaid.

$L_B = L$ and $l_E = l_B = l$, then equation 3.5 can be simplified:

$$y^2 = \frac{ZeB^2l}{Am_u E} \left[\frac{l}{2} + L \right] x. \quad (3.6)$$

An example of how the tracks are identified by using the deflection equation 3.6 is shown in figure 3.7. The scan of the CR39 is from a Thomson ion spectrometer looking at ions from an underdense foam shot. In figure 3.7 (a), the main features of the data are shown, in particular, the neutral point where there has been no deflection. Calculating parabolic tracks using the deflection equations and how they overlay with the experimental data is shown in figure 3.7 (b) and this shows a good fit.

To determine the energy of an ion, the velocity, v , from the ion's kinetic energy, $E_{ion} = \frac{1}{2} A m_u v^2$, is substituted into the dispersion relation from the magnetic field deflection shown in equation 3.4:

$$E_{ion} = \frac{[ZeBl_B(\frac{1}{2}l_B + L_B)]^2}{2Am_u} \frac{1}{y^2}. \quad (3.7)$$

This analytic method for calculating the parabolic shapes of the tracks is fairly good for predicting where the ion tracks are likely to be. However, it does not take

into account any magnetic fringe fields that may be present and it is only for the parallel electric field plate case. The fringe fields were measured using a Hall probe and were found to be negligible. A calibration has been performed previously [31], to compare the analytic solution shown in equation 3.6 and a numerical model. The numerical model tracked charged particles trajectories through the measured magnetic field by solving the ion equation of motion. It confirmed that the effect of the fringe field was negligible. As a further confirmation the CR39 detector was filtered with various materials of particular thicknesses to show cut off points on the proton parabola. This works by only allowing protons above a certain energy through to the CR39. These cut off positions are then compared to the calculated position to confirm the calibration. The point where the proton parabola appears on the back surface of the CR39 can also be used as a further calibration point. For a 1 mm thick piece of CR39 this happens at 10.5 MeV. Filter calibrations similar to these were performed for the Thomson ion spectrometers used in the experiments described in this thesis.

Analysis of the ion spectra

Producing the ion spectra from the CR39 detector in the Thomson ion spectrometers involves counting the pits at a particular position and calculating the energy of the ion from the deflection. The pits are observed using a microscope with a travelling image plane (x - y plane). Two different microscopes were used in the analysis. The first of the systems used was a Leica DMLB microscope coupled to a high resolution digital camera (Leica DC300 with a 3.3 Megapixel sensor) and then connected to a computer at Imperial College London. The second system, at the Max-Planck-Institut für Quantenoptik, Garching in Germany, is similar but has an automated translation stage and pattern recognition software to fit ellipses to the ion pits as the images are taken. The pit diameter and position information is stored on the computer for analysis. An example of the ion pits under a microscope is shown in figure 3.8.

To obtain the energy spectra $dN(E_{ion})/dE_{ion} \simeq \Delta N(E_{ion})/\Delta E_{ion}$, the number of ions, $\Delta N(E_{ion})$, within the energy interval $[E_{ion}, E_{ion} + \Delta E_{ion}]$ needs to be found.

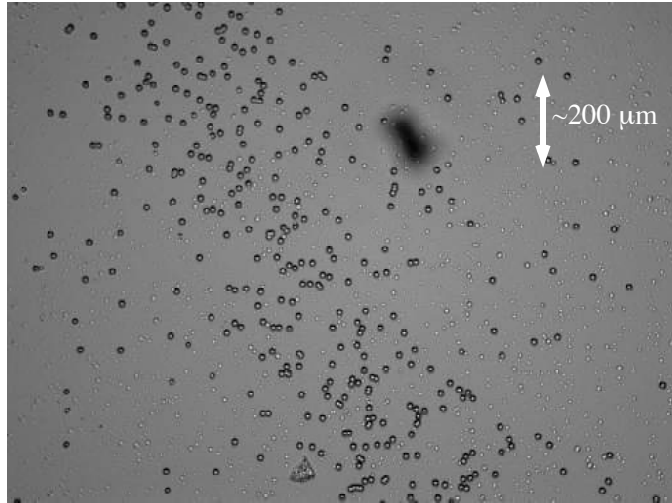


Figure 3.8: Helium ion pits from a laser gas-jet experiment, as seen under an optical microscope.

The energy interval, $[E_{ion}, E_{ion} + \Delta E_{ion}]$, corresponds to a y deflection interval of $[y, \Delta y]$ according to the dispersion relation, equation 3.7. Low energy ions with a sample width, Δy , will correspond to a small energy interval width, ΔE_{ion} . For high energy ions where the deflections are smaller, Δy will correspond to a much larger ΔE_{ion} . Therefore, the spectra can either be sampled at constant energy interval, ΔE_{ion} , or at constant deflection interval, Δy over the length of the parabola track. It has been observed by Kaluza [155] that counting in intervals of Δy that are smaller than the pinhole size will generate artificial noise in the spectrum, therefore it is preferable to use a constant deflection interval larger than the pinhole size when sampling the spectra. It is usual to divide the energy spectra by the solid angle to give the number of ions per energy interval per steradian. The solid angle is determined by the pinhole at the entrance of the spectrometer.

Errors in the number of ions in the counted spectra will arise from the accuracy to which the number of pits in a sample is counted and the sample size. An estimate of this error can be made by counting a sample many times and looking at the differences in the numbers counted. This estimate for error in the number of ions is around 5%. The energy error will be determined by the size of the pinhole, which will cause a blurring of the energies as the ions are deflected. At the higher energies, the energy errors will become larger because of the smaller deflections. There are

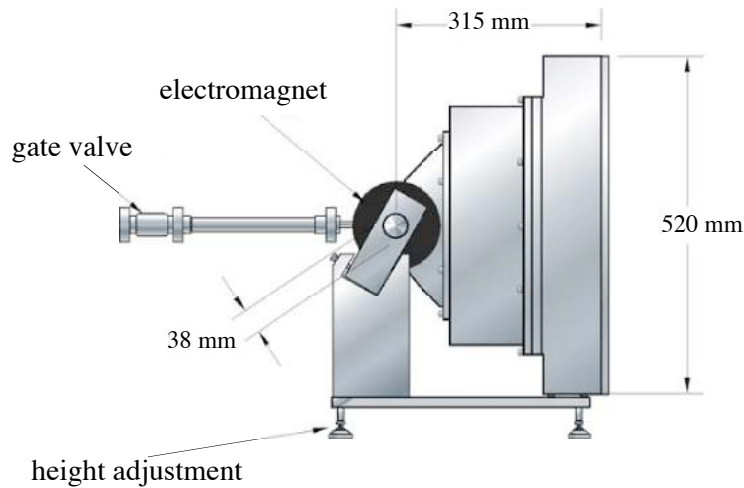


Figure 3.9: Schematic of the basic design of the electron spectrometers (courtesy of S. P. D. Mangles, based on a technical drawing courtesy of B. Fell, CCLRC Rutherford Appleton Laboratory).

other errors, such as the accuracy to which the deflection distances are measured, which are assumed to be small compared with the pinhole size error.

3.3.2 Charged particle spectrometer

The charged particle spectrometers were primarily used for electron spectra measurements, where electrons are deflected according to their energy with a magnetic field created by an electromagnet. The principles are exactly the same as those described in section 3.3.1 for the Thomson ion spectrometer, but without the electric field. It is unnecessary to have an electric field in an electron spectrometer as there is only one species of negatively charged particles, electrons, that would have been created during the interactions described in this thesis. However, the spectrometers were designed so that detectors can also be placed on the positively charged deflection side. The electromagnets were fully characterised by Mangles [91] for the deflection of electrons. The strength of the magnetic field between the magnets is controlled by the current to the electromagnet. It was found that the analytic solution for the deflection of electrons agreed well with a tracking code which accounted for any fringe fields. Therefore, it is assumed that the deflection of positively charged particles entering the spectrometer will be well described by the analytic solution.

The angle selection for the charged particle spectrometers is a lead slit and determines the energy resolution, ΔE . As with the Thomson ion spectrometer, the energy resolution is reduced for higher energies because of the reduced deflection. The spectrometers sat outside the target chamber with pipes under vacuum connecting the spectrometers to the chamber. A gate valve separated the main target chamber from the spectrometers, which were pumped down separately, so that the detectors could be changed without letting up the main target chamber. Figure 3.9 shows a technical drawing of one of these spectrometers. The triangular shaped vacuum housing after the magnet was symmetric in the positive and negative deflection sides. The detector sat at the back of the vacuum housing, usually behind a thin ($\sim 15 \mu\text{m}$) aluminium foil to shield the detector from stray laser light. For the electrons, image plates (section 3.2.3) were used as the detector. Image plates were also placed in the positively charged particle side but for some of the shots, CR39 was used as an additional detector. The zero deflection position in the spectrometer is visible on the image plates as an x-ray signal in the shape of the slit.

The analysis of the electron data uses the calibration of the image plates to relate the PSL intensity to the number of electrons at a particular position and the deflection to create the spectra. For the ions, pits in the CR39 can be counted to find the number at a particular position. The analysis is very similar to that described in the section 3.3.1 for Thomson ion spectrometers, the main difference being that there may be several species of ions present on the detector. Providing there are not too many different ion species, i.e. for a pure helium target, the different species can be identified by the size of the pits at a particular position. Also, it is not practical to count all of the pits across the width of the slit which defines the solid angle. It is easier to recalculate the solid angle for the sample that has been counted. The slit width still defines the energy error.

3.3.3 Imaging detector stacks

The detector stack diagnostic is a simple passive diagnostic for imaging proton beams. It is particularly useful for protons because the Bragg peak in the stopping

power of protons means that a particular layer in the stack will correspond to a well defined proton energy. Detectors used in the stacks are usually radiochromic film, often with some CR39 to confirm that the signal is protons. Sometimes iron spacers were used to slow down higher energy protons. For each stack composition, the Monte Carlo code TRIM [152] was run to calculate the stopping range for a proton of a particular input energy. This gives the energy measured in each layer of a stack. The RCF stacks can therefore provide information on the proton beam's angular divergence at different energies.

Measuring the angular divergence of the proton beam is not the only useful feature of these RCF stacks. Proton radiography is a technique which utilises the small source size and high spatial quality of laser produced proton beams [46–48]. By passing a proton beam through another interaction of interest, protons are deflected by electromagnetic fields and absorbed in high density regions of the interaction. A detector stack records the imprinted proton beam giving an image of the probed interaction. Hence, if the interaction being probed is of short enough duration, a time history is also recorded by the proton beam by looking at different layers in the stack. Different energy protons will pass through the interaction at different times because they are travelling at different velocities. The fastest (highest energy) protons will see an earlier time than the slower (lower energy) protons. The highest energy protons are stopped at the back of the detector stack, so images from the front of the stack observe later times.

3.3.4 Activation detector stacks

Nuclear activation of copper can be used to obtain spatially integrated proton spectra. This technique has been used previously in laser plasma interactions and is described in [31]. Copper occurs naturally in two isotopes, ^{63}Cu , which makes up 69.2% and ^{65}Cu , which makes up the other 30.8%. Table 3.2 shows the possible products from nuclear reactions from incident protons and γ -rays. The nuclear reactions with the largest cross sections in ^{63}Cu for protons are $^{63}\text{Cu}(p, n)^{63}\text{Zn}$ and $^{63}\text{Cu}(p, np)^{62}\text{Cu}$. The (p,n) reaction's cross section peaks at proton energies of

Reaction	Product	Peak X-section (barns)	Peak p or γ energy (MeV)	Threshold (MeV)	$T_{\frac{1}{2}}$ of product
In ^{63}Cu					
(p,n)	^{63}Zn	~ 0.5	~ 11	4	38.47 m
(p,2n)	^{62}Zn	~ 0.1	~ 25	13	9.186 h
(p,n+p)	^{62}Cu	~ 0.9	~ 25	14	9.67 m
(γ ,n)	^{62}Cu	~ 0.1	~ 17	10	9.67 m
(p,2n+p)	^{61}Cu	~ 0.3	~ 35	20	3.333 h
(p,n+p+ α)	^{58}Co	~ 0.2	~ 40	26	70.86 d
In ^{65}Cu					
(p,n)	^{65}Zn	~ 0.9	~ 10	2	243.7 d
(p,3n)	^{63}Zn	~ 0.16	~ 35	30	38.47 m
(p,n+p)	^{64}Cu	~ 0.6	~ 24	13	12.70 h
(γ ,n)	^{64}Cu	~ 0.15	~ 18	10	12.70 h
(p,X)	^{62}Cu	~ 0.2	~ 50	30	9.67 m

Table 3.2: The possible products from reactions with cross sections ≥ 0.1 barns which decay by β^+ emission from proton and γ interactions with ^{63}Cu and ^{65}Cu . The cross section for the interaction and the product decay information is given. The threshold is the lowest energy of p or γ at which a particular reaction can occur.

around 13 MeV and the (p,np) cross section peaks for 26 MeV protons. In ^{65}Cu there is a $^{65}\text{Cu}(p, 3n)^{63}\text{Zn}$ interaction which peaks for protons with an energy of 35 MeV and a $^{65}\text{Cu}(p, X)^{62}\text{Cu}$ (X indicates that there are many products), which peaks for protons with energy of 50 MeV.

Very few protons with this energy are expected, therefore the contribution to the activation expected from reactions with ^{65}Cu will be negligible. It is also possible for γ s to activate the copper to ^{62}Cu and ^{64}Cu . Although the cross sections for the $^{63}\text{Cu}(\gamma, n)^{62}\text{Cu}$ and $^{65}\text{Cu}(\gamma, n)^{64}\text{Cu}$ interactions are smaller than for the protons, a large number of γ s may be expected for some of the geometries used in the experiments described in this thesis. These would mainly be generated by bremsstrahlung as a hot electron beam travels through the stack. For this reason, the proton spectra

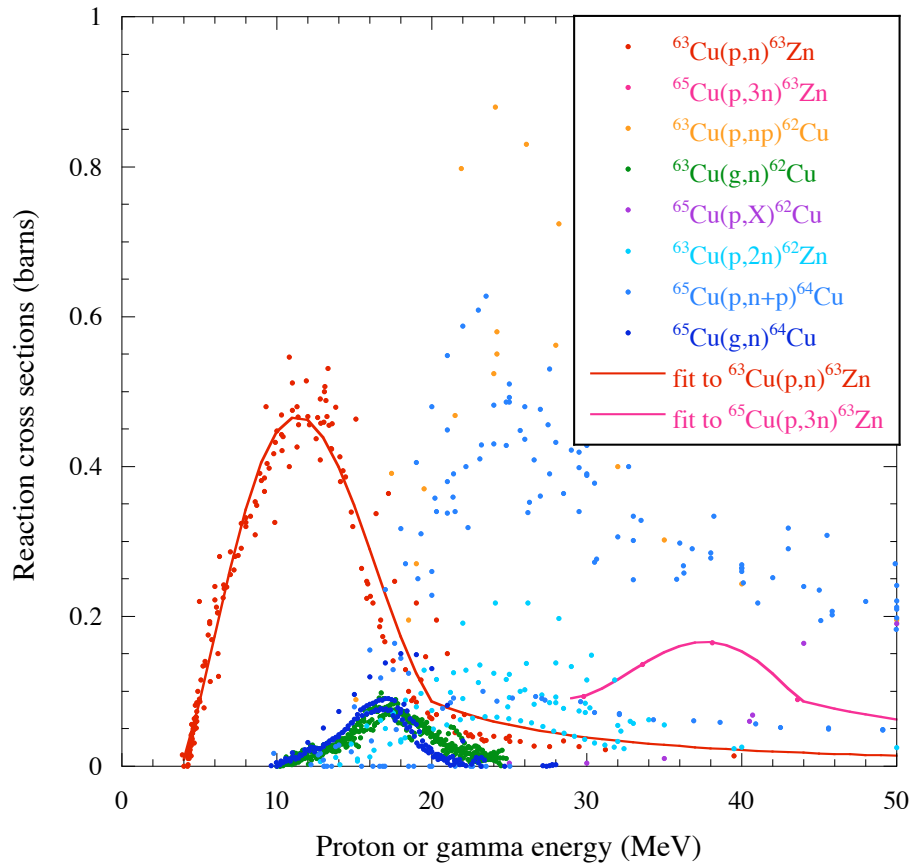


Figure 3.10: Cross section data for the reactions caused by incident protons and γ s likely to generate measurable contributions to the activation. The fits to the reaction with ^{63}Zn products are shown.

will be calculated from the ^{63}Zn component of the activation.

The cross sections for the most prominent reactions are shown in figure 3.10 and are from the database in reference [156]. Other reactions that will occur are assumed to be negligible to the measurements due to having a long half life, having a small cross section at the proton and γ energies expected or because they create a stable product. This is, of course, an approximation and these other reactions will contribute to the error in the measurement of the proton spectra.

The isotopes ^{63}Zn , ^{62}Cu and ^{64}Cu decay with a positron emission; ^{63}Zn has a half-life of 38.47 minutes, ^{62}Cu has a half-life of 9.67 minutes and ^{64}Cu has a half-life of 12.70 hours [156]. In order to calculate the contributions from the proton and the γ activation, the contribution from each decay needs to be identified. The activity is measured using two scintillator/photomultiplier tubes arranged to measure coin-

cident events from the decaying activated atoms. When a decay occurs, the emitted β^+ will be annihilated within the copper, producing 511 keV photons in opposite directions. This enables the β^+ decays to be distinguished from other radiation. A count will only be recorded when both scintillator/photomultiplier detectors, looking at opposite sides of the sample, measure an event at the same time. The detector efficiency is calibrated using a ^{22}Na source.

The activity (counts per second, dN/dt) of a sample was measured at some time after the shot was taken and the count is then corrected for detector efficiency. At a time when the sample is measured, t_1 , the total activity will be the sum of the contributions from the ^{63}Zn , ^{62}Cu and ^{64}Cu decays and is given by

$$A_{total}(t_1) = N_Z(0)\lambda_Z e^{-\lambda_Z t_1} + N_{C62}(0)\lambda_{C62} e^{-\lambda_{C62} t_1} + N_{C64}(0)\lambda_{C64} e^{-\lambda_{C64} t_1}, \quad (3.8)$$

where $N_Z(0)$, $N_{C62}(0)$ and $N_{C64}(0)$ are the total number of activations at the time of the shot, t_0 and λ_Z , λ_{C62} and λ_{C64} are the decay constants for ^{63}Zn , ^{62}Cu and ^{64}Cu respectively. The decay constants are given by $\lambda = \ln 2/\tau_{\frac{1}{2}}$ [s^{-1}] so $\lambda_Z = 3.0 \times 10^{-4} \text{ s}^{-1}$, $\lambda_{C62} = 1.19 \times 10^{-3} \text{ s}^{-1}$ and $\lambda_{C64} = 1.52 \times 10^{-5} \text{ s}^{-1}$.

Then the activity is measured at a second and third time, t_2 and t_3 , and similarly the total activity is found for each of these times:

$$A_{total}(t_2) = N_Z(0)\lambda_Z e^{-\lambda_Z t_2} + N_{C62}(0)\lambda_{C62} e^{-\lambda_{C62} t_2} + N_{C64}(0)\lambda_{C64} e^{-\lambda_{C64} t_2}, \quad (3.9)$$

$$A_{total}(t_3) = N_Z(0)\lambda_Z e^{-\lambda_Z t_3} + N_{C62}(0)\lambda_{C62} e^{-\lambda_{C62} t_3} + N_{C64}(0)\lambda_{C64} e^{-\lambda_{C64} t_3}. \quad (3.10)$$

The measuring times need to be suitably delayed so that the ratio of activities of the different isotopes changes significantly. Due to the difference in half-life times of the products, this is possible. By solving the three simultaneous equations, 3.8, 3.9 and 3.10, the initial numbers of each of the isotopes are found, in particular, $N_Z(0)$. The activities $A_{total}(t_1)$, $A_{total}(t_2)$ and $A_{total}(t_3)$ have been measured and λ_Z , λ_{C62} and λ_{C64} are known so the initial ratio of the different activated atoms can be calculated. The errors on each of the measurements are estimated by assuming that the decay counts recorded, κ , have an error of $\sqrt{\kappa}$. The mean $N_Z(0)$ and the associated error can be calculated from κ .

Once the initial activations from each product component in each copper piece have been found, the spectrum needs to be de-convolved. The ^{63}Zn activation is used to calculate the proton spectrum because this product is, to a good approximation, generated by protons only. Having measured the activation due to ^{63}Zn in all m of the copper pieces, it can be related to the initial proton spectrum entering the stack by the equation 3.11 where there are n energy bins:

$$N_{Zn,i} = \sum_{j=1}^n R_{i,j} S_j \Delta E_j, \quad \text{for } i = 1, 2, \dots, m. \quad (3.11)$$

The energy spectrum S_j is the number of protons per MeV in energy bin ΔE_j and $R_{i,j}$ are the average sensitivities (number of activated atoms per incident proton) in the energy bin ΔE_j for the reactions generating ^{63}Zn .

The sensitivity of each of the copper layers then needs to be determined in terms of the number of ^{63}Zn atoms produced per incident proton as a function of proton energy. The proton spectrum alters as it passes through the stack due to energy losses. The spectrum going through each copper layer was calculated by accounting for how a particular initial energy would change as it reached a layer in the stack by using the dE_p/dx of the different stack materials [157]. A simple tracking code was used to track the proton spectrum changes and added the contributions to a layer sensitivity for a step thickness, dx , after each step. The cross sections for the $^{63}\text{Cu}(p, n)^{63}\text{Zn}$ and $^{65}\text{Cu}(p, 3n)^{63}\text{Zn}$ reactions, shown in figure 3.10, were used to find the total ^{63}Zn activation per incident proton in each piece of copper. The sensitivity for a particular layer with a density, ρ and a thickness, L , to a particular reaction with a cross section, σ , is therefore given by

$$R_{i,j} = \rho \sigma L. \quad (3.12)$$

To assess the proton spectrum for a given set of activation measurements, a code was developed to iteratively solve the spectrum. This code was based on the random perturbation method used in YOGI, described within the references [31, 158, 159]. The trial proton spectrum used is initially set to be flat so that no assumptions are made about the shape. An energy bin is selected at random to have a random value added (the maximum perturbation is predetermined), or

equally likely subtracted, from the initial value. If the perturbation makes the energy bin spectrum number below zero, it is instead set to zero. The activation, $N_{Zn,i}$, generated by the trial spectra is then calculated according to equation 3.11. This trial is then compared with the measured activation and if an improvement has been made to the difference between the measured and trial activations, (i.e. the variance gets smaller) the perturbation is kept and the next randomly selected energy bin is perturbed. The process is repeated until the variance reaches some predetermined level.

The main sources of error in the proton spectra will originate from the measurement of the initial number of ^{63}Zn in each of the layers. There are several factors contributing to this error, including the accuracy of the activation measurements, the determination of the contribution of ^{63}Zn to the total measured activation and the accuracy of the thickness of the copper detecting sheets (small error). There is also the possibility of errors having been introduced when calculating the sensitivities for the layers, although this is assumed to be small.

The largest error contribution is attributed to the determination of the initial number of ^{63}Zn . The assumption that only three isotopes contribute to the measured activities will be a significant contribution to this error, so an estimate was made of the error on the ^{63}Zn measurements, which would be due to the counting statistics of radioactive decay. The measured activities were perturbed according to a Poisson distribution and the ^{63}Zn was recalculated for many different perturbations. Considering the difference in the determined ^{63}Zn gives a measure of the error, which was found to be smaller than the threshold variance assumed for the spectral fitting process.

The activated copper pieces can also be used as a beam divergence measurement [160]. After having their activation measured, they can be imaged by placing them on image plates to record an image of the signal.

Chapter 4

Collimated ion acceleration from underdense plasmas in high-intensity laser plasma interactions

In this chapter, the first experimental results of longitudinal ion acceleration from high intensity ($\sim 10^{20}$ Wcm $^{-2}$) laser interactions with helium gas jet targets ($0.04n_c$) are presented. The ion beam was found to have a maximum energy for He $^{2+}$ of (40_{-8}^{+3}) MeV and was directional along the laser propagation path, with the highest energy ions being collimated to a cone of less than 10° [161]. 2D particle-in-cell (PIC) simulations using the code OSIRIS were used to investigate the acceleration mechanism for different parameters and the effect on the ion acceleration. The investigated parameters include plasma density and plasma ramp length.

4.1 Previous work

The ion acceleration results presented in this chapter draw on several different aspects of laser plasma interactions. A brief description of previous work where ion acceleration has been observed from high intensity laser interactions with under-

dense plasma is presented. These earlier measurements of ions from underdense plasmas have only observed MeV energy ions in the radial direction. An important influence on the ion acceleration is the fast electron generation and electron acceleration from underdense plasma is also reviewed. Finally, an account of proton and ion beams that have been observed from laser interactions with solid targets (overdense plasma), which are generated by fast electrons leaving the target is given.

Prior measurements of the high energy ions accelerated from laser interactions with underdense plasmas have been confined to the radial direction. The mechanism responsible for this acceleration is the Coulomb explosion, which is due to the movement of electrons by the ponderomotive force of the laser (see section 2.2.5). The first reported direct measurements of MeV energy ions accelerated in this way from high intensity laser interactions with underdense plasma were by Krushelnick et al. [101]. Krushelnick et al. measured neon ions having energies of up to 6 MeV and 3.6 MeV helium ions produced primarily at 90° to the laser propagation axis with 50 TW laser pulses [101].

Collisionless shock acceleration was recently found to enhance the tail of energetic ions. A plateau structure observed in the radial ion energy spectrum from underdense plasma interactions with the Vulcan Petawatt laser was identified by Wei et al. [23]. A plateau in the ion spectrum is a signature of the shock acceleration mechanism. They observed helium ions with energies up to (13.2 ± 1.0) MeV from the interaction of a $3 \times 10^{20} \text{ Wcm}^{-2}$ laser with a $1.4 \times 10^{19} \text{ cm}^{-3}$ gas jet plasma. In these interactions, the highest energy ions are accelerated in a direction slightly forward of 90° due to the angle of propagation of the shock fronts.

There has been some simulation work to explore ion acceleration from underdense plasma in the forward direction [32, 107–109]. These papers investigate the ion acceleration mechanism in different targets, including underdense targets. Goloviznin and Schep find that relativistically strong (10^{18} – 10^{19} Wcm^{-2}) laser pulses can be used to drive mega-ampere ion currents in underdense plasmas with a view to creating an efficient neutron source [32]. Esirkepov et al. present simulations that show the interaction between a circularly polarised laser pulse ($a = 20$) and a $0.2n_c$ density plasma [107]. In addition to the space charge electric field that is set up as

the fast electrons leave an unneutralised ion column, an inductive electric field is generated by the rapid change of the magnetic field as the electrons expand from the rear of the target into the vacuum. This field accelerates the ions. A pinching effect on the electrons due to the self generated magnetic field helps to collimate the accelerated ion beam.

Supersonic gas jet targets allow relatively long underdense plasma interaction lengths, compared with solid target interactions, therefore very high-energy, broad-spectra and high-charge electron beams can be generated. The acceleration mechanism is dependent upon the intensity and pulse duration of the laser. Up to intensities of about 10^{18} Wcm^{-2} , wakefield acceleration is the dominant acceleration mechanism in laser interactions with underdense plasma. For laser intensities greater than about 10^{18} Wcm^{-2} , the ponderomotive force is too great for a wakefield to form and the laser expels virtually all of the electrons from the focal volume. In this case, the direct laser acceleration (DLA) mechanism becomes dominant (see section 2.2.4). Using Petawatt class lasers it has been possible to accelerate electrons through the direct laser acceleration (DLA) mechanism to high energies (350 MeV) [99].

Ion acceleration from solid target interactions has been extensively investigated since the first high energy ion beams were observed [13, 17–22, 28, 33–37, 40, 43, 46, 49, 57, 69, 109, 124–129, 135–137, 162–173]. The ponderomotive push on electrons at the interaction surface can accelerate ions from the front surface through charge separation so that they travel through the target and emerge from the rear side. When fast electrons generated at the front of the target travel through and move out into the vacuum at the rear of the target, an electric sheath field forms. This leads to the target normal sheath acceleration mechanism which can accelerate rear surface ions to multi-MeV energies. The effects of a large range of target parameters (thickness, material) and laser parameters (pulse duration, prepulse levels, intensity) on ion have been investigated in experiments [13, 17, 19–21, 28, 33–35, 43, 46, 69, 124–128, 136, 137, 163, 164, 166–169, 171, 172]. These interactions can be understood with simple plasma expansion in vacuum models [18, 129–134].

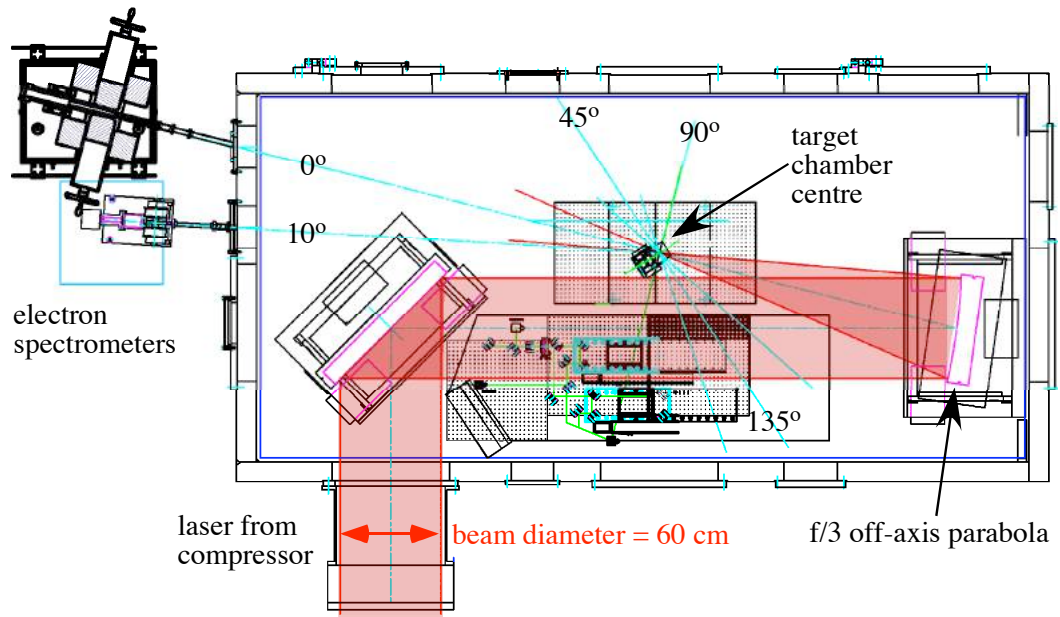


Figure 4.1: Schematic of the Vulcan Petawatt target vacuum chamber (based on a technical drawing by B. Fell, CCLRC Rutherford Appleton Laboratory).

4.2 The experiment

The experiment was performed using the Vulcan Petawatt laser (see section 3.1) in 2004. A schematic of the Target Area Petawatt (TAP) vacuum chamber is shown in figure 4.1. The beam path is highlighted, as are the main diagnostic directions for this experiment.

4.2.1 Laser parameters

A summary of the laser parameters for this experiment are given in table 3.1 in the 2004 column. The laser pulse had a duration of ~ 1000 fs, with an energy of up to 593 J (60% on target), to give a maximum average power of 360 TW. The focal spot had a FWHM diameter of $7 \mu\text{m}$ to provide a cycle averaged peak vacuum intensity of $1.5 \times 10^{20} \text{ Wcm}^{-2}$, which corresponds to a cycle averaged normalised vector potential of $a_0 = 11$. The contrast ratio was 10^{-5} .

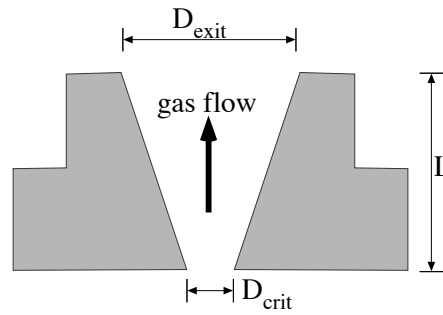


Figure 4.2: A cross section of a conical gas jet nozzle.

4.2.2 Supersonic gas jet targets

To create a uniform underdense plasma ($n_e < n_c = 10^{21} \text{ cm}^{-3}$ for a wavelength of 1.053 nm), the target material is usually a gas. The easiest way to form a target with a gas is to force it under high pressure through a gas jet nozzle. The gas line is only opened for a short time (on the order of milliseconds) before the shot to ensure that the vacuum boundary is as sharp as possible, as well as to prevent the vacuum chamber from flooding with gas.

Supersonic nozzles produce a uniform density profile over a given distance (depending on the diameter of the nozzle) and a reasonably sharp density ramp, at the edge of the gas jet ($< 250 \mu\text{m}$). The shape of the nozzle determines how the gas exits into the vacuum [174]. It was found that a conical nozzle was best for producing a flat density profile with short density ramps to vacuum and a schematic is shown in figure 4.2. The important parameters are the aperture through which the gas enters, D_{crit} , the aperture diameter at the exit of the nozzle, D_{exit} , and the distance L between the entrance and the exit apertures. Semushin and Malka [174] found the optimum values for various nozzles and calculated the density at the nozzle exit. It is important that the smallest orifice in the gas line is at the entrance to the nozzle, D_{crit} , to avoid instabilities in the flow.

The gas jet nozzle used for data presented in this thesis had $D_{\text{crit}} = 1 \text{ mm}$, $D_{\text{exit}} = 2 \text{ mm}$ and $L = 6 \text{ mm}$. The density profile of this gas jet was determined prior to the high intensity shots at Imperial College by M. C. Kaluza, using interferometry. Examples of an interferogram, the phase map created from a 2 mm nozzle at a

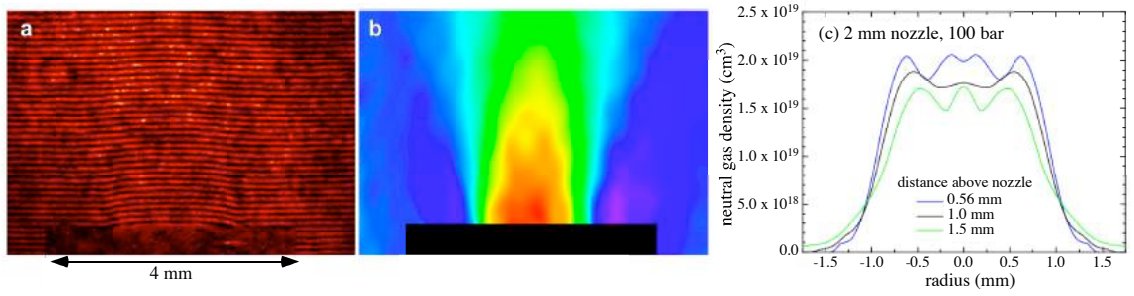


Figure 4.3: Gas jet interferometry: (a) is an interferogram of a 2 mm nozzle with a backing pressure of 100 bar, (b) is the phase map obtained from the interferogram and (c) show the neutral gas density at different heights above the nozzle recovered using an inverse Abel transform (images are courtesy of M. C. Kaluza).

backing pressure of 100 bar argon are shown in figure 4.3. The density map is created by comparing the interferogram with a reference image of the fringes with no gas. Applying an inverse Abel transform, which assumes that the gas jet is cylindrically symmetric, creates the 2 dimensional density map of the gas jet. The neutral density profile of the target is found by taking a line out at the height above the gas jet at which the laser is shot.

The density of the gas jet depends upon a number of factors. These include the triggering time relative to the laser arrival time, the solenoid type, the voltage used to open the solenoid, the backing pressure of the target gas, the diameter of the nozzle and the shape of the nozzle. For this experiment the solenoid that was used was a Parker series 99 (1.2 mm orifice) and the voltage used to open it was 100 V. The backing pressure of the gas jet nozzle was varied from 5 bar to 100 bar so that the electron density of the fully ionised plasma could be set between $0.7 \times 10^{19} \text{ cm}^{-3}$ and $4 \times 10^{19} \text{ cm}^{-3}$. The frequency separation of the forward Raman scattered laser spectra (see section 2.2.2, $\Delta\omega = \omega_{pe} = (n_e e^2 / m_e \epsilon_0)^{1/2}$) was used to confirm the electron density n_e of the interaction during the data shots as described in section 2.2.2.

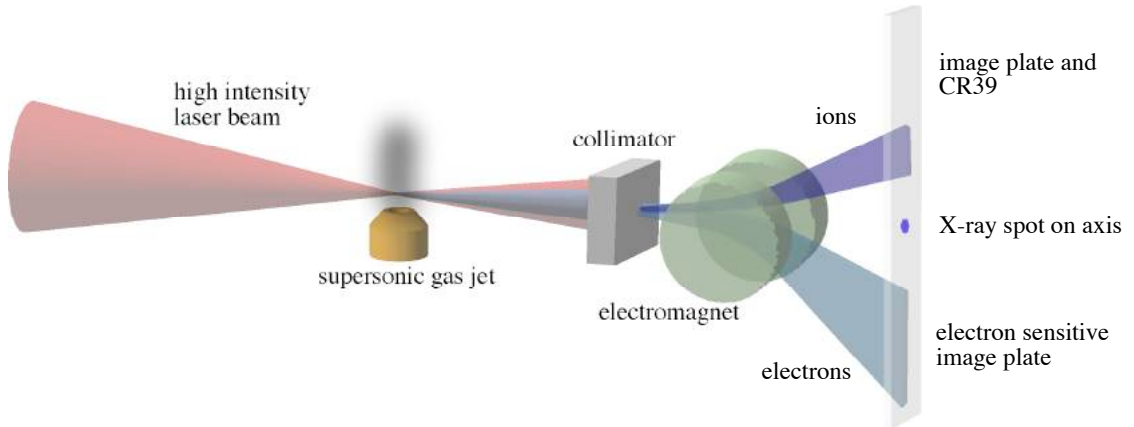


Figure 4.4: Schematic of the experimental setup showing the on-axis charged-particle spectrometer (based on a figure by S. P. D. Mangles).

4.2.3 Diagnostics

A summary of the main diagnostics is described below. The ion energy spectra were measured at four different angles to determine the angular emission of the ions. Thomson ion spectrometers, described in section 3.3.1, were placed at 45° and 90° to the direction of the laser propagation. The energy resolution was determined by the pinhole at the entrance to the spectrometer. At 90° the pinhole diameter was $250 \mu\text{m}$, which gave a solid angle of 7.0×10^{-8} steradians. At 45° the pinhole diameter was $250 \mu\text{m}$, which gave a solid angle of 1.0×10^{-7} steradians. The voltage across the 90° Thomson parabola was 2 kV and across the 45° Thomson parabola was 24 kV.

In addition, there were two magnetic charged particle spectrometers (described in section 3.3.2), one placed at 10° and one directly on the axis of propagation of the laser (0°). Though primarily used to measure the energetic electron spectra emitted from the interaction, the open geometry of the magnetic spectrometers also allowed the measurement of ions and other positively charged particles. Figure 4.4 shows a schematic of the on-axis charged-particle spectrometer, measuring both the electrons and ions. The energy resolution of the ion spectra was determined by the width of the entrance slit to the charged particle spectrometer, which was 2 mm wide for the 0° spectrometer and 1 mm wide for the 10° spectrometer. To begin with, there were image plate detectors on both the negative and the positive deflection sides

of the spectrometer. The positive deflection side image plate was usually used as a background subtraction for the electron spectra. However, a signal started to appear on the positive deflection side of the image plates for high plasma density shots. The nuclear track detector, CR39, was used to confirm that the positive deflection image plate signal was from ions, because CR39 is insensitive to positrons.

The other main diagnostics for this experiment included the electron spectra from the charged particle spectrometers, the transmitted laser spectrum and a transverse optical probe beam. Electron spectra were measured simultaneously on each shot by using image plate detectors in the charged particle spectrometers at 0° and 10° . The transmitted laser spectrum was collected using a glass plate with a hole in it (to allow a line of sight to the 0° charged particle spectrometer), collimated with a spherical mirror, to be transported out of the chamber and then focused onto an optical spectrometer. The Raman satellites provided a plasma density measurement for each shot [85]. The optical probe beam is created by collecting a small portion of the main beam (from the bottom centre) and converting the light into 2ω . A timing slide allows the relative arrival of the main beam and the probe beam to be adjusted. The parallel light was then passed through the interaction at 90° to the main interaction beam and collected with a lens on the other side. Interferometry and shadowgraphy were performed with this beam. Imaging of the self emission from the plasma helped provide an overall picture of the interaction.

4.3 Experimental results

During the experimental campaign, for plasma densities $\lesssim 2 \times 10^{19} \text{ cm}^{-3}$ energetic ions were found to be emitted primarily in the transverse direction consistent with previous measurements [23, 101]. However, above this density a clear, reproducible signal of ions was observed in the 0° and 10° spectrometers. The ions were first observed on the image plate detector. The signal was then confirmed to be due to ions using CR39 in front of the image plate on the positive deflection side.

The He^{2+} ion spectra from a shot with on-target energy of 340 J ($I_0 \approx 6 \times 10^{20} \text{ Wcm}^{-2}$) incident on a helium plasma with an electron density of $n_e = 4 \times$

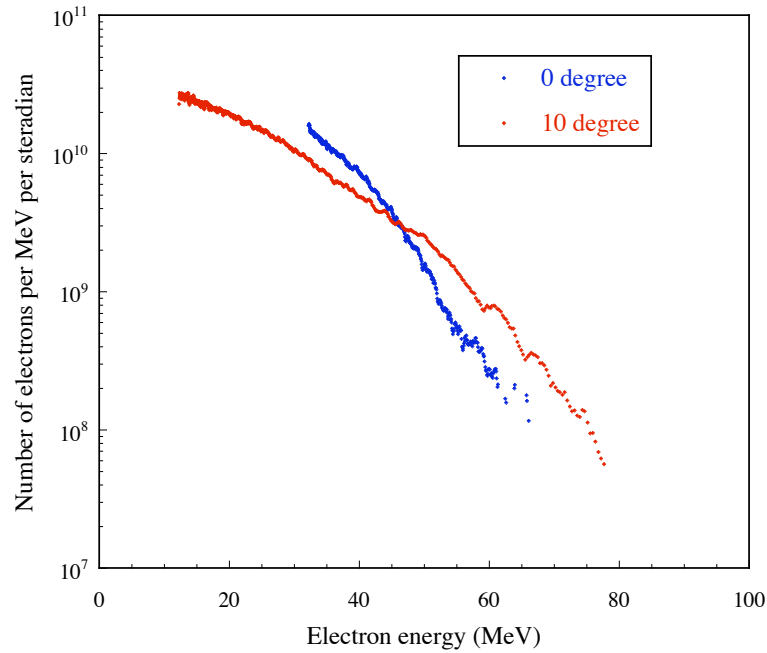


Figure 4.5: The electron spectra for the shot into a helium plasma of density $4 \times 10^{19} \text{ cm}^{-3}$. The temperature of the electron spectra at 0° is 7.4 MeV and at 10° is 9.8 MeV.

10^{19} cm^{-3} , is presented. The on-axis electron spectrum for this shot has a maximum energy of $66 \pm 2 \text{ MeV}$, with a characteristic temperature of $T_e = 7.4 \text{ MeV}$ and is shown in figure 4.5. The 10° electron spectrum, also shown in figure 4.5, was a little hotter ($T_e = 9.8 \text{ MeV}$), possibly due to filamentation and hosing in the interaction. These effects are discussed in more detail later in the chapter.

Figure 4.6 shows how the He^{2+} and the He^{1+} ions were identified. The larger pits are from lower energy ions being stopped closer to the surface of the CR39 and the smaller pits are from higher energy ions stopping deeper in the CR39. Due to their higher charge, the He^{2+} ions are deflected more in the magnetic field, so for a particular deflection, the He^{2+} ions will have a higher energy. This means that the He^{2+} ions form the smaller pits and the He^{1+} ions form the larger pits.

The helium spectra at various angles are shown in figure 4.7. The spectrometer limits marked in figure 4.7 are due to an x-ray diagnostic film pack, which covered the CR39 detector near the spectrometer axis. In the transverse direction He^{2+} had a maximum energy of $(7.8 \pm 0.6) \text{ MeV}$ and He^{1+} had a maximum energy of

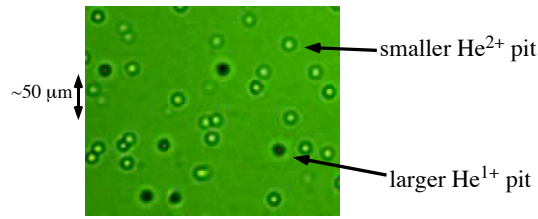


Figure 4.6: An optical microscope image of the pits etched into the CR39 to show the identification of the He^{2+} and the He^{1+} ion pits.

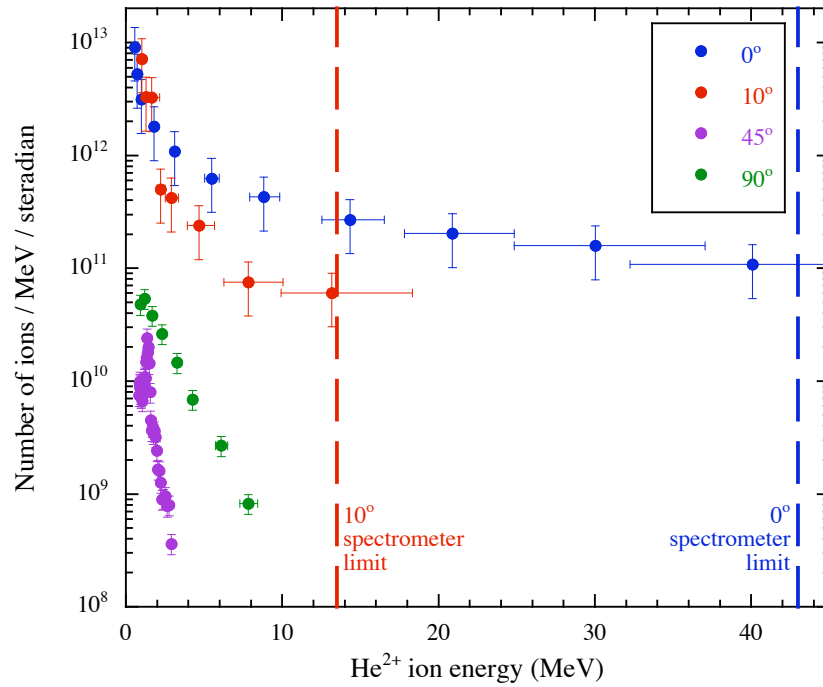


Figure 4.7: He^{2+} ion spectra at angles of 0° , 10° , 45° and 90° to the laser axis.

(3.4 ± 0.3) MeV. In the longitudinal direction He^{2+} had a maximum energy of (40_{-8}^{+3}) MeV and He^{1+} had a maximum energy of (10_{-2}^{+3}) MeV. Noticeably, the maximum energy at 45° is less than both the transverse and longitudinal energies. Hence, one can deduce that the highest energy ions form a well collimated beam in the forward direction with a divergence angle of less than 10° .

Figure 4.8 shows similar trends for the He^{1+} ion spectra at the different angles. The notable exception is the larger number of He^{1+} ions in the 10° direction.

To visualise how the ion emission changes with angle from the laser axis, figure 4.9 presents the number of He^{2+} ions with 2 MeV and 5 MeV at the different

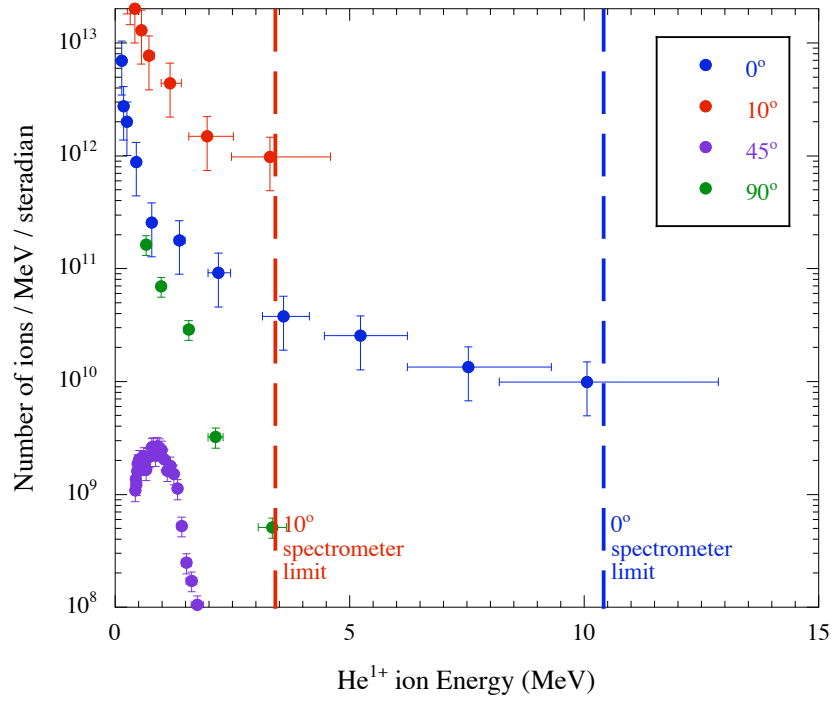


Figure 4.8: He^{1+} ion spectra at angles of 0° , 10° , 45° and 90° to the laser axis.

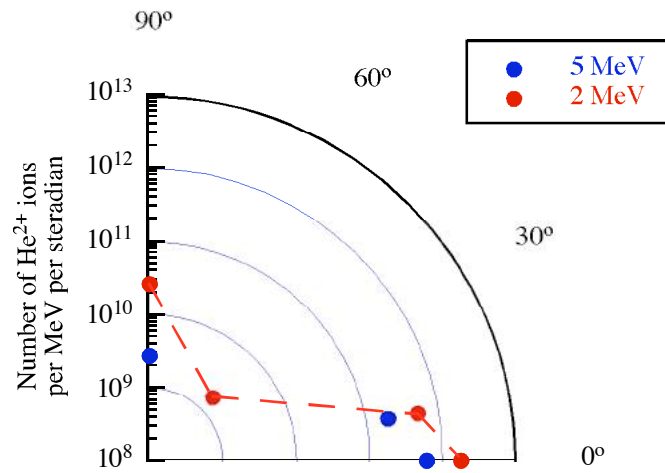


Figure 4.9: A polar plot showing the number of He^{2+} ions at different diagnostic angles for 2 MeV and 5 MeV ions.

diagnostic angles. It can be seen that the He^{2+} ions form 2 lobes, one in the forward direction along the laser axis and the other in the radial direction. There is no data point for the 5 MeV He^{2+} ions at 45° because none were detected and therefore is not on the chosen scale.

4.4 PIC simulations

To gain physical insight of the experimental data it is often helpful to perform numerical modelling of the interaction. The code OSIRIS is a 3D-3V (3 dimensions in both space and velocity) collisionless particle-in-cell (PIC) code, written by the OSIRIS consortium of UCLA, IST (Portugal) and USC [105, 106]. Running in 3 spatial dimensions is very computationally expensive and the resolution is decreased considerably. For this thesis, OSIRIS was run as a 2D-3V code at Imperial College London on the 24-node cluster called Arc and the newer 48-node cluster called Caesar. It is possible to set up the simulation to run using a box which co-propagates at the speed of light in a vacuum, c , or to have a stationary box so that plasma dynamics can be observed after the laser has left the simulation box. The simulations are initialised by preparing the input parameters of the density profile and the chosen laser parameters using the normalised units shown in table 4.1. The output files of the simulation are also in these normalised units.

4.4.1 Simulation setup

The stationary simulation box was $251 \times 251 \mu\text{m}$, with a resolution of 20.9 cells $/\lambda$ in the longitudinal (x) direction and 12.6 cells $/\lambda$ in the transverse direction (y). There was 1 negative particle and 1 positive particle per cell, due to computational constraints. Since ionisation effects are not included in this version of the code, a He^{2+} plasma was used to avoid complications due to balance of the different charge states. The ion acceleration was investigated with various values of plasma electron density, of $0.1 n_c$, $0.05 n_c$ and $0.01 n_c$, where n_c is the non-relativistic critical density. The density profile for these simulations had a $71 \mu\text{m}$ long linear density ramp at the front of the plasma, $25 \mu\text{m}$ of plasma at maximum density and a $71 \mu\text{m}$ density

quantity	OSIRIS unit
length	$\frac{c}{\omega_0}$
time	$\frac{1}{\omega_0}$
velocity	c
charge	e
mass	m_e
momentum	$m_e c$
density	$n_c = \frac{\epsilon_0 m_e \omega_0^2}{e^2}$
electric field	$\frac{cm_e \omega_0}{e}$
magnetic field	$\frac{m_e \omega_0}{e}$

Table 4.1: The normalised units used by OSIRIS.

ramp at the back of the target. The vacuum then extended a further $84 \mu\text{m}$ behind the plasma. The laser pulse was linearly polarised with the laser's electric field in the y -direction, with a full-width-half-maximum pulse length of $\tau_l = 500$ fs and a wavelength of $1.053 \mu\text{m}$. It was focused to a full-width-half-maximum diameter spot of $8 \mu\text{m}$ at the top of the front density ramp, to give a peak normalised vector potential $a_0 \approx 15$.

Another parameter investigated was the length of the density ramp at the rear of the target. In solid target ion acceleration, density ramps formed by pre-plasma at the rear of the target have been found to be detrimental to ion acceleration [136]. The reason for this is, if the pre-plasma has a scale length of greater than the Debye length, $\lambda_D = \sqrt{\epsilon_0 k_B T / e^2 n_{e0}}$ (see section 2.1.6), the electrons are able to move to shield ions from the accelerating electric field preventing efficient acceleration. For solid targets the Debye length will be of the order of nanometers, but for the underdense targets discussed here, the Debye length is of the order of μm . Taking the electron temperature to be $T_e = 7$ MeV and the electron density to be $4 \times 10^{19} \text{ cm}^{-3}$ gives a Debye length of $\lambda_D \sim 3 \mu\text{m}$. It is therefore expected that the density ramp on the gas jet targets used in the experiment will have a detrimental effect on the ion acceleration, and that the simulations can provide an approximate scaling with the ramp length. For these simulations, the simulation box was $598 \times 168 \mu\text{m}$ with

a resolution of 19.8 cells $/\lambda$ in the longitudinal (x) direction and 9.4 cells $/\lambda$ in the transverse direction (y). This time a hydrogen ion species was used to give a proton plasma. The initial plasma electron density used was $0.05n_c$ (equivalent to $5 \times 10^{19} \text{ cm}^{-3}$, which is similar to the experiment) and the laser parameters were the same as those described above. The lengths of the density ramps at the rear vacuum plasma interface were $0 \mu\text{m}$, $100 \mu\text{m}$ and $200 \mu\text{m}$. The centre of each of these ramps was at the same position so that the total amount of plasma the laser travels through is the same for all of the simulations. The laser pulse was linearly polarised with the laser's electric field in the y -direction, with $\tau_l = 500 \text{ fs}$ and a wavelength of $1.053 \mu\text{m}$. It was focused to a full-width-half-maximum diameter spot of $2.4 \mu\text{m}$ at the top of the front density ramp to give a peak normalised vector potential $a_0 \approx 45$.

The simulations assume an initially fully-ionised plasma and, in the case of an interaction with a relativistic laser pulse, the effects should be minimal as the front of the laser pulse will rapidly ionise any atoms it passes by. Care must be taken, when examining the simulation results when periodic boundary conditions have been used, to make sure the effect of any recirculation of particles is minimal, or to look at the result before recirculation occurs. The boundary conditions for these simulations were periodic in the transverse direction.

4.4.2 Simulation results

Presented first is a simulation looking at the ion acceleration mechanism. Then the effect of the plasma density on the ion acceleration is considered. Finally, simulations investigating the density ramp length are presented.

Ion acceleration mechanism

Figure 4.10 shows the results from a simulation of a $0.05n_c$ helium plasma. The azimuthal (z -direction) magnetic field, the longitudinal (x -direction) electric fields, the radial (y -direction) electric fields, the electron number density and the ion number density are all shown for each time step in the simulation, 0.5 ps, 1.0 ps, 1.5 ps,

2.0 ps and 2.5 ps.

At the earliest time, 0.5 ps, the laser pulse is still inside the plasma. The electrons start to form a cavitated channel as the ponderomotive force of the laser moves the electrons from the regions of highest intensity. A large radial electric field has already been generated and will act to radially accelerate the ions in a Coulomb explosion. There is also a magnetic field forming around the channel, which is due to the electron current being accelerated by the DLA mechanism.

After 1 ps into the simulation, the laser pulse starts to emerge from the rear of the plasma into vacuum. The accelerated electrons move out into the vacuum region at the rear of the plasma. The ions do not immediately respond to the movement of the electrons due to their large mass and therefore a large space charge electric field is set up. This longitudinal electric field in the simulation, E_{sim} is at its maximum value of ≈ 0.7 TV/m at 1 ps and is shown in figure 4.11 (a).

To find the relative contributions from the charge separation and the induced electric fields to the accelerating field, consider the electric field in terms of the vector potential, \mathbf{A} and the scalar potential, ϕ :

$$\mathbf{E} = -\frac{\partial \mathbf{A}}{\partial t} - \nabla \phi. \quad (4.1)$$

Taking the divergence of this equation gives

$$\nabla \cdot \mathbf{E} = -\frac{\partial}{\partial t} \nabla \cdot \mathbf{A} - \nabla^2 \phi. \quad (4.2)$$

If the Coulomb gauge is assumed, so that $\nabla \cdot \mathbf{A} = 0$, then the scalar potential, ϕ , is equivalent to the electrostatic potential. Therefore, the induced electric field is given by

$$\mathbf{E}_{\text{B}} = -\frac{\partial \mathbf{A}}{\partial t}. \quad (4.3)$$

The charge separation contribution to the longitudinal electric field, E_{ρ} , is found by numerically solving Poisson's equation:

$$\nabla \cdot \mathbf{E}_{\rho} = -\nabla^2 \phi = \frac{\rho}{\epsilon_0}, \quad (4.4)$$

using the ion and electron density data from the simulation. To compute the space charge electric field, Poisson's equation is transformed into Fourier space so that

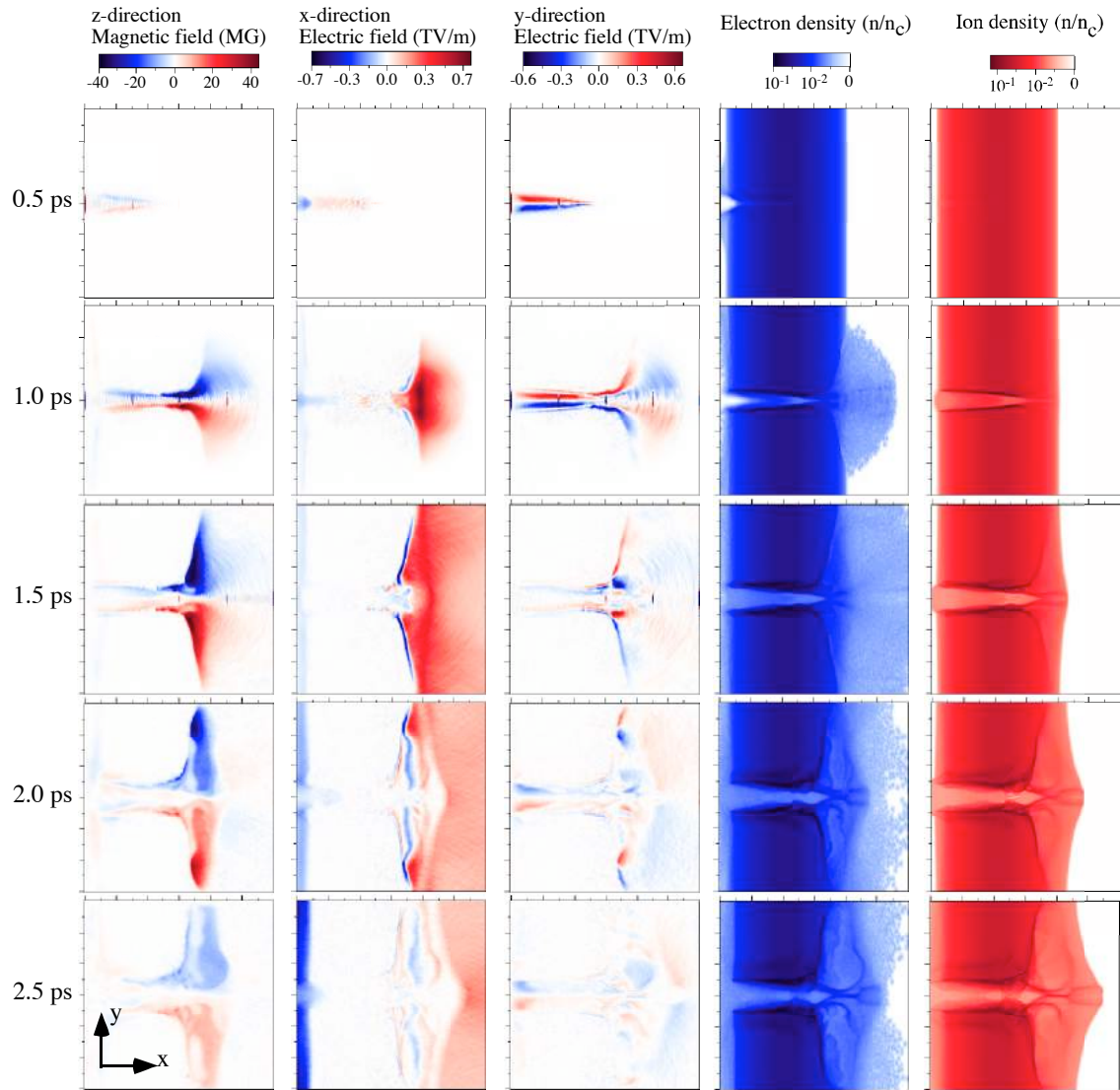


Figure 4.10: Results from a simulation of a $0.05n_c$ plasma showing (from left to right) the azimuthal magnetic field, the longitudinal electric fields, the radial electric fields, the electron number density and the ion number density. These are all shown for each time step in the simulation, 0.5 ps, 1.0 ps, 1.5 ps, 2.0 ps and 2.5 ps. The simulation box size is $251 \mu\text{m} \times 251 \mu\text{m}$.

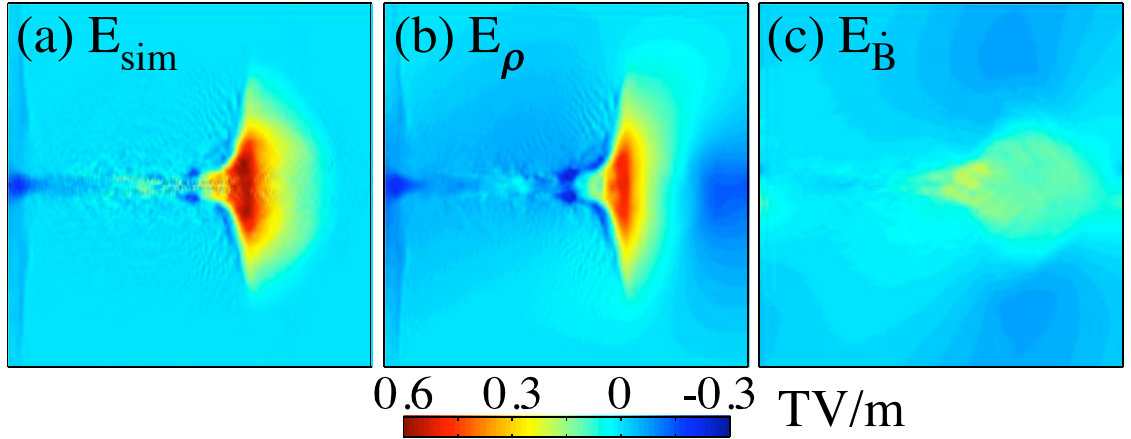


Figure 4.11: The longitudinal electric field components at 1 ps: (a) the total longitudinal electric field seen in the simulation, E_{sim} , (b) the charge separation contribution, E_{ρ} and (c) the time varying magnetic field contribution, $E_{\dot{B}}$. The simulation box size is $251 \mu\text{m} \times 251 \mu\text{m}$.

$\phi(k)$ can be calculated. The inverse Fourier transform is then performed on $\phi(k)$ to get $\phi(x)$, and thus the electric field can be found. This charge separation generated electric field is the usual contributor to the target normal sheath acceleration mechanism, as discussed in section 2.3.3. The charge density component of the longitudinal electric field is found to constitute the largest part of the accelerating field as seen in figure 4.11 (b). It is found that there is always a discrepancy in the longitudinal electric fields E_{sim} and E_{ρ} , so there must be an additional electric field generation mechanism.

It has previously been suggested that the magnetic field will be important [107–109]. The electron current generates a magnetic field around it and, as this moves into the vacuum, the magnetic field follows the electric current. The magnetic flux is conserved as the plasma expands into the vacuum, which can be seen in figure 4.10. This time-varying magnetic field contribution to the longitudinal electric field, $E_{\dot{B}}$, can also be calculated by studying the temporal evolution of the vector potential due to the quasi-static magnetic field alone. The magnetic field data from two consecutive data dumps was used and the time step between the simulation data dumps used for this calculation was 10 fs. Taking the curl of the equation $\mathbf{B} = \nabla \times \mathbf{A}$

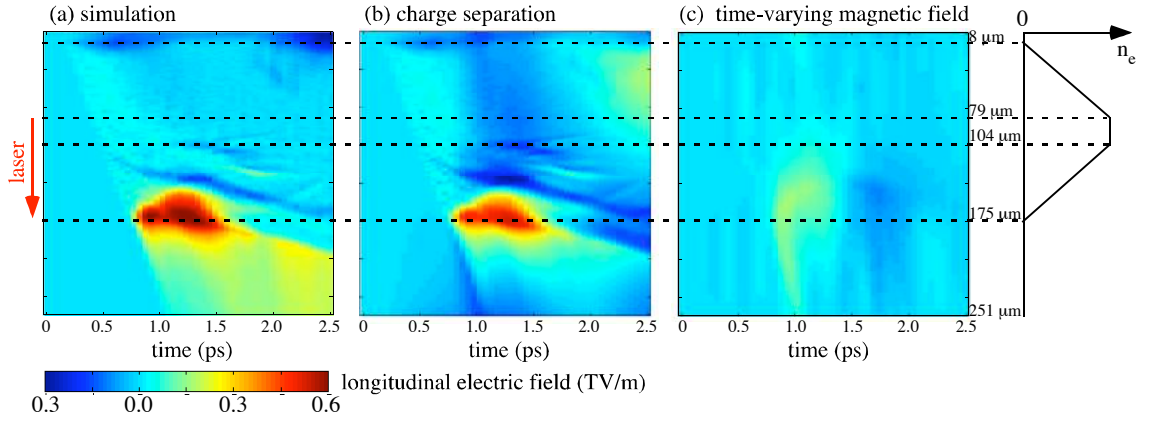


Figure 4.12: (a) The simulation longitudinal electric field and the relative contributions to the longitudinal electric field from (b) the charge separation and (c) the time-varying magnetic field. These are shown as a function of time, averaged in the radial direction over a $34 \mu\text{m}$ wide selection in the centre of the simulation box.

gives

$$\nabla \times \mathbf{B} = -\nabla^2 \mathbf{A}, \quad (4.5)$$

using the Coulomb gauge (i.e. $\nabla \cdot \mathbf{A} = 0$). Taking the Fourier transform of equation 4.5 and rearranging to find $\tilde{\mathbf{A}}(k)$ yields

$$\tilde{\mathbf{A}}(k) = \frac{i(\mathbf{k} \times \tilde{\mathbf{B}}(k))}{k^2}. \quad (4.6)$$

By taking the inverse Fourier transform of $\tilde{\mathbf{A}}(k)$ to give $\mathbf{A}(y)$, the induced electric field can thus be calculated from equation 4.3. The longitudinal electric field contribution due to the time varying magnetic field is shown in figure 4.11 (c) and is found to be the remaining contribution to the longitudinal electric field [175]. The peak value of $E_{\tilde{B}}$ is about 0.2 TV/m which compares to a peak value of 0.5 TV/m for E_{ρ} . Furthermore, the contribution E_{ρ} is much larger than $E_{\tilde{B}}$ at all times throughout the simulation, as is shown in figure 4.12. Figure 4.12 presents the longitudinal electric field averaged in the radial direction over a $34 \mu\text{m}$ wide selection from along the centre of the box and shows how it evolves over time for (a) the simulation, (b) the contribution calculated from the charge separation and (c) the contribution calculated to be due to the time-varying magnetic field. The longitudinal electric field reaches a maximum in all simulations, once electrons have just left the plasma

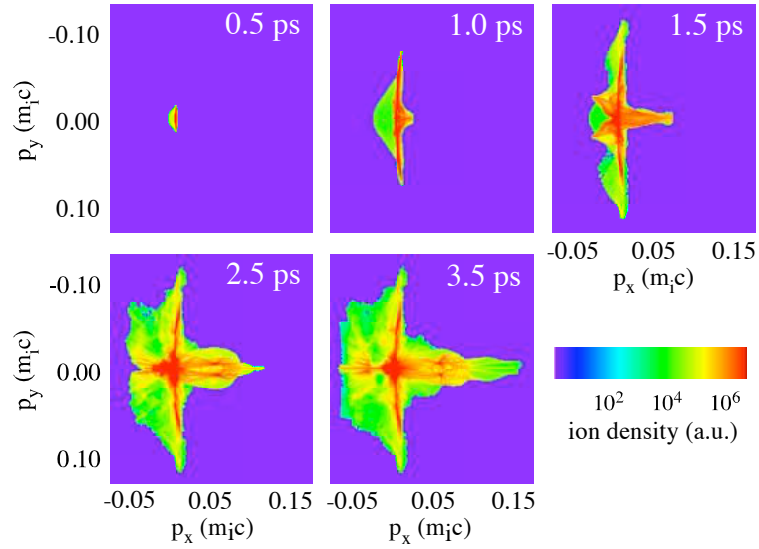


Figure 4.13: He^{2+} ion p_x against p_y momentum at times of 0.5 ps, 1.0 ps, 1.5 ps, 2.5 ps, and 3.5 ps.

and are entering into the vacuum, which is from ≈ 1 ps for 0.5 ps (approximately the length of the laser pulse). There are discrepancies between the field recorded in the simulation and the calculated total, particularly at later times where a significant field is seen in the vacuum region. This is due to the fact that particles leaving the simulation box will no longer be included in the calculated charge separation field. They are, however, remembered by the simulation and taken into account for the field calculations.

After 1.5 ps, a strong radial (y -direction) electric field is also observed at the exit of the channel into the vacuum. This radial electric field acts to focus ions in the region between this strong, positive and negative electric field and this can be seen in figure 4.10. By the analysis of the charge density, the radial focusing electric field forms because of charge separation. The effect of the quasi-static magnetic field is to cause a pinching of the electrons, which therefore produces the collimating electric field for the ions. This can be seen in the ion density plots at late times (see figure 4.10).

Figure 4.13 shows the ion p_x against p_y momentum at times of 0.5 ps, 1.0 ps, 1.5 ps, 2.5 ps, and 3.5 ps. Initially, before the fast electron current exits the plasma, acceleration is only seen in the transverse direction p_y . This is the transverse accel-

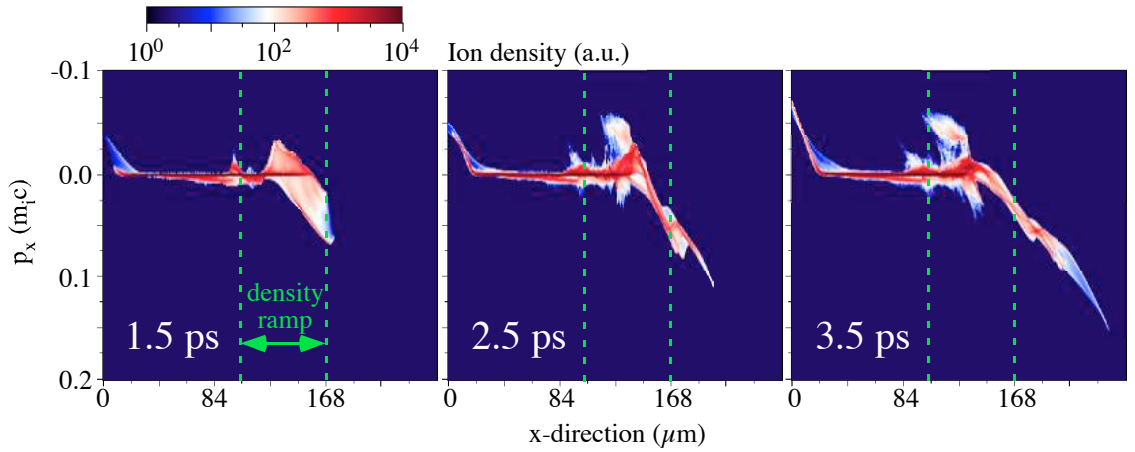


Figure 4.14: He^{2+} ion p_x against x -direction at times of 1.5 ps, 2.5 ps, and 3.5 ps. The initial boundaries of the rear density ramp are shown by the green dashed lines.

eration due to the radial ‘Coulomb explosion’ [29–32]. Once the hot electrons leave the target and the back surface sheath field is set up via charge separation and the time-varying magnetic field, then a beam of ions is accelerated in the longitudinal direction. The He^{2+} ion beam has a maximum energy of about 45 MeV and a divergence of 7° half-angle at 25 MeV at the end of the simulation. It is also noted that in the simulations, the exit of the return current from the front of the target results in ions being ejected from the front surface too. However, with the thicker targets used and the experimental constraints in terms of placing diagnostics, this feature has yet to be observed experimentally.

The ion acceleration region is illustrated in figure 4.14, which shows the longitudinal momentum p_x against the x -direction for times into the simulation of 1.5 ps, 2.5 ps, and 3.5 ps. The dashed green lines indicate the initial rear density ramp boundaries. From this it can be seen that all of the high energy ions accelerated in the forward direction originate from the back of the density ramp near the plasma vacuum interface.

The azimuthal magnetic field will exert a magnetic pressure on the electrons preventing the return current, which will allow the electric field to persist for longer. Also, this will act to enhance the accelerating field for the ions by preventing cold electrons from entering the charge imbalanced region and allowing the ions to feel

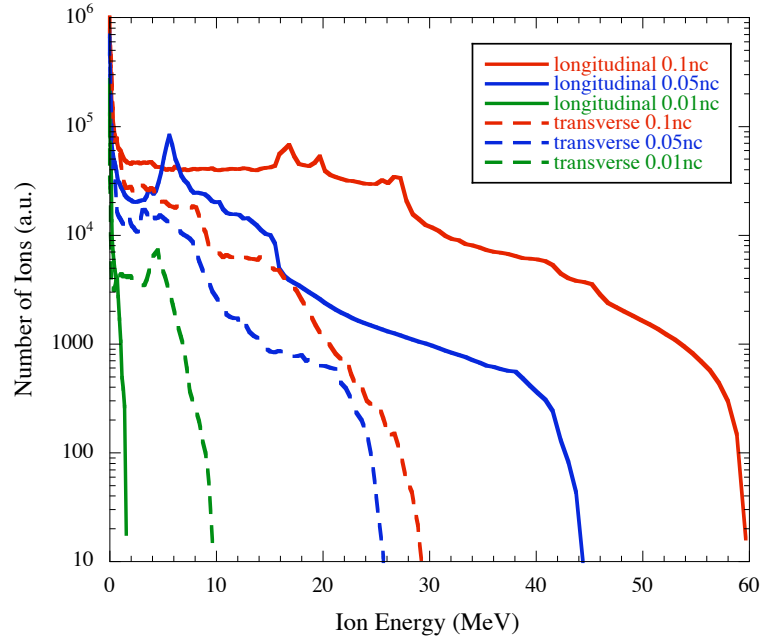


Figure 4.15: Simulated He^{2+} ion spectra at 3.5 ps for plasma densities of (a) $0.1n_c$, (b) $0.05n_c$ and (c) $0.01n_c$.

the accelerating fields for longer [107–109]. At a particular position the magnetic pressure, P_B , is given by

$$P_B = \frac{B^2}{2\mu_0}. \quad (4.7)$$

However, it is very difficult to quantify the overall influence of the magnetic pressure on the ion acceleration process from the simulations. It can be deduced that the magnetic field presence is not a requirement for ion acceleration from underdense plasma, as 1D simulations show similar ion acceleration for a purely space charge generated electric field.

Effect of plasma density

A number of simulations were performed to investigate the influence of the plasma density on the ion acceleration. The simulated He^{2+} ion spectra, in both the longitudinal and transverse directions for different density plasmas, are shown in figure 4.15. The density scan reveals the same dependence as that observed experimentally. At the lowest density ($0.01n_c$), the ion acceleration is almost purely in the transverse direction. However at $0.05n_c$ the longitudinal acceleration is already more effective

than the radial acceleration. At the highest density, even though the radial ion acceleration has increased well beyond the ponderomotive potential and shows the plateau-like feature attributed to shock acceleration [22, 23, 28], the longitudinal acceleration is still more effective. Indeed, the amount of acceleration is limited in the simulations by the amount of vacuum behind the plasma (again due to computational constraints).

Effect of plasma ramp length

To investigate the effect of the plasma ramp length, simulations with rear density ramp lengths of 0 μm , 100 μm and 200 μm were performed. Due to the different positions of the plasma vacuum interface for each of the different ramp lengths, the ions (protons in these simulations) start to accelerate at different times in the simulation. The times at which the ions are observed to start accelerating in the longitudinal direction are 1.5 ps for the 0 μm ramp, 1.7 ps for the 100 μm ramp and 1.9 ps for the 200 μm ramp. It is therefore difficult to find a suitable time to compare the results of the different ramp lengths. For the best illustration of the results, the comparisons made here are given when the ion front has moved 100 μm from the initial rear plasma-vacuum interface. For the 0 μm ramp this is at 2.4 ps, for the 100 μm ramp this is at 2.9 ps and for the 200 μm ramp this is at 3.1 ps. The simulated proton spectra for each of the ramp lengths for these times are shown in figure 4.16. At these times, the half-width divergence angles for the different ramp lengths are plotted as a function of proton energy in figure 4.17. The general trend observed from the divergence angles is that for the longer density ramp lengths there is an improvement in the proton beam collimation. The effect of the longer ramp length reduces the maximum energy protons accelerated in the longitudinal direction, but the collimation seems to be generally improved. If comparisons are made between the simulations at the same time into the simulation or at the time when protons begin to exit the simulation box, the same trends are seen between the plasma ramp length and the observed proton energies and collimation.

To understand the reduction in maximum ion energy and improved collimation with increasing ramp length, consider the electric field formation and magnetic fields

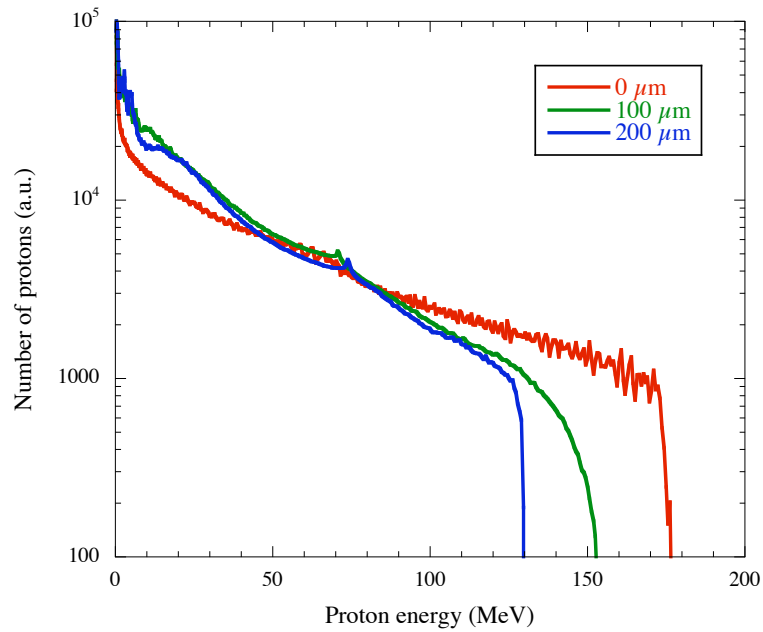


Figure 4.16: The simulated proton spectra for the different ramp lengths at a time when the ion front has expanded 100 μm.

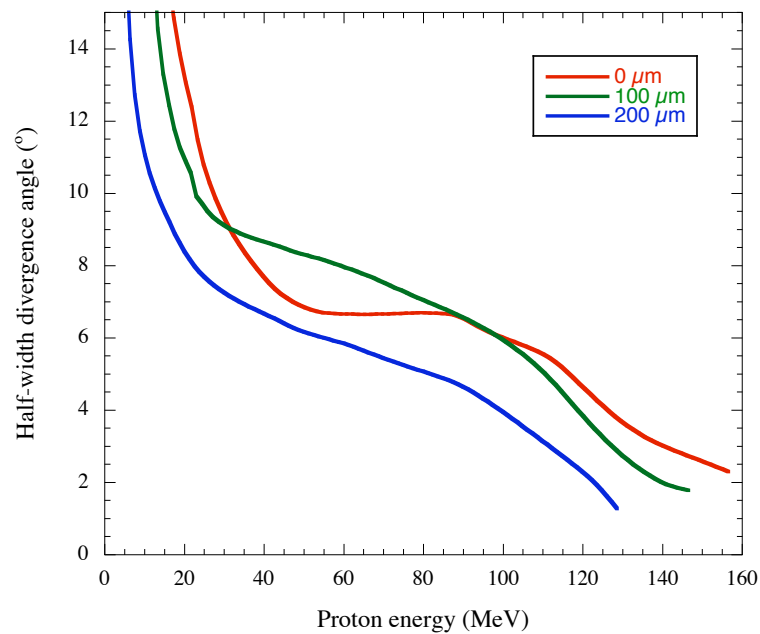


Figure 4.17: The half-width divergence angles as a function of energy for the different ramp lengths at a time when the ion front has expanded 100 μm.

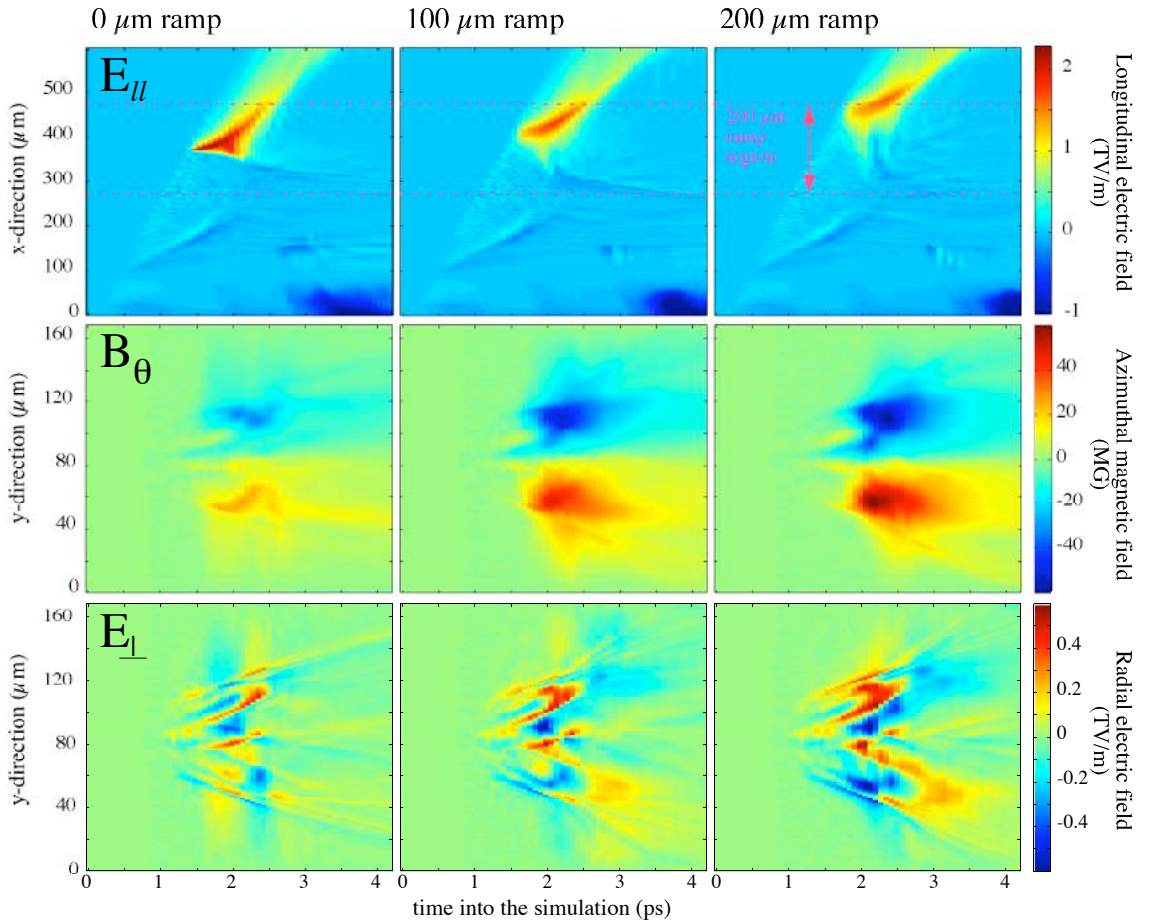


Figure 4.18: Time histories of the longitudinal electric field, azimuthal magnetic field and radial electric field for each of the ramp lengths. The longitudinal electric field is averaged over the central $50 \mu\text{m}$ of the width of the box and the azimuthal magnetic field and radial electric field are averaged over a $200 \mu\text{m}$ length centred on each of the ramps.

for each density ramp length. To visualise how this changes with time, figure 4.18 shows how each of the longitudinal electric field, azimuthal magnetic field and the radial electric field vary throughout the simulations. The longitudinal electric field is averaged over the central $50 \mu\text{m}$ of the width of the simulation box and the azimuthal magnetic field and radial electric field are averaged over $200 \mu\text{m}$ centred on the ramps. It can be seen from this that the largest longitudinal electric field is generated at the rear of the sharpest ramp, the $0 \mu\text{m}$ ramp. Also, the electric field appears at the plasma vacuum interface, then moves out into the vacuum with time as the fast electrons and ions move. This is what allows the ions to gain energies

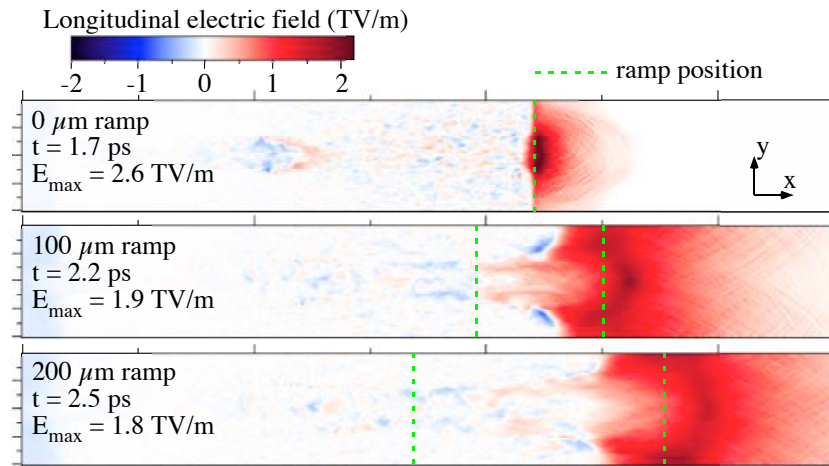


Figure 4.19: The maximum longitudinal electric fields for each of the ramp lengths; for the $0 \mu\text{m}$ ramp this is at 1.7 ps, for the $100 \mu\text{m}$ ramp this is at 2.2 ps and for the $200 \mu\text{m}$ ramp this is at 2.5 ps. The initial rear density ramp positions are shown for each simulation. The simulation box size is $598 \times 168 \mu\text{m}$.

many times $k_B T_{fast}$. The azimuthal magnetic field contains the largest amount of energy for the longest ramp length, $200 \mu\text{m}$. The effect of this can be seen in the radial electric field time history; the longer the ramp, the more azimuthal magnetic field there is and the stronger the pinching force on the electrons, which generates a focusing radial force on the ions.

Figure 4.19 shows the maximum longitudinal electric field for each of the ramp lengths; for the $0 \mu\text{m}$ ramp this is 2.6 TV/m at 1.7 ps, for the $100 \mu\text{m}$ ramp this is 1.9 TV/m at 2.2 ps and for the $200 \mu\text{m}$ ramp this is 1.8 TV/m at 2.5 ps. Therefore, since the longitudinal electric field is responsible for the ion acceleration, it is expected and is seen to be the case that the highest energy ions will be accelerated from the $0 \mu\text{m}$ ramp.

To investigate the improved collimation for longer ramp lengths, consider the azimuthal magnetic field for each of the simulations as shown in figure 4.20. The longer ramp sustains a longer and stronger azimuthal magnetic field, which will increase the pinching of electrons and provide a stronger focusing force for the ions. The radial electric fields for each of the ramp lengths is shown in figure 4.21 for a time of 2 ps into the simulation. The direction of the radial electric field in the ramp

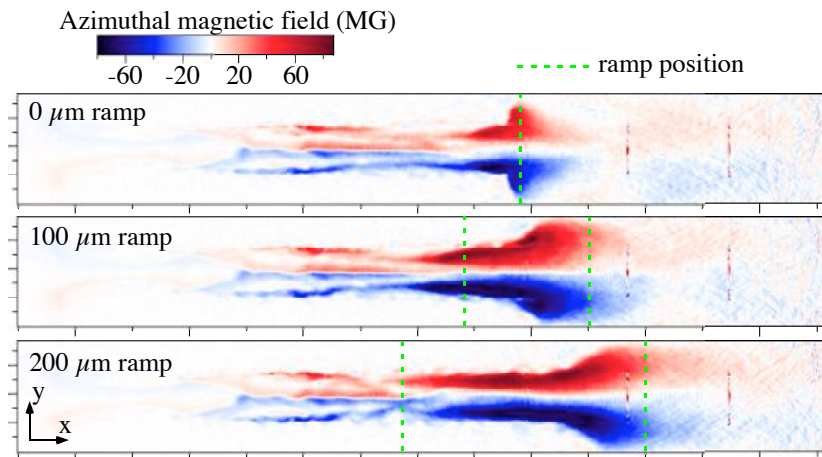


Figure 4.20: The azimuthal magnetic fields, 2.3 ps after the start of the simulation for density ramp lengths of 0 μm , 100 μm and 200 μm . The initial rear density ramp positions are shown for each simulation. The simulation box size is $598 \times 168 \mu\text{m}$.

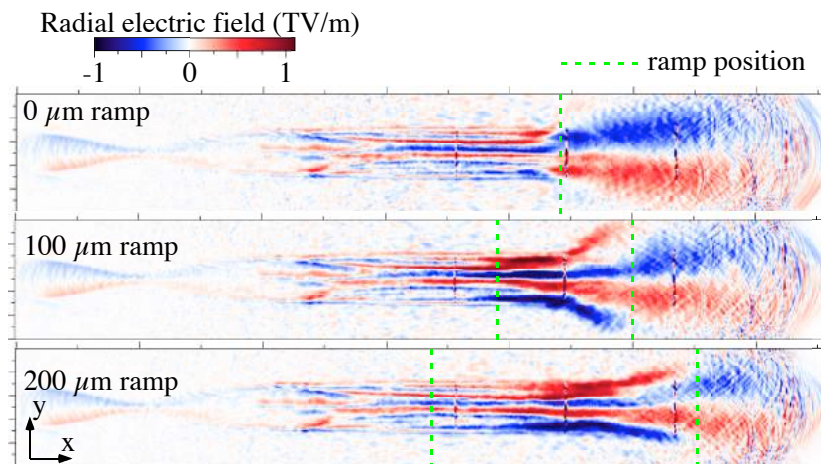


Figure 4.21: The focusing radial electric fields for density ramp lengths of 0 μm , 100 μm and 200 μm at 2 ps into the simulations. The initial rear density ramp positions are shown for each simulation. The simulation box size is $598 \times 168 \mu\text{m}$.

regions are directed such that ions in that field will be focused. These simulation results seem to agree quite well with the experimental observations of collimation.

4.5 Discussion

The experimental results presented in this chapter show that a well collimated MeV energy ion beam can be accelerated from a gas jet target. The simulations presented show that an electric sheath field is generated at the rear of the target through charge separation and time varying magnetic field induction. The azimuthal magnetic field will also enhance the lifetime of the longitudinal electric field as well as generating a focusing force on the ions. For the simulated plasma densities, it has been seen that ion acceleration is best at high plasma densities. The density ramp length of the plasma can have a significant effect, not only on limiting the maximum possible ion energies but also on the collimation of the beam. There are other experimental factors that have not been considered in the results sections, such as the effect of laser intensity and laser filamentation. These factors are discussed below.

4.5.1 Comparison to sheath acceleration models

A simple plasma expansion into a vacuum model [18, 132], described in appendix C, can be used to model ion acceleration by an electrostatic sheath. An expression for the maximum ion energy from this model is (equation 2.64)

$$\mathcal{E}_{max} \simeq 2Zk_B T_e [\ln(\tau + \sqrt{\tau^2 + 1})]^2, \quad (4.8)$$

where $\tau = \omega_{pi} t / \sqrt{2e_E}$, t is the time that the electrons are hot and e_E denotes the numerical constant 2.71828... The model suggests that increasing the fast electron temperature, the fast electron density ($\omega_{pi} \propto \sqrt{n_e}$) and increasing the acceleration time, t , should all improve the maximum ion energy that can be achieved. It should therefore be possible to improve ion acceleration by increasing the number and energy of accelerated electrons. For a plasma density of $4 \times 10^{19} \text{ cm}^{-3}$ with a measured electron temperature of $T_e = 7.4 \text{ MeV}$ and a laser pulse length of 1 ps, the model gives a maximum ion energies of 117 MeV. This model assumes a sharp

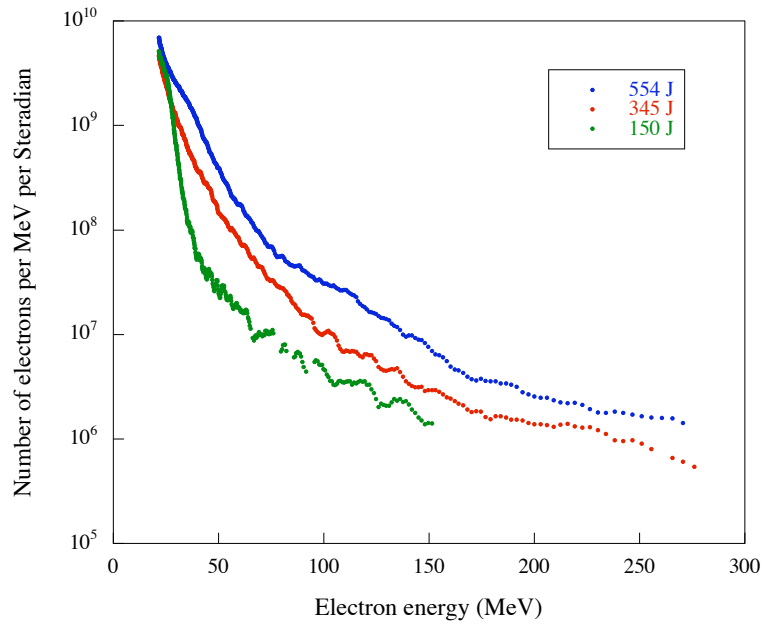


Figure 4.22: On-axis electron spectra from three shots with different laser energies into a $2 \times 10^{19} \text{ cm}^{-3}$ helium gas jet (data courtesy of S. R. Nagel).

boundary between the plasma and the vacuum and it is expected that a density ramp would reduce the ion acceleration (see section 4.5.4 for further discussion).

4.5.2 Effect of laser intensity and pulse length

The relative significance of the laser energy or intensity, laser pulse length and laser filamentation on the ion acceleration is discussed here.

Laser energy

It has been observed experimentally that as the laser intensity increases, the electron acceleration improves. Figure 4.22 shows electron spectra for three different laser energies into a $2 \times 10^{19} \text{ cm}^{-3}$ helium gas jet. It is clear that increasing the laser intensity produces more and higher energy electrons, which means that the temperature and fast electron number density is higher. The plasma expansion model suggests that an increase in laser energy would be favourable for the ion acceleration (providing the pulse length remained constant), so as to increase T_e in equation 4.8.

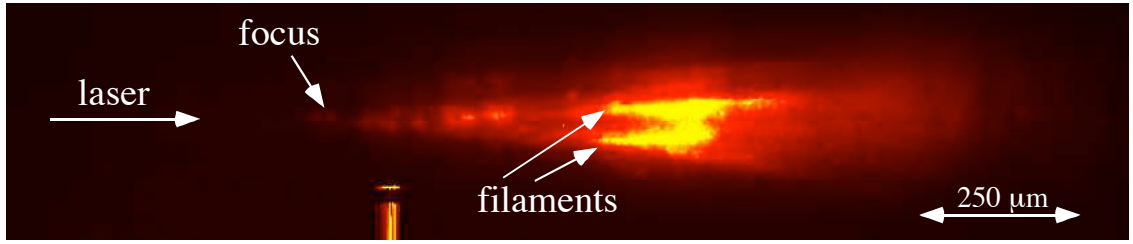


Figure 4.23: A self-emission image of a helium plasma interaction with a $n_e = 4 \times 10^{19} \text{ cm}^{-3}$ using a 450 TW, 650 fs duration laser pulse (data courtesy of P. M. Nilson). This shows the laser initially guiding over a distance longer than the Rayleigh range ($\approx 30 \mu\text{m}$) before breaking up into a pair of filaments.

Laser filamentation

It would seem that to improve the ion acceleration, the intensity should simply be increased. However, increasing the intensity at high densities can cause additional complications to the interaction, such as laser filamentation. It was observed using the 2ω optical probe that at higher plasma densities the laser is likely to break up into smaller filaments. Figure 4.23 shows the self-emission image of an interaction where laser filamentation took place in a $7 \times 10^{20} \text{ Wcm}^{-2}$ interaction with a $4 \times 10^{19} \text{ cm}^{-3}$ helium plasma. The filamentation is observed to get worse at higher plasma densities. The effect of the laser beam breaking up in this way is that the laser intensity is reduced and a number of individual plasma channels are formed. Electrons can still be accelerated in these individual channels containing the laser filaments, but at lower intensity. Therefore the electrons emerge from the back of the target in a number of lower temperature beams. This electron beam filamentation has also been observed experimentally and figure 4.24 shows electron beam divergence measurements made from detector stack data of a $n_e = 4 \times 10^{19} \text{ cm}^{-3}$ plasma [91]. Due to computational constraints, the simulation boxes used to look at the ion acceleration are not big enough to simulate the same interaction lengths as were used in the experiments. This is presumably why filamentation of the laser did not occur over the plasma lengths used in the underdense simulations. However, filamentation has been observed in previous simulations over the full target length, performed using a moving simulation box [91].

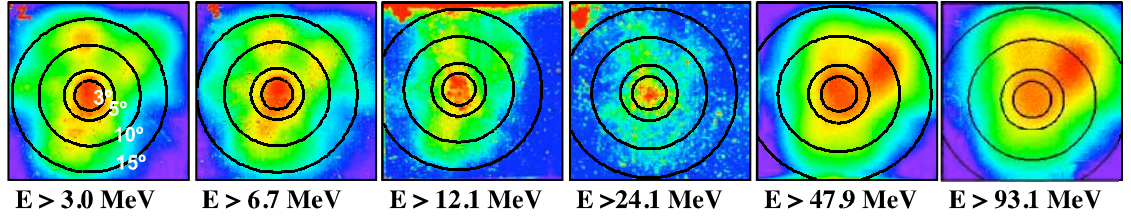


Figure 4.24: Electron beam profiles from an interaction with helium plasma of $n_e = 1.5 \times 10^{19} \text{ cm}^{-3}$. The circular contours mark 3° , 5° , 10° and 15° and are centred on the principle electron beam at that energy. The images show the signal above the given energy cutoff and are normalised to the peak signal (data courtesy of S. P. D. Mangles).

At this higher plasma density the electron beam has filamented into a number of different beamlets. The effect of this laser beam break up, which leads to electron beam filamentation, will be that the electron temperature and energy will not be as high as may be expected for higher plasma densities. The ion acceleration will therefore be affected by this reduction in electron temperature and also by the reduction in fast electron density, since the fast electrons will emerge from a larger area at the rear of the target. The fast electron current will be reduced and the azimuthal magnetic fields generated will be smaller. The sheath field would be affected and would be structured differently depending on the position the filaments emerge from. This could lead to filamentary structures in the accelerated ion beam, although this is yet to be observed experimentally. Recent results show that filamentation of the laser and electron beam can be reduced by changing the focusing geometry to a longer focal length [176]. If the laser can be guided for longer distances at high density without filamentation, the electron acceleration is expected to improve, which would be beneficial to the ion acceleration.

Laser pulse length

The effect of different laser pulse lengths on the ion acceleration has not been investigated experimentally or computationally here. Assuming that the laser pulse length is directly related to the acceleration time, the plasma expansion model suggests that a longer pulse length would lead to higher ion energies. However, length-

ening the pulse would not necessarily give better acceleration since the intensity would decrease (assuming the energy remains the same) and as already discussed, could mean less efficient electron acceleration. However, studies seem to imply that $T_e \propto a_0 \propto \sqrt{\tau_L}$, whereas lengthening the pulse may lead to an acceleration time increase $\propto t$. Therefore, there is likely to be an optimum pulse length for a particular intensity, to get the best ion acceleration. Hence increasing the pulse length would certainly be of interest in future studies.

4.5.3 Plasma density effects

Both the experiment and simulation results show that the ion acceleration in the longitudinal direction improves with increasing plasma density. The simulations show that increasing the density from $0.01n_c = 1 \times 10^{19} \text{ cm}^{-3}$ to $0.05n_c = 5 \times 10^{19} \text{ cm}^{-3}$ would cause a dramatic improvement to take place in the longitudinal ion acceleration. This sudden improvement in longitudinal ion acceleration was also seen in the experiment. This is largely unsurprising, as it is expected that more electrons could be accelerated from a higher density plasma, leading to stronger accelerating sheath fields. However, it should be noted that increasing the plasma density may decrease T_e . Obviously, the density dependent decrease in T_e is easily compensated by the increase in n_e . Also, the magnetic field associated with the fast electron current would increase and the time-varying magnetic field contribution to the sheath electric field and the magnetic pressure would both increase. The number of ions available for acceleration also increases with plasma density, which is obviously advantageous for detection and for applications.

4.5.4 Plasma ramp length effects

The plasma expansion into vacuum model, already discussed in section 2.3.3 and section 4.5.2, assumes that there is a zero scale-length plasma on the rear surface, therefore it may be considered surprising that ion energies of this order are observed. For solid density targets, increased rear-end density scale-length has been shown to dramatically reduce the acceleration, since the maximum electric field is given by

$E_{max} \approx T_e/(eL)$, where L is the sheath scale length [129,136]. In the experiment and the simulations, the scale-length due to the initial gas density ramp ($\sim 250 \mu\text{m}$) is larger than the Debye length $\lambda_D = (\epsilon_0 k_B T_e / n_{eo} e^2)^{1/2} \sim 3 \mu\text{m}$ and may be expected, by the previous reasoning, to reduce the maximum electric field by greater than an order of magnitude. It is worth noting that for solid plasma densities, $\lambda_D \sim \text{nm}$. The simulations show that a larger fraction of the hot electrons can escape in the underdense case, because of the higher electron temperature. This is aided by the magnetic pressure on the background electrons, which are impeded from entering the sheath field region, which will have the effect of increasing the Debye length in this region. There is also the assistance of the azimuthal magnetic field, which acts to enhance the electrostatic accelerating field, as shown in the simulations presented [107–109, 175, 177]. Another interesting effect associated with the rear plasma ramp length is the improved collimation of the ion beam with increasing ramp length as seen in the simulations, which is again a consequence of the magnetic field generation.

Chapter 5

Ion acceleration from near critical density plasmas in high-intensity laser plasma interactions

This chapter presents experimental results from high intensity ($\sim 10^{21} \text{ Wcm}^{-2}$) laser interactions with low density foam targets, which have densities ranging from $0.9n_c$ to $30n_c$. This enables the investigation of interactions with the threshold densities between the plasma being transparent (underdense) to the plasma being opaque (overdense) to the laser.

High temperature electron spectra were measured from the low density foam interactions, while the solid target comparison shot produced no electrons above the $\sim 20 \text{ MeV}$ low energy spectrometer threshold. The proton spectra measured indicate that it is possible to achieve similar proton energies and numbers from low density foams to those from solid target interactions. The laser light transmitted through the foam targets was monitored to assess the degree to which the highly relativistic laser pulse is able to propagate. 2D particle-in-cell (PIC) simulations using the code OSIRIS were used to investigate the laser propagation and electron acceleration for different plasma densities, and how this effects the ion acceleration.

5.1 Previous work

The work presented here follows on from the ion acceleration from underdense plasmas that has been described in the previous chapter. In particular, this work extends the investigated density range of measurements of the ions accelerated in the longitudinal direction from the rear surface of a target by a sheath field. Simulations performed for chapter 4 suggest that the ion acceleration could be improved by increasing the plasma density and shortening the plasma scale length at the rear plasma vacuum interface. In addition, if the laser is able to propagate through the plasma, the interaction length for direct laser acceleration will be increased before the electrons outrun the laser pulse. In solid targets the interaction of the laser with the plasma occurs over a relatively short scale length and therefore the interaction time is shorter due to the reflection out of, rather than propagation of the laser through, the plasma.

Another possible ion acceleration mechanism in near critical density foams has been presented by Okihara et al. [178]. They found that isotropic ion emission from foams indicates that a Coulomb explosion mechanism from sub-wavelength structures within the foam accelerates the majority of the detected ions to energies of up to 200 keV. In this type of experiment, the Coulomb explosion originates from the disassembly of small scale structures within the target, rather than the explosion of a channel as described in section 2.2.5. Gas-cluster targets have also been used to study this type of Coulomb explosion mechanism [179] and simulations of this process suggest that the efficiency of the Coulomb explosion mechanism for generating energetic ions may be better in the low density foam target than from gas-cluster targets. However, foam targets have not yet been able to demonstrate the $> \text{MeV}$ ion energies seen in cluster experiments. The foam material used by Okihara et al. [178] has a lamella structure with a 20 nm period with a local density that can be high enough to support the Coulomb explosion, but the average density is low enough to allow laser propagation. Interestingly, the dimensionality of the foam target microexplosion is approximately two dimensional due to the lamella structure, in contrast to the three dimensional disassembly of an atomic cluster.

Collisionless shocks could also be launched from the penetration of the laser interaction surface through the plasma [22]. If these shocks travel ahead of the laser pulse, which is most likely to occur when the laser is unable to propagate far into the plasma, ions can be accelerated from the shock front too (see section 2.2.6).

Most of the interesting ion acceleration occurs at the plasma vacuum interfaces, either at the front or the rear of the target. Another ion acceleration mechanism capable of achieving large numbers at moderate energies has been observed to occur inside a low-density foam target and is referred to as bulk acceleration [180]. This work was performed in the petawatt power regime but at lower intensity (a larger focal spot than the experiment presented in this chapter). Due to the high density threads and voids making up the foam structure, hot electron transport can be severely affected by the space-charge electric fields set up. Electrons travelling through voids in the structure are not neutralised by ions, which remain in the high density threads, and this sets up electrostatic fields. The electrons are inhibited from travelling through the foam, whereas the ions are accelerated. The effectiveness of this ion acceleration is limited by the void size in the foam structure; the smaller the voids are, the shorter the acceleration length. It was seen in the simulations performed by Li et al. [180] that the number of ions accelerated by bulk acceleration was significantly enhanced, compared with surface acceleration, even though the maximum energy was reduced.

Batani et al. [181] performed an investigation into the inhibition of the propagation of fast electrons in plastic foams by resistive electric fields. As a fast electron beam passes through a target, a return current must be set up to maintain the quasineutrality or the fast electron beam will be unable to propagate. At lower plasma densities, such as those found in foam targets, there are fewer background electrons to supply the return current and therefore a larger inhibition to the fast electrons is expected.

Work has been undertaken to investigate the propagation of a relativistic laser pulse through underdense and overdense plasmas [182, 183]. These experiments set up an underdense plasma of $0.1n_c$ by exploding thin foils and the main interaction laser had an intensity of $\sim 5 \times 10^{19} \text{ Wcm}^{-2}$. Borghesi et al. [182] found that there was

an improvement in the laser energy transmission through the plasma if a preformed channel had been made. Without the preformed channel through the $0.1n_c$ plasma, the transmission of the laser energy was limited to a few percent. Reducing the transmission through the target could be beneficial for electron and ion acceleration because this implies that more of the laser energy would be reflected from or, more importantly, absorbed into the plasma. Overdense plasmas with densities of between $2n_c$ and $6n_c$ were formed by soft x-ray ionisation of foam targets. Filamentary structures in the fast electron beam were observed at the rear of the target and were deduced to have occurred because of either a relativistically induced transparency effect or the breaking up of the hot electron beam as it propagated through the plasma. These studies suggested that depletion in pulse energy will seriously limit the laser propagation, even at plasma densities below the relativistically enhanced critical density [182].

Gu erin et al. [184] studied the propagation of ultraintense laser pulses through overdense plasma ($n_e = 1.5n_c$) using 1D particle in cell simulations. A model for predicting the transmission of the laser through the plasma was found by considering the propagation speed of the laser in the plasma and the movement of the front from which the laser is reflected. At relativistic intensities, the group velocity of the laser is given by equation 2.23. An estimate for the wave front velocity, v_f , is presented by Gu erin et al. [184], which accounts for the rate of reflection of the laser. The model is simplified to a temporal top hat laser pulse with no self-focusing, i.e. a constant $\langle\gamma\rangle$. Also, because this model is 1 dimensional, it does not consider the reduction in plasma density on the laser axis. This would act to increase the group velocity of the laser and improve the propagation.

5.2 The experiments

These experiments were performed using the Vulcan Petawatt laser (see section 3.1). Two different experimental campaigns will be considered in this chapter, the first in 2005, the second in 2006. Although very similar in principle, there are some differences in the laser characteristics, targets and diagnostics used on these experiments,

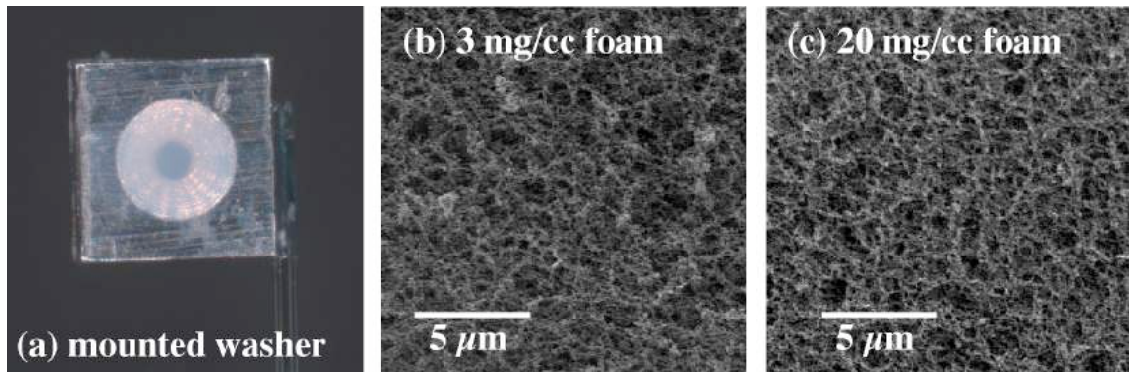


Figure 5.1: (a) The foams were mounted in washers of $250\ \mu\text{m}$ thickness, and (b) and (c) are high magnification SEM images showing the structures in the low density foams (gold coated). The $5\ \mu\text{m}$ scale is similar to the focal spot diameter (images taken by C. Spindloe).

which are detailed below.

The schematic of the Target Area Petawatt (TAP) vacuum chamber has been presented in figure 4.1 and the overall chamber arrangement for the foam target experiment is similar.

5.2.1 Laser parameters

A summary of the laser parameters are given in table 3.1 in the 2005 and 2006 columns. For both of the experiments, the laser pulse had a duration of ~ 550 fs. Laser energies of up to 694 J (55% on target) were achieved to give a maximum average power of 670 TW. The focal spot had a diameter of $5\ \mu\text{m}$ to provide a cycle averaged peak vacuum intensity of $5.5 \times 10^{20}\ \text{Wcm}^{-2}$, which is an $a_0 = 21$. The contrast ratio was 10^{-7} .

5.2.2 Low density foam targets

The foam targets used were of relatively low density and, once ionised, produced a plasma near the critical density for $1\ \mu\text{m}$ light. The foams were fabricated by W. Nazarov at St Andrews University, Scotland, using the in situ polymerisation technique (similar to the method described in [185]). The composition of the foams is 71% carbon, 27% oxygen and 2% hydrogen by weight. Due to the delicate nature

Foam density (mg/cm ³)	Maximum electron number density	
	(cm ⁻³)	(n_c)
3	9×10^{20}	0.9
10	3×10^{21}	3
15	4.5×10^{21}	4.5
20	6×10^{21}	6.0
45	1.35×10^{22}	13.5
100	3×10^{22}	30

Table 5.1: Table of the foam densities and the corresponding maximum electron number densities assuming a fully ionised plasma.

of the foams, they were mounted in washers as shown in figure 5.1 (a), which were all 250 μm thick. The foams were made to fill the washer holes so that the foam surface was flush with the washer. For the 2006 experiment, the washer hole was tapered so that the foams did not fall out if they shrank after production. The density of the CHO foams was varied to get different electron number densities when the foams become ionised by the laser. Figure 5.1 (b) and (c) are images of the 3 mg/cm⁻³ and 20 mg/cm⁻³ foams showing the foam structure and pore size. The pore sizes are sub-micron, so when considering the laser focal spot is around 5 μm , it seems reasonable to assume that the plasma is fairly homogeneous on this scale. It should be noted that the pore size is much smaller than used in other foam investigations [178, 180, 182, 183]. The maximum electron density is calculated by assuming that the foams become fully ionised in the laser field. For the foam densities used in these experiments, the equivalent maximum electron number densities are shown in table 5.1.

For Vulcan, a 1 μm wavelength laser, the non-relativistic critical electron density is $n_c \approx 1.0 \times 10^{21} \text{ cm}^{-3}$. However, at the high laser intensities used in the experiments, the plasma is relativistic and may allow the laser to propagate beyond this, due to the relativistic variation of the plasma frequency, $\omega_{pe}/\sqrt{\gamma}$. The lowest density foam, 3 mg/cm³, is slightly under the non-relativistic density n_c , and therefore even if fully ionised, it will form an underdense plasma ($\sim 9 \times 10^{20} \text{ Wcm}^{-2}$). The

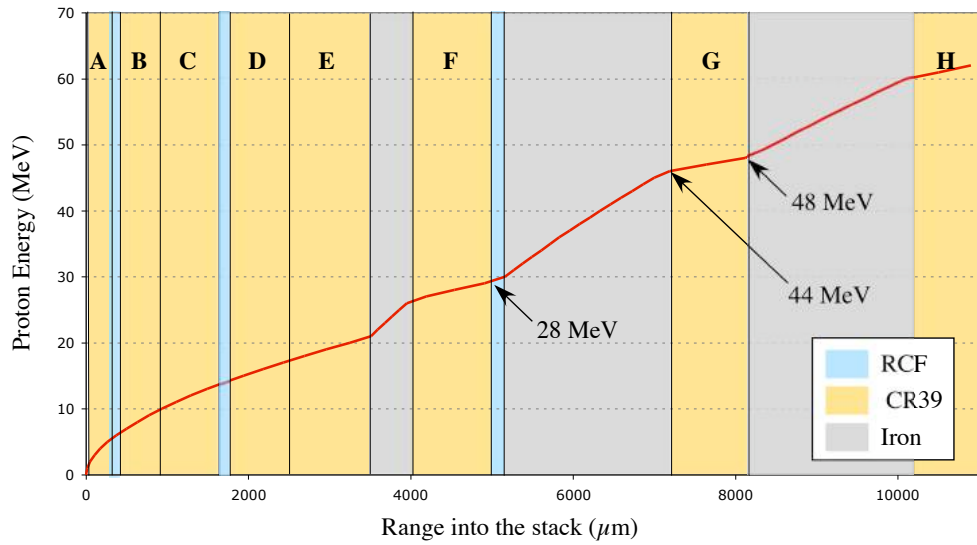


Figure 5.2: The stack composition for the 2005 campaign and the range at which different energy protons are stopped.

Vulcan Petawatt is linearly polarised so the average relativistic critical density is $n_{c\gamma} = \langle \gamma \rangle n_c$, where the time averaged gamma factor is $\langle \gamma \rangle = \sqrt{1 + a_0^2/2}$ for linearly polarised light. Hence, for the parameters used in these experiments, an $a_0 \approx 21$, the relativistic critical density is $n_{c\gamma} \approx 15n_c$.

5.2.3 Diagnostics

There were some differences between the diagnostics used for the 2005 and 2006 experiments. These are described here.

2005 experiment

It was possible to shoot the foam targets at normal incidence to the laser, because back reflections should not pose a significant damage threat to the laser system, while the mylar target had to be shot at 45° incidence to prevent back reflections. To diagnose the foam target interactions, two shots were taken at each density, the first with an imaging stack (see section 3.3.3) made from RCF, CR39 and iron and the second shot without a stack so that the on-axis electron spectrometers had a line of sight to the target. The front of the imaging stacks were placed 100 mm from the rear of the target, in the direction normal to the rear side of the target.

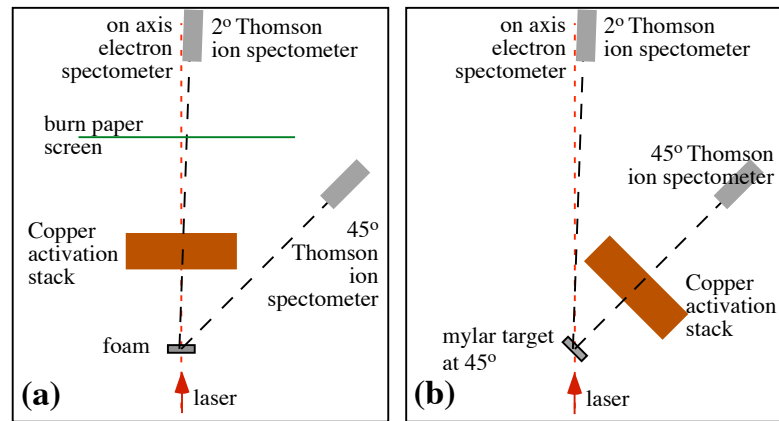


Figure 5.3: The 2006 experimental set up for (a) the foam targets and (b) the mylar targets.

The stack composition and the depth at which different energy protons are stopped (calculated in TRIM [152]) is shown in figure 5.2.

2006 experiment

A larger number of foam densities were shot in 2006 and additional diagnostics were used in this campaign. Copper activation stacks were used to characterise the proton spectra from the interactions (see section 3.3.4) and were placed normal to the rear surface of the targets. The slightly different set up for the mylar shots and the foam shots are shown in figure 5.3.

The layer composition of the activation stacks is given in table 5.2. The analysis of the activation stack data is described in section 3.3.4 and requires the sensitivities for each layer to deconvolve the proton spectra. Figure 5.4 shows the layer sensitivities as calculated by a tracking code (see section 3.3.4), which were then used to calculate the proton spectra.

There was also a second set of shots taken without a copper activation stack. Instead, a piece of burn paper was set up as a screen to record the laser light transmitted through the foam targets. Where laser energy is incident upon the burn paper, a darker region is produced. The strength of the burn is proportional to the laser intensity; this is a non-linear relationship. The front side of the burn paper was imaged using a CCD camera with a ω filter to record the scattered light

Layer	Material	Thickness (μm)	Layer	Material	Thickness (μm)
1	Al	25	10	Cu	270
2	Cu	25	11	RCF (MD-55)	250
3	Cu	50	12	Cu	500
4	Cu	50	13	Cu	500
5	RCF (HD-810)	100	14	CR39	750
6	Cu	100	15	Cu	1000
7	Cu	100	16	Cu	1000
8	RCF (HD-810)	100	17	CR39	750
9	Cu	270	18	Cu	1000

Table 5.2: Table of the activation stack composition used to measure the proton spectra in the 2006 experimental campaign.

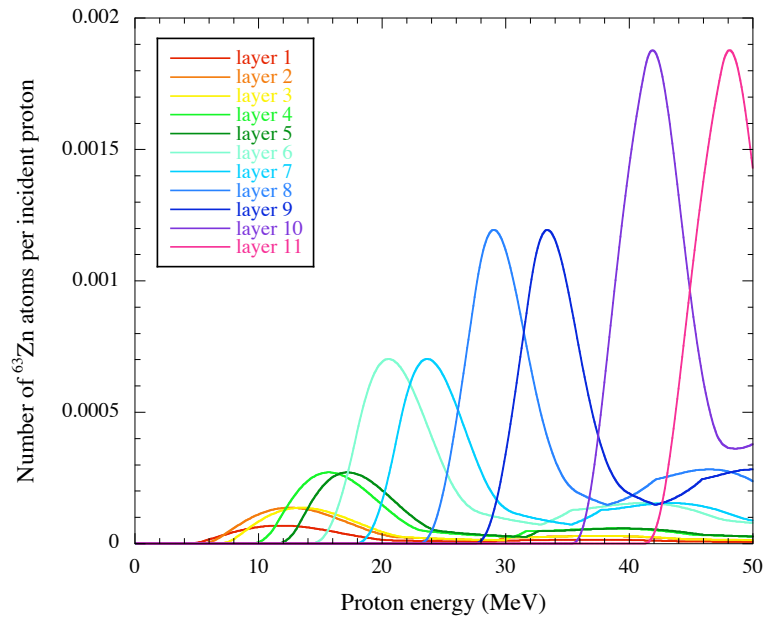


Figure 5.4: The number of ^{63}Zn atoms per incident proton as a function of proton energy for each layer in the activation stack.

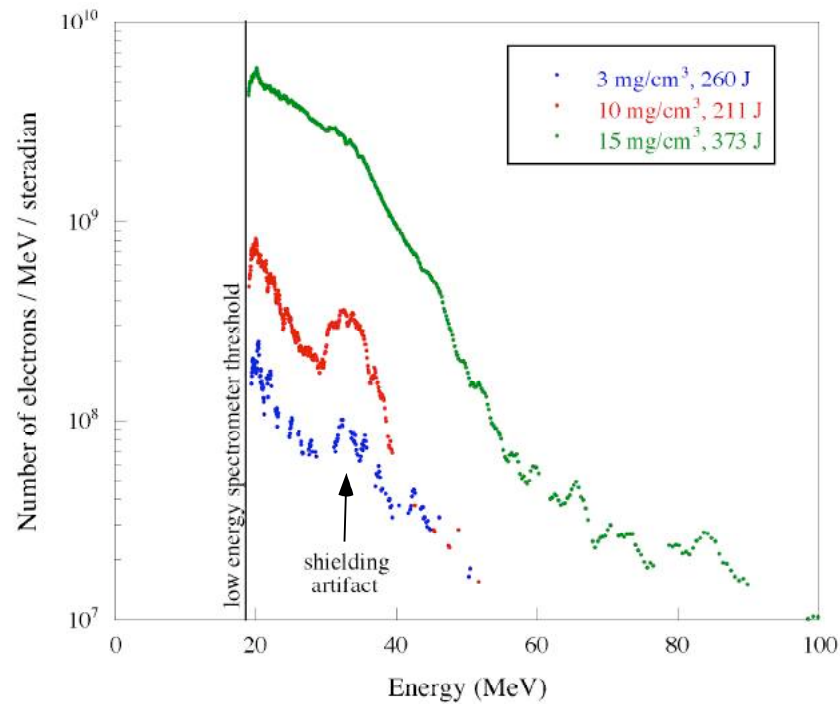


Figure 5.5: The electron spectra taken on the laser axis during the 2005 campaign. (On-axis means in the target normal direction for the foam shots, at 45° to the back surface for the mylar.)

from the screen, at the fundamental laser frequency.

5.3 Experimental results

5.3.1 2005 experimental results

The foam targets (2005) had densities of 3 mg/cm^3 , 5 mg/cm^3 and 15 mg/cm^3 and a comparison shot was made on a $10 \mu\text{m}$ thick mylar target. The electron spectra measured from these shots are presented in figure 5.5. The bump seen at around 35 MeV is due to a shielding artifact, where there was a gap of insufficient shielding in front of the spectrometer, leading to an x-ray signal on the image plate. The foam targets all produce high energy electron spectra, whereas the mylar target electron signal was below the low energy spectrometer threshold ($\sim 20 \text{ MeV}$) and no electrons were recorded for this shot. The 15 mg/cm^3 shot had a higher laser energy and may partially explain the improved electron acceleration recorded.

A summary of the maximum proton energy, as identified by the imaging stacks in the 2005 campaign, is shown in table 5.3. The main problem with these stacks was that the energy resolution was quite poor and it was not possible to ascertain absolute proton numbers from them. However, the foam target shots have produced protons of similar maximum energy and number as the mylar target.

Target	Laser energy	Max. proton energy
3 mg/cm ³	260 J	44 ± _{0.5} ⁴ MeV
10 mg/cm ³	345 J	28 ± _{0.5} ¹⁶ MeV
15 mg/cm ³	380 J	44 ± _{0.5} ⁴ MeV
10 μm mylar	310 J	28 ± _{0.5} ¹⁶ MeV

Table 5.3: Summary of the maximum proton energies seen in the imaging stacks from the 2005 campaign.

5.3.2 2006 experimental results

During the 2006 experimental run, a wider range of foams of densities (3, 20, 45 and 100 mg/cm³) were shot. The full proton beam spectra from the rear of the foam targets were measured using copper activation (see section 3.3.4) and this was compared to a shot onto a 10 μm mylar target. The activity measurements allow the calculation of the initial number of ⁶³Zn in each of the layers of the stack and these are presented in figure 5.6 as the initial number of ⁶³Zn atoms per μm of copper. This can be deconvolved, using the technique described in section 3.3.4, into the full beam proton spectra shown in figure 5.7.

The proton spectra for the 10 μm mylar target and the 3 mg/cm³ foam target are fairly similar and both extend to around 35 MeV. It is worth noting that there was approximately 35% more laser energy on the 3 mg/cm³ foam target, which could partly account for more efficient proton acceleration. The other proton spectra from the 20 mg/cm³, 45 mg/cm³ and 100 mg/cm³ foams do not produce such high proton numbers or temperature as the other targets. There may be a slight increase in proton energy and number with increasing density for these 3 shots. This would be consistent with a higher plasma density being able to generate a larger number of

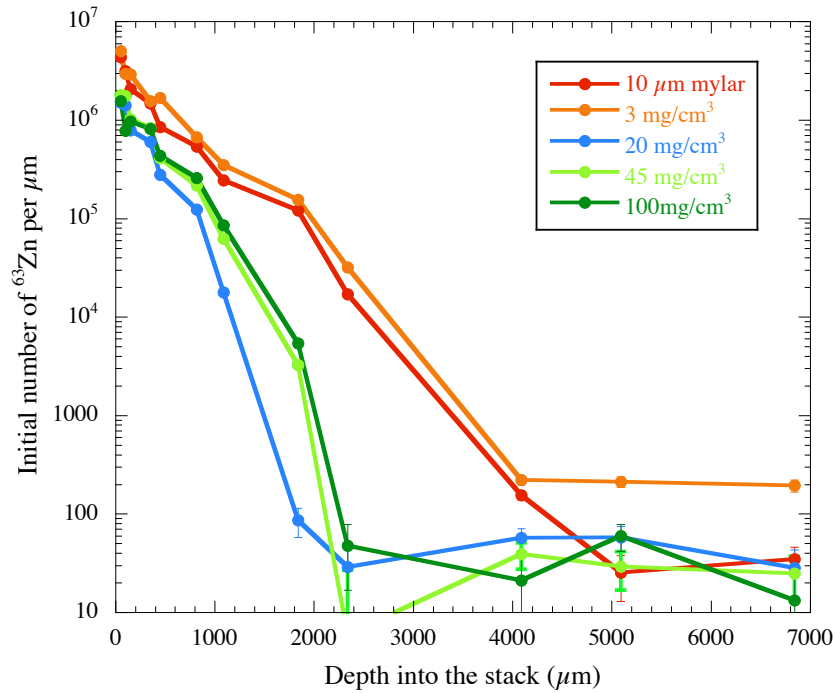


Figure 5.6: The initial number of ^{63}Zn atoms per μm obtained from the activation stacks for the different targets.

hot electrons as well as there being a larger number of ions to accelerate. However, this is not consistent with the better proton spectra generated by the $3 \text{ mg}/\text{cm}^3$ foam target, but at this lower density, the laser is far more likely to propagate through the full thickness of the target, therefore electrons can be accelerated to high energies over the whole target thickness, leading to improved proton and ion acceleration.

This activation technique is not able to identify any small variations in the spectra as a Thomson ion spectrometer is able to, but it does allow the spectrum of the whole beam to be measured.

It may be useful to consider the conversion efficiency of the laser energy into high energy protons. As a percentage of the laser energy on target that goes into the number of protons with an energy of above 4 MeV, the conversion efficiencies are 3.1% for the $10 \mu\text{m}$ mylar, 2.6% for the $3 \text{ mg}/\text{cm}^3$ foam, 0.6% for the $20 \text{ mg}/\text{cm}^3$ foam, 0.9% for the $45 \text{ mg}/\text{cm}^3$ foam and 1.1% for the $100 \text{ mg}/\text{cm}^3$ foam. These are shown in figure 5.7, which presents the maximum proton energy at 10^9 protons per MeV and the conversion efficiency as a function of the foam density. The trend that

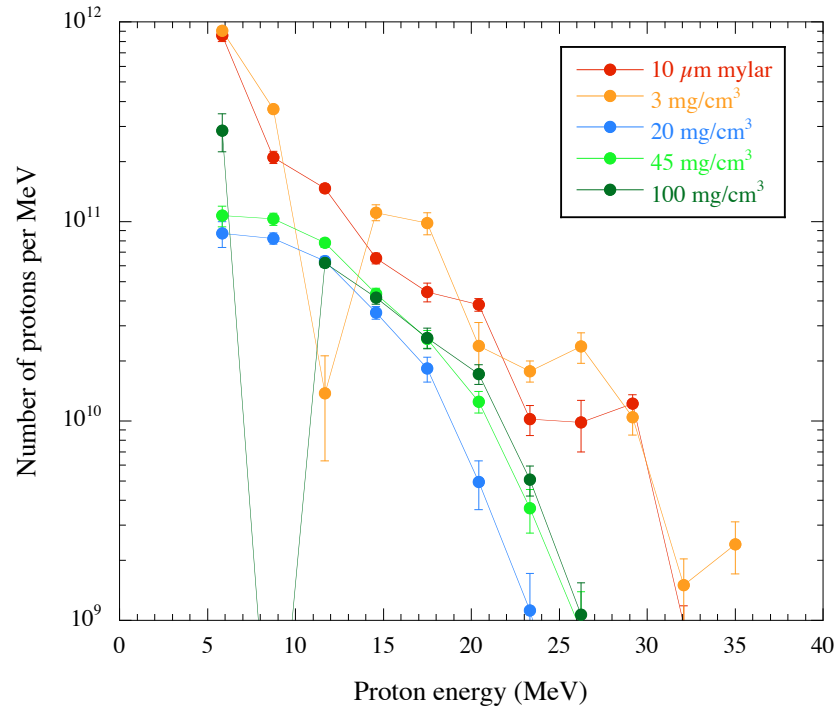


Figure 5.7: Proton spectra obtained from the activation stacks calculated by finding best fit to the measured initial number of ^{63}Zn .

can be seen in this plot is that between 3 mg/cm^3 and 20 mg/cm^3 , the conversion efficiency and maximum proton energy drops drastically. As the density increases from 20 mg/cm^3 , the conversion efficiencies and maximum proton energies show a slight improvement as illustrated in figure 5.8.

In the same stacks there were a number of radiochromic film pieces at different depths to record the proton beam profile (shown in figure 5.9). The different shots are shown in columns, with the label at the top showing the target type and laser energy on target for that shot. The top row of RCF images show proton energies of $> 7 \text{ MeV}$, the middle row $> 12.5 \text{ MeV}$ and the bottom row are $> 22 \text{ MeV}$. The angles at the bottom of figure 5.9 indicate the FWHM of the proton beams for the $> 22 \text{ MeV}$ protons. The signal on the RCF will be predominantly due to the protons at the cut-off energy because of the Bragg peak.

The 3 mg/cm^3 target was aligned at 10° to the laser axis and the shift seen on the radiochromic film is in agreement with the proton beam being accelerated normal to this angled surface. This provides evidence that the ion beams from the

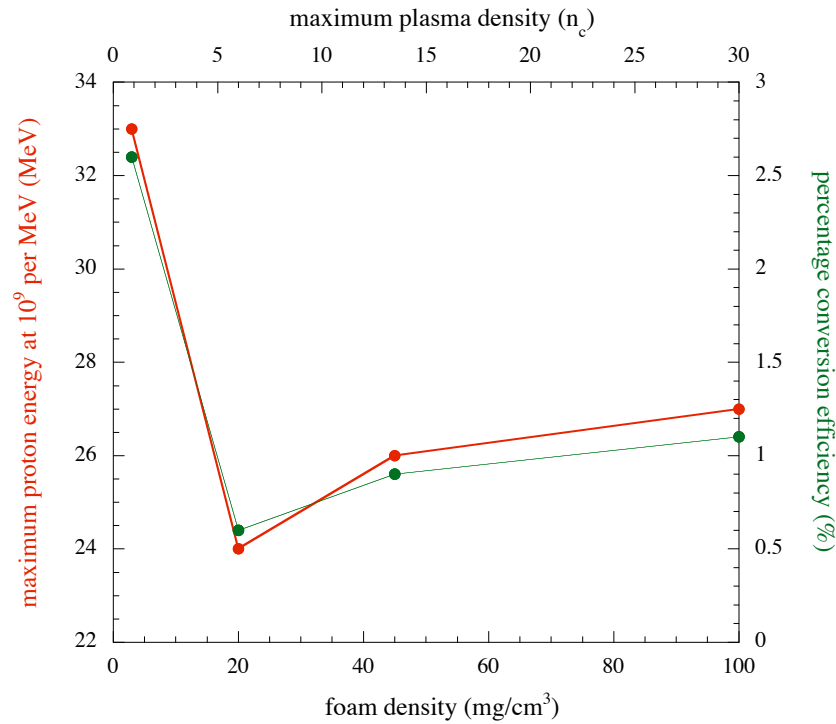


Figure 5.8: The maximum proton energy at 10^9 per MeV and the conversion efficiency of laser energy into protons with > 4 MeV against foam density and maximum plasma density for the stack shots.

foams are being accelerated by the TNSA mechanism in the same way as from solid targets.

There are a few interesting structural features to note in the proton beams. There are wispy horizontal-vertical cross features seen at low energy and extend across the film. At high energy for some of the foam shots, an almost regular structure can be seen. Also visible on the RCF at the lowest energy (> 7 MeV) protons from the 20 mg/cm^3 , the 45 mg/cm^3 and the 100 mg/cm^3 foam target shots, is a reduction in the number of protons in the centre of the film, which seem to be leading to a ring structure in the proton beam. The RCF pieces are saturated in some places so this is not very clear, but the activated copper pieces also show this feature. The beam profiles from the second copper layers of the 20 mg/cm^3 , 45 mg/cm^3 and 100 mg/cm^3 stacks are shown in figure 5.10. These were recorded by placing the activated copper pieces onto an image plate after the measurements had been taken (see section 3.3.4). The activation does not saturate in the same way as the RCF

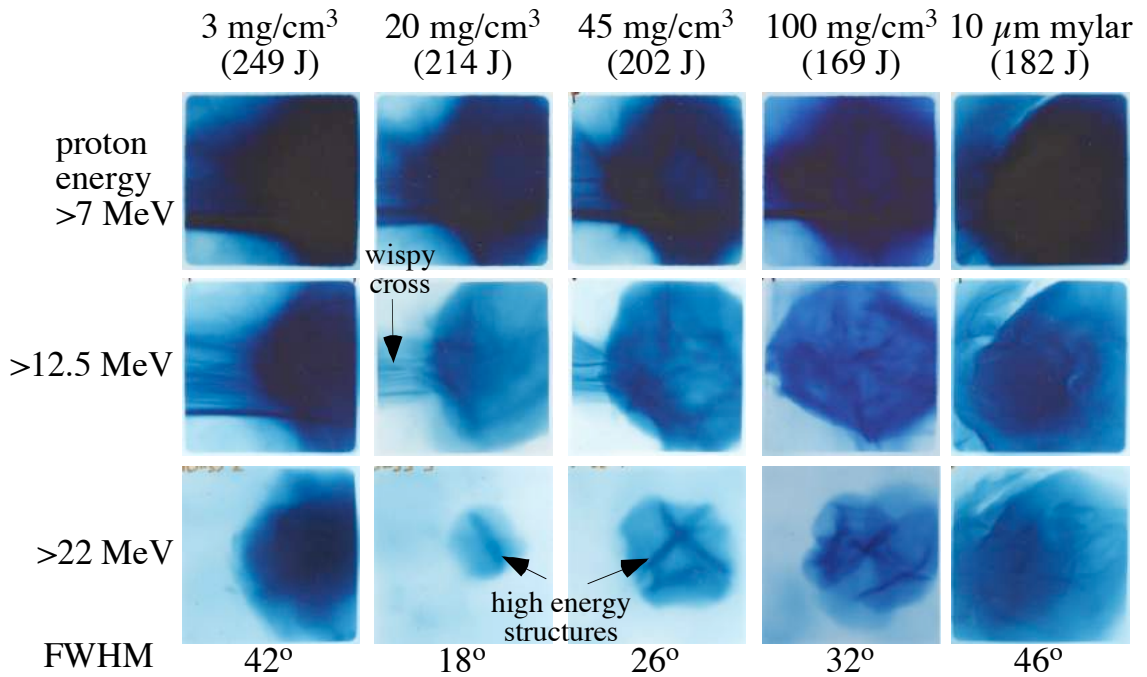


Figure 5.9: Proton beam profile from the RCF interleaved in the activation stacks. The labels at the top show the target type and laser energy on target. The labels down the side show the proton energies detected by the layer. The angles at the bottom indicate the FWHM of the proton beams for the > 22 MeV protons.

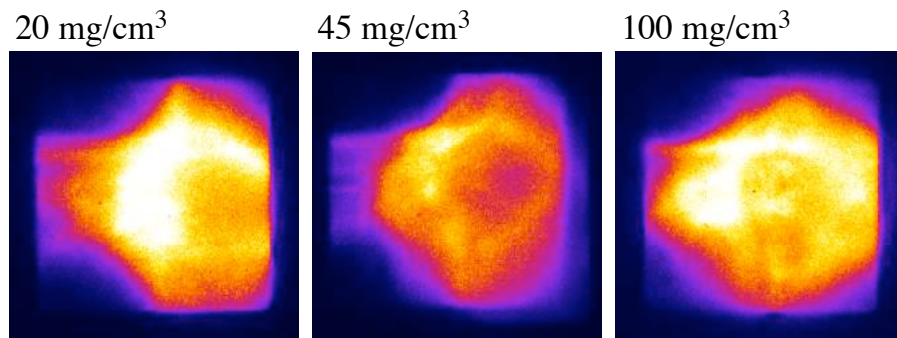


Figure 5.10: The proton beam profiles recorded on the second copper layer in the stacks from the 20 mg/cm^3 , 45 mg/cm^3 and 100 mg/cm^3 foam targets. (Beam intensity not on the same scale)

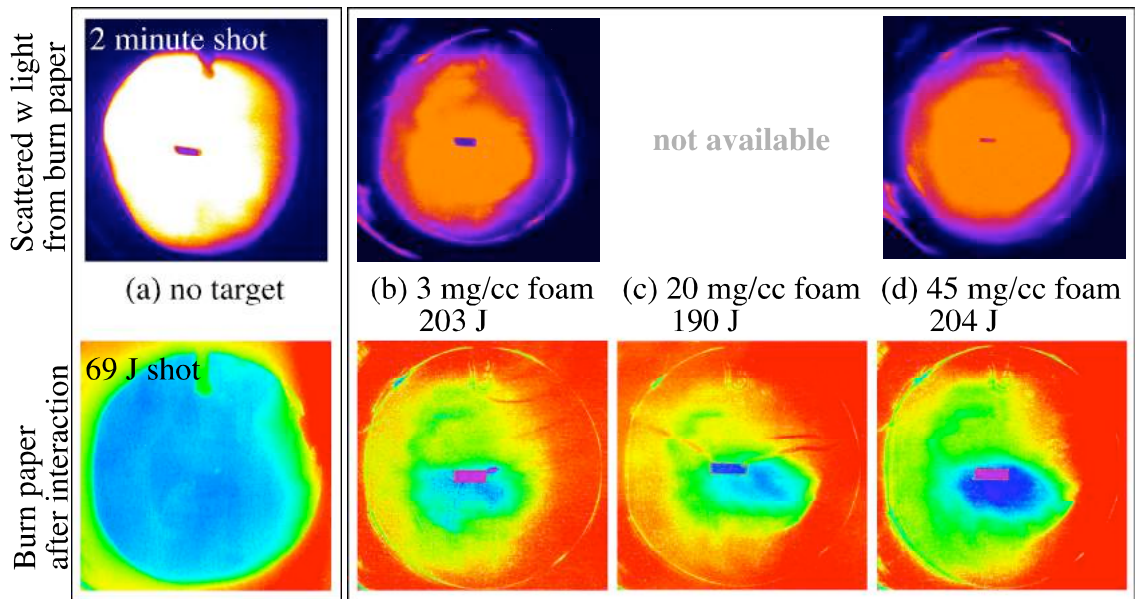


Figure 5.11: The top row of images show scattered ω light from the burn paper during the shots (scale is normalised for the filtering and laser energy). The lower row of images are background corrected burn paper images (on the same scale).

and a clearer profile is produced.

Figure 5.11 shows the results of the transmitted light diagnostics, the scattered ω light imaging and the burn paper. The rectangular regions visible in the center of the burn papers are holes, allowing diagnostic line of sight. The scattered image labelled ‘2 minute shot’ is from a low power shot with no target present and the scattered light images were filtered with an interference filter to detect only the laser frequency. From the high power shots onto foam targets, the light at ω is still well collimated after the interaction. The central regions of the two full energy scattered light images are saturated and irregular, which makes it difficult to take an angular divergence measurement. However, it does appear significantly reduced after the interaction. Unfortunately there is no calibration available for the 2 minute shot energy so an absolute value of the energy transmission is not possible. It is estimated that the 2 minute shot would contain 100 mJ of energy on target, and this is what the images in figure 5.11 have been normalised to.

The burn paper has a non-linear response to energy. However, the strength of

burns suggests that a few Joules of energy are transmitted through the foam targets, which corresponds to a few percent transmission.

5.4 PIC simulations

A series of relativistic 2D3V PIC simulations were performed with the code OSIRIS [105, 106] (see section 4.4), to model this type of interaction. The simulations investigate the laser propagation and ion acceleration at different plasma densities.

5.4.1 Simulation setup

Two types of simulations were performed to investigate the near critical plasma interactions. The first type are essentially the same as for the underdense plasma simulations in chapter 4. A stationary box was used to look at the rear surface ion acceleration. The simulation box was $251 \times 251 \mu\text{m}$ with a resolution of 20.9 cells $/\lambda$ in the longitudinal (x) direction and 12.6 cells $/\lambda$ in the transverse direction (y). The number of particles used was 2 or 4 per cell due to computational constraints and a single proton ion species was used for simplicity. The ion acceleration was investigated with changing plasma density and initial plasma densities of $0.9n_c$, $1.5n_c$, $4.5n_c$ and $15n_c$ were simulated. The density profile had a $1 \mu\text{m}$ long linear density ramp at the front of the plasma, $158 \mu\text{m}$ of plasma at maximum density and a $1 \mu\text{m}$ density ramp at the back of the target. The vacuum then extended a further $84 \mu\text{m}$ behind the plasma. The laser pulse was linearly polarised with the electric field in the y -direction, with a full-width-half-maximum pulse length of, $\tau_l = 500$ fs and a wavelength of $1.053 \mu\text{m}$. It was focused to a full-width-half-maximum diameter spot of $8 \mu\text{m}$ at the top of the front density ramp, to give a peak normalised vacuum vector potential of $a_0 \approx 15$.

The second type of simulations employed a moving box to investigate the laser propagation and electron acceleration in near critical density plasmas. The simulation box was $302 \times 118 \mu\text{m}$ with a resolution of 40 cells $/\lambda$ in the longitudinal (x) direction and 12 cells $/\lambda$ in the transverse direction (y), and moves at the speed of light, c , in the x -direction. The number of particles per cell used was 4 due to

computational constraints and a single proton ion species was used for simplicity. The laser propagation and electron acceleration were investigated for different initial plasma densities of $0.5n_c$, $0.9n_c$ and $1.5n_c$. The density profile had a $3\ \mu\text{m}$ long linear density ramp at the front of the plasma, $249\ \mu\text{m}$ of plasma at maximum density and an $3\ \mu\text{m}$ density ramp at the back of the target. The laser pulse was linearly polarised with the electric field in the z -direction, $\tau_l = 500\ \text{fs}$ and a wavelength of $1.053\ \mu\text{m}$. It was focused to a full-width-half-maximum diameter spot of $8\ \mu\text{m}$ at the top of the front density ramp, to give a peak normalised vacuum vector potential of $a_0 \approx 20$.

5.4.2 Simulation results

The moving box simulations are able to investigate the laser propagation and electron acceleration at near critical plasma density. The main problem with the moving box simulations is that the laser pulse moves at a group velocity considerably lower than the speed of light (which is the speed of the simulation box), therefore the laser pulse starts to shift out of the back of the simulation box. This problem worsens with increasing plasma density and time into the simulation.

As the laser pulse moves through the $0.5n_c$, $0.9n_c$ and $1.5n_c$ plasmas, all of the simulations show signs of filamentation and hosing in the laser beam. Figure 5.12 shows the z -direction electric field, i.e. the direction of the laser polarisation, for each of the densities at a time of $1.08\ \text{ps}$ after the start of the simulation. The retardation of the laser pulse in the higher density plasma is also clear in figure 5.12, as the laser front has not progressed as far as for lower plasma densities.

With this filamentation of the laser energy, the electron acceleration is affected and so the electron beam also filaments. This is shown in figure 5.13, which presents data from the $0.5n_c$ density simulation at a time of $1.08\ \text{ps}$. Figure 5.13 (a) shows part of the filamented laser pulse and figure 5.13 (b) shows the longitudinal electron momentum, p_x . The positions in the y -direction of the laser filaments correspond to the positions of the greatest electron acceleration, indicating that the electron beam is filamenting.

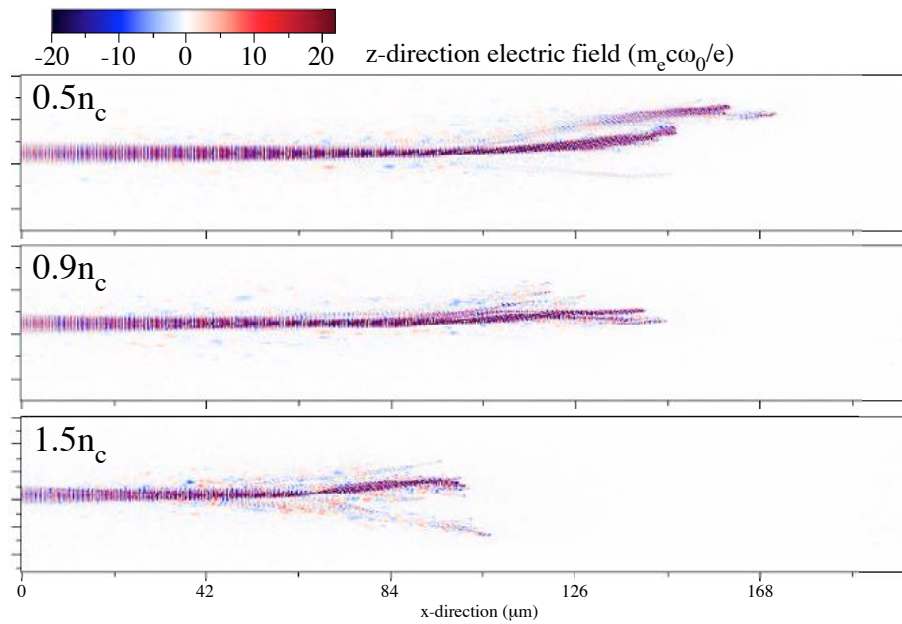


Figure 5.12: The z -direction electric field at a time of 1.08 ps into the moving box simulations for initial plasma densities of $0.5n_c$, $0.9n_c$ and $1.5n_c$. (NB: the full length of the box is not shown.)

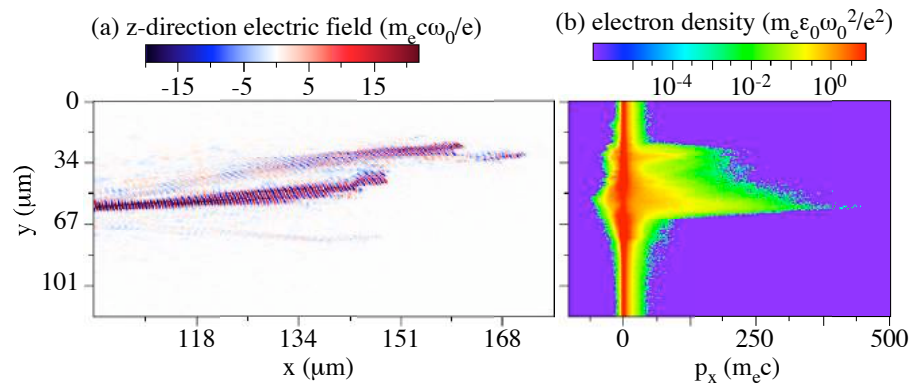


Figure 5.13: For a time of 1.08 ps into the $0.5n_c$ density simulation showing (a) the z -direction electric field (the laser pulse), and (b) the longitudinal electron momentum, p_x , across the y -direction to show the effect on the laser beam filamentation on the electron acceleration.

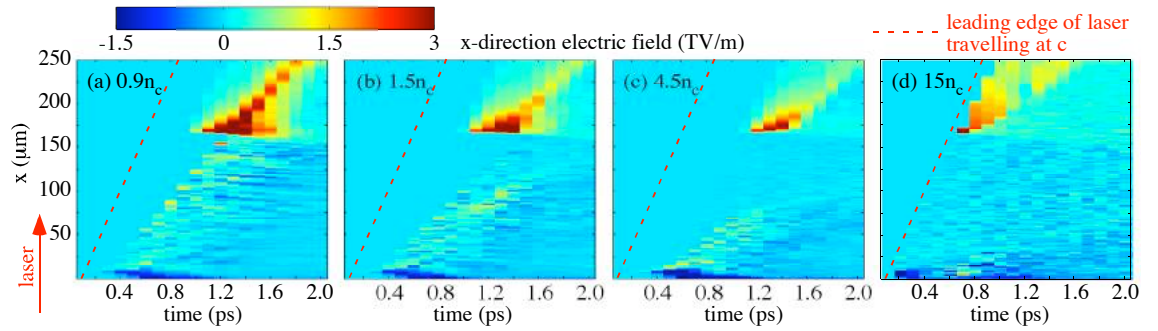


Figure 5.14: The longitudinal electric fields seen in the simulations of different density plasmas, (a) $0.9n_c$, (b) $1.5n_c$, (c) $4.5n_c$ and (d) $15n_c$. These are shown as a function of time, averaged in the y -direction over a $17 \mu\text{m}$ wide selection in the centre of the simulation box. The dashed red line shows the position of the leading edge of the laser pulse travelling at c . The pulse peak is approximately 650 fs behind this.

The laser beam exhibits strong self-focusing and the maximum a_0 reached in $0.5n_c$ plasma is 38, $0.9n_c$ plasma is 38 and $1.5n_c$ plasma is 45, compared with the vacuum focusing of $a_0 \approx 20$. This happens despite the filamentation, which occurs simultaneously.

The stationary box simulations allow the effect of plasma density on ion acceleration to be investigated. The characteristics of the interactions are quite different for all the densities investigated, $0.9n_c$, $1.5n_c$, $4.5n_c$ and $15n_c$. In figure 5.14, the x -direction electric fields are shown as a function of time across a radially averaged $17 \mu\text{m}$ selection down the centre of each simulation box. These give a good indication of the relative strengths of the average field in the centre of the box. The dashed red line indicates the position of the leading edge of a laser pulse travelling through vacuum at the speed of light, c . The peak of the laser pulse travels approximately 650 fs behind this edge. The maximum averaged x -direction electric fields for each case are 7.5 TV/m for the $0.9n_c$ simulation, 4.3 TV/m for the $1.5n_c$ simulation, 3.3 TV/m for the $4.5n_c$ simulation and 5.5 TV/m for the $15n_c$ simulation. This data is presented in figure 5.15 and shows the maximum longitudinal electric field against the plasma density used in the simulation and compares this to the experimentally measured maximum proton energy at 10^9 per MeV. The maximum longitudinal (x -direction) electric fields occur at 1.2 ps for all densities apart for the

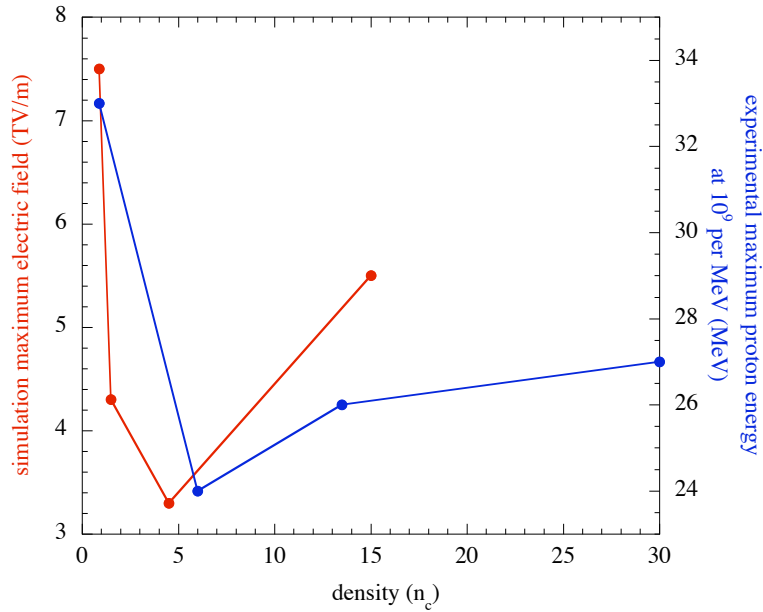


Figure 5.15: The maximum longitudinal electric fields seen in the central region of the simulations and the experimentally measured maximum proton energy at 10^9 per MeV plotted as a function of plasma density.

$15n_c$ simulation, which occurs much earlier at around 0.6 ps. The peak of the $15n_c$ simulation longitudinal electric field occurs when electrons generated by the leading edge of the pulse at the front surface arrives at the rear surface. This is in opposition to the peak of the laser pulse arriving at the rear surface and coinciding with the peak electric field, as is found for all of the other simulation densities. To account for the maximum field not being in the centre of the simulation box, perhaps due to filamentation shifting the concentration of fast electrons, the maximum electric field in the x -direction was also found. For $0.9n_c$ the maximum x -direction electric field is 13.1 TV/m, for $1.5n_c$ it is 9.6 TV/m, for $4.5n_c$ it is 8.3 TV/m and for $15n_c$ it is 15.3 TV/m.

In the lowest plasma density, $0.9n_c$, the laser is able to propagate through the full thickness of the target. This can be seen in figure 5.16 (a), which shows the ion density at a time of 2.0 ps into the simulation, after the laser has passed through. The laser has been able to propagate through the entire thickness of the plasma, leaving behind a plasma channel through the full plasma thickness. The region of high ion density situated at the rear of the cavitated channel is a remnant of laser

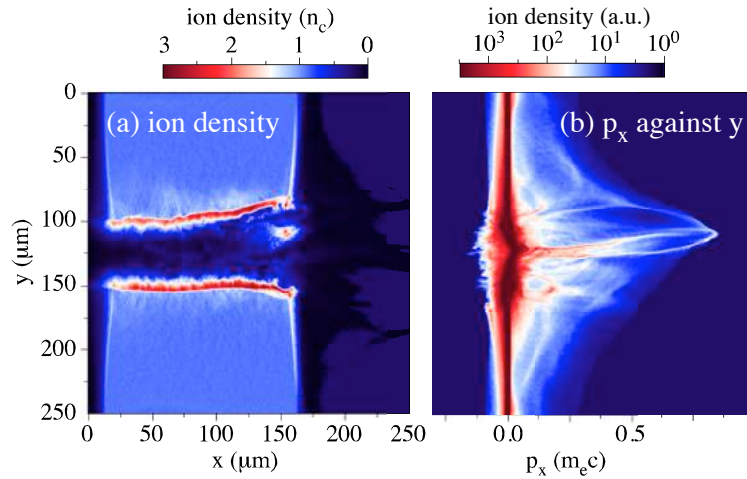


Figure 5.16: (a) The ion density at a time of 2.0 ps into the simulation from the $0.9n_c$ plasma density simulation and (b) the longitudinal momentum, p_x , against the y -direction at a time of 1.7 ps into the simulation, showing structure in the accelerated beam.

filamentation. Because the group velocity of the laser is slowed in the plasma, some of the accelerated fast electrons are able to outrun the laser pulse and arrive at the rear of the target first. As soon as fast electrons start to emerge from the rear side of the target, ions begin to accelerate in the longitudinal direction from the plasma vacuum interface. The ion acceleration is improved when the laser reaches the rear surface and a large number of fast electrons move out into the vacuum. Structure in the accelerated ion beam is observed and can be seen in figure 5.16 (b), showing the longitudinal momentum p_x against the y -direction at a time of 1.7 ps into the simulation. The origin of the filamentary structures appears to be the highest density regions on the rear of the target since the p_x ion filamentary structures positions in y correspond to the high density regions in figure 5.16 (a).

When the initial plasma density is increased to $1.5n_c$, the simulations show that the laser was able to propagate a substantial, but not the entire distance through the target, before the energy has been either absorbed by the plasma or reflected. This is despite the density being below the relativistically corrected critical density. This can be seen in figure 5.17, which shows the ion density at a time of 2.0 ps into the simulation. The ion channel has not evolved through the entire thickness of the plasma. The laser was able to propagate a significant distance into the plasma,

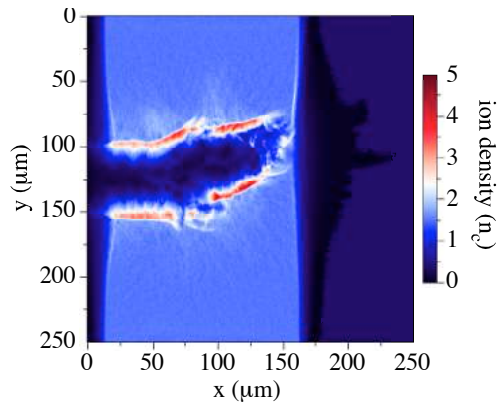


Figure 5.17: The ion density at a time of 2.0 ps into the simulation from the $1.5n_c$ plasma density simulation.

meaning that it was possible for a large number of electrons to be accelerated to high energy. Although a large number of electrons were still able to leave the plasma, significantly more electrons were drawn back into the target as a return current in comparison with the $0.9n_c$ simulation. The peak longitudinal electric field achieved at the target rear surface is only around half of what is seen in the $0.9n_c$ simulation. The ion acceleration did not occur as rapidly as in the $0.9n_c$ simulation and the ion front remained in the box for longer (as it was travelling slower).

At $4.5n_c$ the laser had significantly more trouble propagating through the plasma and only managed to bore a channel approximately half way through the target. Again, this is despite $n_e < \langle \gamma \rangle n_c$. The ion density at a time of 2.0 ps can be seen in figure 5.18 (b). Shock accelerated ions travelling in the forward direction were accelerated at the beginning of the interaction from the front surface of the target. These shock accelerated ions are indicated in figure 5.18 (a), which presents p_x as a function of x at a time of 1.5 ps. It has already been shown that the rear plasma vacuum interface sheath field was smallest in the $4.5n_c$ simulation, but it was also the least efficient density for the longitudinal ion acceleration investigated in this set of simulations.

The $15n_c$ simulation showed quite a different interaction. The laser failed to penetrate the plasma until the peak of the pulse arrived. Even then it generated only a small cavity at the front surface of the target. This can be seen in figure 5.19, which

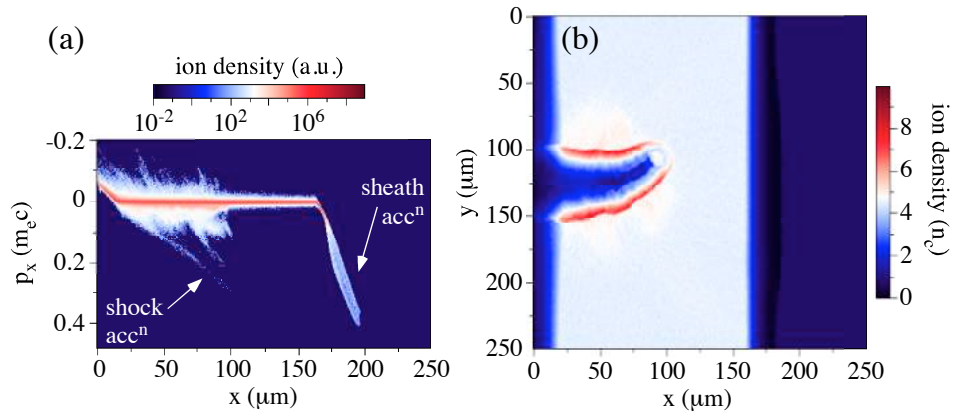


Figure 5.18: From the $4.5n_c$ plasma density simulation showing (a) the longitudinal momentum, p_x , against the x -direction showing the shock accelerated ions from the front surface at a time of 1.5 ps into the simulation, and (b) the ion density at a time of 2.0 ps into the simulation.

shows the ion density at a time of 2.0 ps. The leading edge of the pulse generated the highest energy electrons and these propagate through the target to generate the peak longitudinal electric field. It is possible that this was due to the sharp plasma vacuum boundary present at the start of the simulation, allowing efficient vacuum heating (see section 2.3.1), the efficiency of which would rapidly decrease as expansion on the front surface increases the plasma scalelength. The peak of the laser pulse generated a large, but lower temperature, fast electron current. By the time the peak current arrived at the rear surface, plasma expansion was already significant and the sheath electric field prevents such a high fraction of the electrons from escaping the target.

5.5 Discussion

In this chapter, ion acceleration results from near critical density foam targets have been presented. The lowest density foam targets, when fully ionised, produces a plasma with a density below the non-relativistic critical density of the laser. In all of this work it has been assumed that the foams form a homogeneous plasma density. The validity of this assumption will be discussed. The proton spectra obtained from the lowest density foam targets were comparable to the proton spectra from a solid

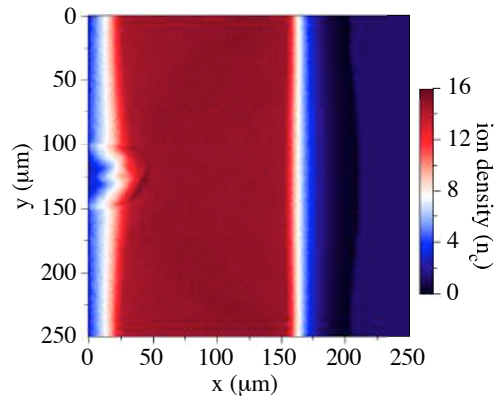


Figure 5.19: The ion density at a time of 1.5 ps into the simulation from the $15n_c$ plasma density simulation.

target seen in the target normal direction. However, for the higher density foams, the proton acceleration was not quite as effective.

From the simulations, it seems that the acceleration can be improved if the laser is able to propagate all the way through to the rear of the target and emerge with a large number of fast electrons. If the laser only propagates part of the way through the target, the rear side ion acceleration is reduced. In contrast, the highest density simulation was quite different. The laser failed to penetrate the target and a large number of electrons were accelerated from the front surface. There was efficient ion acceleration from the rear surface as the electrons left the back of the target.

The transition between underdense and overdense plasma has been observed in both the experiments and the simulations. The effect of the transition on the proton acceleration is discussed below.

5.5.1 Effect of the foam structure

The calculated maximum plasma densities of foams, assuming a full ionisation, may lead to the belief that the laser should propagate through all but the highest density foam due to relativistic effects. The effect of the pre-pulse in these experiments is likely to be significant. The contrast ratio of the main pulse to the nanosecond pre-pulse is of the order of 10^7 , so if the peak intensity is $\sim 10^{21}$ Wcm^{-2} , the pre-pulse intensity, assuming the focusing is similar, will be $\sim 10^{14}$ Wcm^{-2} . At this pre-pulse

intensity a plasma with a moderate temperature, $T_{hot} \sim \text{keV}$, will be generated. A conservative estimate of the electron temperature from the ponderomotive energy would be 10 eV. From this electron temperature, the sound speed for a singly ionised carbon is approximately $10 \mu\text{m ns}^{-1}$. This conservative estimate suggests that the foam with a typical pore size of $\sim 1 \mu\text{m}$ would be able to homogenise in the nanosecond of pre-pulse.

The pre-plasma density created will depend on the foam density and also on the ionisation state reached. It is unlikely that more than the first few ionisation states will be reached in either the carbon or oxygen and the plasma density will therefore be significantly lower than when the high intensity pulse arrives. This may mean that the pre-pulse is able to propagate further through the target, as it may be underdense to the pre-pulse. An additional complication is that the pre-pulse will not self-focus and therefore will reduce in intensity as it moves out of focus. The Rayleigh range for the experimental focusing geometry was $\approx 30 \mu\text{m}$, so the intensity will fall off rapidly over the $250 \mu\text{m}$ foam thickness. Since good ion acceleration is observed from the foams, this suggests that the pre-plasma is not significant at the rear side of the target when the main pulse arrives, so a steep rear plasma vacuum interface is maintained. This in turn implies that the assumption that the plasma is completely homogeneous at the time of the arrival of the main pulse may not be valid through the entire thickness of the foam, so the main laser pulse is likely to encounter irregular high and low density regions based on the foam structure, especially further into the foam.

The possibility that the foam could act like a cluster type interaction and accelerate ions in Coulomb explosions [178] seems unlikely to have occurred in the experiment presented, as the signature of such a Coulomb explosion acceleration mechanism is isotropic ion emission at low energy ($< \text{MeV}$). However, the proton emission observed from the rear of the target is beam-like, which is indicative of a rear side acceleration mechanism. The foams used by Okihara et al. were made by a different technique and had threads and pores on a much larger scale ($\sim 10 \mu\text{m}$), while the foams used as targets in the experiment presented here have smaller structures. This would mean that the electric fields generated from exploding adjacent

threads would quickly overlap. This is suggestive that for these finer structure foams, the interaction is closer to a uniform plasma density (gas or solid target) experiment in its dynamics, than to a cluster explosion. Furthermore, the beam of protons would not have been generated through this type of Coulomb explosion as a near isotropic emission is expected.

Li et al. describe another mechanism which may occur when fast electrons propagate through a structured material such as a foam, and set up internal longitudinal electric fields leading to bulk ion acceleration [180]. However, the diagnostics fielded on the experiments presented here are not designed for looking at large numbers of low energy ions. It is likely that the pore sizes used are different in the Li et al. experiment. In their experiments, the foams were made from deuterated polystyrene with densities of 50 mg/cm^3 and 160 mg/cm^3 prepared by the sol gel-aerosol method. This is the same technique as used to prepare the Okihara et al. experimental foam targets [178], which produces much larger foam structures ($\sim 10 \mu\text{m}$). If the pore scales are much smaller as for the experiment presented here, the accelerating electric fields will have a shorter scale. This would be beneficial for the fast electron temperature, since the setting up of internal electric fields in the target would dissipate energy and lead to a reduction in electron temperature.

5.5.2 Laser propagation at near critical density

Considering the simulation results, it seems that the increased laser propagation into the target can be beneficial to the rear side acceleration of ions. The further the laser can propagate, the longer the interaction length over which electrons can be accelerated. This leads to an improvement in electron beam characteristics such as temperature, number and reduced exit area at the vacuum interface. The laser can also ionise the target to a higher degree if it propagates through the target, resulting in a higher background electron density. A higher background electron density means that there can be a larger return current, enabling the fast electron current to be greater [181].

The experimental measurements of the transmitted laser energy, particularly the

burn paper, indicates that at least a few Joules of energy are transmitted through the 3 mg/cm^3 , the 20 mg/cm^3 and the 45 mg/cm^3 foam targets. The percentage of transmitted light seems to be fairly constant with changing foam density. To fully ionise the oxygen in the target, the laser intensity needs to reach around $4 \times 10^{19} \text{ Wcm}^{-2}$. Until the intensity reaches this threshold, the plasma will not be fully ionised and the electron density will be lower than its maximum potential density. Therefore, the rising edge of the pulse is likely to see a lower density plasma and may allow a significant transmission of the laser energy before maximum ionisation is achieved. For a Gaussian pulse with a FWHM pulse length of 550 fs, around 1.5% of the energy would arrive before this intensity is reached. This is a possible explanation for the energy measured by the transmitted light diagnostics. The simulations use a fully ionised plasma and do not include ionisation effects, and are therefore unable to model this initial transmission before full ionisation.

There is a possibility that the fast electrons generated by the main pulse will outrun the leading edge of the laser. The speed of the laser pulse in the plasma is retarded, while the fast electrons are travelling close to the speed of light in a vacuum. Chen et al. [186] have previously reported that the fast electrons outrunning the laser can modify the refractive index in front of the laser pulse, causing the laser to be deviated from its original propagation direction. The simulations presented at $1.5n_c$ and $4.5n_c$ clearly show this effect. This may happen in the experiment in regions where the pre-pulse has successfully smoothed the foam to a uniform plasma density. Even if the region ahead of the laser pulse is not yet ionised, the fast electrons outrunning the laser pulse could preheat the material. Certainly, any remaining foam structure will seed filamentation.

Another possible complication to the interaction is that in the most intense regions of the main pulse, the plasma will become more ionised than off-axis as the plasma is unlikely to be fully ionised before the main pulse arrives. This will initially increase the plasma density on the laser axis. It might be thought that this would encourage the defocusing of the laser to off-axis regions of lower density plasma. However, the peak of the laser pulse should be strong enough (unless severally energy depleted) to expel a significant fraction of these electrons to form a channel

and promote self-focusing (see section 2.2.1), as seen in the simulations.

5.5.3 Transition through the critical density

In both the experiments and the simulations, a transition in the proton acceleration from underdense and overdense plasma has been observed. The activation stacks provide maximum energies and conversion efficiencies from laser energy into proton energy, both of which follow the same trend. The 3 mg/cm^3 foam gave the best ion acceleration with the highest energy protons and the highest conversion efficiency out of the foam targets. Increasing the foam density to 20 mg/cm^3 showed a marked drop in ion acceleration, with slight improvement as the foam densities were increased to 45 mg/cm^3 and 100 mg/cm^3 . The 3 mg/cm^3 foam should produce an underdense plasma, allowing the laser to propagate without reflection. Nevertheless, it is possible the ponderomotive force may pile up plasma ahead of the pulse to create a ponderomotive shock, causing an increase in the electron density, which the leading edge of the pulse would encounter.

The simulations show a trend in the maximum longitudinal electric field as a function of plasma density, which is in very good agreement with the experimental data trends. At the lowest densities, below the critical density, the largest longitudinal electric field out of all of the simulations performed were produced. There was a sudden drop in the maximum longitudinal electric field at around the critical density, as there was in the maximum proton energy and conversion efficiency measured in the experiment. The simulation longitudinal electric field and the experimental maximum proton energy and conversion efficiency all showed improvement as the plasma density was increased further above the critical density.

It might be thought that even if the laser is able to propagate some distance into the target, the increased interaction length would lead to improved electron acceleration. However, this does not seem to be the case. Instead, after the initial efficiency dip near the critical density, the electron acceleration improves at higher density, due to the number of electrons available for acceleration increasing. With larger numbers of electrons being accelerated, larger electric fields are generated at

the rear surface. If the laser propagates through to the rear side of the target, the electron current emerges from a small, concentrated region. Hence the higher density of electrons due to the laser channelling compensates for the smaller total number of accelerated electrons.

5.5.4 Proton beam structure

The wispy horizontal-vertical cross features on some of the radiochromic films at low proton energies have been observed before [28, 31, 187]. For these observations, such structures have been attributed to the movement of plasma from the front to the rear of the target [28, 31], or due to the emission from the edges of the target [187]. Zepf et al. found that the cross structure was aligned to the principle axis of square targets and the intensity was reduced with increasing target size. In the experiment presented here, the square washers supporting the foams were small (1 mm by 1 mm by 0.25 mm) and may therefore have been particularly prone to this type of phenomenon.

Structure in the proton beam can be deliberately imposed experimentally by using a target foil with shallow grooves etched onto the rear surface [21]. The micromachined grooves (200 nm deep, 3.6 μm apart) meant that when the electric field normal to the target surface was set up, local focusing electric fields were formed around the groove. Therefore the protons were accelerated in beamlets from along the groove, and regular variations in the proton beam intensity was detected. In relation to the results presented here, it is possible that the structure seen in the proton beam at high energy, could have been due to the foam surfaces having structure on a larger scale than the small threads and pores. Larger scale surface structures could have led to focusing in the accelerated proton beam. However, the same structures were not observed at all energies. This suggests that if surface structures are responsible for the features, the structures had been homogenised before the low energy ions began to accelerate. Evidence for beam structure has been seen in the $0.9n_c$ simulation and here it was not even necessary for the plasma to have a predetermined structure. The emergence of the laser filaments at the rear

surface provided variation in the ion density at the accelerating surface, leading to structure in the ion beam.

A ring structure was observed in the proton beam at lower energies for some of the foam targets. Ring structures in laser generated proton beams have previously been observed in other experiments [27, 28]. Clark et al. [27] observed the protons being emitted in rings, where the radius reduced as the proton energy increased. Their explanation was that the protons were generated from the front surface and were deflected in magnetic fields inside the target. Deflection is dependent on the proton energy, so the lowest energy protons were deflected the most. Zepf et al. [28] also found a population of protons forming a ring structure and they concluded that this supports the internal field deflection explanation. The ring feature observed in the presented experiment was only visible at lower energies and was a lot thicker than previous observations [27, 28]. Both radial electric fields and azimuthal magnetic fields exist in these experiments. The influence of radial electric fields on the rear surface would be stronger on the lower energy protons. This could be the source of the low energy, wide ring structures.

Chapter 6

Proton radiography of two beam laser-solid interactions

It has been observed in previous experiments that extremely large magnetic fields (hundreds of Megagauss) can be generated in laser plasma interactions [138–141]. The magnetic fields investigated in the experiments presented in this chapter are self-generated through the $\nabla n_e \times \nabla T_e$ mechanism (see section 2.3.4). This $\nabla n_e \times \nabla T_e$ mechanism generates a magnetic field azimuthally around the laser focal spot. The presented experiment focused two laser spots in close proximity to examine the interaction of the plasma and the magnetic fields. As described below, under certain conditions, a driven magnetic reconnection geometry was created, allowing theoretical models of this phenomenon to be tested in a laboratory situation. In particular, the interaction between the different plasma plumes and their associated magnetic fields has particular significance to holraums. Multiple laser beams are focused into a holraum to create a radiation source for high energy density experiments. The interaction between plasma and magnetic fields needs to be understood to fully benchmark multi dimensional radiation hydrodynamic codes, in particular the effect on electron transport in magnetic fields.

In the experiment presented in this chapter, two laser beams were focused to intensities of $\sim 10^{15} \text{ Wcm}^{-2}$ in close proximity (from ~ 5 to ~ 15 spot diameter separation, a spot diameter being $\sim 50\mu\text{m}$). To diagnose the interaction, optical

probing was fielded to give plasma density and dynamic information, Thomson scattering provided plasma temperature measurements, x-ray pinhole cameras provided focal spot size and proton probing of the interaction provided magnetic field measurements. The combination of observing plasma jet formation under certain conditions and increased plasma temperature in the interaction region indicates that a magnetic reconnection geometry was formed. The proton probing diagnostic, fielded by the author, will be the particular focus of this chapter, but complimentary results from the other diagnostics will also be presented to complete the experimental description and aid in forming a conclusion. Estimates for the strength and extent of the magnetic field are discussed.

6.1 Previous work on magnetic field measurements from laser plasma interactions

The first measurements of the $\nabla n_e \times \nabla T_e$ magnetic field were made by Stamper et al. [138] using a magnetic probe. The spontaneously generated magnetic fields were of the order of a kilogauss. Later, measurements of the magnetic field using Faraday rotation of an external optical beam were made [139, 188]. The Faraday rotation technique relies on the rotation of polarisation of an optical probe beam as it passes through regions with high magnetic field. The amount of rotation is proportional to the strength of the magnetic field. Stamper et al. measured magnetic fields on the order hundreds of kilogauss from polystyrene and steel targets with an irradiation of 10^{16} Wcm⁻² at 1.06 μm [189]. Also, Raven et al. measured up to megagauss fields from aluminium targets with 2×10^{16} Wcm⁻² at 1.06 μm [190]. Very few experiments looking at multiple beam geometries have been reported. Yates et al. used a CO₂ laser with a wavelength of 10.6 μm at an intensity of 5×10^{13} Wcm⁻² to investigate the effect of the magnetic field on the thermal electron transport in multiple beam geometries [191]. It was found that the energy deposition was non-uniform, due to the self-generated magnetic fields.

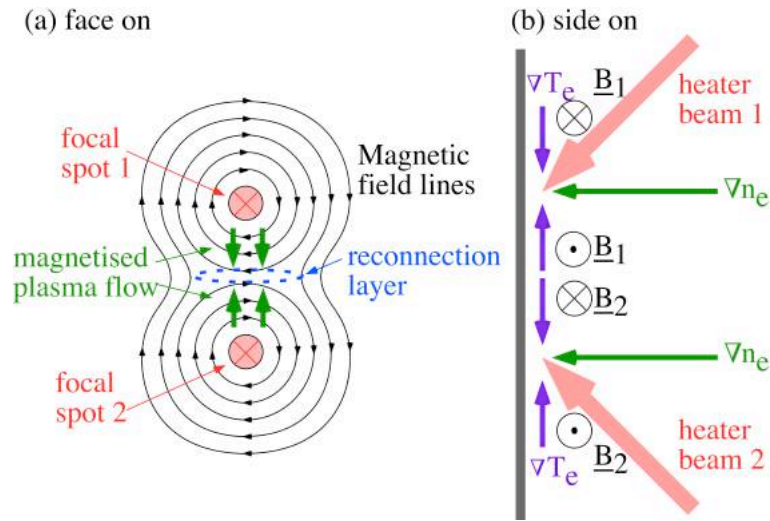


Figure 6.1: A schematic of the heater beams and their magnetic field geometry in the reconnection geometry; (a) is a face-on view and (b) is a side-on view.

6.2 Experimental method

The experiment was carried out in Vulcan's Target Area West (TAW, see section 3.1.4) in July and August of 2005. To create a geometry where a magnetic reconnection would be possible, opposing polarity magnetic fields needed to be aligned in close proximity. Figure 6.1 shows how this could be achieved using two laser heater beams.

6.2.1 Experimental layout

Important requirements for this experiment were the ability to measure simultaneously the plasma density, the magnetic field and the electron temperature and to image the x-ray emission. The beam geometry was carefully planned to enable all of the diagnostics lines of sight and a schematic is shown in figure 6.2.

The main interaction beams had pulse duration of 1 ns with up to 200 J of energy at the fundamental wavelength of $1.053 \mu\text{m}$. The beam energies were verified with full beam diameter calorimeters before the beams were directed into the chamber to account for any losses in the area. They were focused by $f/10$ lenses with focal lengths of 1m to focal spots with FWHM diameters of $50\mu\text{m}$, giving laser intensities

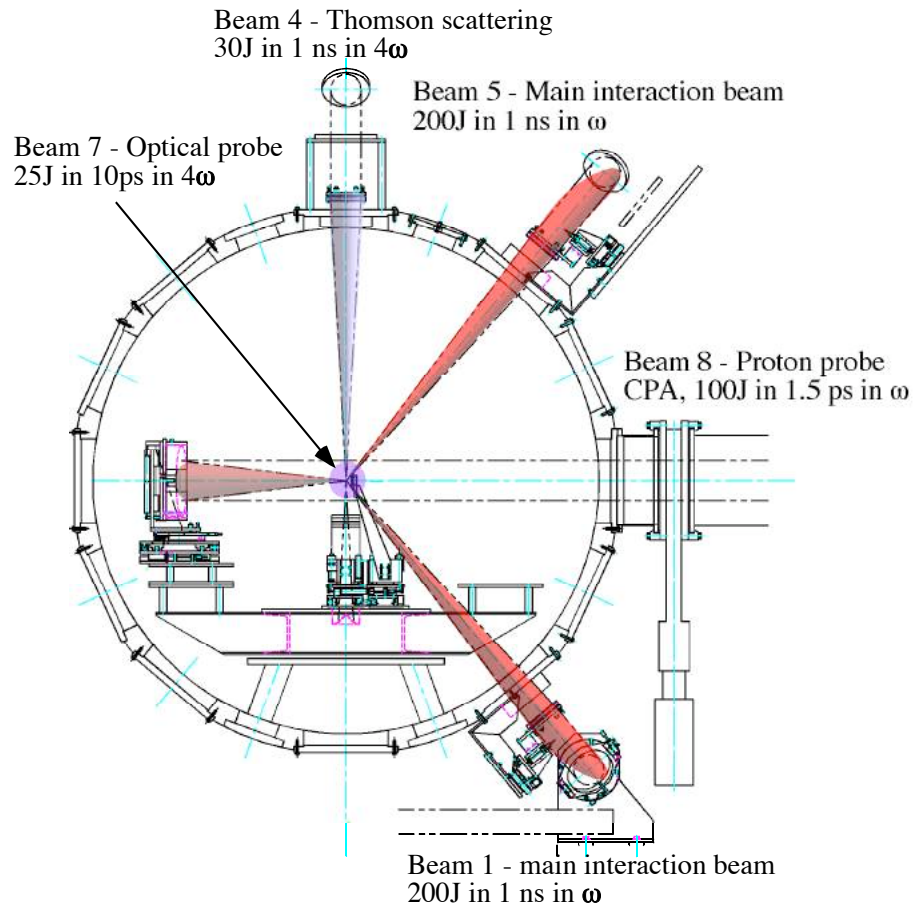


Figure 6.2: The multiple beam geometry into the chamber (modified from a CLF engineering drawing).

of $1 \times 10^{15} \text{ Wcm}^{-2}$. The separation of the two focal spots could be varied on the main target. To monitor the focal spot quality and relative positioning, a single lens was coupled to a CCD camera, which allowed the alignment of the two beams before each shot. The arrival times of the two pulses were adjusted to arrive simultaneously at the target using a streak camera, which re-imaged the interaction position. Timing slides enabled any timing corrections to be made on each individual beam line, so the interaction beams could be set to arrive simultaneously to within ± 25 ps.

The main interaction targets used were $3 \text{ mm} \times 5 \text{ mm}$ aluminium or gold foils with thicknesses of $100 \mu\text{m}$, $50 \mu\text{m}$ and $25 \mu\text{m}$. As shall be seen, the $25 \mu\text{m}$ foils were used for a large part of the experiment as it was found that the thicker targets produced a large amount of scattering in the proton beam, which blurred the proton images. The main interaction foils were made no thinner than $25 \mu\text{m}$, to prevent the main

interaction beams from breaking out of the back of the foil while the measurements were being made and thus complicating the interaction. An external alignment rig, consisting of three mutually orthogonal high magnification optical CCD cameras and monitors, referenced the target chamber centre so that the main target (and the other target components) could be accurately positioned before placement in the chamber. The targets were aligned on a kinematic base so that accurate positioning of the target chamber centre and of the external alignment system could be achieved.

6.2.2 Proton deflectometry diagnostics

The proton beam was generated using a high intensity laser interaction with a solid target through the TNSA mechanism. Proton beams generated in this way have a number of desirable qualities for a probe. The virtual source size is very small ($\sim 3 \mu\text{m}$ [46]), meaning that the resolution of the images taken with it are excellent. The virtual source was located in front of the target by $400 \pm 150 \mu\text{m}$ [48]. The beams are also well collimated with a half divergence angle of between 10° and 15° [47]. The proton beam is generated in a short time, of the order of the fast electron current duration and therefore the CPA laser pulse length. This means that the temporal resolution is on the order of a picosecond. In addition to the good spatial and temporal resolution of a proton probe beam, it is also possible to get temporal information about the probed interaction. Since different energy protons travel at different velocities, the time taken to travel from the source foil to the main interaction produces a natural delay between the highest energy protons, which arrive first, and the lower energy protons, which arrive later. The different energies can be detected separately in a film detector stack (see section 3.3.3), where because the signal is dominated by the proton Bragg peak, the signal on each layer of film will be dominantly produced by a single proton energy population close to their maximum range. This is of particular benefit when the probed interaction is of the order of picoseconds. However, for the longer (nanosecond) interactions investigated in this chapter the temporal separation of the different proton energies is small compared with the length of the probed interaction. A timing slide was used

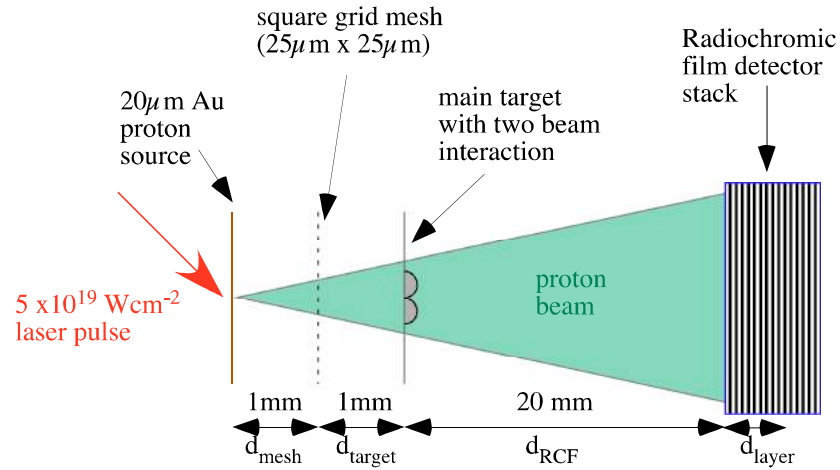


Figure 6.3: A schematic showing the rear projection geometry of the proton probing diagnostic.

to change the CPA beam arrival on the foil so that different times in the interaction being studied could be observed.

The CPA beam had a pulse duration of 1.5 ps with an energy on target of up to 100 J. Focused with a $f/3.5$ off-axis parabola to a focal spot with a FWHM diameter of $10 \mu\text{m}$ containing around 40% of the total energy, to achieve peak intensities of $5 \times 10^{19} \text{ Wcm}^{-2}$. This interacted with a $20 \mu\text{m}$ gold foil to generate the proton beam. The proton source foil was glued onto one side of a 1 mm thick washer and on the other side there was a $25 \mu\text{m} \times 25 \mu\text{m}$ mesh. The 1 mm thick washer ensured that the relative positioning of the proton source, mesh and target was easy to align. The back of the mesh was placed a further 1 mm away from the main target.

Figure 6.3 shows the geometry for the proton probing on this experiment. The protons were projected through the rear of the main target and detected on a $25 \text{ mm} \times 25 \text{ mm}$ radiochromic film stack (see section 3.3.3). Figure 6.4 shows which proton energies would be stopped in a specific layer of the film stack, as calculated by the Monte Carlo code TRIM [152] for the stack composition used in the experiment. The stack composition, from front to back, was made up of a $25 \mu\text{m}$ aluminium foil acting as a light and debris shield at the front of the stack, followed by six pieces of HD-810 type radiochromic film, then eight pieces of the more sensitive MD-55 type radiochromic film.

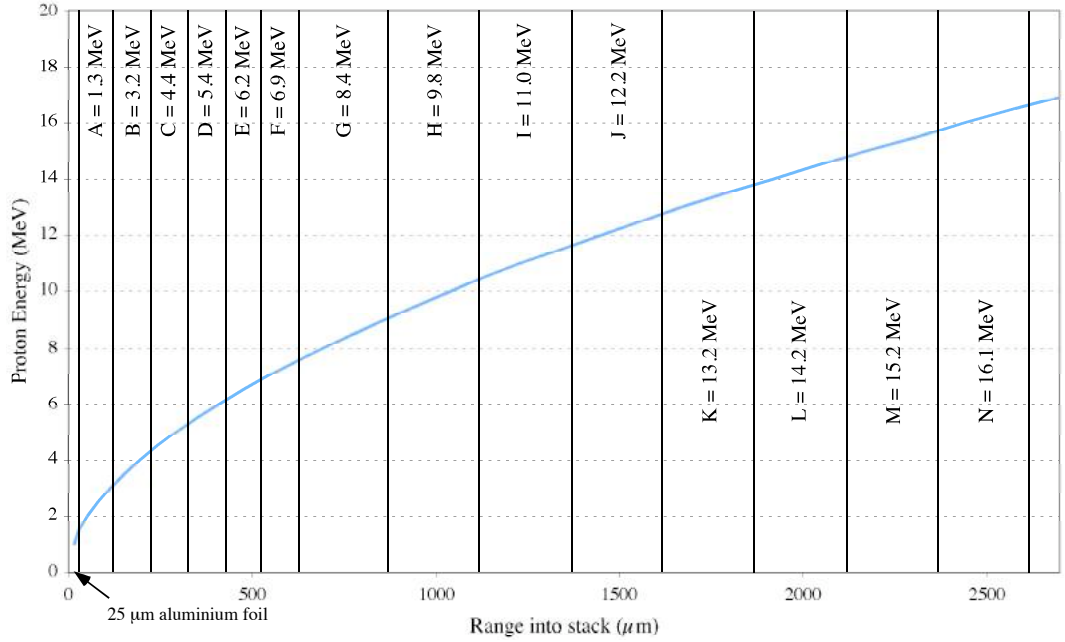


Figure 6.4: Proton stopping ranges in the proton detector stacks. Layers A to F are HD-810 type (the active layer is on the front surface) and layers G to N are MD-55 type (the active layer is sandwiched in the middle).

The magnifications of both the mesh and the main interaction are important for the analysis of the proton data. By geometric arguments and using the distances defined in figure 6.3 the magnifications are given by

$$M_{mesh} = \frac{(d_{mesh}) + (d_{target} + d_{RCF} + d_{layer})}{d_{mesh}} = \frac{22 + d_{layer}}{1} \quad (6.1)$$

and

$$M_{interaction} = \frac{(d_{mesh} + d_{target}) + (d_{RCF} + d_{layer})}{(d_{mesh} + d_{target})} = \frac{22 + d_{layer}}{2}. \quad (6.2)$$

The distance into the RCF stack, d_{layer} , is measured in mm and depends on the particular layer of the stack and therefore a particular proton energy, so care must be taken when calculating the exact magnifications. The approximate magnifications are $M_{mesh} \sim 20$ and $M_{interaction} \sim 10$.

If the protons pass through an electric or magnetic field then they are deflected from their original path and are displaced from a position relative to an unaffected proton beam. The embedding of the mesh structure onto the proton beam enables quantitative measurements about the electromagnetic field strengths to be made. The rear projection geometry was chosen for this experiment because the electric fields

(which are dominantly in the interaction target normal direction) experienced by the protons would not deflect the protons. Therefore, any deflection seen in the proton beam should be due to the effect of self generated azimuthal magnetic fields, which are expected (see section 2.3.4).

In the rear projection geometry, the protons would be deflected out of the focal spot region by an azimuthal magnetic field. If however, the protons were projected from the front of the interaction target and detected behind the main interaction, the protons would be bent into the focal spot by the azimuthal magnetic field.

For a particular detector layer, the proton energy, E_p , and the magnification are well defined. The deflection equation is essentially the same as for the magnetic field component of the Thomson ion spectrometer (see section 3.3.1) and the deflection is given by

$$d \approx \frac{qBL}{\sqrt{2m_p E_p}} \left(b - \frac{L}{2} \right), \quad (6.3)$$

where d is the deflection in the detector plane, L is the spatial extent of the magnetic field and b is the target to detector distance. It is the magnetic field, B , that needs to be determined. However, there is another variable, the spatial extent of the magnetic field, L , which is also unknown. The extent of the field may be estimated from the density gradient scale observed by the interferometry. If it is assumed that $b \gg L$, then it can be found from equation 6.3 that the product $\mathbf{B} \cdot \mathbf{L}$ is approximately

$$\mathbf{B} \cdot \mathbf{L} \simeq \sqrt{2m_p E_p} \frac{d}{qb}. \quad (6.4)$$

Therefore, if there is an uncertainty in the thickness of the magnetic field, it may be better to present the results as $\mathbf{B} \cdot \mathbf{L}$.

Figure 6.5 illustrates how the deflection at the detector plane depends on the magnetic field strength for different proton energies. Both plots were made by assuming an extent of the magnetic field of $100 \mu\text{m}$ and a target to detector distance, b , of 20 mm . Figure 6.5 (a) shows the magnetic field strength against proton energy for different detector plane deflections. Figure 6.5 (b) shows the detector plane deflections against proton energy for different magnetic field strengths.

It would be possible to confirm that the deflection was purely due to a magnetic field in a single shot if the deflection information was available for both a low energy

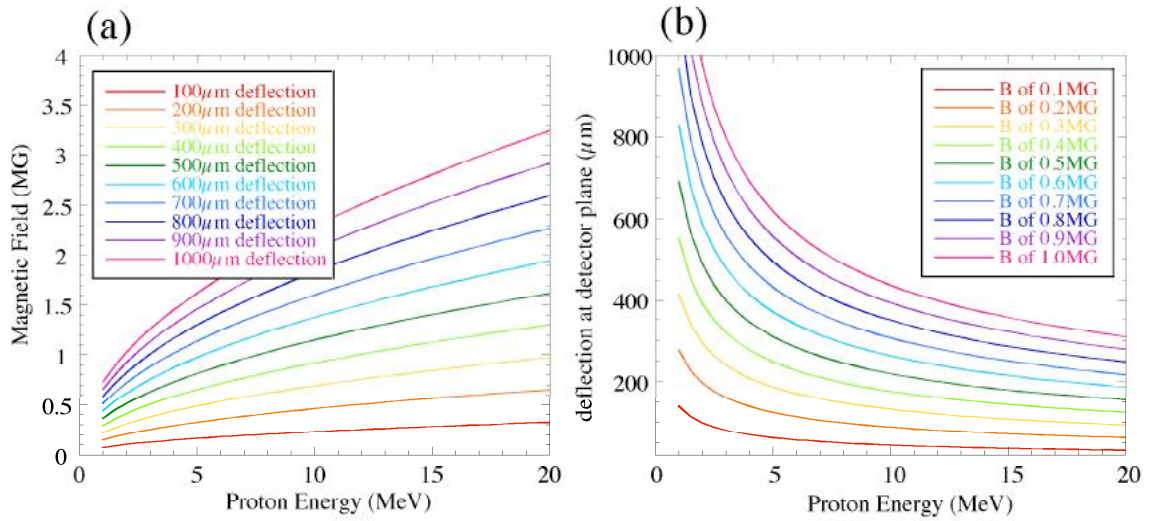


Figure 6.5: Assuming a thickness, $L = 100 \mu\text{m}$ and $b = 20 \text{ mm}$, then (a) shows magnetic field strength against proton energy for different detector plane deflections and (b) shows detector plane deflections against proton energy for different magnetic field strengths.

($E_p \lesssim 2 \text{ MeV}$) and a higher energy. This is because deflection in a magnetic field is proportional to v^{-1} , whereas the deflection in an electric field is proportional to v^{-2} . Therefore, by comparing how quickly the deflection drops off with energy, the type of field deflecting the protons could be determined.

6.2.3 Other experimental diagnostics

The other experimental diagnostics run during the experiment are briefly described below. There are further diagnostic details provided in P. M. Nilson's thesis [92]. The transverse optical probe provided information on the electron density and plasma dynamics. Thomson scattering provided electron temperature measurements at different positions in the interaction while x-ray pinhole camera imaging provided time integrated x-ray images of the two laser generated plasmas, thereby also providing information on the plasma size and heating.

Transverse optical probe

The transverse optical probe used a CPA beam line, which was compressed in air to a pulse length of $\sim 10 \text{ ps}$ before being frequency-doubled twice to a wavelength of

263 nm. By going to a shorter wavelength it is possible to probe to higher plasma densities. The beam aperture at 263 nm was limited to a 10 mm diameter and was aligned to pass parallel to the main target.

A lens after the target collected the scattered light to be relayed out of the chamber to the diagnostic channels. The final magnification used was around $13\times$. The different diagnostic channels included a modified Nomarski interferometer and a shadowgraphy channel. The detectors were 16 bit Andor cameras with a combination of reflective and bandpass ($\Delta\lambda \approx 10$ nm) interference filters to minimise the self-emission signal from the plasma.

The Nomarski interferometer was implemented to measure the plasma refractive index variations (and therefore the plasma electron density along the path length of the probe) of the interaction. For the Nomarski method, a birefringent Wollaston prism splits the imprinted probe beam into two orthogonally polarised ordinary and extraordinary beams. The two beams take separate paths and are then made to interfere using a polariser at 45° to both beams. The interference between these two beams produces fringes and in regions in which one of the beams has passed through a plasma, the fringe shifts are proportional to the plasma density. Providing the plasma can be assumed to be cylindrically symmetric, the phase shift can then be deconvolved using an Abel transform and converted into plasma electron density maps.

The shadowgraphy channel provided images which are useful for studying the plasma dynamics in the interaction. As the probe beam passed through the plasma, the beam refracted and produced intensity variations dependant upon the plasma density variations. All of the probing diagnostics were fielded by P. M. Nilson and the techniques are described in greater detail in P. M. Nilson's thesis [92].

Collective Thomson scattering

The electron temperature was measured at two positions in the interaction plasma using collective Thomson scattering. The first location was in one of the ablated plasma plumes and the second position was located between the two focal spots where the reconnection layer forms. These positions are shown in figure 6.6.

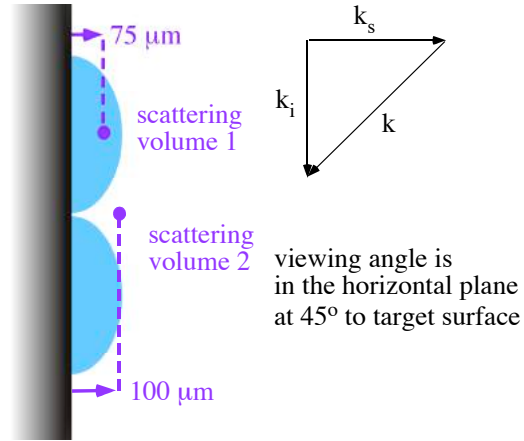


Figure 6.6: A schematic of the Thomson scattering geometry showing the positions of the scattering volumes with respect to the target surface. Shown on the right are the wave vectors for the incident light, \mathbf{k}_i , the scattered light \mathbf{k}_s and the electron plasma wave, \mathbf{k} .

The experimental probe beam was a 10 J pulse with a duration of 1 ns (the temporal profile was square). It was frequency doubled twice to a wavelength of 263 nm and focused to a $50 \mu\text{m}$ spot by an $f/10$ lens. The scattered light was collected at an angle of 90° to the incoming beam. The light was then re-imaged onto a $100 \mu\text{m}$ wide slit at the entrance to a 1 m spectrometer containing a 3600 lines per mm grating and had a wavelength resolution of about 0.05 nm. A streak camera was coupled to the output of the spectrometer to give a temporal resolution of about 100 ps.

The incident probe beam with wave vector \mathbf{k}_i and frequency ω_i was scattered from a volume with electron density fluctuations of wave vector \mathbf{k} and frequency ω . The momentum and energy must be conserved in the scattering, which provides the two conservation equations

$$\mathbf{k}_s = \mathbf{k}_i + \mathbf{k} \quad (6.5)$$

and

$$\omega_s = (\omega_i + \omega) + \mathbf{k} \cdot \mathbf{U}_i, \quad (6.6)$$

where \mathbf{k}_s and ω_s are the wave vector and frequency of the scattered light respectively. A Doppler term to account for the movement of plasma is included and the plasma flow velocity is U_i .

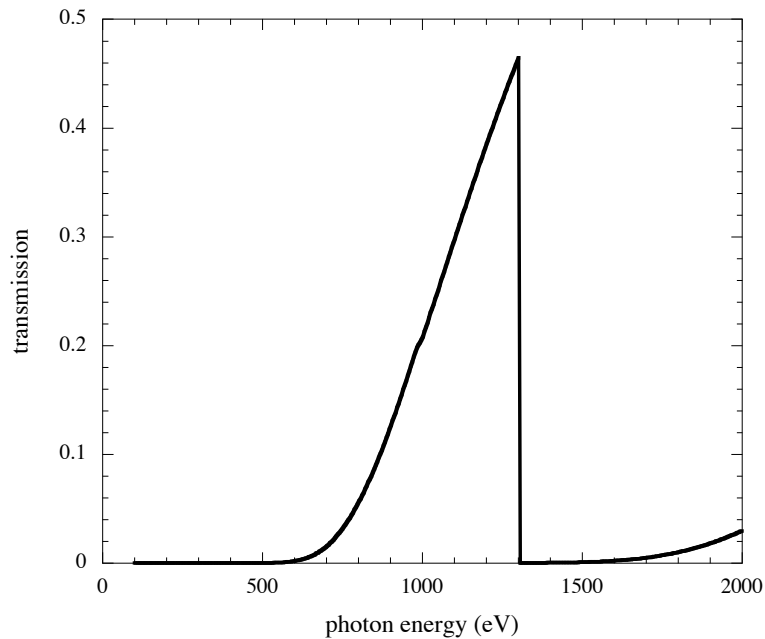


Figure 6.7: The transmission curve for a 10 μm magnesium filter up to a photon energy of 2 keV.

Collective scattering spectra were expected, that is that the light scatters from plasma waves, rather than single electrons. The Thomson scattering diagnostic was fielded by M. C. Kaluza and the experimental set up, analysis method and data is presented in more detail in P. M. Nilson's thesis [92].

X-ray pinhole imaging

The time-integrated imaged x-ray emission provided information about the focal spot size and quality as x-rays were emitted from regions of high plasma electron temperature. Two different positions were used for the x-ray pinhole camera, the first looking normal to the front of the target and the second position looked almost side on. The cameras used 25 μm pinholes with a 10 μm thick magnesium filter, which means that it was particularly sensitive to x-ray energies of around 1 keV. The transmission curve [192] for 10 μm magnesium is shown in figure 6.7. The x-rays were recorded on Kodak DEF film.

6.3 Proton probing results

To explain how the data was taken and analysed, some typical data from a single beam interaction is used to illustrate how the proton images were analysed. The layer in the stack with the clearest image was selected before the images were enhanced and processed to create the magnetic field maps. The time at which the heater beams reached the target is defined as t_0 . Figure 6.8 presents a complete RCF stack from a single focal spot shot onto an aluminium main target at a time of $t_0 + 500\text{ps}$. The approximate proton energies corresponding to the particular layer are indicated. The layers at the front of the stack (the front of the stack being layer A) stopped the low energy protons. The front layers are often burnt to the orange colour as can be seen on layer A. In places the proton beam saturated the RCF to the darkest blue and the information in these regions was lost. Because the front layers were saturated, it is not possible to use these layers to determine if the deflections were due to magnetic or electric fields. It is often the case that different parts of the interaction will show up best on different layers depending on the proton beam density for a particular shot.

The analysis method for calculating the magnetic field maps is presented here (using a layer from the shot shown in figure 6.8). For example, consider the 12.2 MeV proton layer (layer J), which shows a reasonably clear image of the interaction and mesh. Figure 6.9 demonstrates the image enhancement and magnetic field strength analysis method. Figure 6.9 (a) is the raw image of the RCF. This raw image was then bandpass filtered to enhance the features of the mesh size. The bandpass filter performs a fast Fourier transform on the raw image and uses a Gaussian filter to select structure relating to a defined range of spatial frequencies. The enhanced image is shown in figure 6.9 (b). Using the enhanced image as a template the imprinted mesh was traced (in yellow) as shown in figure 6.9 (c). In figure 6.9 (d), the regular grey mesh is a regular grid to which the trace mesh was compared, in order to calculate the deflection of the protons.

The magnetic map calculated from the layer J image is presented in figure 6.9 (e) and (f). The image has been smoothed around the data points to give an easier-to-

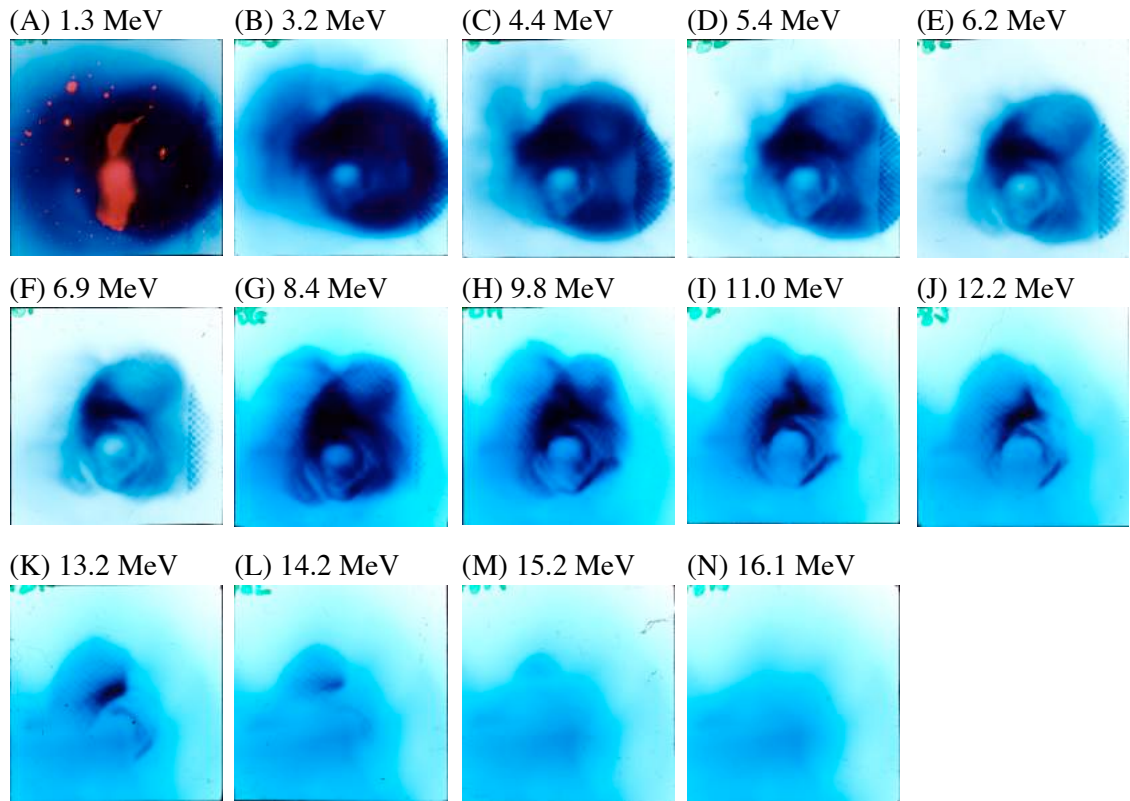


Figure 6.8: RCF pieces from a stack with proton data from a shot with the main interaction on an aluminium target at a time of $t_0 + 500\text{ps}$. The layer labels and proton energy stopped by the RCF are given.

view representation of the magnetic field. It is often not possible to get a complete picture of the magnetic field surrounding the focal spot because in some areas the protons were concentrated in a particular area by deflecting fields and saturated the film. The points at which the mesh crossings are undefinable are indicated by the green areas on the magnetic field maps, as can be seen in figure 6.9 (f). The data is presented as the product of the thickness of the magnetic field with the magnitude of the magnetic field, as explained in section 6.2.2, and is presented in units of $\mu\text{m MG}$. The thickness of the magnetic field region is estimated to have been $\sim 100 \mu\text{m}$, as seems reasonable from the interferometry data (see section 6.4.1). For the example presented in figure 6.9, the peak field measured is estimated to have been $\sim 1\text{--}3 \text{ MG}$.

First, a single spot interaction is considered at different times into the interaction. The magnetic field maps are presented and the relative strengths against radius for the different times is considered. These can be compared with other mea-

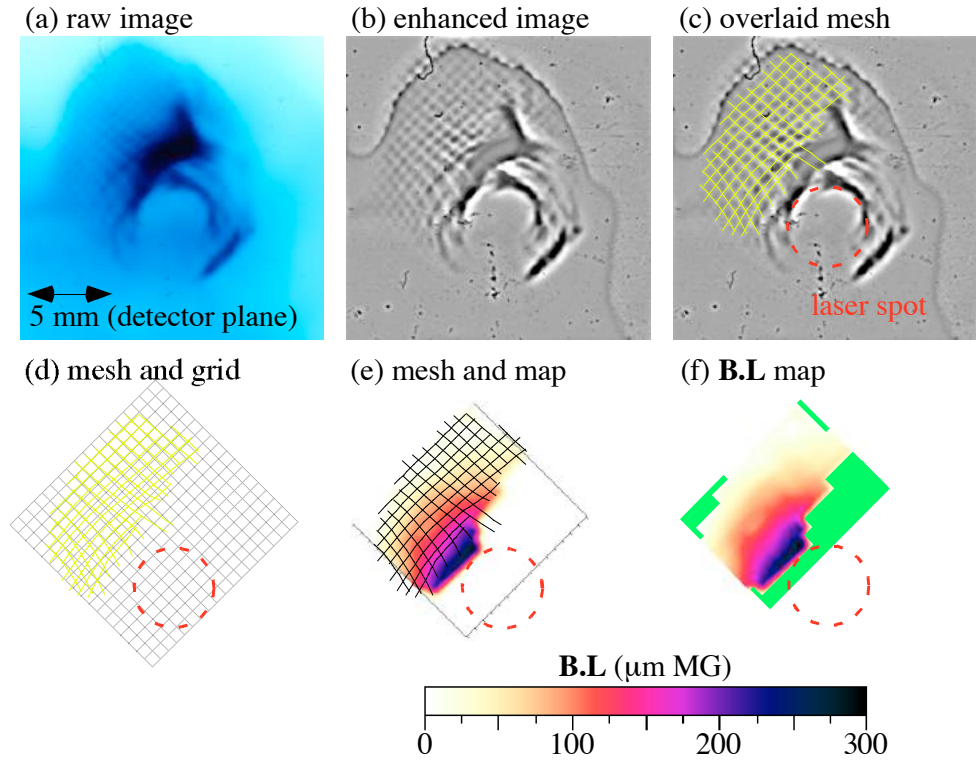


Figure 6.9: The analysis process for the layer J from figure 6.8 showing (a) the raw image, (b) a bandpass filtered image, showing the enhanced mesh structure, (c) a trace of the warped mesh pattern (yellow) over the enhanced image and the laser focal spot (red), (d) the warped mesh matched with a regular grid, (e) the magnetic field map in units of $\mu\text{m MG}$ with the overlaid grid on top and (f) the magnetic field map with the green areas indicating where no measurement could be made.

measurements made of a single focal spot interaction. Second, two beam interactions are considered and the magnetic field measurements from aluminium targets are presented. The time evolution and the effect of varying spot separation upon the two beam interaction are considered. Finally, the results of the proton radiography of the gold targets are presented.

6.3.1 A single beam interaction on aluminium targets

Figure 6.10 shows some examples of proton radiographs of single spot interactions at times after t_0 of 50 ps, 100 ps, 500 ps and 800 ps, with the raw images presented in the top row and the magnetic field maps calculated from these images shown in

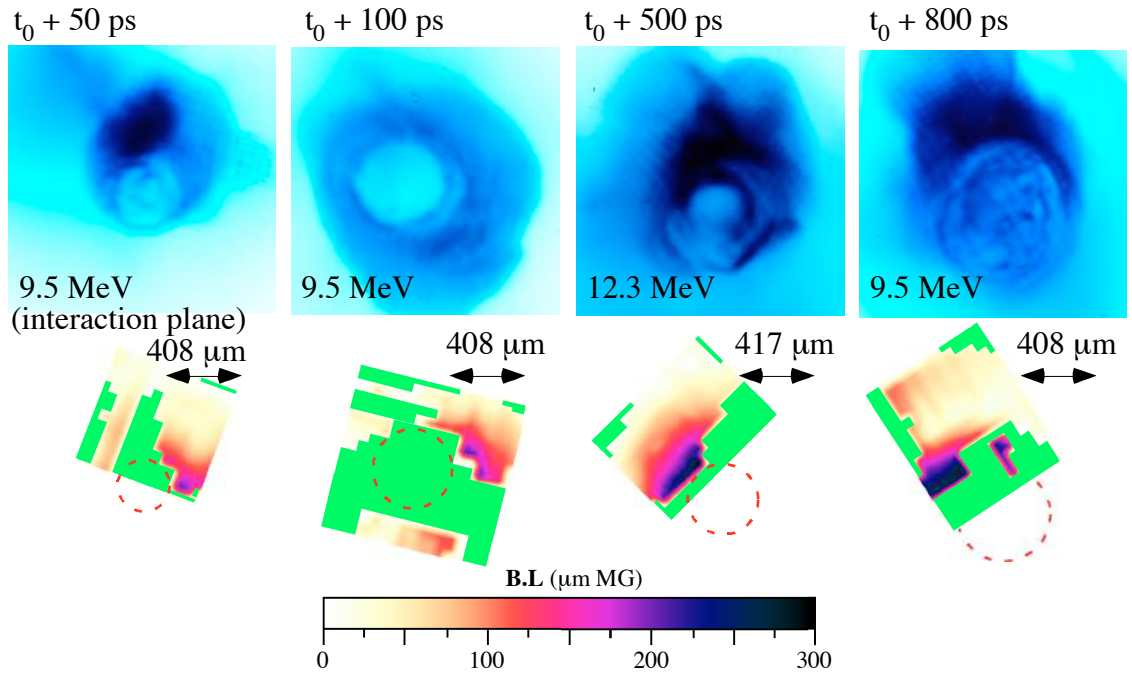


Figure 6.10: Proton radiographs of single spot interactions using the proton energy indicated on the images to look at times after t_0 of 50 ps, 100 ps, 500 ps and 800 ps. The top row shows the raw images and the bottom row shows the magnetic field maps. The green areas are regions where no measurement could be made.

the bottom row.

As seen before by Schiavi [193], the plasma spots exhibit a rose-like pattern. These perturbations cannot have been completely due to plasma density perturbations alone as the scattering in the plasma would be similar to that in the solid target. Also the plasma spot size increased with time as expected. The expansion velocity along the target surface is estimated to have been $\sim 5 \times 10^5 \text{ ms}^{-1}$. Visible in these proton radiographs is the mesh warping that occurred due to the deflection of the protons in the magnetic field.

By taking profiles along a number of angles from the centre of the focal spot of the magnetic field maps shown in figure 6.10, average $\mathbf{B} \cdot \mathbf{L}$ products at each of the different times, as a function of distance from the centre of the focal spot, could be found. The product $\mathbf{B} \cdot \mathbf{L}$ is shown as a function of radial distance for times after t_0 of 50 ps, 100 ps, 500 ps and 800 ps is presented in figure 6.11. These results exhibit deflections from the focal spot. Even at early times, these deflections were

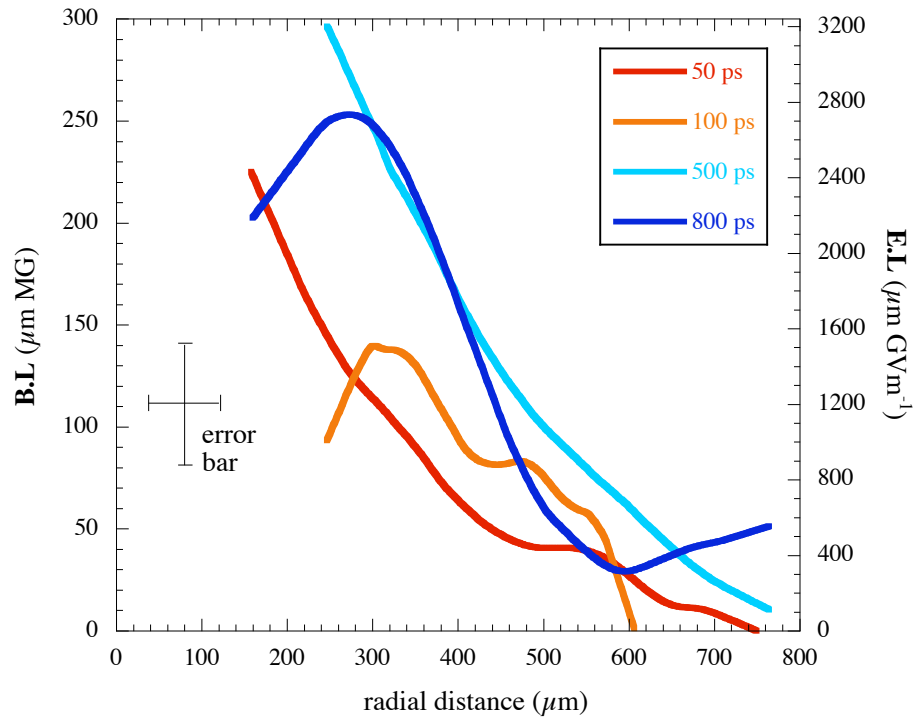


Figure 6.11: The product of the magnetic field and the spatial extent ($\mathbf{B} \cdot \mathbf{L}$) against distance from the focal spot for times after t_0 of 50 ps, 100 ps, 500 ps and 800 ps.

well outside the plume produced by the main interaction. For consideration, the electric field thickness product with the electric field strength required to produce the same deflections is shown on the right axis of figure 6.11. The origin of these deflections are discussed further in section 6.5.

6.3.2 Time dependance of the two beam interaction on aluminium targets

The CPA beam used to generate the proton beam was delayed to probe different times in the main interaction. Images taken at different times from the start of the interaction are shown in figure 6.12 for spot separations of between $350 \mu\text{m}$ and $450 \mu\text{m}$ using 9.8 MeV protons (layer H) of the RCF stack. The top row shows the raw RCF images and the bottom row shows the same images after the bandpass filtering process required to enhance the mesh structure.

The two plasma plumes are both distinct and separate for only the image taken

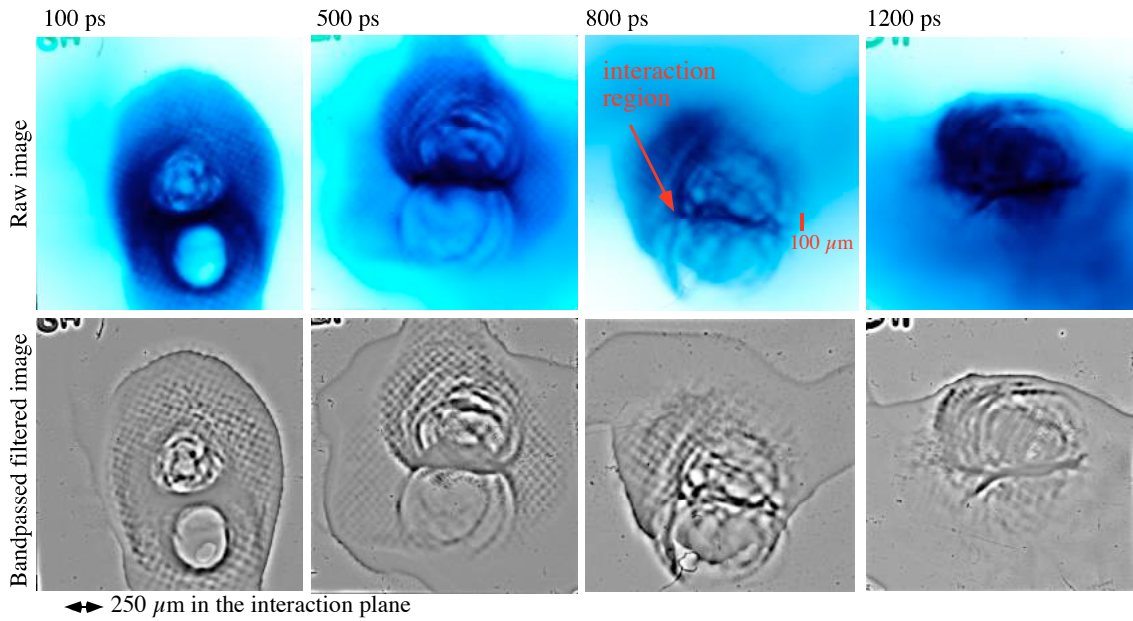


Figure 6.12: Proton radiographs of two beam interactions using 9.8 MeV protons to show interactions with focal spot separations of between $350 \mu\text{m}$ and $450 \mu\text{m}$, for times of $t_0 + 100 \text{ ps}$, $t_0 + 500 \text{ ps}$, $t_0 + 800 \text{ ps}$ and $t_0 + 1200 \text{ ps}$ as labelled. The top row of images shows the raw image of the RCF and the bottom row shows the images after the bandpass filtering to enhance the mesh structure.

at 100 ps after the start of the interaction. As the time of the proton probe was increased to 500 ps, the two plasma plumes and the associated magnetic fields started to move across the target surface and interact with one another. At even later times, the interaction layer with a width of about $100 \mu\text{m}$ developed an instability, as indicated in the figure 6.12.

6.3.3 Spot separation effects on the two beam interaction from aluminium targets

The separation between the focal spots was varied over a series of shots. Figure 6.13 shows proton radiographs using 12.2 MeV protons at $t_0 + 100 \text{ ps}$ of $750 \mu\text{m}$, $600 \mu\text{m}$, $450 \mu\text{m}$ and $250 \mu\text{m}$. The top row of images are of the raw image of the RCF and the bottom row of images are after the bandpass filtering process to enhance the mesh structure. When the two spots had a large separation between them, say $750 \mu\text{m}$,

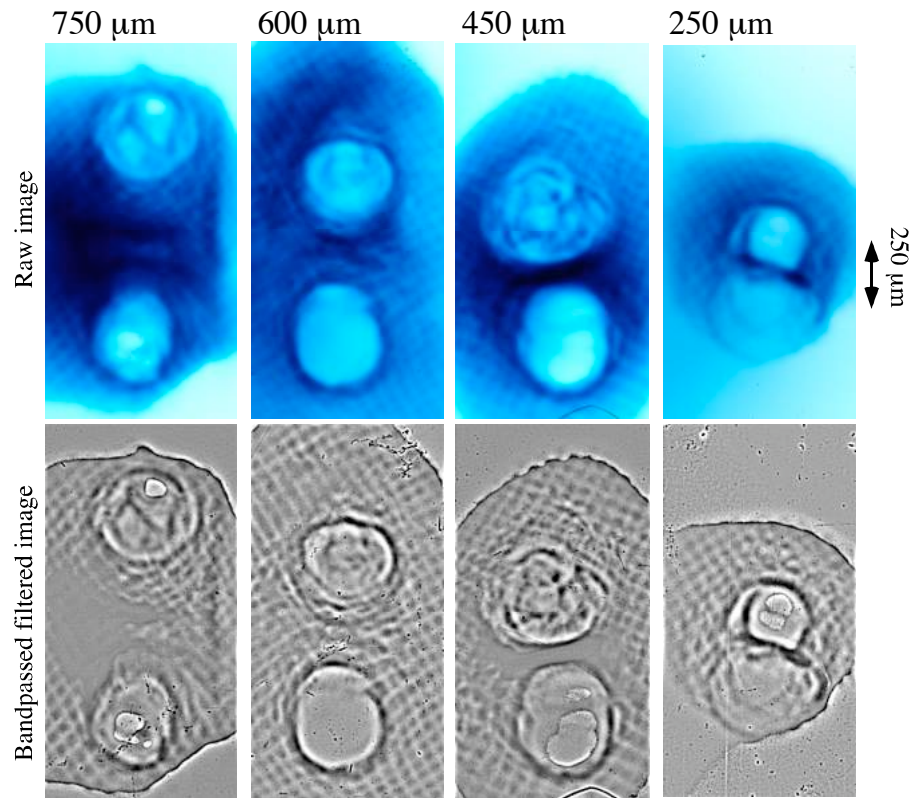


Figure 6.13: Proton radiographs of two beam interactions using 12.2 MeV protons at $t_0 + 100$ ps for various spot separations of $750 \mu\text{m}$, $600 \mu\text{m}$, $450 \mu\text{m}$ and $250 \mu\text{m}$ as shown by the labels at the top. The top row of images are of the raw image of the RCF and the bottom row of images are after the bandpass filtering process to enhance the mesh structure.

the spots were distinct and the fields were separate and not interacting, particularly at that early stage in the interaction. However, when the spots were moved closer together so that the separations were smaller, the magnetic fields started to move together in between the spots.

6.3.4 Proton probing of gold targets

The proton radiography technique was not as effective when using the as the main interaction target material compared with the aluminium targets. The scattering in the gold targets was so severe that the proton images of the interaction appeared very blurred and the mesh was indistinguishable. Therefore no magnetic field measurements could be made for the gold target interactions. Some examples of images

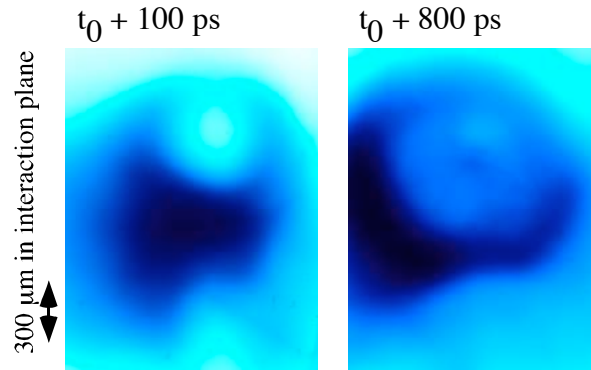


Figure 6.14: Proton radiographs of gold target interactions using 9.8 MeV protons at times after t_0 of 0.1 ns and 0.8 ns.

taken from the gold interaction targets are shown in figure 6.14.

6.4 Other experimental results

In this section the data of the other diagnostics run on the experiment are presented from the x-ray pinhole camera, the optical probe and the Thomson scattering. These results have been previously presented in greater detail in P. M. Nilson's thesis [92] and have also been published in Physical Review Letters [194]. It is important for the overall interpretation of the experimental results to also present them here.

6.4.1 Optical probe data

The optical probe produced a number of interesting observations including colliding and stagnating plasma flows, and jet formation. Different features were observed in the interaction between two laser-plasma plumes, dependant on the laser spot separation, the time after t_0 and the target material.

Spot separations considered in this experiment were $\sim 150 \mu\text{m}$ and $\sim 400 \mu\text{m}$. At the closer separation of $\sim 150 \mu\text{m}$ the plasma plumes collided and formed a quasi-homogeneous blow-off plasma as can be seen in the late time shadowgrams in figure 6.15. Figure 6.15 (a) shows an aluminium target at $t_0 + 1.5 \text{ ns}$ and figure 6.15 (b) shows a gold target at $t_0 + 2.0 \text{ ns}$. The plasma expansion at these late times indicates that the plasma expansion centered around the midplane of the interaction

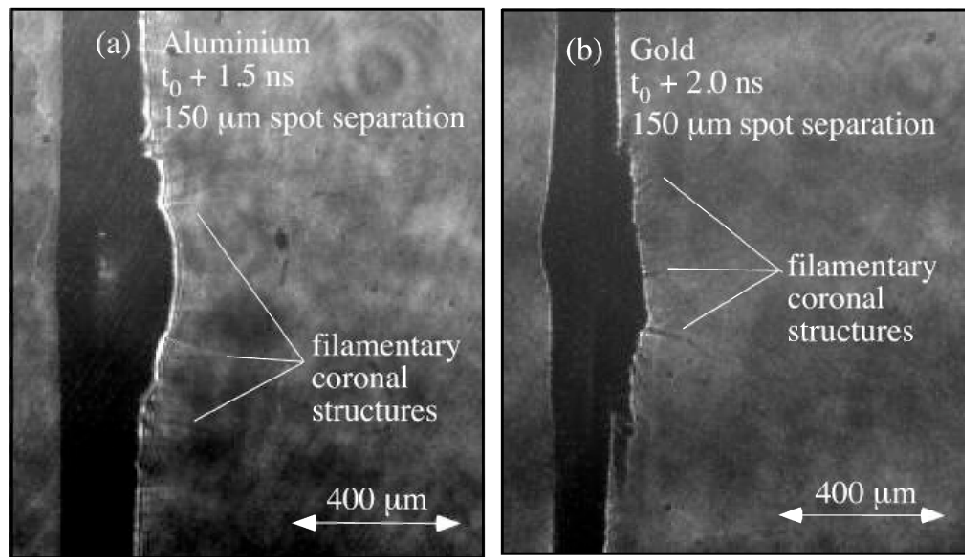


Figure 6.15: Transverse shadowgrams for spot separations of $\sim 150 \mu\text{m}$, on (a) an aluminium target at $t_0 + 1.5$ ns and (a) a gold target at $t_0 + 2.0$ ns (data is courtesy of P. M. Nilson).

was about $600 \mu\text{m}$. The electron densities calculated from interferograms taken simultaneously showed the electron plasma number density to be $(1\text{--}3) \times 10^{19} \text{cm}^{-3}$ at a distance of around $< 150 \mu\text{m}$. The expansion of the plasma perpendicular to the target surface was calculated to be of the order of 10^5ms^{-1} .

At the larger spot separation of $\sim 400 \mu\text{m}$ the interactions were more interesting; figure 6.16 shows images for this separation on an aluminium target. The plumes were far enough away to appear separate and distinct in the optical probe images and again the coronal plasma was determined to have an electron plasma number density of $(1\text{--}3) \times 10^{19} \text{cm}^{-3}$. At early times, as shown in the shadowgram (figure 6.16 (a)) and in the electron number density map of the midplane of the interaction (figure 6.16 (b)), the collision between the two plumes was observed. The plasma density in this colliding midplane at a time of $t_0 + 0.4$ ns, was $(5\text{--}6) \times 10^{19} \text{cm}^{-3}$, as seen in figure 6.16 (b). At the later time of $t_0 + 1.5$ ns (figure 6.16 (c)) the two plumes were still distinct. However, there was the additional observation of a highly directional flow originating in the midplane of the interaction. As will be shown later, this was actually created by two jets emerging at 40° to the target surface (see figure 6.17). Based on this angle and a series of shots at different times, which

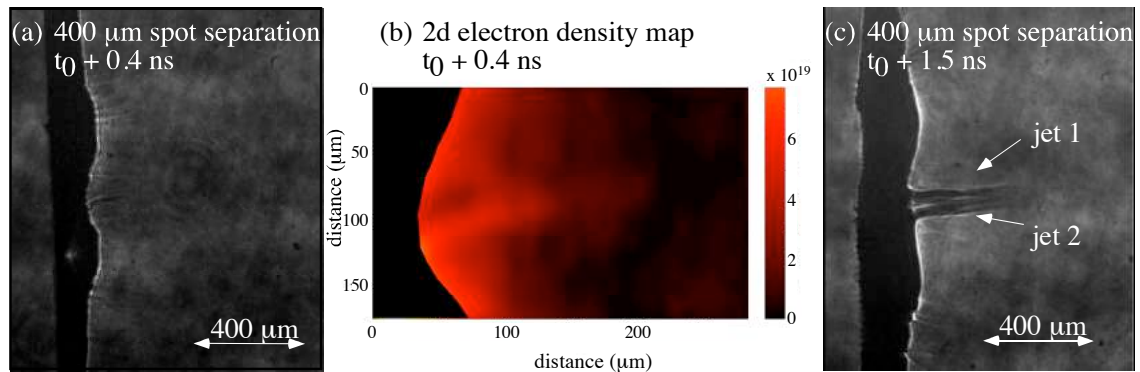


Figure 6.16: Transverse images for spot separations of $\sim 400 \mu\text{m}$ onto aluminium targets, where (a) shows a shadowgram at a time of $t_0 + 0.4 \text{ ns}$, (b) shows a deconvolved electron number density map of the midplane plasma region at a time of $t_0 + 0.4 \text{ ns}$ and (c) shows a shadowgram at a time of $t_0 + 1.5 \text{ ns}$ (data courtesy of P. M. Nilson).

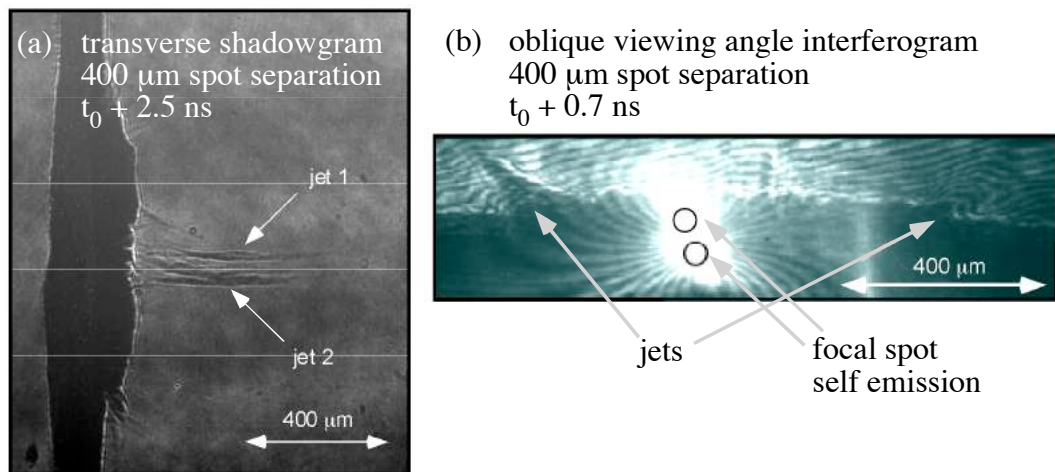


Figure 6.17: For spot separations of $\sim 400 \mu\text{m}$ onto gold targets, where (a) shows a transverse shadowgram at a time of $t_0 + 2.5 \text{ ns}$ and (b) shows an interferogram with an oblique viewing angle so that the spots are aligned at a time of $t_0 + 0.7 \text{ ns}$ (data courtesy of P. M. Nilson).

measured the expansion of the jets, it was calculated that the velocity of the tip of jets was $(8.5 \pm 2.0) \times 10^5 \text{ ms}^{-1}$. An estimate of the electron plasma number densities in the jets has been made of $1 \times 10^{20} \text{ cm}^{-3}$ in the centre and $\sim (6-7) \times 10^{20} \text{ cm}^{-3}$ in the outer region. The density fell off rapidly to vacuum in about $70 \mu\text{m}$, indicating that these plasma jets were highly collimated.

For the gold targets with spot separations of $\sim 400 \mu\text{m}$, the interactions showed similar features. In figure 6.17 (a) is a shadowgram taken at $t_0 + 2.5 \text{ ns}$ and shows the two jets again. On another shot, as shown in the interferogram of figure 6.17 (b), the spots were aligned in the other direction so that the viewing angle of the probe was at 90° to the other images. This interferogram was taken at a time of $t_0 + 0.7 \text{ ns}$ and shows that instead of a single central stagnation column, there were two jets emerging at 40° to the target surface.

6.4.2 Thomson scattering data

The two scattering volumes from which the experimental data was taken are shown in figure 6.6. All of the Thomson scattering data was taken from aluminium targets. Scattering volume 1 is $75 \mu\text{m}$ from the target surface in one of the plasma plumes. Scattering volume 2 is $100 \mu\text{m}$ from the target surface in the midplane between the two laser spots where the plasma plumes interacted with each other.

The experimental data for scattering volume 1 is presented in figure 6.18 (a). The scattering beam was timed such that the measurement was made for times from $t_0 + 1.0 \text{ ns}$ to $t_0 + 2.0 \text{ ns}$, i.e. just after the heater beams were turned off. The two ion acoustic features were observed and the decrease in the separation between the peaks indicated a decreasing electron temperature with time. This is expected and is due to hydrodynamic expansion of the plasma plume into the vacuum. By comparing a lineout of the experimental data taken for a particular time, with a theoretical fit, the electron temperature can be estimated. For scattering volume 1, the theoretical fit is from the standard collisionless theory of the dynamic form factor. Lineouts of the experimental data and theoretical fits to this data are presented in figure 6.18 (b) and (c) for times of $t_0 + 1.5 \text{ ns}$ and $t_0 + 2.25 \text{ ns}$ respectively. The theoretical

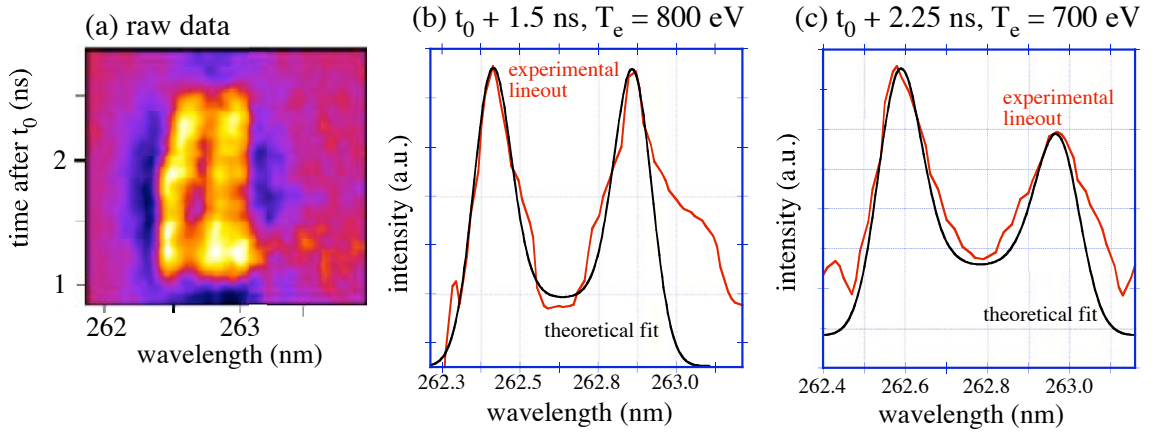


Figure 6.18: Experimental data for scattering volume 1, where (a) shows the time resolved raw data. (b) and (c) show lineouts at $t_0 + 1.5$ ns and $t_0 + 2.25$ ns respectively with the experimental data in red and the theoretical fits in black (experimental data is courtesy of M. C. Kaluza and the fit data is courtesy of W. Rozmus).

fits are consistent with electron temperatures of $T_e = 800$ eV at $t_0 + 1.5$ ns and $T_e = 700$ eV at $t_0 + 2.25$ ns with a 10–20% error expected from this analysis.

The experimental data for scattering volume 2 is presented in figure 6.19 (a). The scattering beam was timed such that the measurement was made for times from $t_0 + 0.5$ ns to $t_0 + 1.5$ ns. After $t_0 + 1.0$ ns, the ion acoustic peak separation increased significantly. Fitting the data using a Maxwellian velocity distribution function (a plasma in equilibrium) at $t_0 + 1.2$ ns gives an electron temperature, $T_e = 5.4$ keV. This fit was found to be unreasonable since electron drift velocities required to explain the asymmetry in the peaks was a few 10^6 ms^{-1} , which seemed too high. The temperature of 5.4 keV seemed unreasonably high compared to the coronal temperatures measured to be 700 – 800 eV. Instead, non-equilibrium plasma conditions were assumed to be present in this region and the theoretical fit was recalculated accordingly (full details are presented in P. M. Nilson’s thesis [92]). Good agreement was found between the experimental data and theory for a Maxwellian electron velocity distribution and a non-equilibrium ion distribution function, which gave an electron temperature $T_e = 1.7$ keV. It should be noted that this was greater than double the temperature in the expanding plume even though it was at a distance of > 100 μm from the laser heated regions. This comparison

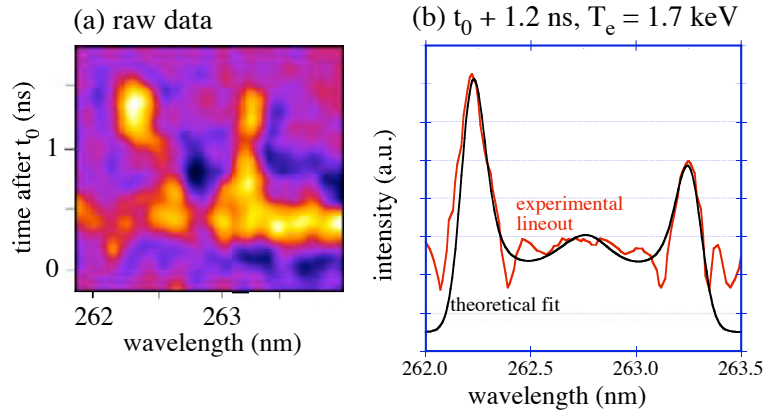


Figure 6.19: Experimental data for scattering volume 2, where (a) shows the time resolved raw data and (b) shows the experimental lineout at $t_0 + 1.2$ ns in red and the non-equilibrium theoretical fit in black (experimental data is courtesy of M. C. Kaluza and the theoretical fit is courtesy of W. Rozmus).

between the experimental data and the theoretical fit is shown in figure 6.19 (b).

6.4.3 X-ray pinhole camera data

Shown in figure 6.20 are x-ray pinhole camera images taken of two laser beam interactions with gold targets. The cameras were filtered with $10 \mu\text{m}$ of magnesium, which means that the cameras were particularly sensitive to x-rays with energy of ~ 1 keV. Figure 6.20 (a) is a side-on view to the interaction, whereas (b) is a face-on view. In both images there is a large amount of emission from each of the two plasma plumes associated with the laser spots. In the mid-plane between the two laser spots there is also significant x-ray emission. The resolution is good enough to show striations in the hot plasma that emitted the x-rays at the edge of the plasma. This data confirms the Thomson scattering, which showed a strong source of heating in the mid-plane between the laser heated regions.

6.5 Discussion

The proton probing data provides estimates for the magnetic field strength generated around a laser focal spot. The combination of the results from all of the diagnostics

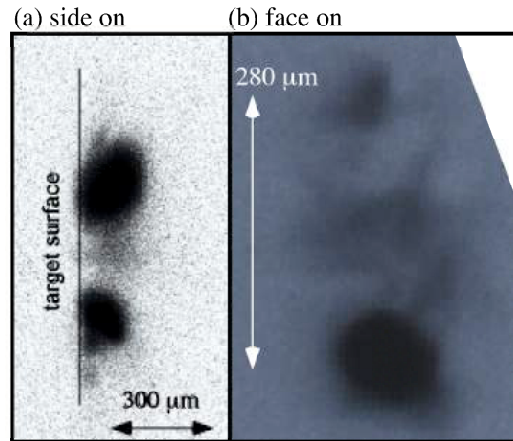


Figure 6.20: Time integrated x-ray pinhole camera images of ~ 1 keV emission from a gold target: (a) is the emission seen side-on and (b) is the emission seen face-on (data courtesy of C. Kamperidis).

provides evidence for magnetic reconnection. Both of these results are discussed in more detail below.

6.5.1 Magnetic field measurements

Here the results of a single spot interaction are compared with previous measurements made with the Vulcan laser [193], and other more recent measurements made of the magnetic field around a single laser spot using proton radiography from both the Vulcan laser [52] and the OMEGA laser [51].

The development in time of the plasma generated by a single beam interaction seen in this experiment was similar to the results presented in A. Schiavi's thesis [193]. For Schiavi's experiment, the main interaction beam was converted to 2ω , the pulse length was 600 ps and the intensity was about $8 \times 10^{14} \text{ Wcm}^{-2}$ with a focal spot of between $100 \mu\text{m}$ and $300 \mu\text{m}$. The dynamics of the single spot interactions in both experiments appear very similar. Schiavi made face-on as well as side-on proton images, which identified filamentary structures extending out perpendicular to the target surface. In the face-on proton images, the filamentary structures give the rose-like pattern. By performing ray tracing simulations, Schiavi found that the modulation in the proton beam could be attributed to the effect of radial electric field in filament structures with a strength in the region of 10^9 Vm^{-1} . An electro-thermal

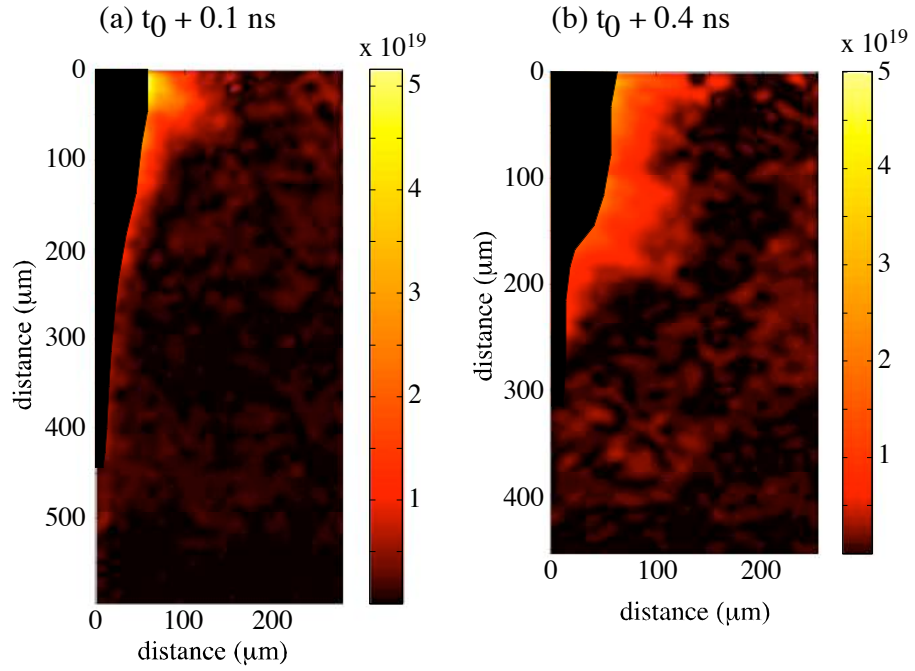


Figure 6.21: The electron density maps of plasma plumes from aluminium targets at times of $t_0 + 100$ ps and $t_0 + 400$ ps (data is courtesy of P. M. Nilson).

instability [195] is believed to have formed the density and temperature filaments; perturbations in the temperature wavefront would seed such an instability. The focal spots in both the Schiavi experiment and the one presented in this thesis would have contained hot spots so it is not surprising that the filaments were observed.

However, for the experiment presented here, there was the addition of a mesh so that the electromagnetic fields could be calculated. Unfortunately, the filamentary structures disrupt the mesh image in the central regions so the mesh is unidentifiable. However, deflections in the mesh are visible out of these disrupted regions, at radial distances of greater than $\sim 150 \mu\text{m}$. This is quite surprising, as the probe interferometry at such early times showed minimal plasma in this region. Figure 6.21 shows the electron density maps of plasma plumes from aluminium targets at times of $t_0 + 100$ ps and $t_0 + 400$ ps. Indeed, it is surprising that a focal spot with a FWHM diameter of $50 \mu\text{m}$ should have created a plasma at such radial distances. For a Gaussian focal spot, with a peak intensity of $I_0 = 2 \times 10^{15} \text{ Wcm}^{-2}$, the intensity should have fallen off to 10^{12} Wcm^{-2} , approximately the threshold for plasma generation, at a radius of $< 100 \mu\text{m}$.

Unless beam smoothing techniques are used on the incoming interaction beam, it is expected that the beam would contain hot spots from the amplification process. When this type of beam is focused down, the hot spots will be seen in the focal spot and significant amounts of energy may be outside of the FWHM diameter. As previously discussed, these hot spots can seed instabilities in the plasma.

It is also likely that a fast electron population will be generated in 10^{15} Wcm^{-2} interactions through resonance absorption (see section 2.3.1) with a temperature on the order of 10 keV. The thermal velocity for a $T_e = 10 \text{ keV}$ electron population is $v_{T_e} = 4 \times 10^7 \text{ ms}^{-1}$. Hot electrons would be able to expand along the target surface faster than normal to it, due to the reservoir of cold electrons available for the return current. There is evidence for this in both the shadowgrams and the proton probing images where the plasma expansion was seen to expand faster along the target surface than normal to the target surface. The expansion speed along the target surface estimated from the proton images is $\sim 5 \times 10^5 \text{ ms}^{-1}$, and assuming that this is the sound speed gives an estimate of the electron temperature, $T_e \sim 5 \text{ keV}$.

To understand how the magnetic field could have travelled so quickly away from the generation region, consider the following. It is possible that non-local transport would have influenced the magnetic field dynamics. The Nernst effect has been shown to dominate magnetic field advection at a rate faster than the classical frozen-in-flow rate [196]. An advection equation can describe the evolution of the magnetic field:

$$\partial_t B + \partial[(C + v_N)B] = 0, \quad (6.7)$$

where C is the plasma flow velocity, $v_N = 2\mathbf{q}_e/5n_eT_e$ is the Nernst velocity and \mathbf{q}_e is the classical Bragniskii heat flow. The frozen-in-flow description for the plasma carrying along the magnetic field, travels at C , which is usually of the order of the ion sound speed. The heat flow is carried out from the focal spot by the faster particles, those with $\sim 2-3$ times the electron thermal velocity, v_{T_e} , as these particles are far less collisional. Since v_{T_e} is much greater than c_s (for the presented experiment $v_{T_e}/c_s \sim 70$), the Nernst effect could potentially have carried the magnetic field much faster than the bulk plasma movement. It is possible that the Nernst effect

was observed in the proton probing results, especially as the interaction intensity ($I \sim 10^{15} \text{ Wcm}^{-2}$) would have produced such a hot electron population.

Another possible explanation for the observed deflections is that a global electric field may have been present. However, it can be seen from the scale on figure 6.11 that very large electric fields would have been required to explain the deflections. Therefore, it seems unlikely that electric fields were the dominant cause of the deflection, although smaller electric fields may have contributed to the overall deflection.

The results presented by Cecchetti et al. [52] were performed using the Vulcan laser ($I \sim 10^{14} \text{ Wcm}^{-2}$) and did not observe such disruptive structure in the centre of their plasma plume. Using ray tracing simulations, toroidal magnetic fields of 0.4–0.7 MG with an average radius of 150–200 μm were inferred. The shape of the magnetic fields was not presented and there is no comment on how quickly the fields decayed radially.

Recent results have been published measuring the magnetic field around a single spot of the Omega laser at the University of Rochester using proton radiography [51], where Li et al. used a plastic (CH) foil irradiated with a 10^{14} Wcm^{-2} laser at a wavelength of 0.351 μm . The focal spot sizes, which were determined by the phase plates used, were either 500 μm or 800 μm in diameter. The results of the experiment implied that the magnetic fields were of the order of ~ 0.5 MG. The experimental results were compared to the laser-generated magnetic field package in the hydro code LASNEX and the hybrid code LSP and were in overall agreement.

The main differences between the Li experiment and with the one presented in this thesis, were the target material, the focal spot size and the laser energy and wavelength. The effect of having a plastic (CH) target rather than an aluminium target is that the electron temperatures for aluminium are expected to be higher, which means that the temperature gradients are larger in an aluminium plasma. Also, the plasma blow-off for the lighter material will have been faster, decreasing the density gradient. In the Omega laser experiment, the focal spot was an order of magnitude larger than that of the results presented here. The larger focal spot would also have led to shallower gradients in temperature and density. However, the

Omega laser wavelength, $\lambda = 0.351 \mu\text{m}$, would have a larger absorption than for the presented experiments where $\lambda = 1.053 \mu\text{m}$. Better absorption of the laser energy would have led to greater density gradients. All but one of these factors suggest that the magnetic field measured in the Omega laser experiment, $B \sim 0.5 \text{ MG}$ should have been significantly lower than in the presented work.

The LASNEX simulations performed by Li et al. [51], indicate that the magnetic field was found in a thin shell around the outer surface of the expanding plasma bubble. Due to the 3-dimensional nature of the bubble, a proton projected through the outer extremities of the magnetic field will travel through a longer region of magnetic field. Furthermore, the strength of the magnetic field is greatest in this region. Therefore, the deflection of the proton projected through the edge of the plasma bubble would have been deflected the furthest. The plasma expansion in the experiment presented in this thesis, is not observed to expand in a uniform way, with the expansion along the target surface being greater than the target normal expansion, leading to a less spherical magnetic bubble shape.

6.5.2 Evidence for magnetic reconnection

Evidence from the optical probe, the proton radiography and x-ray pinhole camera all suggest that the interaction between the two plasma plumes depended strongly upon the separation distance of the focal spots. A table of plasma parameters for a fully ionised aluminium plasma, which are important for this discussion are presented in table 6.1. Parameter values were calculated for two different densities: at the critical density, $1 \times 10^{21} \text{ cm}^{-3}$, and in the coronal plasma, at a density of $5 \times 10^{19} \text{ cm}^{-3}$. The electron and ion temperatures were assumed to be equal.

Plasma stagnation

The optical probe diagnostic showed that when the laser spots were focused close together, $\sim 150 \mu\text{m}$, the plasma expanded as a quasi-homogeneous plume. The ion sound velocity for a plasma with $T_e = 800 \text{ eV}$ is $c_s = 1.9 \times 10^5 \text{ ms}^{-1}$. The expansion velocity was $M c_s$, where M is the flow mach number and was typically 1-3. This

Aluminium plasma parameters				
parameter	symbol	critical	corona	units
plasma density	n_e	1×10^{21}	5×10^{19}	cm^{-3}
electron temperature	T_e	800	800	eV
ion temperature	T_i	800	800	eV
electron plasma frequency	ω_{pe}	1.8×10^{15}	4.0×10^{14}	rads^{-1}
ion plasma frequency	ω_{pi}	2.9×10^{13}	6.5×10^{12}	rads^{-1}
Debye length	λ_D	7	33	nm
electron thermal velocity	v_{Te}	1.3×10^7		ms^{-1}
ion thermal velocity	v_{Ti}	5.3×10^4		ms^{-1}
ion sound speed	c_s	1.9×10^5		ms^{-1}
e-e energy relaxation time-scale	τ_{ee}^E	0.8	14	ps
i-i energy relaxation time-scale	τ_{ii}^E	0.3	3.0	ps
e-i energy relaxation time-scale	τ_{ei}^E	3.3	50	ns
electron collision rate	ν_e	8.4×10^{11}	5.1×10^{10}	s^{-1}
ion collision rate	ν_i	1.9×10^{12}	1.6×10^{11}	s^{-1}
magnetic field	B	—	1	MG
Alfvén velocity	v_A	—	2.1×10^5	ms^{-1}
electron Larmor frequency	ω_{ce}	—	1.8×10^{13}	rads^{-1}
ion Larmor frequency	ω_{ci}	—	4.6×10^9	rads^{-1}
electron Larmor radius	r_e	—	0.7	μm
ion Larmor radius	r_i	—	12	μm
Hall parameter	$\omega_{ce}\tau_{ei}$	< 1	> 1	

Table 6.1: Table of the plasma parameters for a typical aluminium plasma created by a single heater beam. The critical surface and coronal parameters are shown for comparison. The estimate that $Z = 13$ and that $T_i = T_e$ were made to complete this table.

agrees with the measured expansion velocity of the plasma from a laser focal spot, $\sim 10^5 \text{ ms}^{-1}$.

The energy relaxation time-scale for the electron population in the coronal aluminium plasma was about $\tau_{ee}^E \approx 14 \text{ ps}$ and between the ion population was $\tau_{ii}^E \approx 3 \text{ ps}$. Therefore, both the electron and ion populations can equilibrate to Maxwellian distributions on a time-scale far shorter than the laser pulse length, 1 ns. However, the energy relaxation time-scale between the electron and ion time-scale was $\tau_{ei}^E \approx 50 \text{ ns}$, therefore, over the duration of the heater pulses there is not sufficient time for plasma system to equilibrate through electron-ion collisions.

The plasma from each of the laser spots will expand and in the region between the two focal spots, the plasmas will collide. The conditions at the midplane will be determined by the spot separation, with higher plasma densities for smaller spot separations. Where the plasmas meet the opposing streams can be slowed down by the electric field associated with the pressure gradient and through collisions. Later in time and for larger spot separations, the electric field will be less important and the ion-ion collisions will be the dominant effect for slowing the plasmas.

The ion kinetic energy, $E_i = \frac{1}{2}m_i u_i^2 = \frac{1}{2}M^2 Z k_B T_e$, is converted into ion thermal energy density, $\frac{3}{2}n_i k_B T_i$, where the plasmas stagnate [197]. The mean free path due to classical ion-ion collisions (taking $M = 3$) has been shown to be given by [197]

$$\lambda_{ii}[\text{cm}] = \frac{0.5T_e^2}{n_i[10^{20} \text{ cm}^{-3}]Z^2}. \quad (6.8)$$

As the plasma expands from the focal spot, the plasma density reduces and therefore λ_{ii} will depend on the distance from the focal spot. Where the plasmas collide the plasma density will increase, which means that λ_{ii} will decrease and the plasma becomes more collisional. For an aluminium plasma with $T_e = 800 \text{ eV}$, $Z = 13$ and $n_i = 1 \times 10^{20} \text{ cm}^{-3}$, equation 6.8 gives $\lambda_{ii} = 20 \text{ }\mu\text{m}$. This is an approximate estimate only and the actual ion-ion mean free path at the midplane will depend heavily on the spot separation.

Reconnection layer formation

For intermediate laser focal spot separations, more interesting plasma dynamics

were observed. Two highly collimated jets were observed emanating from the region between the two laser focal spots. The Thomson scattering measured high electron temperature in the mid-plane between the focal spots. Further evidence of a heated region between the laser spots could be seen in the x-ray pinhole camera images. These showed a region of increased x-ray emission in the mid-plane between the spots. The proton probing showed that the plasma plumes were pressing against one another forming flattened sides to the plumes in the mid-plane.

The proton probing data showed that there was a large magnetic field on the periphery of the plasma plume, where the plasma density was relatively low. This introduced some additional parameters into the system. In the presence of a magnetic field the charged particles have their trajectories altered. Taking the magnetic field to be $B = 1$ MG in an aluminium plasma, the electrons have a Larmor radius of $r_e = 0.7 \mu\text{m}$ and a Larmor frequency of $\omega_{ce} = 1.8 \times 10^{13} \text{ rads}^{-1}$ and the ions have $r_i = 12 \mu\text{m}$ and $\omega_{ci} = 4.6 \times 10^9 \text{ rads}^{-1}$. If the Hall parameter, $\omega_{ce}\tau_{ei}$, is greater than 1, as it was in the coronal plasma, the plasma transport would have been affected. The plasma could have then been considered magnetised as this is the condition for frozen-in-flow.

As the spot separation was increased from the situation where the plasma stagnation was observed, the balance between the thermal pressure, $P_{th} = n_e k_B T_e$, and the magnetic pressure, $P_B = B^2/2\mu_0$ changes. The ratio of the thermal pressure to the magnetic pressure is known as the plasma beta:

$$\beta = \frac{P_{th}}{P_B} = \frac{2\mu_0 n_e k_B T_e}{B^2}. \quad (6.9)$$

When $\beta \gg 1$ the thermal pressure dominates, whereas when $\beta \ll 1$ the magnetic pressure dominates and the plasma movement is dictated by the magnetic field. In the low β case, the hydrodynamics of the plasma is strongly affected by the magnetic field topology.

For the situation where the focal spot separation was around $400 \mu\text{m}$, the mid-plane plasma density was reduced, compared to that of shots at the smaller spot separation. The plasma flows from each of the plumes carried with them the opposing magnetic fields into the collision region. As the plasma flowed from the focal

spot, the density, n_e would drop and the relative importance of the magnetic field in the plasma dynamics would increase. In essence, the plasma beta, β , would get smaller. The magnetic fields pressed up against each other as the plasma flows collide, but the frozen-in-flow condition would prevent the interpenetration of the converging plasmas. This caused the magnetic field lines to become stressed. This configuration is unstable; the presence of a small resistivity could have allowed the diffusion of the magnetic field lines in this region, leading to a rearrangement of the field lines. This is known as magnetic reconnection. This process can become unstable and once the rearrangement begins, further reconnection can occur. The rapid change in direction of the magnetic field as the reconnection occurs requires that a current sheet is formed in the interaction region.

A strong signature that reconnection had occurred in the experiment, is the observation of the two jets that propagated from the collision region. It is a prediction of standard magnetic reconnection theory that pairs of jets will be generated. The energy stored in the magnetic field will be released as the magnetic field reconnects to a lower energy state. The plasma flow into the reconnection region gains energy from the released magnetic energy as the field lines adjust to a lower energy state. The plasma flows out of the reconnection region with a higher temperature, flowing along the outgoing, reconnected magnetic field lines. The geometry of the experiment meant that there was a complicated 3-dimensional system, which affected the direction of the propagation of the jets. The jets emerged at $\sim 40^\circ$ to the target surface instead of along the target surface as would have been expected for a simpler 2-dimensional geometry. A 3-dimensional illustration of how the magnetic fields interacted, and the geometry of the jets, is shown in figure 6.22.

The jet velocity was estimated to be $v_{jet} = (8.5 \pm 2.0) \times 10^5 \text{ ms}^{-1}$. The Alfvén velocity is $v_A = 2.1 \times 10^5 \text{ ms}^{-1}$ so therefore the jet had an Alfvén mach number of $M_A \sim 4$. The speed of the out-flowing jets is consistent with their formation due to magnetic reconnection [144]. The jet formation from this type of interaction clearly shows the presence and importance of the magnetic field and that the deflection of the protons is due to a magnetic field as opposed to an electric field.

The Thomson scattering data measured an increased temperature in the inter-

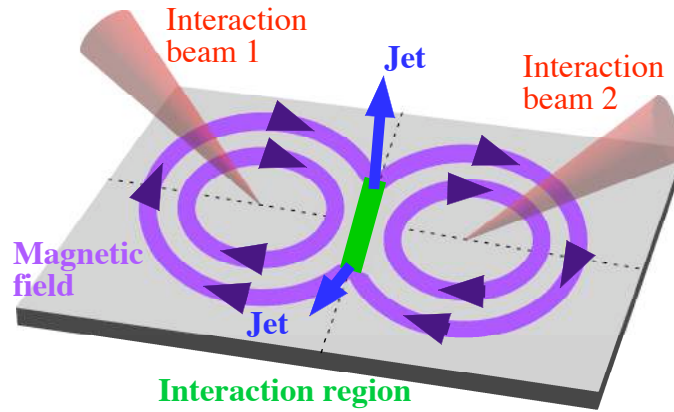


Figure 6.22: A schematic to show the 3 dimensional nature of the jet formation.

action region. In the plasma plume, the electron temperature was measured to be $T_e = 800$ eV in the corona and $T_e = 1.7$ keV in the interaction region. The x-ray image also suggests that there was a region of hotter plasma formed in the region between the two plasma plumes. This is surprising as there is no direct heating of the plasma from the laser in this region. The possible mechanisms for the heating of the plasma in the interaction region could have been stagnation heating, Ohmic heating and the conversion of magnetic energy into plasma thermal energy.

As previously discussed, stagnation heating will preferentially heat the ions. However, the energy relaxation time between the ions and the electrons is $\tau_{ei}^E = 50$ ns. Therefore, there was not enough time for the electrons to have gained the energy in this way.

The plasma expanded from the focal spot carrying out the magnetic field. Where the plasma met the plasma from the other spot, it encountered the opposing magnetic field at the midplane. The opposing magnetic fields would have resisted each other, causing the magnetic energy density to increase. The magnetic field moving through the plasma would have induced currents, thereby leading to Ohmic heating of the plasma. The time-scale over which the energy from the magnetic field is converted into thermal energy can be estimated from

$$\tau_{Ohmic} = \frac{2k_B T_e}{n_e e^2 v_D^2 \eta_{\perp}}, \quad (6.10)$$

where v_D is the $\mathbf{E} \times \mathbf{B}$ drift velocity and the Spitzer resistivity perpendicular to the magnetic field is η_{\perp} . For an aluminium plasma with $T_e = 800$ eV, $n_e = 1 \times$

10^{20} cm^{-3} , $v_D \sim 10^5 \text{ ms}^{-1}$ and $\eta_{\perp} = 6.0 \times 10^{-7} \text{ } \Omega\text{m}$ the estimate of the Ohmic heating time-scale gives $\tau_{Ohmic} = 16 \text{ ns}$. Therefore the Ohmic heating would not have caused a sufficient temperature increase in the experimental time-scale to explain the Thomson scattering measurement.

This leaves the conversion of magnetic energy into plasma energy, which could have occurred during a reconnection event. The characteristic time-scale for a magnetic field to penetrate a plasma with a scale-length of L is given by

$$\tau_R = \frac{\mu_0 L^2}{\eta}. \quad (6.11)$$

Also, the Alfvén transit time-scale across a scale-length L is given by,

$$\tau_A = \frac{L}{v_A}, \quad (6.12)$$

where v_A is the Alfvén velocity. The time-scale, as predicted by the Sweet-Parker model, is

$$\tau_{SP} = \frac{L}{v_{in}}, \quad (6.13)$$

where v_{in} is the in flowing plasma velocity and L is the hydrodynamic scale-length. Therefore, substituting for v_{in} as found from 2.76 and using $v_{out} = v_A$ yields

$$\tau_{SP} = L \sqrt{\frac{\mu_0 L}{\eta v_A}} = \sqrt{\frac{\mu_0 L^2}{\eta}} \sqrt{\frac{L}{v_A}} = \sqrt{\tau_R \tau_A}. \quad (6.14)$$

An estimate of the hydrodynamic scale-length present in the interaction region can be made from the proton probing data to be $L = 100 \text{ } \mu\text{m}$. Taking the resistivity to be $\eta = 6.0 \times 10^{-7} \text{ } \Omega\text{m}$ gives a resistive diffusion time-scale of $\tau_R = 20 \text{ ns}$. The Alfvén velocity in the coronal plasma, assuming a magnetic field of 1 MG, is about $v_A = 2 \times 10^5 \text{ ms}^{-1}$, which gives an Alfvén transit time-scale of $\tau_A = 0.5 \text{ ns}$. Therefore the Sweet-Parker reconnection rate is about $\tau_{SP} = 3 \text{ ns}$.

This estimate for the magnetic reconnection time-scale to convert magnetic energy into plasma energy is also too slow to explain the experimental measurement of T_e , but it is much closer to the observed time-scale of the heating and jet formation seen in the experiment. However, the errors of the estimate are expected to be large due to the assumptions made and the Sweet-Parker model is known to predict reconnection rates far too slow to account for events such as solar flares. It is possible that

there may have been anomalous resistivity in the reconnection layer. Anomalous resistivity is generally enhanced by turbulence in the plasma. The proton probing images showed signs of instabilities in the reconnection layer, which is certain to have increased the resistivity in the current sheets. Therefore, a reconnection event seems the most viable explanation to explain the increased electron temperature in the interaction region.

Extremely recent results, published by Li et al. [198] as an extension to their single spot measurements, present direct measurements of magnetic field topology changes due to magnetic reconnection. The conclusions about the magnetic reconnection time-scale are largely the same as in Nilson et al. [194].

Chapter 7

Summary

This thesis has presented work investigating ion beam acceleration from ultra-high intensity laser interactions with plasmas and presents the implementation of such an ion beam to measure large, transient magnetic fields. Using ultra-high intensity lasers allows highly relativistic regimes to be accessed. Each of the experimental chapters are summarised below.

7.1 Longitudinal ion acceleration from underdense plasma

In chapter 4, results are presented from an experiment and from simulations of ion acceleration from underdense plasma ($n_e \sim 10^{19} \text{ cm}^{-3}$). The experimental results have shown that it is possible to accelerate ions to high energies from underdense plasmas created by a supersonic gas jet target. The interaction of a $I_0 \approx 1.5 \times 10^{20} \text{ Wcm}^{-2}$ laser pulse with a $n_e = 4 \times 10^{19} \text{ cm}^{-3}$ electron density helium plasma was found to accelerate ions in the forward direction. In the longitudinal direction, He^{2+} ions were measured to have a maximum energy of $(40_{-8}^{+3}) \text{ MeV}$ and were well collimated in a half angle of less than 10° .

Simulations with similar parameters to the experiment indicate that a large electric field is generated at the rear plasma vacuum interface as the fast electrons travel out into the vacuum. The longitudinal electric field is found to be generated through

two mechanisms, the first being the usual space charge separation and the second being due to the time varying magnetic field generated by the fast electron current, which induces an electric field. The time-varying magnetic field influences the enhancement of the longitudinal electric field through the generation of an induced electric field, and possibly by extending the lifetime of the charge separation due to the magnetic pressure aiding the ion acceleration. In addition, an ion collimation mechanism is provided by the pinching of electrons at the exit region, generating a radial electric field acting to focus the ion beam. It was found that a longer ramp length improved the collimation of the ion beam through the focusing force on the electrons from the magnetic field, despite the maximum ion energies being lower.

The experiments and simulations presented in this thesis used laser pulse lengths on the order of $\tau \sim 500$ fs. When the next generation of ultra-short pulse petawatt class lasers become available (on the order of 10s of fs), the electric field induced by the time varying magnetic field will become more substantial and magnetic field effects will have even greater importance.

An interesting continuation of this work would be to develop and improve the gas jet target. If the gas jet can be operated at higher pressures, the maximum density would be increased and, as the simulations suggest, this should be good for the maximum ion energy achievable. Producing a sharper density ramp on the gas jet would also be advantageous.

An advantage of the gas jet over conventional solid targets is that target gas can be very pure, without the contaminants found on solid targets. Using a pure hydrogen gas as a target would enable the production of a pure proton beam without any other ion species contaminating the beam. On the other hand, theoretical work has suggested that varying the relative percentage of protons to heavier ions could modify the accelerating electric field structure, leading to modulations in the proton spectra [37]. A gas jet target could offer a simple way to perform these experiments, as the ratio of hydrogen to a heavier gas could be easily controlled. Also, a gas jet target may be advantageous for high repetition rate systems.

7.2 Longitudinal ion acceleration from near-critical density plasma

In chapter 5, low density foam targets were used for near critical density experiments and a comparison was drawn between the proton acceleration from the foam targets and that of a more conventional thin solid mylar (overdense) target. Plasma densities of between $0.9n_c$ and $30n_c$ were created from the low density foam targets.

Below the critical density of the laser, the proton acceleration measured from the experiment achieved similar spectra and maximum proton energies, as seen from the solid target. The divergence of the proton beam was marginally reduced for the low density foams, compared with the solid target. The measurements of the transmitted light was less conclusive. However, burn paper observations suggest that a low percentage of the laser energy was transmitted in the foam target shots.

Simulations showed the trend in the maximum electric field for the different near critical density runs followed a similar pattern to that of the experiments. At densities below the critical density, the maximum electric field was large. On increasing the density, through and above the critical density, decreases in the maximum electric field were observed. However, for further increases in density above n_c , the maximum electric field also increased. It is concluded that this is related to the laser propagation through the plasma. The further the propagation into the target, the larger the electron acceleration volume and the bigger the electric field at the rear surface was. When the density was increased so that the laser was unable to propagate, the smaller acceleration volume resulted in a dramatic decrease in electron acceleration. Further increases in density did not change the interaction volume, but it does mean that there were more electrons within the volume to be accelerated, therefore increasing the ion acceleration efficiency.

There are a number of future directions for this work. Laser propagation in these near critical density plasmas appears to be important for both the electron and ion acceleration. It could also have important implications in the hole boring fast ignitor scheme, since at these densities it is easier to study electron beam transport at densities comparable to the ambient density. Better monitoring of the laser energy

transmitted through the foam targets could lead to better understanding of the interaction. Optical imaging of the rear surface exit mode would indicate the extent of filamentation of the laser.

The foam targets would be interesting for the study of shock acceleration of ions. Since the plasma density is lower than a solid target, the shock speed will be faster, therefore the maximum possible energy accelerated from the shock should be higher than for a solid target.

The foams used were the lowest density possible for this manufacturing technique. Therefore, one way to investigate densities even further below the critical density, using this type of foam, would be to shorten the wavelength and thus increase the critical density. This could be done either by frequency doubling a 1 μm laser pulse (difficult for the Vulcan Petawatt system) or by using a Titanium Sapphire system operating at 800 nm, such as the Astra Gemini laser system [199].

7.3 Proton radiography of a two-beam laser interaction

In chapter 6, proton probing results of single and two laser focal spot produced plasmas were presented. Around a laser focal spot, a self generated azimuthal magnetic field was produced from the perpendicular density and temperature gradients. By positioning two long pulse (1 ns) laser focal spots in close proximity to one another, the region between the two spots had opposing magnetic field lines, setting up a magnetic reconnection geometry. Proton deflectometry was used to measure the electromagnetic fields associated with the laser plasma interaction.

The magnetic fields around a single spot have been investigated. At the intensities investigated ($I \sim 10^{15} \text{ Wcm}^{-2}$), fast electron production is thought to have affected the dynamics of the magnetic field. The Nernst effect may be responsible for carrying the magnetic field away from the generation region quicker than expected by the bulk plasma motion.

Signatures of magnetic reconnection were observed between two laser focal spots

using a number of experimental diagnostics. The proton probing showed that the plasma plumes remained discrete as they pushed up against each other in the interaction region. The optical probe observed a pair of high velocity jets emanating from the interaction region. Electron temperatures measured by Thomson scattering indicated that the plasma in the interaction region had been heated. On the observation timescale, the conversion of magnetic energy into plasma energy through reconnection was the most viable heating mechanism.

It would be interesting to repeat both the single beam and two beam parts of the experiment. Using beam smoothing techniques, namely phase zone plates (PZP) [200], the interaction should be less prone to filamentation instabilities, giving a cleaner, clearer interaction to proton probe. This may allow the mesh to be traced through the centre of the focal spot, giving a more complete description of the magnetic fields in the interaction. It should be possible, by reducing the intensity (lower energy or a larger focal spot), to prevent the production of hot electrons, which adds complexity to the interaction. Changes observed in the magnetic field dynamics around a single laser spot as the intensity is increased, could lead to a direct measurement of the Nernst effect. As the hot electron production is increased, the influence of the Nernst effect should also increase and carry the magnetic field out of the interaction region more quickly.

It would be useful to perform optical probe Faraday rotation measurements to confirm the proton probing results. Faraday rotation occurs when the polarisation of the optical probe rotates according to the magnetic field that it passes through. Taking these measurements of a single spot would provide the shape and strength of the magnetic field across the target surface direction to compliment the proton data. This would also remove any ambiguity as to whether the proton deflections are due to magnetic or electric fields.

Scattering of the protons within the target, which leads to blurred images and loss of resolution, could be reduced by using thinner targets. This would be particularly important for the gold interaction, where the scattering was worst. Care should be taken, however, that the interaction laser breaking through to the rear of the foil does not significantly affect the plasma dynamics on the front side, if the results are

to be considered useful for holraum physics.

To explore the magnetic reconnection between the two laser focal spots further, it would be useful to make more detailed studies with the diagnostics. More extensive mapping of the electron temperature through the Thomson scattering measurements would be helpful for estimating the reconnection timescale more accurately. Optical and proton probing, in directions both parallel and perpendicular to the reconnection layer, would provide more detailed information about the jet propagation angle as well as about the electric fields associated with the jets.

Appendix A

Equation of motion for a single electron in a laser field

A simple equation of motion can be written for a single electron in an electromagnetic wave, $E(\mathbf{r}, t), B(\mathbf{r}, t) \propto \exp[i(\mathbf{k} \cdot \mathbf{r} - \omega_L t)]$ using the Lorentz force:

$$\frac{d\mathbf{p}}{dt} = -e(\mathbf{E} + \mathbf{v} \times \mathbf{B}), \quad (\text{A.1})$$

where \mathbf{v} and $\mathbf{p} = \gamma m_e \mathbf{v}$ are the electron quiver velocity and quiver momentum respectively and $\gamma = (1 - v^2/c^2)^{-\frac{1}{2}} = (1 + p^2/m_e c^2)^{\frac{1}{2}}$ is the relativistic Lorentz factor. The $\mathbf{v} \times \mathbf{B}$ force due to the laser field only becomes significant when the momentum of the electron, \mathbf{p} , becomes comparable to the rest mass of an electron because $|\mathbf{E}| = c|\mathbf{B}|$.

For high intensity, $a_0 \gtrsim 1$, the equation of motion (equation A.1) can be solved analytically to find the electron trajectories in a linearly polarised, plane, electromagnetic wave [78]. Assuming that the electric and magnetic fields of the laser are in the same geometry as described as in section 2.1.1, then \mathbf{E} and \mathbf{B} can be written in terms of the vector potential, \mathbf{A} ,

$$\mathbf{E} = -\nabla\phi - \frac{\partial\mathbf{A}}{\partial t}, \quad (\text{A.2})$$

$$\mathbf{B} = \nabla \times \mathbf{A}, \quad (\text{A.3})$$

where ϕ is the electrostatic potential. Substituting these into the equation of motion

and also using the vector identity, $\mathbf{v} \times (\nabla \times \mathbf{A}) = (\nabla \mathbf{A}) \cdot \mathbf{v} - (\mathbf{v} \cdot \nabla) \mathbf{A}$, gives

$$\frac{d\mathbf{p}}{dt} = -e \left[-\nabla\phi - \frac{\partial \mathbf{A}}{\partial t} + (\nabla \mathbf{A}) \cdot \mathbf{v} - (\mathbf{v} \cdot \nabla) \mathbf{A} \right]. \quad (\text{A.4})$$

Using the convective derivative, $\frac{d}{dt} = \frac{\partial}{\partial t} + (\mathbf{v} \cdot \nabla)$ equation A.4 can be written as

$$\frac{d\mathbf{p}}{dt} = -e \left[-\nabla\phi - \frac{d\mathbf{A}}{dt} + (\nabla \mathbf{A}) \cdot \mathbf{v} \right]. \quad (\text{A.5})$$

For the single electron case, $\nabla\phi = 0$, and $\mathbf{p} = \gamma m_e \mathbf{v}$ so equation A.5 becomes

$$\frac{d}{dt} (\mathbf{p} - e\mathbf{A}) = -e(\nabla \mathbf{A}) \cdot \left(\frac{\mathbf{p}}{\gamma m_e} \right). \quad (\text{A.6})$$

Knowing that $\mathbf{A} = A\hat{\mathbf{x}}$ (i.e. a plane wave so $\partial \mathbf{A} / \partial x = 0$) and considering the $\hat{\mathbf{x}}$ component of equation A.6 gives the conservation of canonical momentum,

$$\frac{d}{dt} (p_x - eA) = 0. \quad (\text{A.7})$$

Considering an electron which starts at rest at $t = 0$ means that

$$\frac{p_x}{m_e c} = a, \quad (\text{A.8})$$

where a is the normalised vector potential (see equation 2.4). Taking the $\hat{\mathbf{z}}$ component of equation A.6 gives

$$c \frac{dp_z}{dt} = -e c v_x \frac{\partial A_x}{\partial z}. \quad (\text{A.9})$$

By substituting the p_x from equation A.8 into the relativistic energy-momentum equation, $p^2 = p_x^2 + p_z^2 = (\gamma^2 - 1)m_e^2 c^2$, provides the expression for the longitudinal momentum, p_z :

$$\frac{p_z^2}{m_e^2 c^2} = \gamma^2 - 1 - a^2. \quad (\text{A.10})$$

The energy equation can be derived using the equation of motion (equation A.1) and $p^2 = m_e^2 c^2 (\gamma^2 - 1)$:

$$\frac{d(\gamma m_e c^2)}{dt} = -e \mathbf{v} \cdot \mathbf{E}. \quad (\text{A.11})$$

Considering the $\hat{\mathbf{z}}$ component of the energy equation gives

$$m_e c^2 \frac{d\gamma}{dt} = -e v_x \frac{\partial A_x}{\partial t}. \quad (\text{A.12})$$

By subtracting equation A.12 from equation A.9 gives

$$c \frac{dp_z}{dt} - m_e c^2 \frac{d\gamma}{dt} = -ev_x \left(c \frac{\partial A_x}{\partial z} - \frac{\partial A_x}{\partial t} \right). \quad (\text{A.13})$$

It can be shown that the right hand side of this equation is 0 for a wave with $A_x = A_{x0} \exp(\omega t - kx)$. Therefore, integrating equation A.13 means that

$$\gamma = \frac{p_z}{m_e c} + 1. \quad (\text{A.14})$$

So now by eliminating γ from equations A.10 and A.14 yields

$$\frac{p_z}{m_e c} = \frac{a^2}{2}. \quad (\text{A.15})$$

Using the x and z momentum components gives an expression for γ in terms of a :

$$\gamma = \frac{a^2}{2} + 1. \quad (\text{A.16})$$

From these momentum relations the x and z components of the electron trajectory can be found. The momentum relations can be rewritten:

$$\gamma \frac{dx}{dt} = ca, \quad (\text{A.17})$$

$$\gamma \frac{dz}{dt} = \frac{ca^2}{2}. \quad (\text{A.18})$$

Begin by changing to $\tau = t - z(t)/c$, which is the wave frame since $a = a(t - z/c)$.

This means that

$$\gamma \frac{d}{dt} = \gamma \frac{d\tau}{dt} \frac{d}{d\tau} = \gamma \left(1 - \frac{1}{c} \frac{dz}{dt} \right) \frac{d}{d\tau} = \left(1 + \frac{a^2}{2} - \frac{a^2}{2} \right) \frac{d}{d\tau} = \frac{d}{d\tau} \quad (\text{A.19})$$

and equations A.17 and A.18 are now

$$\frac{dx}{d\tau} = ca, \quad (\text{A.20})$$

$$\frac{dz}{d\tau} = \frac{ca^2}{2}. \quad (\text{A.21})$$

These equations can then be integrated by assuming that the laser is described by $\mathbf{a} = a_0 \cos(\omega_L \tau) \hat{\mathbf{x}}$ to find the equations describing the electron trajectory:

$$x(\tau) = \frac{ca_0}{\omega_L} \sin(\omega_L \tau), \quad (\text{A.22})$$

$$z(\tau) = \frac{ca_0^2}{4} \left(\tau + \frac{1}{2\omega_L} \sin(2\omega_L \tau) \right). \quad (\text{A.23})$$

Appendix B

Inverse bremsstrahlung absorption

Using the equation of motion for an electron in an oscillating electric field and adding a damping term proportional to the electron-ion collision frequency, ν_{ei} , allows the dispersion relation for inverse bremsstrahlung absorption of the laser field to be derived:

$$m_e \frac{d\mathbf{v}}{dt} + m_e \nu_{ei} \mathbf{v} = -e\mathbf{E}, \quad (\text{B.1})$$

where

$$\nu_{ei} \propto \frac{n_e Z_i}{T_e^{3/2}} \quad [\text{s}^{-1}]. \quad (\text{B.2})$$

The case where $[\mathbf{E}(\mathbf{r}, t), \mathbf{B}(\mathbf{r}, t), \mathbf{v}(\mathbf{r}, t)] \propto e^{i(\mathbf{k}\cdot\mathbf{r} - \omega_L t)}$ and ω_L is the laser frequency, gives the following from equation B.1 and Maxwell's equations:

$$\mathbf{v} = \frac{e\mathbf{E}}{m_e(i\omega_L - \nu_{ei})}, \quad (\text{B.3})$$

$$\mathbf{k} \times \mathbf{E} = \omega_L \mathbf{B}, \quad (\text{B.4})$$

and

$$\mathbf{k} \times \mathbf{B} = i\mu_0 n_e e \mathbf{v} - \frac{\omega_L}{c^2} \mathbf{E}. \quad (\text{B.5})$$

Taking $\mathbf{k} \times$ of equation B.4 and substituting it in B.3 and B.5 gives

$$(\mathbf{k}\cdot\mathbf{E})\mathbf{k} - \left(k^2 + \frac{\omega_L}{c^2(\omega_L + i\nu_{ei})} \frac{n_e e^2}{\epsilon_0 m_e} - \frac{\omega_L}{c^2} \right) \mathbf{E} = 0. \quad (\text{B.6})$$

Since $\omega_p^2 = n_e e^2 / \epsilon_0 m_e$ and because \mathbf{k} and \mathbf{E} are perpendicular in the laser field so that $(\mathbf{k}\cdot\mathbf{E}) = 0$, the dispersion relation for inverse bremsstrahlung absorption is

found:

$$c^2 k^2 = \omega_L^2 - \frac{\omega_L}{\omega_L + i\nu_{ei}} \omega_p^2. \quad (\text{B.7})$$

In the coronal plasma where the inverse bremsstrahlung absorption is taking place, $\nu_{ei} \ll \omega_L$ so the dispersion relation can be approximated to the following:

$$\left(\frac{kc}{\omega_L} \right)^2 = 1 - \frac{\omega_p^2}{\omega_L^2} + i\nu_{ei} \frac{\omega_p^2}{\omega_L^3}. \quad (\text{B.8})$$

Appendix C

Target normal sheath acceleration

An analytic estimate of the initial electric field at the beginning of the acceleration process is presented by Wilks [129] and is based on earlier papers describing hot electrons driving plasma expansion into a vacuum [130–134]. A 1D model describing the evolution of the electric field as the electrons expand into the vacuum is presented by Mora [18]. This leads to an estimate for the maximum ion energies, which has been shown to be able to accurately predict rear side acceleration. Following Mora’s model to find an estimate for the initial electric field, it is assumed that the ions are cold and initially at rest with a step like density distribution, so that $n_i = n_{i0}$ for $x < 0$ and $n_i = 0$ for $x > 0$. Then the electrons are described as having a Boltzmann distribution characterised by the temperature, T_e :

$$n_e(x) = n_{e0} \exp\left(\frac{e\Phi_e(x)}{k_B T_e}\right), \quad (\text{C.1})$$

where $\Phi_e(x)$ is the electrostatic potential. Poisson’s equation provides a link between the electron and ion densities by using the charge distribution $\rho(x)$:

$$\frac{\partial^2 \Phi_e(x)}{\partial x^2} = -\frac{\rho(x)}{\epsilon_0} = \frac{e(n_e - Zn_i)}{\epsilon_0}. \quad (\text{C.2})$$

For $x \leq 0$ it is assumed that $Zn_i = n_{e0}$ so that Poisson’s equation is,

$$\frac{\partial^2 \Phi_e(x)}{\partial x^2} = \frac{en_{e0}}{\epsilon_0} \left[\exp\left(\frac{e\Phi_e(x)}{k_B T_e}\right) - 1 \right], \quad (\text{C.3})$$

which implies charge neutrality for $x \rightarrow \infty$. For $x > 0$, Poisson’s equation is,

$$\frac{\partial^2 \Phi_e(x)}{\partial x^2} = \frac{en_{e0}}{\epsilon_0} \exp\left(\frac{e\Phi_e(x)}{k_B T_e}\right). \quad (\text{C.4})$$

An expression for the initial electric field, $E_{front,0}$, at $t = 0$ and $x = 0$ can be obtained by integrating equation C.4 from $x = 0$ to $x = \infty$:

$$E_{front,0} = \sqrt{\frac{2}{e_E}} \cdot \frac{k_B T_e}{e \lambda_D} = \sqrt{\frac{2}{e_E}} E_0, \quad (\text{C.5})$$

where e_E denotes the numerical constant $2.71828\dots$ and $E_0 = \sqrt{k_B T_e n_{e0}/\epsilon_0}$. Note that the electric field strength depends only on the electron temperature and density.

Starting from these initial conditions, the ion distribution expands into the vacuum and the acceleration can continue for as long as the electron temperature remains high. This in practical terms is related to the laser pulse length, as electron temperature will be hot for as long as the laser is accelerating them. However, as the ions expand, the ion density distribution changes and partly shields the electric field. Providing the equations C.1 and C.2 remain valid for $t > 0$, the plasma expansion into the vacuum is then described by the equations of continuity and motion:

$$\left(\frac{\partial}{\partial t} + v_i \frac{\partial}{\partial x} \right) n_i = -n_i \frac{\partial v_i}{\partial x}, \quad (\text{C.6})$$

$$\left(\frac{\partial}{\partial t} + v_i \frac{\partial}{\partial x} \right) v_i = - \left(\frac{Z e}{m_i} \right) \frac{\partial \Phi_e}{\partial x}, \quad (\text{C.7})$$

where $v_i = v_i(x, t)$ is the local velocity and $n_i = n_i(x, t)$ is the local density of the ions. The ion acoustic velocity is given by $c_s = \sqrt{(Z k_B T_e + k_B T_i)/m_i} \approx \sqrt{Z k_B T_e/m_i}$ assuming $T_i \ll T_e$. A self-similar solution to equations C.6 and C.7 for $x + c_s t > 0$ can be found if quasi-neutrality is assumed in the expanding plasma, with

$$n_e = Z n_i = n_{e0} \exp \left(-\frac{x}{c_s t} - 1 \right) \quad (\text{C.8})$$

and

$$v_i = c_s + \frac{x}{t}, \quad (\text{C.9})$$

so that the self similar solution is,

$$E_{ss} = \frac{k_B T_e}{e c_s t} = \frac{E_0}{\omega_{pi} t}, \quad (\text{C.10})$$

where $\omega_{pi} = \sqrt{n_{e0} Z e^2 / m_i \epsilon_0}$ is the ion plasma frequency.

If the initial Debye length, $\lambda_D = \sqrt{\epsilon_0 k_B T_e / n_e e^2}$ is larger than the self-similar scale length, $c_s t$, then the self-similar solution has no meaning. Also, for $\omega_{pit} \gg 1$,

the self-similar solution predicts the velocity to increase without limit for $x \rightarrow \infty$. However, physically the ion velocity is limited and the ions originally at $x = 0$ form a well defined ion front [131]. The self-similar solution becomes invalid when the local Debye length, $\lambda_D = \lambda_{D0} \sqrt{n_{e0}/n_e} = \lambda_{D0} \exp[(1 + x/c_s t)/2]$, equals the density scale length, $c_s t$. This provides an approximate position for the ion front given by $1 + x/c_s t = 2 \ln(\omega_{pi} t)$. Therefore, a prediction of the velocity of the ion front is given by $v_{i,front} = 2c_s \ln(\omega_{pi} t)$. This implies that the electric field at the ion front is twice that predicted by the self-similar field, E_{ss} :

$$E_{front} \simeq 2E_{ss} = \frac{2E_0}{\omega_{pi} t}. \quad (\text{C.11})$$

To provide a more accurate expression for the electric field, Mora developed a 1D Lagrangian code [18] which solves equations C.1, C.2, C.6 and C.7. This found that the peak value of the electric field can be very accurately described at all times, $t \geq 0$, by

$$E_{front}(t) \simeq \frac{2E_0}{\sqrt{2e_E + \omega_{pi}^2 t^2}} = \sqrt{\frac{2}{e_E}} \cdot \frac{E_0}{\sqrt{1 + \tau^2}}, \quad (\text{C.12})$$

where $\tau = \omega_{pi} t / \sqrt{2e_E}$.

Now the front velocity, v_{front} , and position, x_{front} can be determined by integrating $dv_{front}/dt = ZeE_{front}/m_i$ and $dx_{front}/dt = v_{front}$ over time:

$$v_{front} \simeq 2c_s \ln(\tau + \sqrt{\tau^2 + 1}), \quad (\text{C.13})$$

$$x_{front} \simeq 2\sqrt{2e_E} \lambda_{D0} [\tau \ln(\tau + \sqrt{\tau^2 + 1}) - \sqrt{\tau^2 + 1} + 1]. \quad (\text{C.14})$$

A good estimate for the maximum rear side ion energy from this model can be made by assuming the acceleration time, t , is the same as the fast electron time or the laser pulse length, to give

$$\mathcal{E}_{max} = \frac{1}{2} m_i v_{front}^2 \simeq 2Zk_B T_e [\ln(\tau + \sqrt{\tau^2 + 1})]^2. \quad (\text{C.15})$$

A further prediction of the Mora self-similar model is the form of the ion energy spectra, which gives the number of ions per unit surface:

$$\frac{dN}{d\mathcal{E}_i} = \frac{n_{i0} t}{\sqrt{2\mathcal{E}_i}} \exp\left(-\sqrt{\frac{2\mathcal{E}_i}{Zk_B T_e}}\right), \quad (\text{C.16})$$

where \mathcal{E}_i is the ion energy. There is still a well defined cutoff to the spectrum as defined by \mathcal{E}_{max} due to the ion front formed in the acceleration process.

Bibliography

- [1] P. Gibbon, *Short Pulse Laser Interactions with Matter*, Imperial College Press (2005).
- [2] D. Strickland and G. Mourou, *Compression of Amplified Chirped Optical Pulses*, Optics Communications **56**, 219 (1985).
- [3] C. Hernandez-Gomez, P. A. Brummitt, D. J. Canny, R. J. Clarke, J. Collier, C. N. Danson, A. M. Dunne, B. Fell, A. J. Frackiewicz, S. Hancock, S. Hawkes, R. Heathcote, P. Holligan, M. H. R. Hutchinson, A. Kidd, W. J. Lester, I. O. Musgrave, D. Neely, D. R. Neville, P. A. Norreys, D. A. Pepler, C. J. Reason, W. Shaikh, T. B. Winstone, and B. E. Wyborn, *Vulcan petawatt-operation and development*, Journal De Physique IV **133**, 555 (2006).
- [4] S. W. Bahk, P. Rousseau, T. A. Planchon, V. Chvykov, G. Kalintchenko, A. Maksimchuk, G. A. Mourou, and V. Yanovsky, *Generation and characterization of the highest laser intensities (10^{22} W/cm²)*, Optics Letters **29**, 2837 (2004).
- [5] R. Bingham, *Plasma physics - On the crest of a wake*, Nature **445**, 721 (2007).
- [6] G. A. Mourou, T. Tajima, and S. V. Bulanov, *Optics in the relativistic regime*, Reviews of Modern Physics **78**, 309 (2006).
- [7] J. T. Mendonca, M. Marklund, R. K. Shukla, and G. Brodin, *Photon acceleration in vacuum*, Physics Letters A **359**, 700 (2006).
- [8] *The Stanford Linear Accelerator Center: www.slac.stanford.edu* (2007).

- [9] *Conseil Européen pour la Recherche Nucléaire: www.cern.ch* (2007).
- [10] T. Tajima and J. M. Dawson, *Laser Electron-Accelerator*, Physical Review Letters **43**, 267 (1979).
- [11] S. P. D. Mangles, C. D. Murphy, Z. Najmudin, A. G. R. Thomas, J. L. Collier, A. E. Dangor, E. J. Divall, P. S. Foster, J. G. Gallacher, C. J. Hooker, D. A. Jaroszynski, A. J. Langley, W. B. Mori, P. A. Norreys, F. S. Tsung, R. Viskup, B. R. Walton, and K. Krushelnick, *Monoenergetic beams of relativistic electrons from intense laser-plasma interactions*, Nature **431**, 535 (2004).
- [12] C. G. R. Geddes, C. Toth, J. van Tilborg, E. Esarey, C. B. Schroeder, D. Bruhwiler, C. Nieter, J. Cary, and W. P. Leemans, *High-quality electron beams from a laser wakefield accelerator using plasma-channel guiding*, Nature **431**, 538 (2004).
- [13] J. Faure, Y. Glinec, A. Pukhov, S. Kiselev, S. Gordienko, E. Lefebvre, J. P. Rousseau, F. Burgy, and V. Malka, *A laser-plasma accelerator producing monoenergetic electron beams*, Nature **431**, 541 (2004).
- [14] W. P. Leemans, B. Nagler, A. J. Gonsalves, C. Toth, K. Nakamura, C. G. R. Geddes, E. Esarey, C. B. Schroeder, and S. M. Hooker, *GeV electron beams from a centimetre-scale accelerator*, Nature Physics **2**, 696 (2006).
- [15] *The Diamond Light Source: www.diamond.ac.uk* (2007).
- [16] *Deutsches Elektronen-Synchrotron: www.desy.de* (2007).
- [17] R. A. Snavely, M. H. Key, S. P. Hatchett, T. E. Cowan, M. Roth, T. W. Phillips, M. A. Stoyer, E. A. Henry, T. C. Sangster, M. S. Singh, S. C. Wilks, A. MacKinnon, A. Offenberger, D. M. Pennington, K. Yasuike, A. B. Langdon, B. F. Lasinski, J. Johnson, M. D. Perry, and E. M. Campbell, *Intense high-energy proton beams from petawatt-laser irradiation of solids*, Physical Review Letters **85**, 2945 (2000).

- [18] P. Mora, *Plasma expansion into a vacuum*, Physical Review Letters **90**, 185002 (2003).
- [19] S. Fritzler, V. Malka, G. Grillon, J. P. Rousseau, F. Burgy, E. Lefebvre, E. d'Humieres, P. McKenna, and K. W. D. Ledingham, *Proton beams generated with high-intensity lasers: Applications to medical isotope production*, Applied Physics Letters **83**, 3039 (2003).
- [20] J. Fuchs, P. Antici, E. D'Humieres, E. Lefebvre, M. Borghesi, E. Brambrink, C. A. Cecchetti, M. Kaluza, V. Malka, M. Manclossi, S. Meyroneinc, P. Mora, J. Schreiber, T. Toncian, H. Pepin, and R. Audebert, *Laser-driven proton scaling laws and new paths towards energy increase*, Nature Physics **2**, 48 (2006).
- [21] T. E. Cowan, J. Fuchs, H. Ruhl, A. Kemp, P. Audebert, M. Roth, R. Stephens, I. Barton, A. Blazevic, E. Brambrink, J. Cobble, J. Fernandez, J. C. Gauthier, M. Geissel, M. Hegelich, J. Kaae, S. Karsch, G. P. Le Sage, S. Letzring, M. Manclossi, S. Meyroneinc, A. Newkirk, H. Pepin, and N. Renard-LeGalloudec, *Ultralow emittance, multi-MeV proton beams from a laser virtual-cathode plasma accelerator*, Physical Review Letters **92**, 204801 (2004).
- [22] L. O. Silva, M. Marti, J. R. Davies, R. A. Fonseca, C. Ren, F. S. Tsung, and W. B. Mori, *Proton shock acceleration in laser-plasma interactions*, Physical Review Letters **92**, 15002 (2004).
- [23] M. S. Wei, S. P. D. Mangles, Z. Najmudin, B. Walton, A. Gopal, M. Tatarakis, A. E. Dangor, E. L. Clark, R. G. Evans, S. Fritzler, R. J. Clarke, C. Hernandez-Gomez, D. Neely, W. Mori, M. Tzoufras, and K. Krushelnick, *Ion acceleration by collisionless shocks in high-intensity-laser-underdense-plasma interaction*, Physical Review Letters **93**, 155003 (2004).
- [24] A. R. Bell, J. R. Davies, and S. M. Guerin, *Magnetic field in short-pulse high-intensity laser-solid experiments*, Physical Review E **58**, 2471 (1998).

- [25] J. R. Davies, A. R. Bell, and M. Tatarakis, *Magnetic focusing and trapping of high-intensity laser-generated fast electrons at the rear of solid targets*, Physical Review E **59**, 6032 (1999).
- [26] J. R. Davies, *Electric and magnetic field generation and target heating by laser-generated fast electrons*, Physical Review E **68**, 56404 (2003).
- [27] E. L. Clark, K. Krushelnick, J. R. Davies, M. Zepf, M. Tatarakis, F. N. Beg, A. Machacek, P. A. Norreys, M. I. K. Santala, I. Watts, and A. E. Dangor, *Measurements of energetic proton transport through magnetized plasma from intense laser interactions with solids*, Physical Review Letters **84**, 670 (2000).
- [28] M. Zepf, E. L. Clark, F. N. Beg, R. J. Clarke, A. E. Dangor, A. Gopal, K. Krushelnick, P. A. Norreys, M. Tatarakis, U. Wagner, and M. S. Wei, *Proton acceleration from high-intensity laser interactions with thin foil targets*, Physical Review Letters **90**, 64801 (2003).
- [29] N. H. Burnett and G. D. Enright, *Population-Inversion in the Recombination of Optically-Ionized Plasmas*, IEEE Journal of Quantum Electronics **26**, 1797 (1990).
- [30] G. S. Sarkisov, V. Y. Bychenkov, V. N. Novikov, V. T. Tikhonchuk, A. Maksimchuk, S. Y. Chen, R. Wagner, G. Mourou, and D. Umstadter, *Self-focusing, channel formation, and high-energy ion generation in interaction of an intense short laser pulse with a He jet*, Physical Review E **59**, 7042 (1999).
- [31] E. L. Clark, *Measurements of Energetic Particles from Ultra Intense Laser Plasma Interactions*, PhD thesis, University of London (2001).
- [32] V. V. Goloviznin and T. J. Schep, *Production of direct fusion neutrons during ultra-intense laser-plasma interaction*, Journal of Physics D-Applied Physics **31**, 3243 (1998).
- [33] H. Schwoerer, S. Pfotenhauer, O. Jackel, K. U. Amthor, B. Liesfeld, W. Ziegler, R. Sauerbrey, K. W. D. Ledingham, and T. Esirkepov, *Laser-plasma accelera-*

- tion of quasi-monoenergetic protons from microstructured targets*, Nature **439**, 445 (2006).
- [34] B. M. Hegelich, B. J. Albright, J. Cobble, K. Flippo, S. Letzring, M. Paffett, H. Ruhl, J. Schreiber, R. K. Schulze, and J. C. Fernandez, *Laser acceleration of quasi-monoenergetic MeV ion beams*, Nature **439**, 441 (2006).
- [35] T. Toncian, M. Borghesi, J. Fuchs, E. d’Humieres, P. Antici, P. Audebert, E. Brambrink, C. A. Cecchetti, A. Pipahl, L. Romagnani, and O. Willi, *Ultra-fast laser-driven microlens to focus and energy-select mega-electron volt protons*, Science **312**, 410 (2006).
- [36] T. Esirkepov, M. Borghesi, S. V. Bulanov, G. Mourou, and T. Tajima, *Highly efficient relativistic-ion generation in the laser-piston regime*, Physical Review Letters **92**, 175003 (2004).
- [37] A. P. L. Robinson, A. R. Bell, and R. J. Kingham, *Effect of target composition on proton energy spectra in ultraintense laser-solid interactions*, Physical Review Letters **96**, 035005 (2006).
- [38] V. S. Khoroshkov and E. I. Minakova, *Proton beams in radiotherapy*, European Journal of Physics **19**, 523 (1998).
- [39] S. V. Bulanov, T. Z. Esirkepov, V. S. Khoroshkov, A. V. Kunetsov, and F. Pegoraro, *Oncological hadrontherapy with laser ion accelerators*, Physics Letters A **299**, 240 (2002).
- [40] E. Fourkal, B. Shahine, M. Ding, J. Li, T. Tajima, and C. Ma, *Particle in cell simulation of laser accelerated proton beams for radiation therapy*, Medical Physics **29**, 1326 (2002).
- [41] V. Malka, S. Fritzler, E. Lefebvre, E. d’Humieres, R. Ferrand, G. Grillon, C. Albaret, S. Meyroneinc, J. P. Chambaret, A. Antonetti, and D. Hulin, *Practicability of protontherapy using compact laser systems*, Medical Physics **31**, 1587 (2004).

- [42] Y. Glinec, J. Faure, V. Malka, T. Fuchs, H. Szymanowski, and U. Oelfke, *Radiotherapy with laser-plasma accelerators: Monte Carlo simulation of dose deposited by an experimental quasimonoenergetic electron beam*, *Medical Physics* **33**, 155 (2006).
- [43] I. Spencer, K. W. D. Ledingham, R. P. Singhal, T. McCanny, P. McKenna, E. L. Clark, K. Krushelnick, M. Zepf, F. N. Beg, M. Tatarakis, A. E. Dangor, P. A. Norreys, R. J. Clarke, R. M. Allott, and I. N. Ross, *Laser generation of proton beams for the production of short-lived positron emitting radioisotopes*, *Nuclear Instruments and Methods in Physics Research Section B-Beam Interactions with Materials and Atoms* **183**, 449 (2001).
- [44] K. W. D. Ledingham, P. McKenna, and R. P. Singhal, *Applications for nuclear phenomena generated by ultra-intense lasers*, *Science* **300**, 1107 (2003).
- [45] K. W. D. Ledingham, P. McKenna, T. McCanny, S. Shimizu, J. M. Yang, L. Robson, J. Zweit, J. M. Gillies, J. Bailey, G. N. Chimon, R. J. Clarke, D. Neely, P. A. Norreys, J. L. Collier, R. P. Singhal, M. S. Wei, S. P. D. Mangles, P. Nilson, K. Krushelnick, and M. Zepf, *High power laser production of short-lived isotopes for positron emission tomography*, *Journal of Physics D-Applied Physics* **37**, 2341 (2004).
- [46] M. Borghesi, D. H. Campbell, A. Schiavi, O. Willi, A. J. Mackinnon, D. Hicks, P. Patel, L. A. Gizzi, M. Galimberti, and R. J. Clarke, *Laser-produced protons and their application as a particle probe*, *Laser and Particle Beams* **20**, 269 (2002).
- [47] M. Borghesi, A. Schiavi, D. H. Campbell, M. G. Haines, O. Willi, A. J. Mackinnon, P. Patel, M. Galimberti, and L. A. Gizzi, *Proton imaging detection of transient electromagnetic fields in laser-plasma interactions (invited)*, *Review of Scientific Instruments* **74**, 1688 (2003).
- [48] M. Borghesi, A. J. Mackinnon, D. H. Campbell, D. G. Hicks, S. Kar, P. K. Patel, D. Price, L. Romagnani, A. Schiavi, and O. Willi, *Multi-MeV proton*

- source investigations in ultraintense laser-foil interactions*, Physical Review Letters **92**, 055003 (2004).
- [49] L. Romagnani, J. Fuchs, M. Borghesi, P. Antici, P. Audebert, F. Ceccherini, T. Cowan, T. Grismayer, S. Kar, A. Macchi, P. Mora, G. Pretzler, A. Schiavi, T. Toncian, and O. Willi, *Dynamics of electric fields driving the laser acceleration of multi-MeV protons*, Physical Review Letters **95**, 195001 (2005).
- [50] M. Borghesi, S. V. Bulanov, T. Z. Esirkepov, S. Fritzler, S. Kar, T. V. Liseikina, V. Malka, F. Pegoraro, L. Romagnani, J. P. Rousseau, A. Schiavi, O. Willi, and A. V. Zayats, *Plasma ion evolution in the wake of a high-intensity ultrashort laser pulse*, Physical Review Letters **94**, 195003 (2005).
- [51] C. K. Li, F. H. Seguin, J. A. Frenje, J. R. Rygg, R. D. Petrasso, R. P. J. Town, P. A. Amendt, S. P. Hatchett, O. L. Landen, A. J. Mackinnon, P. K. Patel, V. A. Smalyuk, T. C. Sangster, and J. P. Knauer, *Measuring E and B fields in laser-produced plasmas with monoenergetic proton radiography*, Physical Review Letters **97**, 135003 (2006).
- [52] C. A. Cecchetti, M. Borghesi, S. Kar, P. A. Wilson, J. Fuchs, P. Antici, L. Romagnani, O. Willi, R. Jung, J. Osterholtz, A. Pipahl, A. M. M. Schiavi, S. Bandyopadhyay, M. Notley, and D. Neely, *Proton deflectometry measurements of self-generated magnetic fields in laser-produced plasma*, CCLRC Rutherford Appleton Laboratory Central Laser Facility Annual Report pg. 21–23 (2005/2006).
- [53] *ISIS: www.isis.rl.ac.uk* (2007).
- [54] K. L. Lancaster, S. Karsch, H. Habara, F. N. Beg, E. L. Clark, R. Freeman, M. H. Key, J. A. King, R. Kodama, K. Krushelnick, K. W. D. Ledingham, P. McKenna, C. D. Murphy, P. A. Norreys, R. Stephens, C. Stoeckl, Y. Toyama, M. S. Wei, and M. Zepf, *Characterization of $Li-7(p,n)Be-7$ neutron yields from laser produced ion beams for fast neutron radiography*, Physics of Plasmas **11**, 3404 (2004).

- [55] S. Karsch, S. Dusterer, H. Schwoerer, F. Ewald, D. Habs, M. Hegelich, G. Pretzler, A. Pukhov, K. Witte, and R. Sauerbrey, *High-intensity laser induced ion acceleration from heavy-water droplets*, Physical Review Letters **91**, 015001 (2003).
- [56] G. Pretzler, A. Saemann, A. Pukhov, D. Rudolph, T. Schatz, U. Schramm, P. Thirolf, D. Habs, K. Eidmann, G. D. Tsakiris, J. Meyer-ter Vehn, and K. J. Witte, *Neutron production by 200 mJ ultrashort laser pulses*, Physical Review E **58**, 1165 (1998).
- [57] L. Disdier, J. P. Garconnet, G. Malka, and J. L. Miquel, *Fast neutron emission from a high-energy ion beam produced by a high-intensity subpicosecond laser pulse*, Physical Review Letters **82**, 1454 (1999).
- [58] *ITER: www.iter.org* (2007).
- [59] *National Ignition Facility Programs: www.llnl.gov/nif* (2007).
- [60] *Laser Megajoule: www-lmj.cea.fr* (2007).
- [61] K. Oades, A. Evans, G. Slark, J. Foster, R. Eagleton, and E. Clark, *Target diagnostics for the future AWE Orion laser facility*, Review of Scientific Instruments **75**, 4222 (2004).
- [62] *The Institute of Laser Engineering Osaka University: www.ile.osaka-u.ac.jp* (2007).
- [63] *HiPER, High Power laser Energy Research facility: www.hiperlaser.eu* (2007).
- [64] A. Taylor, M. Dunne, S. Bennington, S. Ansell, I. Gardner, P. Norreys, T. Broome, D. Findlay, and R. Nelves, *A route to the brightest possible neutron source?*, Science **315**, 1092 (2007).
- [65] J. Lindl, *Development of the Indirect-Drive Approach to Inertial Confinement Fusion and the Target Physics Basis for Ignition and Gain*, Physics of Plasmas **2**, 3933 (1995).

- [66] M. Tabak, J. Hammer, M. E. Glinsky, W. L. Kruer, S. C. Wilks, J. Woodworth, E. M. Campbell, M. D. Perry, and R. J. Mason, *Ignition and High-Gain with Ultrapowerful Lasers*, *Physics of Plasmas* **1**, 1626 (1994).
- [67] R. Kodama, P. A. Norreys, K. Mima, A. E. Dangor, R. G. Evans, H. Fujita, Y. Kitagawa, K. Krushelnick, T. Miyakoshi, N. Miyanaga, T. Norimatsu, S. J. Rose, T. Shozaki, K. Shigemori, A. Sunahara, M. Tampo, K. A. Tanaka, Y. Toyama, Y. Yamanaka, and M. Zepf, *Fast heating of ultrahigh-density plasma as a step towards laser fusion ignition*, *Nature* **412**, 798 (2001).
- [68] R. Kodama, Y. Sentoku, Z. L. Chen, G. R. Kumar, S. P. Hatchett, Y. Toyama, T. E. Cowan, R. R. Freeman, J. Fuchs, Y. Izawa, M. H. Key, Y. Kitagawa, K. Kondo, T. Matsuoka, H. Nakamura, M. Nakatsutsumi, P. A. Norreys, T. Norimatsu, R. A. Snavely, R. B. Stephens, M. Tampo, K. A. Tanaka, and T. Yabuuchi, *Plasma devices to guide and collimate a high density of MeV electrons*, *Nature* **432**, 1005 (2004).
- [69] P. K. Patel, A. J. Mackinnon, M. H. Key, T. E. Cowan, M. E. Ford, M. Allen, D. F. Price, H. Ruhl, P. T. Springer, and R. Stephens, *Isochoric heating of solid-density matter with an ultrafast proton beam*, *Physical Review Letters* **91**, 125004 (2003).
- [70] B. A. Remington, *High energy density laboratory astrophysics*, *Plasma Physics and Controlled Fusion* **47**, A191 (2005).
- [71] M. H. Edwards, D. Whittaker, P. Mistry, N. Booth, G. J. Pert, G. J. Tallents, B. Rus, T. Mocek, M. Koslova, C. McKenna, A. Delserieys, C. L. S. Lewis, M. Notley, and D. Neely, *Opacity measurements of a hot iron plasma using an x-ray laser*, *Physical Review Letters* **97**, 035001 (2006).
- [72] R. A. Smith, J. Lazarus, M. Hohenberger, A. S. Moore, J. S. Robinson, E. T. Gumbrell, and M. Dunne, *Colliding blast waves driven by the interaction of a short-pulse laser with a gas of atomic clusters*, *Astrophysics and Space Science* **307**, 131 (2007).

- [73] A. S. Moore, J. Lazarus, M. Hohenberger, J. S. Robinson, E. T. Gumbrell, M. Dunne, and R. A. Smith, *Investigating the astrophysical applicability of radiative and non-radiative blast wave structure in cluster media*, *Astrophysics and Space Science* **307**, 139 (2007).
- [74] J. W. Cronin, T. K. Gaisser, and S. P. Swordy, *Cosmic rays at the energy frontier*, *Scientific American* **276**, 44 (1997).
- [75] K. Shigemori, R. Kodama, D. R. Farley, T. Koase, K. G. Estabrook, B. A. Remington, D. D. Ryutov, Y. Ochi, H. Azechi, J. Stone, and N. Turner, *Experiments on radiative collapse in laser-produced plasmas relevant to astrophysical jets*, *Physical Review E* **62**, 8838 (2000).
- [76] S. V. Lebedev, D. Ampleford, A. Ciardi, S. N. Bland, J. P. Chittenden, M. G. Haines, A. Frank, E. G. Blackman, and A. Cunningham, *Jet deflection via crosswinds: Laboratory astrophysical studies*, *Astrophysical Journal* **616**, 988 (2004).
- [77] D. J. Ampleford, S. V. Lebedev, A. Ciardi, S. N. Bland, S. C. Bott, G. N. Hall, N. Naz, C. A. Jennings, M. Sherlock, J. P. Chittenden, A. Frank, and E. Blackman, *Laboratory modeling of standing shocks and radiatively cooled jets with angular momentum*, *Astrophysics and Space Science* **307**, 51 (2007).
- [78] J. Meyer-ter Vehn, A. Pukhov, and Z. M. Sheng, *Relativistic Laser Plasma Interactions*, Kluwer Academic/Plenum Publishers, New York (2001).
- [79] P. Sprangle, C. M. Tang, and E. Esarey, *Relativistic Self-Focusing of Short-Pulse Radiation Beams in Plasmas*, *IEEE Transactions on Plasma Science* **15**, 145 (1987).
- [80] W. B. Mori, *The physics of the nonlinear optics of plasmas at relativistic intensities for short-pulse lasers*, *IEEE Journal of Quantum Electronics* **33**, 1942 (1997).

- [81] S. P. Leblanc, R. Sauerbrey, S. C. Rae, and K. Burnett, *Spectral Blue Shifting of a Femtosecond Laser-Pulse Propagating through a High-Pressure Gas*, Journal of the Optical Society of America B-Optical Physics **10**, 1801 (1993).
- [82] S. C. Wilks, J. M. Dawson, W. B. Mori, T. Katsouleas, and M. E. Jones, *Photon Accelerator*, Physical Review Letters **62**, 2600 (1989).
- [83] C. D. Murphy, R. Trines, J. Vieira, A. J. W. Reitsma, R. Bingham, J. L. Collier, E. J. Divall, P. S. Foster, C. J. Hooker, A. J. Langley, P. A. Norreys, R. A. Fonseca, F. Fiuza, L. O. Silva, J. T. Mendonca, W. B. Mori, J. G. Gallacher, R. Viskup, D. A. Jaroszynski, S. P. D. Mangles, A. G. R. Thomas, K. Krushelnick, and Z. Najmudin, *Evidence of photon acceleration by laser wake fields*, Physics of Plasmas **13**, 033108 (2006).
- [84] W. L. Kruer, *The Physics of Laser Plasma Interactions*, Addison-Wesley Publishing Company (1988).
- [85] Z. Najmudin, K. Krushelnick, E. L. Clark, S. P. D. Mangles, B. Walton, A. E. Dangor, S. Fritzler, V. Malka, E. Lefebvre, D. Gordon, F. S. Tsung, and C. Joshi, *Self-modulated wakefield and forced laser wakefield acceleration of electrons*, Physics of Plasmas **10**, 2071 (2003).
- [86] M. Tatarakis, F. N. Beg, E. L. Clark, A. E. Dangor, R. D. Edwards, R. G. Evans, T. J. Goldsack, K. W. D. Ledingham, P. A. Norreys, M. A. Sinclair, M. S. Wei, M. Zepf, and K. Krushelnick, *Propagation instabilities of high-intensity laser-produced electron beams*, Physical Review Letters **90**, 175001 (2003).
- [87] P. Sprangle, J. Krall, and E. Esarey, *Hose-Modulation Instability of Laser-Pulses in Plasmas*, Physical Review Letters **73**, 3544 (1994).
- [88] Z. Najmudin, K. Krushelnick, M. Tatarakis, E. L. Clark, C. N. Danson, V. Malka, D. Neely, M. I. K. Santala, and A. E. Dangor, *The effect of high intensity laser propagation instabilities on channel formation in underdense plasmas*, Physics of Plasmas **10**, 438 (2003).

- [89] V. Malka, J. Faure, J. R. Marques, F. Amiranoff, C. Courtois, Z. Najmudin, K. Krushelnick, M. R. Salvati, and A. E. Dangor, *Interaction of ultraintense laser pulses with an underdense, preformed plasma channel*, IEEE Transactions on Plasma Science **28**, 1078 (2000).
- [90] X. F. Wang, M. Krishnan, N. Saleh, H. W. Wang, and D. Umstadter, *Electron acceleration and the propagation of ultrashort high-intensity laser pulses in plasmas*, Physical Review Letters **84**, 5324 (2000).
- [91] S. P. D. Mangles, *Measurements of Relativistic Electrons from Intense Laser-Plasma Interactions*, PhD thesis, University of London (2005).
- [92] P. N. Nilson, *Measurements of the Dynamics of Laser and Soft X-ray Heated Targets by XUV and Optical Probing*, PhD thesis, University of London (2006).
- [93] F. Vidal and T. W. Johnston, *Electromagnetic beam breakup: Multiple filaments, single beam equilibria, and radiation*, Physical Review Letters **77**, 1282 (1996).
- [94] D. E. Hinkel, E. A. Williams, R. L. Berger, L. V. Powers, A. B. Langdon, and C. H. Still, *Propagation of realistic beams in underdense plasma*, Physics of Plasmas **5**, 1887 (1998).
- [95] J. Meyer-ter Vehn and Z. M. Sheng, *On electron acceleration by intense laser pulses in the presence of a stochastic field*, Physics of Plasmas **6**, 641 (1999).
- [96] M. Tanimoto, S. Kato, E. Miura, N. Saito, K. Koyama, and J. K. Koga, *Direct electron acceleration by stochastic laser fields in the presence of self-generated magnetic fields*, Physical Review E **68**, 26401 (2003).
- [97] A. Pukhov, Z. M. Sheng, and J. Meyer-ter Vehn, *Particle acceleration in relativistic laser channels*, Physics of Plasmas **6**, 2847 (1999).
- [98] A. Pukhov and J. Meyer-ter Vehn, *Relativistic laser-plasma interaction by multi-dimensional particle-in-cell simulations*, Physics of Plasmas **5**, 1880 (1998).

- [99] S. P. D. Mangles, B. R. Walton, M. Tzoufras, Z. Najmudin, R. J. Clarke, A. E. Dangor, R. G. Evans, S. Fritzler, A. Gopal, C. Hernandez-Gomez, W. B. Mori, W. Rozmus, M. Tatarakis, A. G. R. Thomas, F. S. Tsung, M. S. Wei, and K. Krushelnick, *Electron acceleration in cavitated channels formed by a petawatt laser in low-density plasma*, Physical Review Letters **94**, 245001 (2005).
- [100] C. Gahn, G. D. Tsakiris, A. Pukhov, J. Meyer-ter Vehn, G. Pretzler, P. Thirolf, D. Habs, and K. J. Witte, *Multi-MeV electron beam generation by direct laser acceleration in high-density plasma channels*, Physical Review Letters **83**, 4772 (1999).
- [101] K. Krushelnick, E. L. Clark, Z. Najmudin, M. Salvati, M. I. K. Santala, M. Tatarakis, A. E. Dangor, V. Malka, D. Neely, R. Allott, and C. Danson, *Multi-MeV ion production from high-intensity laser interactions with underdense plasmas*, Physical Review Letters **83**, 737 (1999).
- [102] W. B. Mori, C. Joshi, J. M. Dawson, D. W. Forslund, and J. M. Kindel, *Evolution of Self-Focusing of Intense Electromagnetic-Waves in Plasma*, Physical Review Letters **60**, 1298 (1988).
- [103] A. Pukhov and J. Meyer-ter Vehn, *Relativistic magnetic self-channeling of light in near-critical plasma: Three-dimensional particle-in-cell simulation*, Physical Review Letters **76**, 3975 (1996).
- [104] R. G. Hemker, K. C. Tzeng, W. B. Mori, C. E. Clayton, and T. Katsouleas, *Computer simulations of cathodeless, high-brightness electron-beam production by multiple laser beams in plasmas*, Physical Review E **57**, 5920 (1998).
- [105] R. G. Hemker, *Particle in Cell Modeling of Plasma-Based Accelerators in two and three dimensions*, Ph.D. Thesis, University of California Los Angeles (2000).
- [106] R. A. Fonseca, L. O. Silva, F. S. Tsung, W. L. Decyk, C. Ren, W. B. Mori, S. Deng, S. Lee, T. Katsouleas, and J. C. Adam, *OSIRIS: A three-dimensional,*

- fully relativistic particle in cell code for modeling plasma based accelerators*, Vol. 2331, pg. 342–351, Lecture Notes in Computer Science (2002).
- [107] T. Z. Esirkepov, Y. Sentoku, K. Mima, K. Nishihara, F. Califano, F. Pegoraro, N. M. Naumova, S. V. Bulanov, Y. Ueshima, T. V. Liseikina, V. A. Vshivkov, and Y. Kato, *Ion acceleration by superintense laser pulses in plasmas*, JETP Letters **70**, 82 (1999).
- [108] S. V. Bulanov, T. Z. Esirkepov, F. Califano, Y. Kato, T. V. Liseikina, K. Mima, N. M. Naumova, K. Nishihara, F. Pegoraro, H. Ruhl, Y. Sentoku, and Y. Ueshima, *Generation of collimated beams of relativistic ions in laser-plasma interactions*, JETP Letters **71**, 407 (2000).
- [109] Y. Sentoku, T. V. Liseikina, T. Z. Esirkepov, F. Califano, N. M. Naumova, Y. Ueshima, V. A. Vshivkov, Y. Kato, K. Mima, K. Nishihara, F. Pegoraro, and S. V. Bulanov, *High density collimated beams of relativistic ions produced by petawatt laser pulses in plasmas*, Physical Review E **62**, 7271 (2000).
- [110] S. C. Wilks and W. L. Kruer, *Absorption of ultrashort, ultra-intense laser light by solids and overdense plasmas*, IEEE Journal of Quantum Electronics **33**, 1954 (1997).
- [111] L. Schlessinger and J. A. Wright, *High-Energy Bremsstrahlung in an Intense Laser Field*, Physical Review A **22**, 909 (1980).
- [112] D. W. Forslund, J. M. Kindel, and K. Lee, *Theory of Hot-Electron Spectra at High Laser Intensity*, Physical Review Letters **39**, 284 (1977).
- [113] K. Estabrook and W. L. Kruer, *Properties of Resonantly Heated Electron Distributions*, Physical Review Letters **40**, 42 (1978).
- [114] F. Brunel, *Not-So-Resonant, Resonant Absorption*, Physical Review Letters **59**, 52 (1987).
- [115] F. Brunel, *Anomalous Absorption of High-Intensity Subpicosecond Laser-Pulses*, Physics of Fluids **31**, 2714 (1988).

- [116] P. Gibbon and A. R. Bell, *Collisionless Absorption in Sharp-Edged Plasmas*, Physical Review Letters **68**, 1535 (1992).
- [117] W. L. Kruer and K. Estabrook, *JxB Heating by Very Intense Laser-Light*, Physics of Fluids **28**, 430 (1985).
- [118] S. C. Wilks, W. L. Kruer, M. Tabak, and A. B. Langdon, *Absorption of Ultra-Intense Laser-Pulses*, Physical Review Letters **69**, 1383 (1992).
- [119] G. Malka and J. L. Miquel, *Experimental confirmation of ponderomotive-force electrons produced by an ultrarelativistic laser pulse on a solid target*, Physical Review Letters **77**, 75 (1996).
- [120] L. Spitzer and R. Harm, *Transport Phenomena in a Completely Ionized Gas*, Physical Review **89**, 977 (1953).
- [121] H. Alfvén, *On the Motion of Cosmic Rays in Interstellar Space*, Physical Review **55**, 425 (1939).
- [122] A. R. Bell and R. J. Kingham, *Resistive collimation of electron beams in laser-produced plasmas*, Physical Review Letters **91**, 35003 (2003).
- [123] E. Weibel, *Spontaneously Growing Transverse Waves in a Plasma Due to an Anisotropic Velocity Distribution*, Physical Review Letters **2**, 83 (1959).
- [124] E. L. Clark, K. Krushelnick, M. Zepf, F. N. Beg, M. Tatarakis, A. Machacek, M. I. K. Santala, I. Watts, P. A. Norreys, and A. E. Dangor, *Energetic heavy-ion and proton generation from ultraintense laser-plasma interactions with solids*, Physical Review Letters **85**, 1654 (2000).
- [125] M. Zepf, E. L. Clark, K. Krushelnick, F. N. Beg, C. Escoda, A. E. Dangor, M. I. K. Santala, M. Tatarakis, I. F. Watts, P. A. Norreys, R. J. Clarke, J. R. Davies, M. A. Sinclair, R. D. Edwards, T. J. Goldsack, I. Spencer, and K. W. D. Ledingham, *Fast particle generation and energy transport in laser-solid interactions*, Physics of Plasmas **8**, 2323 (2001).

- [126] M. Hegelich, S. Karsch, G. Pretzler, D. Habs, K. Witte, W. Guenther, M. Allen, A. Blazevic, J. Fuchs, J. C. Gauthier, M. Geissel, P. Audebert, T. Cowan, and M. Roth, *MeV ion jets from short-pulse-laser interaction with thin foils*, Physical Review Letters **89**, 85002 (2002).
- [127] A. J. Mackinnon, Y. Sentoku, P. K. Patel, D. W. Price, S. Hatchett, M. H. Key, C. Andersen, R. Snavely, and R. R. Freeman, *Enhancement of proton acceleration by hot-electron recirculation in thin foils irradiated by ultraintense laser pulses*, Physical Review Letters **88**, 215006 (2002).
- [128] H. Habara, K. L. Lancaster, S. Karsch, C. D. Murphy, P. A. Norreys, R. G. Evans, M. Borghesi, L. Romagnani, M. Zepf, T. Norimatsu, Y. Toyama, R. Kodama, J. A. King, R. Snavely, K. Akli, B. Zhang, R. Freeman, S. Hatchett, A. J. MacKinnon, P. Patel, M. H. Key, C. Stoeckl, R. B. Stephens, R. A. Fonseca, and L. O. Silva, *Ion acceleration from the shock front induced by hole boring in ultraintense laser-plasma interactions*, Physical Review E **70**, 46414 (2004).
- [129] S. C. Wilks, A. B. Langdon, T. E. Cowan, M. Roth, M. Singh, S. Hatchett, M. H. Key, D. Pennington, A. MacKinnon, and R. A. Snavely, *Energetic proton generation in ultra-intense laser-solid interactions*, Physics of Plasmas **8**, 542 (2001).
- [130] M. Widner, I. Alexeff, and W. D. Jones, *Plasma Expansion into a Vacuum*, Physics of Fluids **14**, 795 (1971).
- [131] J. E. Crow, P. L. Auer, and J. E. Allen, *Expansion of a Plasma into a Vacuum*, Journal of Plasma Physics **14**, 65 (1975).
- [132] S. Gitomer, *Fast ions and hot-electrons in the laser-plasma interaction*, Physics of Fluids **29**, 2679 (1986).
- [133] J. Denavit, *Collisionless Plasma Expansion into a Vacuum*, Physics of Fluids **22**, 1384 (1979).

- [134] Y. Kishimoto, K. Mima, T. Watanabe, and K. Nishikawa, *Analysis of Fast-Ion Velocity Distributions in Laser Plasmas with a Truncated Maxwellian Velocity Distribution of Hot-Electrons*, *Physics of Fluids* **26**, 2308 (1983).
- [135] M. Passoni, V. T. Tikhonchuk, M. Lontano, and V. Y. Bychenkov, *Charge separation effects in solid targets and ion acceleration with a two-temperature electron distribution*, *Physical Review E* **69**, 26411 (2004).
- [136] M. Kaluza, J. Schreiber, M. I. K. Santala, G. D. Tsakiris, K. Eidmann, J. Meyer-ter Vehn, and K. J. Witte, *Influence of the laser prepulse on proton acceleration in thin-foil experiments*, *Physical Review Letters* **93**, 45003 (2004).
- [137] P. McKenna, K. W. D. Ledingham, J. M. Yang, L. Robson, T. McCanny, S. Shimizu, R. J. Clarke, D. Neely, K. Spohr, R. Chapman, R. P. Singhal, K. Krushelnick, M. S. Wei, and P. A. Norreys, *Characterization of proton and heavier ion acceleration in ultrahigh-intensity laser interactions with heated target foils*, *Physical Review E* **70**, 36405 (2004).
- [138] J. A. Stamper, K. Papadopo, R. N. Sudan, S. O. Dean, E. A. McLean, and J. M. Dawson, *Spontaneous Magnetic Fields in Laser-Produced Plasmas*, *Physical Review Letters* **26**, 1012 (1971).
- [139] M. Borghesi, A. J. Mackinnon, R. Gaillard, O. Willi, A. Pukhov, and J. Meyer-ter Vehn, *Large quasistatic magnetic fields generated by a relativistically intense laser pulse propagating in a preionized plasma*, *Physical Review Letters* **80**, 5137 (1998).
- [140] M. Tatarakis, A. Gopal, I. Watts, F. N. Beg, A. E. Dangor, K. Krushelnick, U. Wagner, P. A. Norreys, E. L. Clark, M. Zepf, and R. G. Evans, *Measurements of ultrastrong magnetic fields during relativistic laser-plasma interactions*, *Physics of Plasmas* **9**, 2244 (2002).
- [141] U. Wagner, M. Tatarakis, A. Gopal, F. N. Beg, E. L. Clark, A. E. Dangor, R. G. Evans, M. G. Haines, S. P. D. Mangles, P. A. Norreys, M. S. Wei,

- M. Zepf, and K. Krushelnick, *Laboratory measurements of 0.7 GG magnetic fields generated during high-intensity laser interactions with dense plasmas*, Physical Review E **70**, 26401 (2004).
- [142] F. F. Chen, *Introduction to plasma physics and controlled fusion*, Vol. 1: Plasma physics, Plenum Press, 2nd. Ed. (1984).
- [143] R. O. Dendy, *Plasma Physics: An Introductory Course*, Cambridge University Press (1995).
- [144] E. R. Priest and A. W. Hood, *Advances in solar system magnetohydrodynamics*, Cambridge University Press (1991).
- [145] I. N. Ross, P. Matousek, M. Towrie, A. J. Langley, and J. L. Collier, *The prospects for ultrashort pulse duration and ultrahigh intensity using optical parametric chirped pulse amplifiers*, Optics Communications **144**, 125 (1997).
- [146] C. N. Danson, P. A. Brummitt, R. J. Clarke, J. L. Collier, B. Fell, A. Frackiewicz, S. Hancock, S. Hawkes, C. Hernandez-Gomez, P. Holligan, M. H. R. Hutchinson, A. Kidd, W. J. Lester, I. O. Musgrave, D. Neely, D. R. Neville, P. A. Norreys, D. A. Pepler, C. J. Reason, W. Shaikh, T. B. Winstone, R. W. W. Wyatt, and B. E. Wyborn, *Vulcan Petawatt - an ultra-high-intensity interaction facility*, Nuclear Fusion **44**, S239 (2004).
- [147] C. N. Danson, P. A. Brummitt, R. J. Clarke, I. Collier, B. Fell, A. J. Frackiewicz, S. Hawkes, C. Hernandez-Gomez, P. Holligan, M. H. R. Hutchinson, A. Kidd, W. J. Lester, I. O. Musgrave, D. Neely, D. R. Neville, P. A. Norreys, D. A. Pepler, C. Reason, W. Shaikh, T. B. Winstone, R. W. W. Wyatt, and B. E. Wyborn, *Vulcan petawatt: Design, operation and interactions at $5 \times 10^{20} \text{ Wcm}^{-2}$* , Laser and Particle Beams **23**, 87 (2005).
- [148] J. L. Collier, C. J. Hooker, S. Hawkes, and C. B. Edwards, *Adaptive optics for the Petawatt upgrade*, CCLRC Rutherford Appleton Laboratory Central Laser Facility Annual Report pg. 181–182 (2001/2002).

- [149] I. O. Musgrave, C. Hernandez-Gomez, D. J. Canny, R. Heathcote, R. J. Clarke, J. L. Collier, and S. Bandyopadhyay, *Nanosecond contrast measurements of the Vulcan Petawatt facility*, CCLRC Rutherford Appleton Laboratory Central Laser Facility Annual Report pg. 197–199 (2004/2005).
- [150] J. Collier, C. Danson, C. Johnson, and C. Mistry, *Uniaxial single shot auto-correlator*, Review of Scientific Instruments **70**, 1599 (1999).
- [151] B. Dromey, Private communication (2006).
- [152] J. F. Ziegler, <http://www.srim.org/> (2006).
- [153] S. G. Gales and C. D. Bentley, *Image plates as x-ray detectors in plasma physics*, Review of Scientific Instruments **75**, 4001 (2004).
- [154] J. J. Thomson, Philosophical Magazine **21**, 225 (1911).
- [155] M. Kaluza, *Characterisation of Laser-Accelerated Proton Beams*, Phd thesis, Max-Planck-Institut für Quantenoptik, Garching, Germany (2004).
- [156] N. N. D. Centre, <http://www.nndc.bnl.gov/> (2006).
- [157] M. J. Berger, J. S. Coursey, M. A. Zucker, and J. Chang, *ESTAR, PSTAR and ASTAR: Computer Programs for Calculating Stopping-Power and Range Tables for Electrons, Protons and Helium Ions (version 1.2.3)*, <http://physics.nist.gov/Star> (2005).
- [158] S. G. Gorbics and N. R. Pereira, *Differential Absorption Spectrometer for Pulsed Bremsstrahlung*, Review of Scientific Instruments **64**, 1835 (1993).
- [159] D. L. Fehl and F. Biggs, *Verification of unfold error estimates in the unfold operator code*, Review of Scientific Instruments **68**, 890 (1997).
- [160] R. J. Clarke, P. T. Simpson, S. Kar, J. S. Green, C. Bellei, D. Carroll, B. Dromey, S. Kniep, K. Markey, P. McKenna, W. Murphy, S. Nagel, L. Willingale, and M. Zepf, *Contact radiography of (p,n) generated radioisotopes from*

- laser-plasma interactions for high dynamic range particle probing*, in preparation for Review of Scientific Instruments (2007).
- [161] L. Willingale, S. P. D. Mangles, P. M. Nilson, R. J. Clarke, A. E. Dangor, M. C. Kaluza, S. Karsch, K. L. Lancaster, W. B. Mori, Z. Najmudin, J. Schreiber, A. G. R. Thomas, M. S. Wei, and K. Krushelnick, *Collimated multi-MeV ion beams from high-intensity laser interactions with underdense plasma*, Physical Review Letters **96**, 245002 (2006).
- [162] K. Krushelnick, E. L. Clark, R. Allott, F. N. Beg, C. N. Danson, A. Machacek, V. Malka, Z. Najmudin, D. Neely, P. A. Norreys, M. R. Salvati, M. I. K. Santala, M. Tatarakis, I. Watts, M. Zepf, and A. E. Dangor, *Ultrahigh-intensity laser-produced plasmas as a compact heavy ion injection source*, IEEE Transactions on Plasma Science **28**, 1184 (2000).
- [163] K. Krushelnick, E. L. Clark, M. Zepf, J. R. Davies, F. N. Beg, A. Machacek, M. I. K. Santala, M. Tatarakis, I. Watts, P. A. Norreys, and A. E. Dangor, *Energetic proton production from relativistic laser interaction with high density plasmas*, Physics of Plasmas **7**, 2055 (2000).
- [164] A. Maksimchuk, S. Gu, K. Flippo, D. Umstadter, and V. Y. Bychenkov, *Forward ion acceleration in thin films driven by a high-intensity laser*, Physical Review Letters **84**, 4108 (2000).
- [165] Y. Sentoku, T. E. Cowan, A. Kemp, and H. Ruhl, *High energy proton acceleration in interaction of short laser pulse with dense plasma target*, Physics of Plasmas **10**, 2009 (2003).
- [166] I. Spencer, K. W. D. Ledingham, P. McKenna, T. McCanny, R. P. Singhal, P. S. Foster, D. Neely, A. J. Langley, E. J. Divall, C. J. Hooker, R. J. Clarke, P. A. Norreys, E. L. Clark, K. Krushelnick, and J. R. Davies, *Experimental study of proton emission from 60-fs, 200-mJ high-repetition-rate tabletop-laser pulses interacting with solid targets*, Physical Review E **67**, 46402 (2003).

- [167] M. Allen, P. K. Patel, A. Mackinnon, D. Price, S. Wilks, and E. Morse, *Direct experimental evidence of back-surface ion acceleration from laser-irradiated gold foils*, Physical Review Letters **93**, 265004 (2004).
- [168] J. Fuchs, Y. Sentoku, S. Karsch, J. Cobble, P. Audebert, A. Kemp, A. Nikroo, P. Antici, E. Brambrink, A. Blazevic, E. M. Campbell, J. C. Fernandez, J. C. Gauthier, M. Geissel, M. Hegelich, H. Pepin, H. Popescu, N. Renard-LeGalloudec, M. Roth, J. Schreiber, R. Stephens, and T. E. Cowan, *Comparison of laser ion acceleration from the front and rear surfaces of thin foils*, Physical Review Letters **94**, 045004 (2005).
- [169] K. Krushelnick, E. L. Clark, F. N. Beg, A. E. Dangor, Z. Najmudin, P. A. Norreys, M. Wei, and M. Zepf, *High intensity laser-plasma sources of ions—physics and future applications*, Plasma Physics and Controlled Fusion **47**, B451 (2005).
- [170] J. Schreiber, F. Bell, F. Gruner, U. Schramm, M. Geissler, M. Schnurer, S. Ter-Avetisyan, B. M. Hegelich, J. Cobble, E. Brambrink, J. Fuchs, P. Audebert, and D. Habs, *Analytical model for ion acceleration by high-intensity laser pulses*, Physical Review Letters **97**, 045005 (2006).
- [171] J. Schreiber, S. Ter-Avetisyan, E. Risse, M. P. Kalachnikov, P. V. Nickles, W. Sandner, U. Schramm, D. Habs, J. Witte, and M. Schnurer, *Pointing of laser-accelerated proton beams*, Physics of Plasmas **13**, 033111 (2006).
- [172] M. S. Wei, J. R. Davies, E. L. Clark, F. N. Beg, A. Gopal, M. Tatarakis, L. Willingale, P. Nilson, A. E. Dangor, P. A. Norreys, M. Zepf, and K. Krushelnick, *Reduction of proton acceleration in high-intensity laser interaction with solid two-layer targets*, Physics of Plasmas **13**, 123101 (2006).
- [173] A. P. L. Robinson and P. Gibbon, *Production of proton beams with narrow-band energy spectra from laser-irradiated ultrathin foils*, Physical Review E **75**, 015401 (2007).

- [174] S. Semushin and V. Malka, *High density gas jet nozzle design for laser target production*, Review of Scientific Instruments **72**, 2961 (2001).
- [175] L. Willingale, S. P. D. Mangles, P. M. Nilson, R. J. Clarke, A. E. Dangor, M. C. Kaluza, S. Karsch, K. L. Lancaster, W. B. Mori, Z. Najmudin, J. Schreiber, A. G. R. Thomas, M. S. Wei, and K. Krushelnick, *Comment on Collimated multi-MeV ion beams from high-intensity laser interactions with underdense plasma - Willingale et al. reply*, Physical Review Letters **98**, 49504 (2007).
- [176] S. Nagel, Private communication (2007).
- [177] S. V. Bulanov and T. Z. Esirkepov, *Comment on Collimated multi-MeV ion beams from high-intensity laser interactions with underdense plasma*, Physical Review Letters **98**, 49503 (2007).
- [178] S. Okihara, T. Z. Esirkepov, K. Nagai, S. Shimizu, F. Sato, M. Hashida, T. Iida, K. Nishihara, T. Norimatsu, Y. Izawa, and S. Sakabe, *Ion generation in a low-density plastic foam by interaction with intense femtosecond laser pulses*, Physical Review E **69**, 26401 (2004).
- [179] T. Ditmire, J. W. G. Tisch, E. Springate, M. B. Mason, N. Hay, R. A. Smith, J. Marangos, and M. H. R. Hutchinson, *High-energy ions produced in explosions of superheated atomic clusters*, Nature **386**, 54 (1997).
- [180] Y. T. Li, Z. M. Sheng, Y. Y. Ma, Z. Jin, J. Zhang, Z. L. Chen, R. Kodama, T. Matsuoka, M. Tambo, K. A. Tanaka, T. Tsutsumi, T. Yabuuchi, K. Du, H. Q. Zhang, L. Zhang, and Y. J. Tang, *Demonstration of bulk acceleration of ions in ultraintense laser interactions with low-density foams*, Physical Review E **72**, 66404 (2005).
- [181] D. Batani, A. Antonicci, F. Pisani, T. A. Hall, D. Scott, F. Amiranoff, M. Koenig, L. Gremillet, S. Baton, E. Martinolli, C. Rousseaux, and W. Nazarov, *Inhibition in the propagation of fast electrons in plastic foams by resistive electric fields*, Physical Review E **65**, 066409 (2002).

- [182] M. Borghesi, D. H. Campbell, A. Schiavi, O. Willi, M. Galimberti, L. A. Gizzi, A. J. Mackinnon, R. D. Snavely, P. Patel, S. Hatchett, M. Key, and W. Nazarov, *Propagation issues and energetic particle production in laser-plasma interactions at intensities exceeding 10^{19} W/cm²*, Laser and Particle Beams **20**, 31 (2002).
- [183] O. Willi, D. H. Campbell, A. Schiavi, M. Borghesi, M. Galimberti, L. A. Gizzi, W. Nazarov, A. J. MacKinnon, A. Pukhov, and J. Meyer-Ter-Vehn, *Relativistic laser propagation through underdense and overdense plasmas*, Laser and Particle Beams **19**, 5 (2001).
- [184] S. Guerin, P. Mora, J. C. Adam, A. Heron, and G. Laval, *Propagation of ultraintense laser pulses through overdense plasma layers*, Physics of Plasmas **3**, 2693 (1996).
- [185] J. W. Falconer, W. Nazarov, and C. J. Horsfield, *In-Situ Production of Very-Low-Density Microporous Polymeric Foams*, Journal of Vacuum Science & Technology a - Vacuum Surfaces and Films **13**, 1941 (1995).
- [186] L. M. Chen, H. Kotaki, K. Nakajima, J. K. Koga, S. V. Bulanov, T. Tajima, Y. Q. Gu, H. S. Peng, X. X. Wang, T. S. Wen, H. J. Liu, C. Y. Jiao, C. G. Zhang, X. J. Huang, Y. Guo, K. N. Zhou, J. F. Hua, W. M. An, C. X. Tang, and Y. Z. Lin, *Self-guiding of 100 TW femtosecond laser pulses in centimeter-scale underdense plasma*, Physics of Plasmas **14**, 40703 (2007).
- [187] F. N. Beg, M. S. Wei, A. E. Dangor, A. Gopal, M. Tatarakis, K. Krushelnick, P. Gibbon, E. L. Clark, R. G. Evans, K. L. Lancaster, P. A. Norreys, K. W. D. Ledingham, P. McKenna, and M. Zepf, *Target charging effects on proton acceleration during high-intensity short-pulse laser-solid interactions*, Applied Physics Letters **84**, 2766 (2004).
- [188] I. H. Hutchinson, *Principles of Plasma Diagnostics*, Cambridge University Press, 2nd. Ed. (2002).

- [189] J. A. Stamper, E. A. McLean, and B. H. Ripin, *Studies of Spontaneous Magnetic-Fields in Laser-Produced Plasmas by Faraday-Rotation*, Physical Review Letters **40**, 1177 (1978).
- [190] A. Raven, O. Willi, and P. T. Rumsby, *Megagauss Magnetic-Field Profiles in Laser-Produced Plasmas*, Physical Review Letters **41**, 554 (1978).
- [191] M. A. Yates, D. B. Vanhulsteyn, H. Rutkowski, G. Kyrala, and J. U. Brackbill, *Experimental-Evidence for Self-Generated Magnetic-Fields and Remote Energy Deposition in Laser-Irradiated Targets*, Physical Review Letters **49**, 1702 (1982).
- [192] *Center for x-ray optics: www-cxro.lbl.gov* (2007).
- [193] A. Schiavi, *Study of laser produced plasmas by x-ray and proton radiography*, PhD thesis, University of London (2003).
- [194] P. M. Nilson, L. Willingale, M. C. Kaluza, C. Kamperidis, S. Minardi, M. S. Wei, P. Fernandes, M. Notley, S. Bandyopadhyay, M. Sherlock, R. J. Kingham, M. Tatarakis, Z. Najmudin, W. Rozmus, R. G. Evans, M. G. Haines, A. E. Dangor, and K. Krushelnick, *Magnetic reconnection and plasma dynamics in two-beam laser-solid interactions*, Physical Review Letters **97**, 255001 (2006).
- [195] M. G. Haines, *Thermal-Instability and Magnetic-Field Generated by Large Heat-Flow in a Plasma, Especially under Laser-Fusion Conditions*, Physical Review Letters **47**, 917 (1981).
- [196] C. P. Ridgers and R. J. Kingham, *Magnetic Field Dynamics and Non-Local Transport in Laser Plasmas*, submitted to Physical Review Letters (2007).
- [197] M. E. Jones, D. Winske, S. R. Goldman, R. A. Kopp, V. G. Rogatchev, S. A. Belkov, P. D. Gasparyan, G. V. Dolgoleva, N. V. Zhidkov, N. V. Ivanov, Y. K. Kochubej, G. F. Nasyrov, V. A. Pavlovskii, V. V. Smirnov, and Y. A. Romanov, *Modeling ion interpenetration, stagnation, and thermalization in colliding plasmas*, Physics of Plasmas **3**, 1096 (1996).

- [198] C. K. Li, F. H. Seguin, J. A. Frenje, J. R. Rygg, R. D. Petrasso, R. P. J. Town, O. L. Landen, J. P. Knauer, and V. A. Smalyuk, *Observation of Megagauss-Field Topology Changes due to Magnetic Reconnection in Laser-Produced Plasmas*, Physical Review Letters **99**, 055001 (2007).
- [199] *Astra Gemini Project: www.clf.rl.ac.uk* (2007).
- [200] R. M. Stevenson, M. J. Norman, T. H. Bett, D. A. Pepler, C. N. Danson, and I. N. Ross, *Binary-Phase Zone-Plate Arrays for the Generation of Uniform Focal Profiles*, Optics Letters **19**, 363 (1994).